Hydrological Processes in a High Alpine Watershed

THÈSE N^O 6534 (2015)

PRÉSENTÉE LE 13 MARS 2015

À LA FACULTÉ DE L'ENVIRONNEMENT NATUREL, ARCHITECTURAL ET CONSTRUIT

LABORATOIRE DE MÉCANIQUE DES FLUIDES DE L'ENVIRONNEMENT

PROGRAMME DOCTORAL EN GÉNIE CIVIL ET ENVIRONNEMENT

ÉCOLE POLYTECHNIQUE FÉDÉRALE DE LAUSANNE

POUR L'OBTENTION DU GRADE DE DOCTEUR ÈS SCIENCES

PAR

Raphaël MUTZNER

acceptée sur proposition du jury:

Prof. A. Berne, président du jury
Prof. M. Parlange, directeur de thèse
Prof. A. Rinaldo, rapporteur
Prof. J. Szilagyi, rapporteur
Prof. P. Tarolli, rapporteur

A Marina, Leo et Liselotte

Acknowledgements

Résumé

L'hydrologie alpine est une science particulièrement difficile en raison de la complexité du terrain montagneux et de la variabilité spatiale et temporelle des paramètres météorologiques tels que la précipitation, la température et l'évaporation. Mesurer le cycle de l'eau en altitude reste une tâche ardue et peu de bassins versants alpins sont intensivement suivis. Pourtant, améliorer la compréhension des processus hydrologiques dans les régions alpines est essentiel dans la gestion des ressources en eau et la protection contre les dangers naturels. Depuis 2009, le bassin versant du haut Val Ferret dans les Alpes suisses en Valais est équipé de nombreux et divers instruments afin de mesurer des paramètres hydrologiques, météorologiques et pédologiques à une haute résolution temporelle et spatiale. Dans ce travail, nous utilisons les données récoltées au cours de trois campagnes de mesures estivales de 2011 à 2013. Nous avons déployé un réseau sans fil de stations météorologiques, mesuré continuellement le débit de la rivière à trois endroits différents et utilisé un modèle numérique de terrain à un mètre de résolution. En particulier, nous nous sommes intéressés à l'influence de la géomorphologie sur différents processus hydrologiques.

La complexité topographique et géomorphologique du bassin versant du Val Ferret est illustrée par la structure du réseau hydrographique qui a été minutieusement relevé sur le terrain. La distribution spatiale du réseau hydrographique est particulièrement hétérogène, notamment dans certaines parties où la densité de sources d'eau souterraine et de rivières pérennes est particulièrement élevée. Les méthodes classiques d'extraction du réseau hydrographique à l'aide du modèle numérique de terrain ne sont pas capables de reproduire cette variabilité spatiale. Celle-ci a cependant eu un impact significatif sur la modélisation des hydrogrammes de crue. Ceux simulés avec les réseaux hydrographiques des différentes méthodes d'extraction reproduisent tous correctement le *timing* du pic de la crue mais pas sa partie décroissante.

Les périodes de tarissement sont définies comme des épisodes sans pluie durant lesquelles la réserve d'eau souterraine diminue et le débit décroit. Leurs liens avec la géomorphologie du bassin versant est analysé en détail. Nous proposons un modèle conceptuel simple basé sur une étude récente où l'évolution du réseau hydrographique est simulée et comparée à une paramétrisation classique des courbes de tarissement. En particulier, nous avons démontré que la variabilité spatiale du réseau hydrographique joue un rôle prépondérant dans les courbes de tarissement.

De plus, nous avons analysé en détail les fluctuations journalières du débit survenant durant les périodes de tarissement. Dans un des sous bassin versant, nous avons observé un cycle de débit diurne induit principalement par l'évaporation d'eau dans la zone riveraine. Dans un autre sous bassin versant, nous avons observé un cycle de débit induit par la fonte d'un petit glacier. Les deux cycles surviennent à des heures similaires mais sont de signe opposé. Durant les campagnes de mesures précédentes, le cycle induit par l'évaporation n'a jamais été observé à l'exutoire du bassin du Val Ferret vu son amplitude inférieur à l'amplitude du cycle dû à la fonte de glace. En analysant minutieusement la géomorphologie de la zone riveraine induisant le cycle d'évaporation, nous avons pu déduire combien d'eau a dû fondre du glacier en tenant compte d'une composante d'évaporation dans le cycle de débit diurne de fonte de glace.

Afin de mieux comprendre la formation de crues, nous avons finalement étudié en détails la relation entre certains paramètres pédologiques et des caractéristiques de l'hydrogramme de crue. Nous avons observé un comportement de seuil entre le potentiel matriciel préalable à l'averse et les coefficients d'écoulement. Au-dessus du seuil de potentiel matriciel, les coefficients d'écoulement augmentent et la réponse du bassin versant devient plus courte. Contrairement à de nombreuses études récentes, nous n'avons pas observé de comportement de seuil entre l'humidité du sol préalable à l'averse et les coefficients d'écoulement. Nos résultats indiquent que les effets d'hystérèse dans la teneur en eau dans le sol pourraient jouer un rôle prépondérant dans l'augmentation du débit lors d'épisodes pluvieux. Ces effets non linéaires ne sont pas encore bien compris et nécessitent plus de recherche afin de pouvoir les implémenter correctement dans les modèles hydrologiques.

Mots clefs : Hydrologie alpine, hydrologie du bassin versant, Géomorphologie, terrain complexe, mesure de débit, modèle numérique de terrain, réseau hydrographique, période de tarissement, cycles diurnes, évaporation, réseau de capteurs sans fil.

Abstract

Alpine hydrology is particularly challenging due to the complexity of mountainous terrain and the spatial and temporal variability of meteorological parameters such as precipitation, temperature and evaporation. Sensing the hydrosphere in high altitude areas remains a tough task and few alpine watersheds have been intensively monitored. Yet improving our understanding of hydrological processes in alpine regions is critical for freshwater management and for protection against natural hazards. Since 2009, the upper Val Ferret watershed (20.4 km^2) in the Swiss Alps is monitored with a large variety of instruments to measure hydrological, meteorological and pedological parameters at high temporal and spatial resolution. In this dissertation, the data collected during three consecutive summer field campaigns from 2011 to 2013 has been utilized. We deployed a wireless network of meteorological stations, continuously measured the stream discharge at three locations and made use of a one meter resolution Digital Elevation Model of the watershed. In particular, we focused on the influence of the geomorphology on several streamflow generation processes.

The topographical and geomorphological complexity of the Val Ferret watershed is illustrated by the structure of the channel network, which was carefully mapped in the field. The spatial distribution of the channel network was particularly heterogeneous, with certain areas characterized by a high density of groundwater channel heads and perennial streams. This highly uneven drainage density had a significant impact on modeling storm hydrographs. Other channel networks, extracted from the Digital Elevation Model using classical methods, were not able to capture this spatial variability. More advanced extraction techniques relying on curvature and openness showed superior efficacy. The hydrograph estimated with the different networks were all able to capture the discharge peak timing but not the recession parts.

Recession events are defined as periods without precipitation during which water stored in the watershed is released and the streamflow is in decline. Although they have been widely studied previously, we have analyzed their link to the basin geomorphology in detail. Based on a recent study, we propose a simple conceptual model in which the temporal variation of the river network is computed and linked to a classic power law parametrization of recession curves. In particular, we show that in high altitude watersheds, the spatially heterogeneous structure of the channel network could play a major role in the streamflow recession.

Furthermore, we analyzed daily streamflow fluctuations that occurred during recession events

Abstract

in the upper Val Ferret watershed. In one of the monitored sub basins, we observed that evaporation from the perennial riparian area was inducing a diurnal streamflow cycle. In another sub basin, we observed a diurnal streamflow cycle induced by ice melt from a small glacier. Both cycles occurred at similar times of the day but with perturbations in opposite directions. However, the evaporation induced streamflow cycle was never observed at the outlet of the watershed as the amplitude of the glacier-fed ice cycle was larger than the one due to evaporation. By analyzing cautiously the geomorphology of the riparian area contributing to the evaporation cycle, we assessed how much water must have melted from the glacier to produce the observed diurnal cycle, given that it is damped by evaporation.

Finally, in order to better understand streamflow generation during precipitation events, we performed an extensive assessment of the relation between antecedent soil water state and stormflow characteristics. We observed previously unreported threshold relations between antecedent soil water potential and runoff coefficients above which runoff coefficients were increasing and the response time of the catchment shortened. Unlike many recent studies, we did not observe threshold behaviors between antecedent soil moisture and runoff coefficients. Our results suggest that hysteresis effects in the hillslopes might play a dominant role in streamflow generation during precipitation events. These nonlinearities are still poorly understood and need to be investigated further before they can be appropriately incorporated into hydrological models.

Key words: Alpine Hydrology, catchment hydrology, Geomorphology, complex terrain, streamflow generation, Digital Elevation Model, drainage network, recession events, diurnal cycles, evaporation, threshold behavior, wireless sensor network.

Contents

Contents

1 Introduction

Our understanding of hydrological processes and ability to predict the discharge in mountainous regions are essential to face societal challenges regarding freshwater management, protection against natural hazards such as floods and droughts or for hydropower production, especially in the actual context of climate change. To tackle those challenges, the use of basin-scale hydrological models has become widespread. In the last several decades, spatially explicit models, also referred to as distributed models, have received increasing interest due to growing computational power and to the advent of numerous technologies allowing us to better sense the hydrosphere (*Beven*, 2011). Yet, simulating the discharge from mountainous watersheds remains an open challenge in the field of hydrology. First, our ability to run distributed hydrological models in mountainous areas is hampered by *the complex structure of the watershed*, epitomized by the heterogeneous nature of its geomorphology, geology, topography, vegetation cover and soils. Second, *the spatial variability* of the forcing fluxes such as rainfall, snowfall and evaporation is difficult to capture in mountainous areas, which is often recognized to be among the main limitations of distributed models performance and robustness (*Beven*, 2011, Chap. 3). In this dissertation, these two critical aspects are treated and exemplified by an extensive study of a high altitude alpine watershed in Switzerland. The complex structure of the catchment is analyzed through its geomorphology and the spatial variability of meteorological parameters partially captured through an ambitious distributed monitoring campaign. Both aspects are developed in the following.

1.1 Basin Geomorphology and Catchment Hydrology

In mountainous areas, the study of the basin geomorphology is of crucial importance for hydrological modeling. Indeed, the streamflow response of a mountainous watershed is strongly influenced by topographic controls such as elevation gradient, aspect or curvature, all reflecting the geomorphology of the basin. For instance, at the hillslope scale, the snow or ice melt rates are mainly governed by the orientation and steepness of the slope which affect the total energy balance locally (*Lehning et al.*, 2006). The rainfall-runoff response of steep hillslopes is also partially controlled by topography. Indeed, it is widely known

that subsurface flow is the dominant process in steep hillslopes compared to infiltration excess overland flow or saturation excess overland flow (*Brutsaert* (2005, Chap. 11) and *Dunne* (1978)). However, the rainfall-runoff response at the hillslope scale or headwater scale of mountainous areas is not fully understood yet but considerable advances were achieved in the last decades through the use of natural or artificial tracers. In that context, experimental sites like Maimai in New Zealand, Panola in Georgia or HJ Andrews and Low Pass in Oregon (just to cite a few) have characterized and demonstrated the importance of macropores, preferential flow paths or flow at the bedrock interface for stormflow generation. This led to important debates in the hydrological community related to residence times in catchments (*Botter et al.*, 2010; *McDonnell*, 2003; *McDonnell et al.*, 2010). Recently, several studies also underlined the importance of non-linearities in rainfall runoff responses, leading to new concepts of stormflow generation (*Spence and Woo*, 2003; *Tromp-van Meerveld and McDonnell*, 2006; *Lin*, 2010; *Sidle et al.*, 2001).

However, upscaling our understanding of processes from the hillslope to the catchment scale remains critical for modeling purposes and is a very active area of research in hydrology (*Tetzlaff et al.*, 2008). In that context and even more for mountainous areas, the geomorphology of the basin, described through a high resolution Digital Elevation Model (DEM), is certainly key to upscale our understanding of hydrological processes. In hydrology, the geomorphology of the basin has been mainly studied through the structure and features of the channel network (*Horton*, 1932, 1945; *Rodriguez-Iturbe and Rinaldo*, 2001; *Strahler*, 1952) and through the geomorphologic theory of the unit hydrograph (*Rodriguez-Iturbe and Valdes*, 1979) which is still widely applied in rainfall-runoff modeling (*Rinaldo et al.*, 2006a,b; *Schaefli et al.*, 2014). In that context, the introduction of DEMs has enabled deeper insights in the structure of channel network and flow paths.

Whereas DEMs were obtained by interpolating contour lines, nowadays airborne or terrestrial LiDAR (Light and Detection RAnging) are used to produce DEM with a resolution of few meters and even less (*Tarolli*, 2014). At national scales, high resolution models are now also provided (50 m in the UK and France, 30 m in the USA, 10 m in Italy, 25 m overall in Switzerland and 2 m below 2000 m above sea level). These high resolution DEMs allow defining the shape of the hillslope accurately and getting new insights of flow pathways from the hillslope to the stream. This was not the case before with coarser DEMs, especially in mountainous regions where the elevation gradients can be in the same order of magnitude as the DEM resolution.

An essential point in the analysis of a DEM remains the distinction between hillslope and channel network, which is a necessary step in running a distributed or semi-distributed hydrological model. The classical and most widely used methods consist of pit removal, computation of flow direction based on several algorithms (*O'Callaghan and Mark*, 1984; *Quinn et al.*, 1991; *Tarboton*, 1997) and determination of the area draining in each cell of the DEM. The channel network is then obtained by selecting a threshold based on drainage area and/or local slope. However, classical methods rely on a unique threshold for channel initiation in the entire catchment, but several studies recently reported that such a unique

threshold does not exist (*Tarolli*, 2014). New methods relying on high resolution DEMs are able to extract channel network that are spatially very heterogeneous (*Tarolli*, 2014). Accurate representation of the channel network together with high resolution DEMs have also brought new insights in distributed riparian zone estimation (*McGlynn and Seibert*, 2003), flowpaths distributions (*Tucker et al.*, 2001) and enabled exploring new links between geomorphology and stream temperature (*Comola et al.*, 2015) or geomorpholgy and baseflow recessions (*Biswal and Marani*, 2010).

1.2   Distributed monitoring

One of the basic rules in mountaineering taught by one's father or grandfather is to always carry an impermeable layer for any outing, short or long. In these environments, temporal and spatial variability of meteorological conditions is an old and well known fact. However, quantifying the spatial variability of precipitation (liquid or solid), evaporation, wind speed and direction or even just temperature remains challenging in alpine environments (*Huwald et al.*, 2009). Besides from feeding spatially explicit hydrological models with distributed forcing fluxes and boundary conditions, distributed monitoring of hydrological, meteorological and pedological parameters have the potential to further increase our understanding of streamflow generation, storage dynamics and transit times at the catchment scale.

Among the recent developments in sensing the hydrosphere, the most spectacular advances have probably been realized with remote sensing techniques. Large datasets provided by satellites provide regular information of hydrological states, inputs and outputs such as soil moisture, snow cover, precipitation, surface temperature or evaporation. However, the spatio-temporal resolution of the dataset makes them usually inappropriate for use in alpine environments (*Botteron et al.*, 2013). Concerning precipitation datasets, many national weather forecast institutions now also provide measurements obtained with ground-based radars. Their spatial (1 to 4 km) and temporal (5-15 min) resolutions make them particularly adapted to applications in high altitude landscapes. However, radar based precipitation measurements remain very challenging in mountainous areas due, among others, to ground clutter or vertical variability of precipitation (*Germann et al.*, 2006). Moreover, radar measurements are usually corrected for global bias with "ground truth" adjustments measured by rain gauges, which are also source of severe errors, typically due to wind effects.

In smaller mountainous areas, there is a need for higher spatial resolution for hydrological applications and recent advances were achieved in that sense. For instance, new applications of Raman scattering distributed temperature sensing (DTS) by fiber-optic cables have recently shown considerable promise in snow pack or streamwater monitoring (*Selker et al.*, 2006), river-groundwater interactions (*Briggs et al.*, 2012) or in indirect soil moisture estimations (*Ciocca et al.*, 2012). Recent advances in LiDAR also provide wind and temperature fields of unprecedented resolutions to probe the atmospheric boundary layer (*Froidevaux et al.*, 2013). However, among the recent developments, wireless sensor networks that can be deployed

in the field have drawn particular attention in catchment hydrology. Indeed, wireless sensor networks allow to spatially monitoring parameters such as precipitation, temperature, wind speed and direction, radiation, snow or water level. Nowadays, those networks are self-organized with multihop routing which makes them particularly suited for deployment in harsh conditions. Besides their affordable costs, wireless sensor networks have proven to be of great potential for hydrometeorological studies in alpine catchments (*Simoni et al.*, 2011; *Tobin et al.*, 2013), forested catchments (*Trubilowicz et al.*, 2009), or in urban areas allowing estimation of sensible heat fluxes at high spatial resolution (*Nadeau et al.*, 2009). Moreover, open-source platforms for micro-controllers such as *Arduino* or *Raspberry pi* systems are now very well documented and will help for further developing wireless sensor networks at very low costs.

1.3 The upper Val Ferret catchment

Though many "instrumented" watersheds exist, there has been relatively few intensive field sensor deployments in high alpine landscapes where distributed measurements of evaporation, precipitation, snow melt, local energy and stream discharge were undertaken. In 2009, the Environmental FLUid Mechanics (EFLUM) laboratory decided to undertake a long term monitoring campaign in the Swiss Alps. There were several major constraints for choosing a field site: 1) find a site with very little anthropogenic influence, 2) have a sufficient cell-phone network coverage to run real time monitoring devices and 3) find a site close enough to Lausanne for logistical reasons. However, in a land where more than half of the electricity is produced by hydropower facilities, the first point was certainly a large constraint and the upper part of the Val Ferret quickly became an evidence.

The Val Ferret catchment is located in the southernmost ridge of the Swiss Alps bordering Italy, covering a total area of 20.4 km^2 with elevation ranging from 1773 m above sea level (asl) at the outlet, to 3236 m asl at the highest point (mean elevation is 2423 m asl). The slopes are moderate to steep (mean 31.6°, maximum 88.9°). The land cover of the watershed consists mainly of mountain grassland (58%), bedrock outcrops (24.7%), rocks (12.7%), shrubs (2%), a small glacier (*Glacier des Angroniettes*, 2%) and three small lakes (*Lacs de Fenêtre*, 0.2%). The riparian area of the watershed is mainly composed of grassland, moss and debris but almost no vegetation with deep roots. The geology of the site is complex, the strata consist mainly of sedimentary shale, quartzite, limestone and sandstone. The analysis of several soil samples revealed a dominance of sandy silt loam and light clay type of soils. Apart from a small drinking water intake of maximum 17 l/s and the presence of two cow herds during summer, there is very little anthropogenic influence on the hydrologic streamflow regime. Individual maps showing the land use of the watershed will be presented in specific chapters of the dissertation.

Since 2009, small automatic meteorological stations have been deployed in the Val Ferret watershed, whereas in parallel, similar stations were also deployed by the EFLUM laboratory in

Burkina Faso (*Ceperley*, 2014; *Mande*, 2013). The stations form a multi-hop and self organized wireless network and rely on Sensorscope technology (*Ingelrest et al.*, 2010), an EPFL spin-off. All the stations are powered with solar panels and transmit their data to a master station which in turn transmit the data to a server through GPRS connection, allowing for quasi real-time monitoring. The meteorological stations typically include measurements of air temperature, humidity, wind speed and direction, incoming shortwave radiation, surface skin temperature, soil moisture and temperature, soil water potential and rainfall gauge (see Figure 1.1 for an illustration). During the period of this dissertation, three field campaigns were undertaken with the deployment of 26 stations in 2011, 25 in 2012 and 20 in 2013, installed from early Summer until late Fall.

<div align="center">(a)   (b)</div>
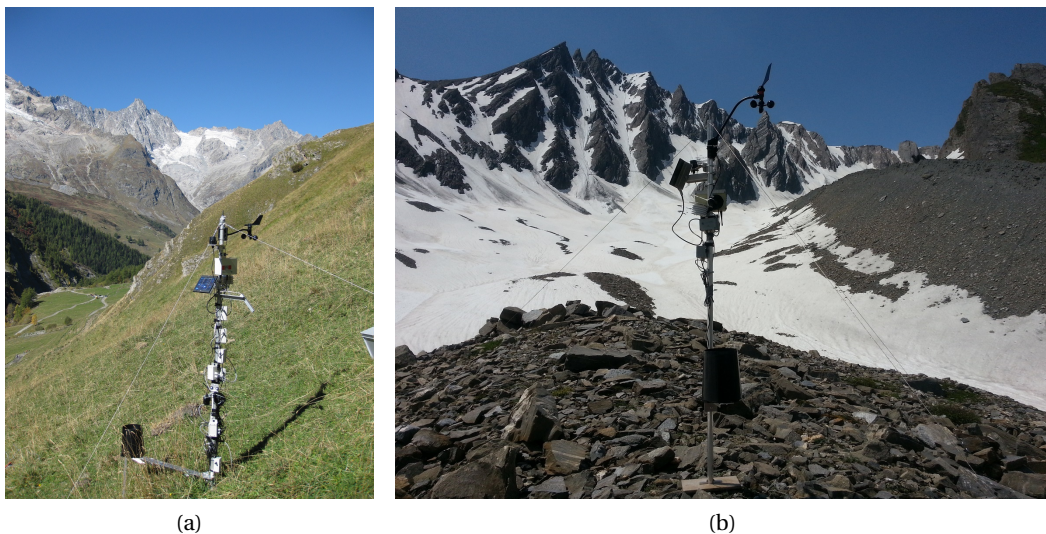
Figure 1.1: Examples of Sensorscope stations (a) close to the outlet of the watershed and (b) close to the *Glacier des Angroniettes.*

The stream water levels were monitored at the outlet of the catchment and at a location 2.9 km upstream of the outlet. During 2012, a third location was also monitored, 2.1 km upstream of the outlet. Water levels were recorded at a temporal resolution of one sample every 5 minutes using pressure sensors (HyMADD, MADD Technologies Sàrl, Switzerland). The data were retrieved on a bi-weekly basis to avoid measurements gaps, errors, thermal effects and seasonal drift (*Cuevas et al.*, 2010; *McLaughlin and Cohen*, 2011). Due to restrictions in the area, it was not possible to install a weir in the stream. Because of year-to-year changes in the streambed, a rating curve had to be computed for each field campaign. The streamflow Q was obtained with the salt dilution technique (*Rantz*, 1982; *Weijs et al.*, 2013) and measured on a bi-weekly basis for establishing a rating curve of the different gauging sites. The largest changes in the streambed occurred during spring and not during the deployments so that the coefficients of the stage-discharge relationship were considered valid and constant during each deployment.

The hydrologic regime of the watershed is largely influenced by snow accumulation. The climate of the watershed is characterized by a long winter where permanent snow cover becomes significant in December and lasts until mid-summer. Spring period runoff is typically snowmelt dominated and summer is generally mild with occasional thunderstorms and typically low-base flows. Heavy rains, and occasional snowfalls, become more regular and important in autumn. In a first study realized in 2010, *Simoni et al.* (2011) applied a simple lumped hydrological model to analyze the streamflow dynamics of the watershed. The discharge was decomposed in four main reservoirs: snowmelt, icemelt due to the presence of the small glacier, baseflow and rainfall-runoff response. In particular, the snow and ice components were simulated with a simple degree-day model (*Hock*, 2003) with a melt factor that was constant during the season. Moreover, the icemelt component was found to be quite constant during the entire deployment and was well captured by the degree day model. The results of the simulation are shown in Figure 1.2. The spatial variability of air temperature and precipitation was also studied in terms of distance and aspect. The Val Ferret watershed has also been chosen to study katabatic and anabatic flows on steep slopes (*Nadeau et al.*, 2013; *Oldroyd et al.*, 2014).
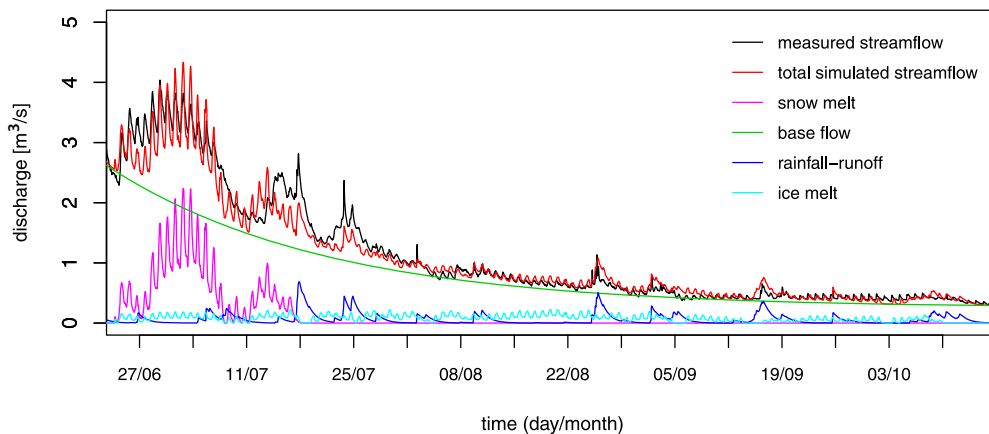
Figure 1.2: Main components of the streamflow as simulated by *Simoni et al.* (2011) for the 2010 field campaign with a simple lumped hydrological model.

Finally, a LiDAR based DEM of one meter resolution has been acquired in August 2010 by the company Helimap System SA. The LiDAR data was acquired from a helicopter using a Riegl VQ-480, flying at an altitude of 500 meters above ground on a clear sky and snow-free day. The flying speed was around 45 knots, the scan angle was 60° and the pulse frequency used was of 25 kHz. The survey point density was specified to 4-5 points/m^2, with an absolute vertical and horizontal accuracy of respectively 10 cm and 15 cm. Vegetation and bare ground points were filtered using the ground routine of the Terrascan® software.

1.4 Research questions and organization of the thesis

The overall objective of the present dissertation is to improve our understanding of streamflow generation in the Val Ferret experimental watershed, seen as a representative high altitude alpine catchment. To that end, a multi-year field observation campaign with selective intensive monitoring periods has been undertaken to further increase our understanding of the dominant processes affecting the monitored hydrograph. Given its importance for any alpine watershed, the geomorphology of the Val Ferret basin is studied in details and its influence on streamflow generation is deciphered. Figure 1.3 illustrates the main hydrological processes addressed in this dissertation and how they are related to the monitored hydrograph.
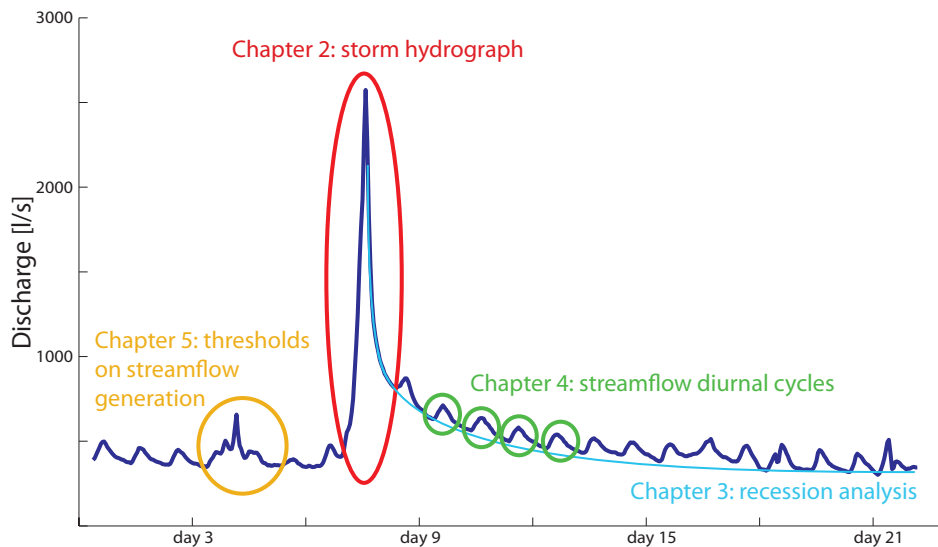
Figure 1.3: Illustration of the processes studied in the different chapters of the thesis and their link to the hydrograph.

In Chapter 2, we extensively study the channel network that was carefully mapped in the field and extracted from the one meter resolution DEM. A particular attention is paid to the key role of spatially heterogeneous drainage density on distributed hydrological modeling. We address the following questions: (i) Are classical channel network extraction methods and more advanced techniques able to reproduce key geomorphological features of the monitored/true network? (ii) What is the influence of the channel network on the hydrological response of the watershed during storm events? (iii) Is it possible to separate the perennial and intermittent portions of the channel network automatically? The channel network obtained in this chapter serves as a basis for the two following chapters.

In Chapter 3, we investigate possible links between basin geomorphology and base flow recession curves. A widely used method linking discharge to temporal discharge variation during recession events (*Brutsaert and Nieber*, 1977) is applied to study base flow features of the Val Ferret and 26 other catchments located in Switzerland. A new conceptual model

inspired by a recent study (*Biswal and Marani*, 2010) is proposed to describe the impact of the basin geomorphology on the recession curves. It is based solely on the analysis of the basin DEM through the temporal evolution of the stream network. The questions we address are: (i) Do catchment recession curves bare the signature of geomorphology? (ii) Can we predict base flow features for ungauged basins through the analysis of a DEM? (iii) Is there a unique Storage-Discharge relation in a basin?

In Chapter 4, we analyze in details two types of streamflow diurnal cycles observed in the Val Ferret catchment. In one monitored sub basin, the streamflow diurnal cycle was dominated by evaporation whereas ice melt from the glacier was mainly feeding the diurnal cycle observed in another sub basin of the watershed. However, earlier results suggested that the streamflow diurnal cycle observed at the outlet were solely due to snow or ice melt (*Simoni et al.*, 2011). The questions addressed in this Chapter are the following: (i) Is the ice melt induced diurnal streamflow cycle affected by the evaporation-induced diurnal streamflow cycle? (ii) What and where is the area contributing to the evaporation-induced diurnal streamflow cycle?

In Chapter 5, we study the influence of antecedent soil moisture and soil water potential on streamflow generation during precipitation events. The soil moisture and soil water potential data were obtained from the wireless network of meteorological stations equipped with soil sensors. The questions we address are the followings: (i) Is there a threshold controlling runoff response in the Val Ferret watershed? (ii) What is the influence of soil moisture and soil water potential on runoff generation? (iii) Are the streamflow generation mechanisms similar for wet or dry antecedent conditions?

Finally, the main findings of this dissertation are presented in Chapter 6 along with recommendations for future study in the Val Ferret watershed or any experimental alpine catchment.

Bibliography

Beven, K. (2011), *Rainfall-Runoff Modelling: The Primer, 2nd ed.*, 2nd ed. ed., Wiley-Blackwell, Chichester, U.K.

Biswal, B., and M. Marani (2010), Geomorphological origin of recession curves, *Geophysical Research Letters*, *37*(24), doi:10.1029/2010gl045415.

Botter, G., E. Bertuzzo, and A. Rinaldo (2010), Transport in the hydrologic response: Travel time distributions, soil moisture dynamics, and the old water paradox, *Water Resources Research*, *46*(3), doi:10.1029/2009wr008371.

Botteron, C., N. Dawes, J. Leclère, J. Skaloud, S. V. Weijs, and P.-A. Farine (2013), Soil moisture & snow properties determination with GNSS in alpine environments: Challenges, status, and perspectives, *Remote Sensing*, *5*(7), 3516–3543, doi:10.3390/rs5073516.

Briggs, M. A., L. K. Lautz, and J. M. McKenzie (2012), A comparison of fibre-optic distributed temperature sensing to traditional methods of evaluating groundwater inflow to streams, *Hydrological Processes*, *26*(9), 1277–1290, doi:10.1002/hyp.8200.

Brutsaert, W. (2005), *Hydrology: An Introduction*, Cambridge University Press.

Brutsaert, W., and J. L. Nieber (1977), Regionalized drought flow hydrographs from a mature glaciated plateau, *Water Resources Research*, *13*(3), 637–643, doi:10.1029/WR013i003p00637.

Ceperley, N. (2014), Ecohydrology of a Mixed Savanna-Agricultural Catchment in South-East Burkina Faso, West Africa, Ph.D. thesis, École Polytechnique Fédérale de Lausanne, doi: doi:10.5075/epfl-thesis-6040.

Ciocca, F., I. Lunati, N. Van de Giesen, and M. B. Parlange (2012), Heated optical fiber for distributed soil-moisture measurements: A lysimeter experiment, *Vadose Zone Journal*, *11*(4), doi:doi:10.2136/vzj2011.0199.

Comola, F., B. Schaefli, A. Rinaldo, and M. Lehning (2015), Thermodynamics in the hydrologic response: Travel time formulation and application to Alpine catchments, *Water Resources Research*, doi:10.1002/2014WR016228.

Bibliography

Cuevas, J., M. Calvo, C. Little, M. Pino, and P. Dassori (2010), Are diurnal fluctuations in streamflow real?, *Journal of Hydrology and Hydromechanics*, *58*(3), 149–162, doi:10.2478/v10098-010-0014-0.

Dunne, T. (1978), Field studies of hillslope flow processes, in *Hillslope Hydrology*, edited by M. Kirkby, pp. 227–293, John Wiley & Sons.

Froidevaux, M., C. W. Higgins, V. Simeonov, P. Ristori, E. Pardyjak, I. Serikov, R. Calhoun, H. van den Bergh, and M. B. Parlange (2013), A Raman lidar to measure water vapor in the atmospheric boundary layer, *Advances in Water Resources*, *51*(0), 345 – 356, doi:10.1016/j.advwatres.2012.04.008.

Germann, U., G. Galli, M. Boscacci, and M. Bolliger (2006), Radar precipitation measurement in a mountainous region, *Quarterly Journal of the Royal Meteorological Society*, *132*(618), 1669–1692, doi:10.1256/qj.05.190.

Hock, R. (2003), Temperature index melt modelling in mountain areas, *Journal of Hydrology*, *282*(1 - 4), 104 – 115, doi:10.1016/S0022-1694(03)00257-9.

Horton, R. (1932), Drainage basin characteristics, *Transactions of the American Geophysical Union*, *13*, 350–361.

Horton, R. (1945), Erosional development of streams and their drainage basins; hydrophysical approach to quantitative morphology, *Geological Society of America Bulletin*, *56*(3), 275–370.

Huwald, H., C. W. Higgins, M.-O. Boldi, E. Bou-Zeid, M. Lehning, and M. B. Parlange (2009), Albedo effect on radiative errors in air temperature measurements, *Water Resources Research*, *45*(8), doi:10.1029/2008WR007600.

Ingelrest, F., G. Barrenetxea, G. Schaefer, M. Vetterli, O. Couach, and M. B. Parlange (2010), SensorScope: Application-Specific Sensor Network for Environmental Monitoring, *ACM Trans. Sen. Netw.*, *6*(2), 1–32, doi:10.1145/1689239.1689247.

Lehning, M., I. Vöksch, D. Gustafsson, T. A. Nguyen, M. Stähli, and M. Zappa (2006), ALPINE3D: a detailed model of mountain surface processes and its application to snow hydrology, *Hydrological Processes*, *20*(10), 2111–2128, doi:10.1002/hyp.6204.

Lin, H. (2010), Linking principles of soil formation and flow regimes, *Journal of Hydrology*, *393*(1–2), 3 – 19, doi:10.1016/j.jhydrol.2010.02.013.

Mande, T. (2013), Hydrology of the Sudanian Savannah in West Africa, Burkina Faso, Hydrology, École Polytechnique Fédérale de Lausanne, doi:doi:10.5075/epfl-thesis-6011.

McDonnell, J. J. (2003), Where does water go when it rains? Moving beyond the variable source area concept of rainfall-runoff response, *Hydrological Processes*, *17*(9), 1869–1875, doi:10.1002/hyp.5132.

McDonnell, J. J., K. McGuire, P. Aggarwal, K. J. Beven, D. Biondi, G. Destouni, S. Dunn, A. James, J. Kirchner, P. Kraft, S. Lyon, P. Maloszewski, B. Newman, L. Pfister, A. Rinaldo, A. Rodhe, T. Sayama, J. Seibert, K. Solomon, C. Soulsby, M. Stewart, D. Tetzlaff, C. Tobin, P. Troch, M. Weiler, A. Western, A. Wörman, and S. Wrede (2010), How old is streamwater? Open questions in catchment transit time conceptualization, modelling and analysis, *Hydrological Processes*, *24*(12), 1745–1754, doi:10.1002/hyp.7796.

McGlynn, B. L., and J. Seibert (2003), Distributed assessment of contributing area and riparian buffering along stream networks, *Water Resources Research*, *39*(4), doi:10.1029/2002WR001521.

McLaughlin, D. L., and M. J. Cohen (2011), Thermal artifacts in measurements of fine-scale water level variation, *Water Resources Research*, *47*(9), doi:10.1029/2010WR010288.

Nadeau, D., W. Brutsaert, M. Parlange, E. Bou-Zeid, G. Barrenetxea, O. Couach, M. O. Boldi, J. Selker, and M. Vetterli (2009), Estimation of urban sensible heat flux using a dense wireless network of observations, *Environmental Fluid Mechanics*, *9*(6), 635–653, doi:10.1007/s10652-009-9150-7.

Nadeau, D. F., E. R. Pardyjak, C. W. Higgins, H. Huwald, and M. B. Parlange (2013), Flow during the evening transition over steep Alpine slopes, *Quarterly Journal of the Royal Meteorological Society*, *139*(672), 607–624, doi:10.1002/qj.1985.

O'Callaghan, J. F., and D. M. Mark (1984), The extraction of drainage networks from digital elevation data, *Computer Vision, Graphics, and Image Processing*, *28*(3), 323–344, doi:10.1016/s0734-189x(84)80011-0.

Oldroyd, H. J., G. Katul, E. R. Pardyjak, and M. B. Parlange (2014), Momentum balance of katabatic flow on steep slopes covered with short vegetation, *Geophysical Research Letters*, *41*(13), 4761–4768, doi:10.1002/2014GL060313.

Quinn, P., K. Beven, P. Chevallier, and O. Planchon (1991), The prediction of hillslope flow paths for distributed hydrological modelling using digital terrain models, *Hydrological Processes*, *5*(1), 59–79, doi:10.1002/hyp.3360050106.

Rantz, S. (1982), Measurement and computation of streamflow; Volume 1, measurement of stage and discharge; volume 2, computation of discharge, *US Geological Survey water-supply paper*, *2175*, 631.

Rinaldo, A., G. Botter, E. Bertuzzo, A. Uccelli, T. Settin, and M. Marani (2006a), Transport at basin scales: 1. Theoretical framework, *Hydrology and Earth System Sciences*, *10*(1), 19–29, doi:10.5194/hess-10-19-2006.

Rinaldo, A., G. Botter, E. Bertuzzo, A. Uccelli, T. Settin, and M. Marani (2006b), Transport at basin scales: 2. Applications, *Hydrology and Earth System Sciences*, *10*(1), 31–48, doi:10.5194/hess-10-31-2006.

Bibliography

Rodriguez-Iturbe, I., and A. Rinaldo (2001), *Fractal river basins: chance and self-organization*, 547 pp., Cambridge Univ Pr, Cambridge, UK.

Rodriguez-Iturbe, I., and J. B. Valdes (1979), The geomorphologic structure of hydrologic response, *Water Resources Research*, *15*(6), 1409–1420, doi:10.1029/WR015i006p01409.

Schaefli, B., L. Nicótina, C. Imfeld, P. Da Ronco, E. Bertuzzo, and A. Rinaldo (2014), SEHR-ECHO v1.0: a Spatially-Explicit Hydrologic Response model for ecohydrologic applications, *Geoscientific Model Development Discussions*, *7*(2), 1865–1904, doi:10.5194/gmdd-7-1865-2014.

Selker, J. S., L. Thévenaz, H. Huwald, A. Mallet, W. Luxemburg, N. van de Giesen, M. Stejskal, J. Zeman, M. Westhoff, and M. B. Parlange (2006), Distributed fiber-optic temperature sensing for hydrologic systems, *Water Resources Research*, *42*(12), doi:10.1029/2006WR005326.

Sidle, R. C., S. Noguchi, Y. Tsuboyama, and K. Laursen (2001), A conceptual model of preferential flow systems in forested hillslopes: evidence of self-organization, *Hydrological Processes*, *15*(10), 1675–1692, doi:10.1002/hyp.233.

Simoni, S., S. Padoan, D. F. Nadeau, M. Diebold, A. Porporato, G. Barrenetxea, F. Ingelrest, M. Vetterli, and M. B. Parlange (2011), Hydrologic response of an alpine watershed: Application of a meteorological wireless sensor network to understand streamflow generation, *Water Resources Research*, *47*(10), doi:10.1029/2011wr010730.

Spence, C., and M.-k. Woo (2003), Hydrology of subarctic Canadian shield: soil-filled valleys, *Journal of Hydrology*, *279*(1–4), 151 – 166, doi:10.1016/S0022-1694(03)00175-6.

Strahler, A. N. (1952), Hypsometric (area-altitude) analysis of erosional topography, *Geological Society of America Bulletin*, *63*(11), 1117–1142.

Tarboton, D. (1997), A new method for the determination of flow directions and upslope areas in grid digital elevation models, *Water Resources Research*, *33*, 309–319, doi:10.1029/96wr03137.

Tarolli, P. (2014), High-resolution topography for understanding Earth surface processes: Opportunities and challenges, *Geomorphology*, *216*(0), 295 – 312, doi:10.1016/j.geomorph.2014.03.008.

Tetzlaff, D., J. J. McDonnell, S. Uhlenbrook, K. J. McGuire, P. W. Bogaart, F. Naef, A. J. Baird, S. M. Dunn, and C. Soulsby (2008), Conceptualizing catchment processes: simply too complex?, *Hydrological Processes*, *22*(11), 1727–1730, doi:10.1002/hyp.7069.

Tobin, C., B. Schaefli, L. Nicotina, S. Simoni, G. Barrenetxea, R. Smith, M. Parlange, and A. Rinaldo (2013), Improving the degree-day method for sub-daily melt simulations with physically-based diurnal variations, *Advances in Water Resources*, *55*(0), 149 – 164, doi:10.1016/j.advwatres.2012.08.008.

Tromp-van Meerveld, H. J., and J. J. McDonnell (2006), Threshold relations in subsurface stormflow: 2. The fill and spill hypothesis, *Water Resources Research*, *42*(2), doi:10.1029/2004WR003800.

Trubilowicz, J., K. Cai, and M. Weiler (2009), Viability of motes for hydrological measurement, *Water Resources Research*, *45*(4), doi:10.1029/2008WR007046.

Tucker, G., F. Catani, A. Rinaldo, and R. Bras (2001), Statistical analysis of drainage density from digital terrain data, *Geomorphology*, *36*(3-4), 187–202, doi:10.1016/S0169-555X(00)00056-8.

Weijs, S. V., R. Mutzner, and M. B. Parlange (2013), Could electrical conductivity replace water level in rating curves for alpine streams?, *Water Resources Research*, *49*(1), 343–351, doi:10.1029/2012WR012181.

2 Geomorphological study of the Val Ferret watershed

This chapter has been submitted for publication with the following citation:

Abstract: *This chapter addresses the role of accurate mapping of spatially heterogeneous drainage densities in high altitude alpine catchments on any spatially explicit modeling of hydrological response. The channel network and its channel heads have been mapped in the field within a high mountain catchment in the Swiss Alps. The monitored channel network is characterized by highly uneven drainage density. Different channel networks were extracted from a one meter resolution LiDAR derived Digital Elevation Model and compared to the monitored channel network through geomorphologic parameters, hillslope-to-channel distance and travel time estimation in the rescaled width function formalism, seen as a basic kinematic characterization of spatially explicit models of the hydrologic response. Travel times are represented by a proxy involving unchanneled and channeled lengths from any site to the outlet. Our results show that the channel network derived by statistical analysis of surface morphology is consistent with the monitored network. Larger discrepancies were observed when the channel network was obtained with classical threshold based approaches relying on cumulative drainage area and local slope. The influence on catchment travel time distributions of the actual arrangement of drainage densities proves important, especially for the recession limb of the hydrograph. Discrepancies among travel time estimations derived from classical extraction methods compared to the ones obtained with the monitored network were the largest. Thus we conclude that spatial heterogeneity of the drainage density plays an important role in runoff formation processes which cannot be captured by classical extraction methods.*

2.1   Introduction

Recently, the increased availability of remote-sensing techniques offered new insight on Earth surface processes. In particular, airborne and terrestrial LiDAR (Light Detection And Ranging) have been used to produce high resolution topographic maps, opening new opportunities for studying river and basin geomorphology (*Jaboyedoff et al.*, 2012; *Tarolli*, 2014). LiDAR-derived Digital Elevation Models (DEMs) provide fine scale knowledge of a watershed's geomorphology which is crucial for environmental, agricultural and flood management. High resolution DEMs also serve as a basis to model the hydrological response in poorly monitored basins (*Beven*, 2011) and are instrumental to describe features needed by topographic threshold of shallow landslides or debris flow (*Simoni et al.*, 2008; *Tarolli et al.*, 2012; *Cavalli et al.*, 2013). In this context, spatially explicit hydrological models capable of accurate geomorphological descriptions are often used to reproduce flood hydrographs (*Szilágyi and Parlange*, 1999; *Schaefli et al.*, 2014; *Singh et al.*, 2014). Among them, the Width Function Instantaneous Unit Hydrograph (WFIUH) model has gained particular interest with the emergence of remote sensing techniques since it is mainly based on the analysis of DEMs. In the WFIUH models, the width function, defined as the number of channelized pixels located at a hydrological distance x from the outlet divided by the number of channelized pixels, is used as a probability density function of travel length (*Kirkby*, 1976; *Troutman and Karlinger*, 1985; *Mesa and Mifflin*, 1986; *Gupta and Mesa*, 1988). However, this approach neglects the travel time across the hillslopes which might be valid only in large basins (*D'Odorico and Rigon*, 2003). Following the idea of *van der Tak and Bras* (1990), *Rinaldo et al.* (1995) introduced the Rescaled Width Function (RWF), defined as the number of cells located at a distance L taken as the sum of flow path inside the river network L_c and the flow path across the hillslope L_h. The latter is amplified by a factor $r = u_c/u_h$ where u_h and u_c are two parameters representing the hillslope and channel velocity respectively.

The RWF formulation of the WFIUH has been extensively used in the past to analyze the contribution of hillslope and channels to the hydrologic response (*D'Odorico and Rigon*, 2003; *Botter and Rinaldo*, 2003), for regionalization and scaling properties of storm hydrographs (*Di Lazzaro*, 2009; *Di Lazzaro and Volpi*, 2011) and to model the hydrological response during flood events (*Giannoni et al.*, 2003; *Borga et al.*, 2007; *Zoccatelli et al.*, 2010). The RWF is also used to estimate basin travel time distribution by dividing the flow path inside the river network L_c and the flow path across the hillslope L_h by their respective velocities. Generally, the hillslope and channel velocities are assumed to be constant on the catchment scale but are typically separated by an order of magnitude. Recent studies proposed to vary the hillslope velocity spatially, based on land use or topographic characteristics(*Noto and La Loggia*, 2007; *Grimaldi et al.*, 2010, 2012; *Petroselli*, 2012).

The RWF model and travel time estimations rely on a proper partitioning of the landscape into hillslope and channel network parts. Surprisingly, few studies have tried to assess the impact of channel identification procedures on RWF models and travel time estimations. The simplest and most widely used method to automatically extract the channel network consists

of computing the contributing area A of each cell, i.e. computing the number of cells draining in each cell following the steepest path among the eight neighboring cells. Then, a constant critical support area is chosen (*O'Callaghan and Mark*, 1984; *Tarboton et al.*, 1991) as criterion for channel initiation. *Gandolfi and Bischetti* (1997) analyzed the effect of the area threshold on the Geomorphologic Instantaneous Unit Hydrograph and geomorphlogical indexes in two small alpine basins using 10 meter resolution DEMs. Their result showed that the choice of threshold area was impacting the hydrologic response significantly especially when the hillslope residence time is in the same order as the residence time in the network. *Nardi et al.* (2008) studied the impact of flow direction computation and flat area removal on the RWF and geomorphological parameters. The second widely used method to automatically extract the channel network is based on experimental data from *Montgomery and Dietrich* (1989). They proposed an empirical threshold for channel initiation depending on contributing area A and local slope S, in the form AS^k. Unlike the method based solely on contributing area thresholding, this method allows the drainage density to vary spatially which is its main advantage. *Giannoni et al.* (2005) proposed a procedure to objectively and automatically establish the AS^k threshold and studied the effect of the threshold on the hillslope path length frequency distribution and on the RWF. Although a deep debate is currently focused on issues of nonstationarity and variance in the hydrologic response, especially of source areas roughly identified here as unchanneled sites (*Rodhe et al.*, 1996; *McDonnell*, 1990; *McGlynn and McDonnell*, 2003; *McGlynn et al.*, 2003; *Davies et al.*, 2011, 2013; *McDonnell and Beven*, 2014), here we argue that the RWF concept is particularly suited to the present investigation, as it contains intact the geomorphological features addressed by extraction methods which ultimately acts as a proxy of the stationary behavior of the system.

Usually, the thresholds used for channel initiation are assumed to be constant on the catchment scale. However, several studies have underlined that a unique threshold for channel head identification and channel network extraction might not exist (*Jaeger et al.*, 2007; *Tarolli and Dalla Fontana*, 2009; *Passalacqua et al.*, 2010a; *Orlandini et al.*, 2011; *Jefferson and McGee*, 2012). Moreover, new extraction methods relying on high resolution DEMs and computation of local curvature and openness are now available and able to suitably detect channel heads and channel networks (see (*Tarolli*, 2014) for a review). Recently, *Passalacqua et al.* (2010a); *Orlandini et al.* (2011); *Henkle et al.* (2011) reported two main processes for channel initiation related to surface erosion/landslide and to groundwater seeping upward processes in alpine terrains. Several studies also highlighted the importance of the differentiation of perennial and intermittent network (*Gregory and Walling*, 1968; *Bishop et al.*, 2008; *Buttle et al.*, 2012; *Godsey and Kirchner*, 2014). At the time, no automatic extraction method is able to differentiate perennial and intermittent channels in the channel network. In most of the hydrological models, the channel network is extracted and compared to orthophotos or official maps but no temporal variation of the channel network is taken into account. However, it was recently proposed (*Botter et al.*, 2013) that a criterion to infer the transition from ephemeral to perennial streams could be identified with the aid of tools like the ones studied here. Therein the transition is identified at the threshold $\lambda/k = 1$ where λ is the frequency of runoff-producing daily rainfall

and k is the inverse of the hydrograph decay rate. Thus scaling of k with total catchment area, or else the point-wise determination of the mean travel time through techniques like the ones outlined here, should be able to differentiate the network sites where the probability of no flow shows departure from zero (*Ceola et al.*, 2014; *Widder et al.*, 2014).

In this work, we investigate the effects of using different channel networks on the estimation of travel time distribution through the RWF approach and on geomorphological characteristics in a high alpine headwater catchment. We also study the effect of differentiating the intermittent and the perennial streams in the channel network. Our contribution does not intend to review the latest (quite lively) work on the hydrologic response specifically focused on the inferences on nonstationarity of travel time distributions. Rather, using the simplest formulation of the rescaled width function approach, entirely DEM-based, we intend to probe the effects of accurate network extraction techniques on key features of the catchment hydrologic response. The chapter is organized as follows: after a description of the site, the available dataset and the monitoring campaign (section 2.), the different extraction techniques and channel network comparison criterions are presented in Section 3 and the results shown in Section 4. After discussing some implications and limitations of our study in Section 5, the conclusions are reported in Section 6.

2.2   Study Area and Survey

For a general description of the watershed, the reader is referred to the Study Area description in the Introduction of the thesis. In this Chapter, we make use of the one meter resolution LiDAR-derived DEM of the watershed that was acquired in August 2010. Aerial photographs are provided by the Swiss Federal Office of Topography with a resolution of 0.25 m (see *www.swisstopo.ch* for more details).

Channel network and channel heads survey

During August 2011, an intensive field campaign was conducted in the Val Ferret watershed aiming at monitoring the channel heads and channel network. During this time of the year, the main river was in its low-flow regime, mainly fed by the release of groundwater and glacier melt. The watershed was systematically walked along all drainage lines up to the catchment divide in order to locate and map 373 channel heads with a vertical accuracy of a few centimeters using a high-precision Global Navigation Satellite System (Topcon GRS-1 GPS and GLONASS), see picture a) in Figure 2.1 for an illustration. Based on field observations, the channel heads were classified in two main categories: 1) 190 groundwater channel heads due to groundwater seeping upward and laterally processes, driven by perennial flow (picture (a) in Figure 2.1), 2) 183 runoff channel heads initiated by soil erosion or landsliding processes due to surface or fast sub-surface runoff during rainfall or snowmelt flow induced events (picture (b) in Figure 2.1). Similarly to (*Orlandini et al.*, 2011), the positions of the channel heads were defined as the upstream limit of concentrated flow, at the hillslope converges to

an observable drainage line and downstream flow path. Four additional channel heads were mapped in the southernmost part of the watershed and are due to water coming out of the moraine and fed by glacier melt, which we called glacier channel heads in Figure 2.2. Some channel heads located in inaccessible and dangerous areas, but well defined as surface runoff channel heads, were also mapped using 1 m resolution hillshade map and aerial photographs, double checked with pictures taken in the field. Based on the observations during the field survey, the channels were classified as perennial when there was water flowing in the transect and intermittent channels otherwise (see Figure 2.2). In the following, the channel network resulting from the survey is referred to as *Monitored network* and the wet part as *Perennial network*.

(a)   (b)

Figure 2.1: Examples of (a) a channel head formed by groundwater seeping upward flow in a low-slope area; (b) a channel head formed by a combination of flow accumulation and slope, with soil erosion in the Val Ferret experimental area.
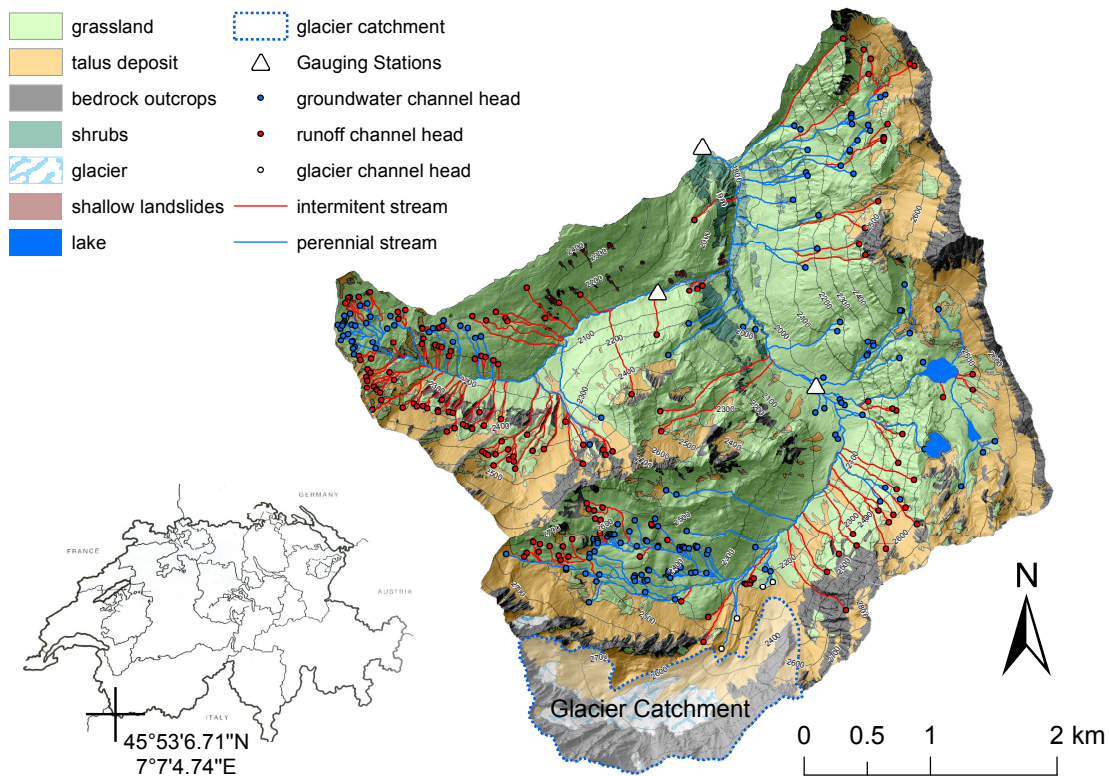
Figure 2.2: Topographic map of the study area. Channel heads and their type, channel and their state, gauging stations and land surface properties are shown in the map.

2.3 Methods

2.3.1 Channel network extraction

Our study case is characterized by the presence of a small glacier in the southernmost part of the watershed (see Figure 2.2). This area results in a complex morphology with pronounced concavities/convexities on the ground that are completely unrelated to the channel network. Therefore we decided to roughly mask these areas, depicted in Figure 2.2 as *glacier catchment*, to prevent glacial channels to be considered as river network. In this work we considered three different channel network extraction methods, described in the following.

Area and Slope-Area threshold approach

The area threshold A_t and the slope-area threshold AS_t^n methods are widely used in the literature and are defined as *classical approaches* to extract the channel network. For each of the channel heads mapped in the field, the values of A and S were considered and averaged for the determination of drainage area threshold A_t and for slope area threshold AS_t^n. Concerning this last approach, we used the function AS_t^n with $n = 2$ as suggested by *Montgomery and*

Dietrich (1992). The resulting thresholds are $A_t = 6092$ m^2 and $AS_t^2 = 1675$ m^2. After removing depressions in the DEM, the flow direction, slope and cumulative area are computed following the steepest path among the neighboring cells (*d8* method) and the network is extracted by applying the aforementioned threshold for hillslope and channel differentiation. The resulting channel networks are referred to as *Area threshold* and *Slope Area threshold* in the following.

Moreover, we also determined larger thresholds so that the resulting networks obtained from the area threshold and the slope-area threshold methods would have the same channel network length as the monitored network, i.e. the same hortonian drainage density D_d, defined as the total length of stream channels divided by the area they occupy (*Horton*, 1932, 1945). This results in thresholds of $A_t = 21959$ m^2 and ($AS_t^2 = 25475$ m^2. The two resulting channel networks are referred to as *Area threshold 2* and *Slope Area threshold 2* in the following.

Statistical approach

A statistical approach has been applied for the automatic extraction of channel network (*Sofia et al.*, 2011). This approach has been chosen because 1) it integrates both curvature (*Evans*, 1972, 1979) and topographic openness (*Yokoyama and Pike*, 2002; *Prima et al.*, 2006), providing a method more sound to errors in the original topographic data (the openness, expressing an angular measure of the relation between the surface morphology and horizontal distance, indeed avoids uncertainties related to the second derivatives operation); 2) it provides a framework for an automatic definition of the scale of topographic attributes analysis. The core idea of the *Sofia et al.* (2011) methodology is to use statistical descriptors to objectively identify channels where terrain geometry denotes a significantly convergent topography. In the proposed approach, surface convergences are highlighted using two topographic attributes: minimum curvature (*Evans*, 1972, 1979) and openness (*Yokoyama and Pike*, 2002). The choice of the optimum scale of analysis (kernel) relies on a statistical analysis of the topographic attributes distributions: the optimum kernel is the one providing the greater asymmetry in the topographic parameter distribution (*Sofia et al.*, 2011). In our study case, applying the procedure described in *Sofia et al.* (2011), the kernel is found to be 15 m for openness, and 11 m for curvature.

The network extraction procedure is then a three-step method based on (a) the normalization and overlapping of openness and minimum curvature in order to highlight the more likely surface convergences, (b) a weighting of a multiple-flow upslope area (*Quinn et al.*, 1991) according to such normalized maps to identify drainage flow paths and flow accumulation consistent with terrain geometry, and (c) the use of a value derived from the z-score normalization of the weighted upslope area as non-subjective threshold for channel network identification (*Sofia et al.*, 2011). To obtain a fully connected network, a noise-filtering and connection procedure is applied to the potential extracted network (*Sofia et al.*, 2011). False positives are discarded according to a majority filter: cells belonging to the extraction are filtered based on the majority of their contiguous neighboring cells. The connection of the network is based on a shortest-cost path approach, where the cost of traveling from one cell to

the other is given by the Euclidean distance of that cell from the extracted network(*Sofia et al.*, 2011). The resulting channel network is referred to as *Statistical approach* in the following.

2.3.2 Geomorphological characterization of the channel network

We use several geomorphological descriptors to compare the channel networks obtained with the different extraction methods: 1) the hortonian drainage density D_d, expressed in km/km^2, 2) the watershed order Ω, 3) the length of the highest order stream $L_{c,\Omega}$ [m], 4) the drainage frequency expressed in number of streams per unit of area [#/km^2] and 5) the distance from the farthest channel head to the outlet along the network $L_{c,max}$ [m]. Obviously, these parameters are influenced by the choice of a channel network extraction method. Moreover, these parameters are often used to compare basins of different size or to establish catchment-scale hydrological parameters.

We also compute the local hillslope-to-channel distance L_h, defined per pixel as the length covered following the steepest descent path until a channelized pixel is reached. The hillslope-to-channel distance L_h relies on the proper identification of the channel network and is therefore a good comparison basis for the different channel network extraction methods. The classical hortonian drainage density D_d is physically related to the mean distance one has to walk from a random location before encountering a channel. It is approximately taken as the inverse of two times the mean hillslope-to-channel distance. Hence, the hillslope-to-channel distance L_h can be seen as a local measure of the drainage density (*Tucker et al.*, 2001). As proposed in *Tucker et al.* (2001), the hillslope-to-channel distance L_h is treated as a spatial random function allowing computing the probability distribution function and covariance function of L_h. The covariance function, computed under the assumption of isotropy and second-order stationarity (*Tucker et al.*, 2001), is then fitted with an exponential model with an effective range Λ, a widely accepted model in geostatistical modeling (*Goovaerts*, 1997). The computation of this effective range aims at finding a suitable scale to compute mean hillslope-to-channel distance and therefore map drainage density at the sub-catchment scale.

2.3.3 Width function and Travel Time Estimation

In a first part, the hillslope contribution to the travel time is neglected and the width function is computed as the number of cells located at a given hydrological distance from the outlet following the river network, normalized by the total number of cells belonging to the channel network. In a second part, we take into account the hillslope contribution to the width function and compute a Rescaled Width Function (RWF) (*Rinaldo et al.*, 1995). The RWF is computed as the number of cells located at a distance L taken as the sum of flow path inside the river network L_c and the flow path across the hillslope L_h, the latter being amplified by a factor r accounting for smaller hillslope velocity. For a cell located at position (x, y) within the watershed, the distance to the outlet is therefore defined as $L(x, y) = L_c(x, y) + rL_h(x, y)$. The number of cells located at a distance L is normalized by the total number of cells, i.e. the

basin area in pixel units. Alternatively, the travel time τ of every cell of the watershed to the outlet is defined as follows (*Rinaldo et al.,* 1995; *Grimaldi et al.,* 2010):

$$\tau(x, y) = \frac{L_h(x, y)}{u_h} + \frac{L_c(x, y)}{u_c} \tag{2.1}$$

Similarly to the hillslope-to-channel distance L_h, the travel time τ is treated as a spatial random function allowing computing a probability distribution function of the travel time.

The computation of the travel time distribution through the flow length approach requires the estimation of the two parameters u_h and u_c. Recent studies have proposed different approaches to account for spatially varying hillslope velocity (*Noto and La Loggia,* 2007; *Grimaldi et al.,* 2010, 2012; *Petroselli,* 2012). However, the hillslope and channel velocities are usually assumed to be separated by one or two orders of magnitude and are considered constant over the watershed. In our study, we decided to use a constant channel velocity of 2 m/s and to compute the travel time distribution for three different hillslope velocity cases, namely $u_h = 0.04$ m/s, $u_h = 0.2$ m/s and $u_h = 0.1$ m/s. The choice of different hillslope velocities will be discussed later but the three different hillslope velocities used in our study are comparable to the value of the factor r reported in the literature. Note that for modeling purposes, the parameters u_c should be carefully calibrated with lag time or concentration time approaches. However, our purpose is not to model rainfall-runoff events but only to test whether the extracted channel networks are able to reproduce the travel time distribution when taking the monitored network as a reference. The choice of the channel velocity value of 2 m/s has been motivated by the observation of glacier melt induced streamflow diurnal cycles at the outlet of a sub-catchment and at the outlet of the watershed. The channel velocity, computed as the time difference in the occurrence of maximum streamflow divided by the distance between the two outlets along the channel network, has been found to be relatively constant at values oscillating between 1.5 m/s and 2.5 m/s.

2.4 Results

2.4.1 Channel heads location and characterization

Table 2.1 reports some simple statistical characteristics of the drainage area and local slope of the monitored channel heads and Figure 2.3 shows box plots of drainage Area A and local Slope S for both channel head type. These values indicate that groundwater channel heads tend to present a lower critical support area and relatively lower slope compared to runoff channel heads. Moreover, the standard deviation of the local drainage area is especially large compared to the mean which reflects a large spatial variability in the channel initiations.

We performed a non-parametric Mann-Whitney U test at a level of significance $\alpha = 0.05$ in

Table 2.1: Statistical characteristics of drainage area and local slope of the monitored channel heads with and without classification. the term *std* stands for standard deviation.

	Area [m^2]			Slope [m m^{-1}]		
	mean	median	std	mean	median	std
All channel heads	6092	1296	17649	0.4472	0.4111	0.2754
Groundwater	2879	895	6801	0.407	0.361	0.273
Runoff	8983	2246	23863	0.488	0.484	0.2725
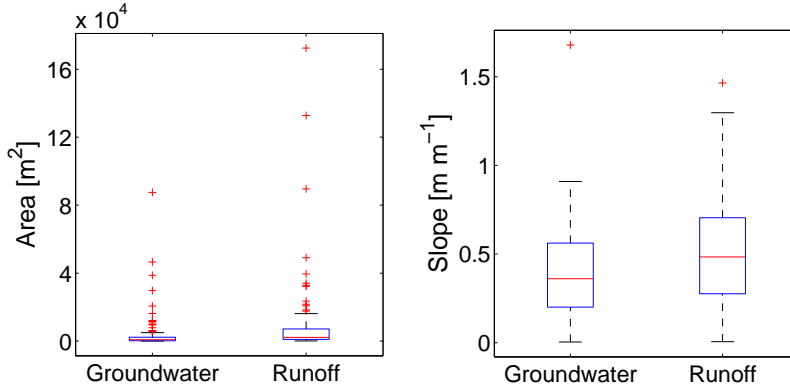
Figure 2.3: Box plots of *A* and *S* for each channel heads types.

order to test the null hypothesis that groundwater and runoff channel heads have identical continuous distribution of drainage area and local slope. Concerning the channel heads drainage areas, we found a very small *p*-value (1.24×10^{-13}) suggesting a highly statistically significant difference between groundwater and runoff channels. In the case of the local slope, the *p*-value was larger but still indicating that the distribution of the slope of the two channel heads groups is different. This simply suggests that the contributing area is a better descriptor for separating groundwater channel heads from runoff channel heads than local slope. A power law was fitted through least squares between the contributing area and the local slope but the correlation was found to be weak for each channel head type ($R^2 = 0.0044$ for groundwater channel heads and $R^2 = 0.031$ for runoff channel heads).

Channel network characterization

Table 2.2 summarizes some geomorphological parameters of the extracted networks. As expected, all the parameters change with the different channel networks. The hortonian drainage density obtained from the classical methods with field-based thresholds is particularly large. Among the two methods, the discrepancy is the largest for the slope-area method. Even though the statistical approach does not capture the watershed order and the length of the highest order stream, the drainage density and drainage frequency are close to the one obtained with the monitored network. We also note that the area and slope-area methods appear to do

satisfactory when used with a larger threshold (*Area threshold 2* and *Slope Are threshold 2*). In particular, the highest order stream length and the drainage frequency are close to the one obtained with the monitored network. Finally, we note that the distance from the farthest channel head to the outlet is similar for the different channel networks. Concerning the state of the monitored network, we found that 52.9% of the total channel network length are perennial channels whereas the remaining 47.1% are intermittent channels activated during storm or snowmelt runoff events. The hortonian drainage density and the drainage frequency of the perennial network are therefore almost half of the monitored network ones.

extraction method	drainage density D_d [km/km^2]	watershed order Ω	highest order stream length $L_{c,\Omega}$ [m]	drainage frequency [#/km^2]	longest distance to outlet $L_{c,max}$ [m]
Monitored network	5.27	6	1436.15	32.99	8046.12
Statistical approach	4.82	5	3827.41	33.97	8002.32
Area method	11.50	6	3211.99	92.45	8291.07
Slope Area method	27.18	7	3211.99	457.06	8348.38
Area method 2	5.27	5	1437.56	26.27	8207.21
Slope Area method 2	5.27	5	1437.56	26.23	8013.11
Perennial network	2.79	5	1436.15	16.27	8046.12

Table 2.2: Geomorphological features of the extracted networks

The width function extracted for the six different networks is represented in Figure 2.4. We note some common features although significant differences can be observed between the different methods. Except for the perennial network, the dominant flow distance (roughly located between 0.5 and 0.65) is for instance well captured by all the extraction methods. This is due to the fact that the highest order channels are well identified by all the methods. The discrepancy is the largest for normalized flow distances between 0.3 and 0.4. The discrepancy is also important for large flow distances, i.e. for the low order streams with some peaks of the monitored network width functions that none of the channel network extraction methods is able to capture. This illustrates the problem of properly identifying the channel heads and the non-uniqueness of a critical support area on a basin scale.

2.4.2   Study of the hillslope-to-channel distance

Figure 2.5 shows both the extracted channel networks in blue and the color-coded hillslope-to-channel distance L_h obtained with the monitored network and different channel network extraction methods. For clarity, the results obtained with the perennial network are not shown in Figure 2.5. As can be seen in panel a), the monitored channel network is characterized by a local drainage density that is not constant spatially. In particular, we observe a high density of channels in the westernmost and south-westernmost parts of the catchment resulting in low values of L_h. The classical methods with low threshold values (*c* and *d*) exhibit clearly a much larger extent of channeled portions of the landscape than the one shown by the real network. When used with larger threshold values (*e* and *f*, same hortonian drainage
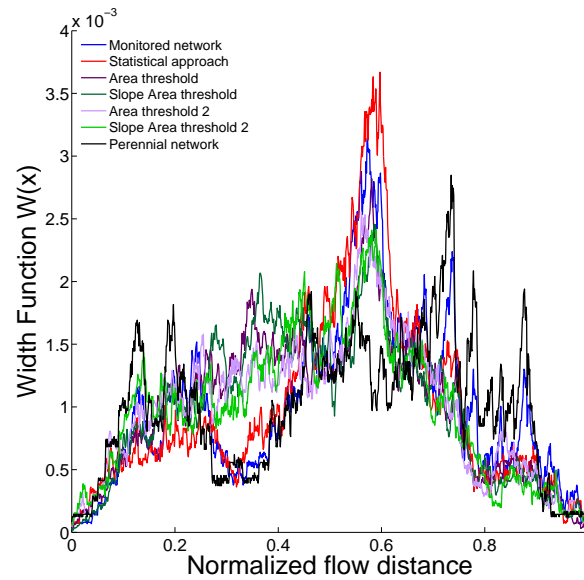
Figure 2.4: Width function of the watershed using the different network extraction methods.

density as the monitored network), the classical extraction methods present a good spatial distribution of the hillslope-to-channel distance L_h. However, with this larger threshold value, the two classical methods are not able to capture the high density of channels observed in the westernmost and south-westernmost parts of the catchment.

As previously mentioned, L_h is treated as a random function. This allows the computation of a probability distribution as in *Tucker et al.* (2001), obtained for the different methods and presented in Figure 2.6. The distances have been normalized by the largest hillslope-to-channel distance found for the true network ($L_{h,max}$ = 1530 m, note that the maximum distance L_h of 2470.2 m mentioned in Figure 2.6 is to be found in the glacier catchment that has been discarded in our calculations, see Methods section). All methods suggest an approximate exponential frequency distribution (note the semi-log axes). The mean, maximum and standard deviations for the different extraction methods are listed in Table 2.3. When used with the lower thresholds, the A_t and $(AS^2)_t$ methods completely underestimate the hillslope-to-channel distance, leading to a severe overestimation of the hortonian drainage density. This is especially the case for the $(AS^2)_t$ methods with a mean hillslope-to-channel distance of 63.6 m, more than four times smaller than the value found with the monitored network. The maximum hillslope-to-channel distance is also largely underestimated with the classical network methods. When used with larger threshold values, the A_t and $(AS^2)_t$ also tend to underestimate the hillslope-to-channel distance L_h. For small values of L_h, the frequency distribution of L_h is relatively close to the one found for the monitored network but the discrepancy is more important for larger values of L_h (see Figure 2.6). Interestingly, the $(AS^2)_t$ method is closer to the monitored network when used with a larger threshold value, which was not the case with the field-based threshold value. The discrepancy between
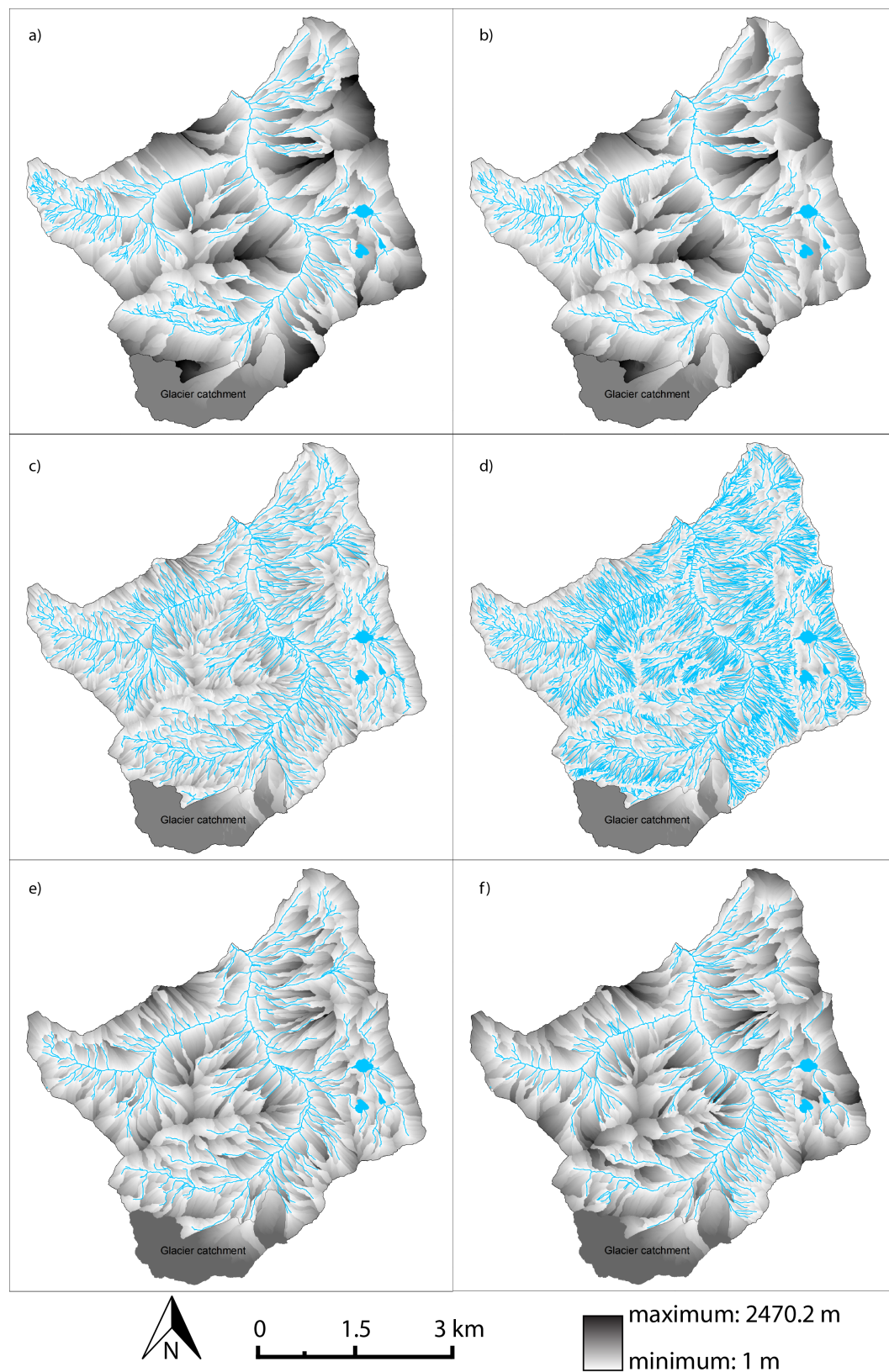
Figure 2.5: Hillslope-to-channel distance L_h and channel network for different methods: a) real network, b) the statistical approach c) the A_t method, d) the $(AS^2)_t$ method, e) the A_t method with larger threshold and f) $(AS^2)_t$ method with larger threshold.

27
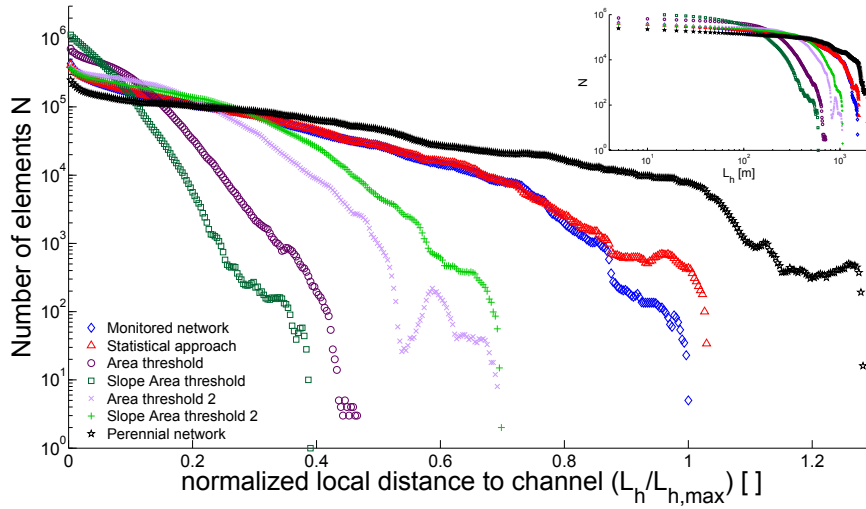
Figure 2.6: Frequency distribution of the hillslope-to-channel distance L_h for the different extraction methods. The local distance to channel has been normalized by the maximum value of L_h ($L_{h,max} = 1530$ m) computed with the real network. Upper right plot: frequency distribution of L_h without normalization.

the statistical approach and the true observed network is smaller even though the statistical approach tends to overestimate the hillslope-to-channel distance L_h. The discrepancy is also relatively large when only the perennial channels of the network are considered. Indeed, the hillslope-to-channel distance tend to be larger when the intermittent channels are not considered, leading to an increase in the mean and maximum hillslope-to-channel distance of 56.3% and 27.9% respectively.

Extraction method	$L_{h,mean}$ [m]	σ_L [m]	$L_{h,max}$ [m]	Effective range [m]	R^2
Monitored network	280.66	256.31	1529.91	645.39	0.9696
Statistical approach	284.82	261.96	1574.52	674.10	0.9403
Area method	100.89	81.65	713.04	243.69	0.9646
Slope Area method	63.60	57.29	595.3	124.75	0.9719
Area method 2	179.76	138.41	1058.93	330.13	0.9555
Slope Area method 2	219.07	170.95	1066.55	395.27	0.9575
Perennial network	438.81	366.74	1957.76	791.02	0.9597

Table 2.3: Properties of the hillslope-to-channel distance obtained with the different extracted networks.
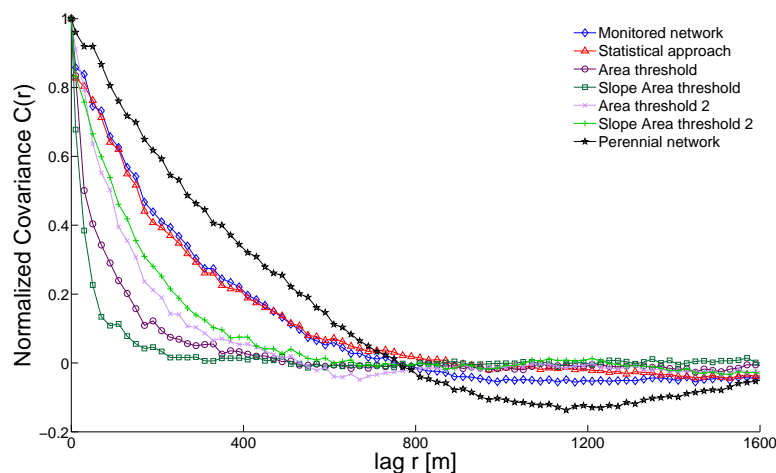
Figure 2.7: Covariance functions of the hillslope-to-channel distance L_h for the different channel network extraction methods. The values have been normalized by the variance of the hillslope-to-channel distance L_h for each method.

The covariance functions of L_h are presented in Figure 2.7. As expected, L_h is strongly autocorrelated at the scale of individual hillslopes (short lag distance r). At larger scales, the correlation breaks down to values oscillating around zero. The covariance of the different networks has been computed for maximum radial distances of 1600 m. Note that the correlation of the perennial network also oscillates around zero but for larger lags which are not shown in Figure 2.7 for clarity purposes. The correlation function of the statistical approach is close to the monitored network, whereas the correlation breaks down relatively faster with the classical methods and slower for the perennial network. As mentioned in the Methods section, an exponential model with an effective range has been fitted to all the computed covariance functions of Fig 2.7. The values of the effective range can be found in Table 2.3 along with the coefficient of determination R^2. The results show again that the statistical approach is much closer to the monitored case than the classical network approaches. Even though the results improve when we use a larger value of the threshold for the A_t and $(AS^2)_t$ methods, the effective range is still approximately half the value than the one found with the monitored network. Among the two classical methods used with larger threshold values, the covariance of the $(AS^2)_t$ method is closer to the monitored network than the A_t method. In the case of the perennial network, the effective range increases by 22.5%. From the results obtained with the monitored network, the hortonian drainage density can be mapped by averaging the inverse of two times L_h using a circular moving window of 645 meters as proposed by *Tucker et al.* (2001). This method allows to quantify the spatial variability of the drainage density D_d, mainly due to the spatial variability of channel heads density and the different processes responsible for the channel initiation.

Figure 2.8 shows the relation between mean hillslope to channel distance and basin area for 50 sub-basins of the Val Ferret catchment. The sub-basins have been selected to cover a large

range of area within the limits of the Val Ferret catchment (starting from 3 ha to 20.4 km^2). As can be observed, the scatter is the largest for the monitored and the statistical approach networks. Concerning the classical methods, we observe some scatter for small values of sub-basin areas and constant mean hillslope-to-channel distances for larger areas across the sub-basins considered, with mean values close to the ones reported in Table 2.3. This illustrates the inability of the classical methods to capture spatially variable drainage density in this mountainous watershed with obvious relevance to (and implications on) spatially explicit models of the hydrologic response.
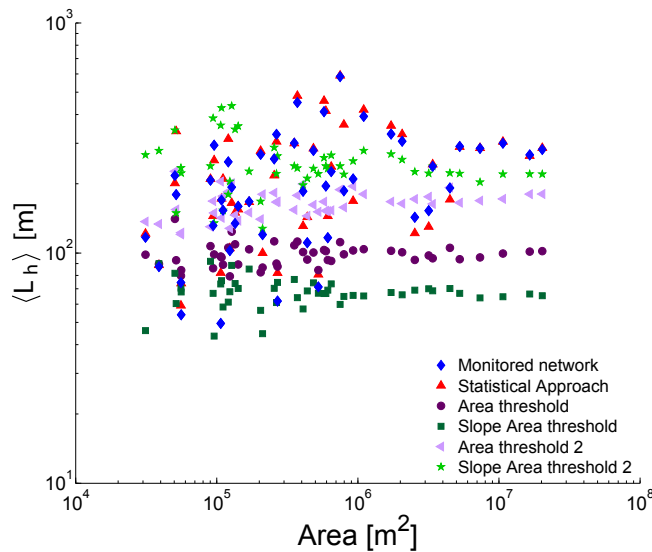
Figure 2.8: Relation between mean hillslope-to-channel distance and basin area for several sub-basins.

2.4.3 Travel time distribution

The distribution of travel time estimation is presented in Figure 2.9 for three different cases and their first four statistical moments along with the time to peak are summarized in Table 2.4. As expected, the mean and standard deviation of the distribution increase with decreasing hillslope velocity as it would take a droplet of water longer to reach a channel network. Concerning the monitored network, the time to peak of the distribution is relatively constant at a value of 50 minutes for all the three cases. This shows that the occurrence of the maximum streamflow is mostly influenced by the channel velocity and not the hillslope velocity. We also observe that all the channel networks are able to represent an estimated time to peak as compared to the monitored network. From Figure 2.9, we also observe that the amplitude of the travel time distribution maximum decreases with decreasing channel velocity. The amplitude of the maximum streamflow is therefore strongly influenced by the choice of the hillslope velocity. However, the scope of this section is not to characterize possible real storm hydrographs but rather to investigate whether the different networks are able to reproduce

this simplistic estimation of travel time.
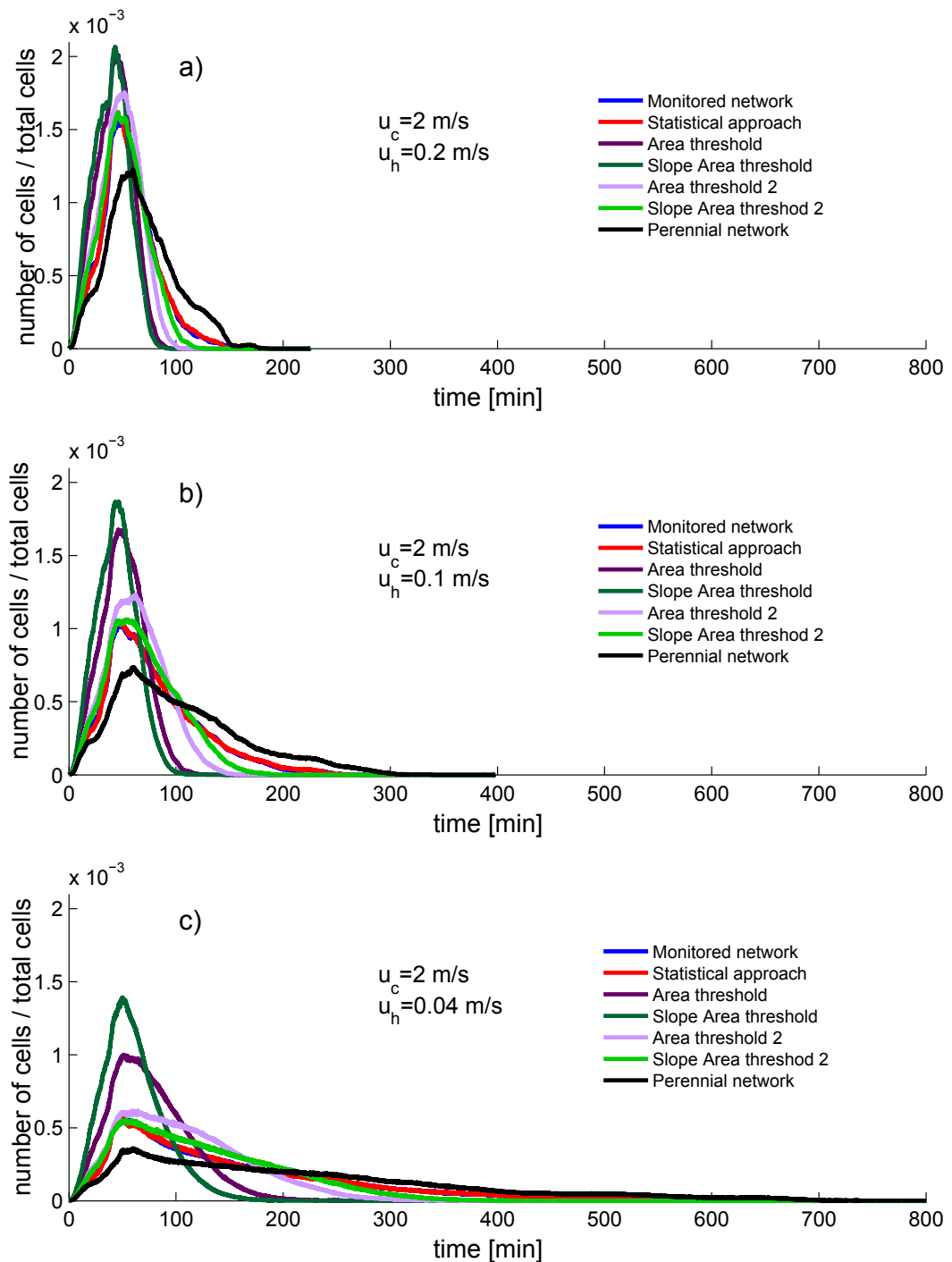
Figure 2.9: Travel time distribution of the watershed using the different channel network extraction methods and different hillslope velocity values.

As noticed by *Rinaldo et al.* (1995), the travel time distribution becomes skewed positively with

decreasing hillslope velocity. Achieving a positive skewness of the travel time distribution is necessary to reproduce real recession events. In the first case where the channel and hillslope celerity are only separated by an order of magnitude, the travel time distributions are less positively skewed in the case of the monitored, perennial and statistical approach networks and almost not skewed at all in the case of the area classical approaches (see Table 2.4). The skewness of the travel time distributions increases with the decrease of the hillslope velocity for all the different networks. In all the different cases, the travel time estimation of the statistical approach is similar to the one obtained with the monitored network. Concerning the classical approaches, the discrepancy between the distributions is larger when the lower threshold is used. However, when a larger threshold is used, the difference between the classical approaches and the monitored network is smaller. As can be seen in Figure 2.9 and Table 2.4, the travel time distribution of the *Slope Area method 2* is closer to the travel time distribution of the monitored network than the one obtained with the *Area method 2*. When the perennial network is considered, the discrepancy is comparable to the cases of the Area threshold and Slope Area threshold networks. In particular, the mean travel time is larger in the case of the perennial network leading to longer recessions.

The mean travel time of the 50 selected sub-basins has been computed in the three different cases of hillslope velocities and are presented in Figure 2.10. Similarly to Figure 2.8, the scatter is the largest for the monitored and the statistical approach networks. Except for the *Slope Area threshold 2* method, the mean travel time computed with the classical extraction methods seems to follow a power law, as has been already proposed in earlier studies (*Robinson and Sivapalan*, 1997). We also note that the discrepancy between the classical methods is larger with decreasing hillslope velocity.
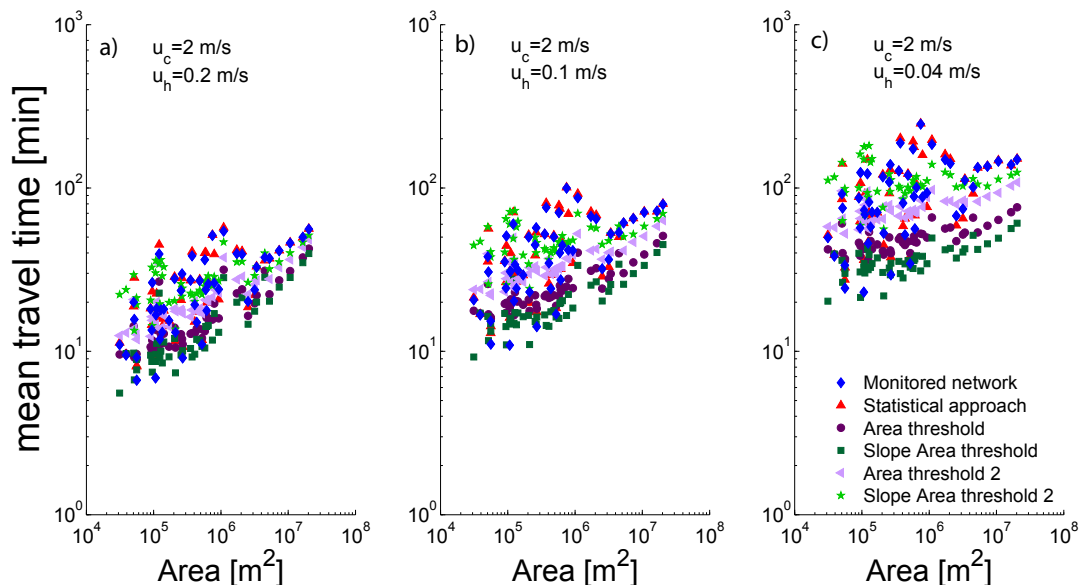
Figure 2.10: Mean travel time versus basin area for several sub-basins using different channel network extraction methods and different hillslope velocity values.

An interesting derived quantity that might shed light on the scaling of mean travel times with total contributing area is illustrated in Figure 2.11. Therein, we present for the sub-streams of the monitored network mean hillslope-to-channel distance versus drained area. The kinematic treatment of Eq. 2.1 suggests that the mean unchanneled length $< L_h >$ is a proxy of mean travel time. The scaling relation sought in Figure 2.11 is meaningful for the broad range of scales typically encompassed by the unchanneled distances within high Alpine catchments. Here, the scaling exponent is practically 0.5, quite different from commonly accepted values in the order of 1/3 (*Robinson and Sivapalan*, 1997).
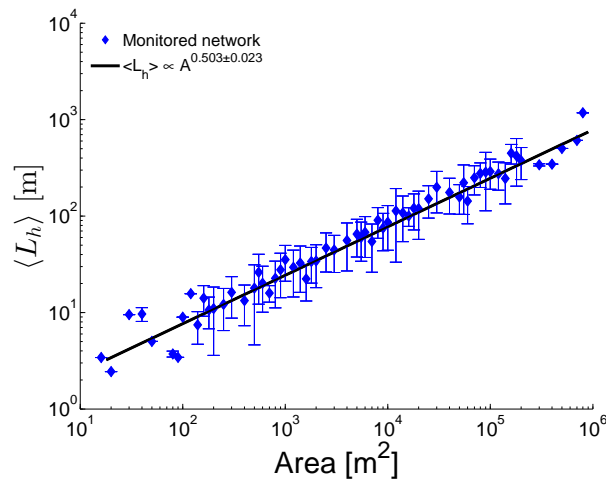
Figure 2.11: Mean hillslope length versus area draining in the sub-streams for the monitored network. The sub-streams have been binned along drained area and the vertical errorbars represent the standard deviation of the hillslope-to-channel distance.

2.5 Discussion

We note that groundwater channel heads occur at lower total contributing drainage area and lower local slope when compared with ephemeral runoff-controlled channel heads, confirming that the initiation process are of different nature. This is in line with previous findings in alpine contexts (*Passalacqua et al.*, 2010a; *Orlandini et al.*, 2011; *Henkle et al.*, 2011). We found that slope is a less powerful criterion to differentiate the two groups of channel heads. High-altitude environments in Alpine landscapes present a complex scenario where different channel initiation processes coexist and where exposed lithology (and shallow soil profiles) concert very heterogeneous conditions as far as drainage density is concerned. This is partly driven by groundwater seepage and saturation from below and partly by other processes unrelated to A and S (like snow melt or vertical cliff erosion in hollows). Moreover, our results also confirm earlier findings that a unique threshold of A or AS^2 for channel head identification might not exist at the catchment scale (*Jaeger et al.*, 2007; *Tarolli and Dalla Fontana*, 2009; *Passalacqua et al.*, 2010b; *Orlandini et al.*, 2011; *Jefferson and McGee*, 2012).

Large differences were observed in the hortonian drainage density D_d among the different channel networks. Moreover, the drainage density was found to be very heterogeneous at the catchment scale. In particular, we observed a high density of streams in the parts of the catchment where a high density of groundwater channel heads was surveyed and relatively lower channel density where runoff channel heads were monitored. We also found that the D_d varied by a factor of two between the entire monitored network and the perennial network. The classical definition of the hortonian drainage density is a good descriptor of how dissected a landscape is by channels but does not reflect the marked heterogeneity in the spatial distribution of the channels observed in mountainous regions. This was also noted by *Marani et al.* (2003) who observed major differences between hortonian and actual drainage densities in tidal environments in the northern lagoon of Venice. We therefore support the approach of *Tucker et al.* (2001) in adopting the framework that describes hortonian drainage density D_d through the features of the probability distribution of unchanneled lengths. The drainage density proves to be strongly spatially heterogeneous, marked by large variations of the hillslope-to-channel distance at the sub-basin scale. We found that the autocorrelation scale of the hillslope-to-channel distance was much smaller than the catchment width, illustrating the fact that the drainage density is highly uneven in this mountainous environment. We also found that the mean hillslope-to-channel and mean travel times are highly variable at sub-basin scales and that this variability was not captured by the classical network extraction methods which suggested a spatially constant hillslope-to-distance.

The analysis of the travel time distribution through the rescaled width function showed that the results were sensitive to the channel network extraction methods. The different channel networks used in this study are able to reproduce the timing of the maximum discharge satisfactory with little differences in the occurrence of the distribution maximum. However, larger discrepancies were observed for longer travel times corresponding to the recession part of the storm hydrographs. This is due to the fact that the classical extraction methods underestimate the hillslope-to-channel distances compared to the ones obtained with the monitored network and the statistical approach. The differences between the networks obtained with the classical methods (field-based thresholds) and the monitored network were increasing with decreasing hillslope velocities which illustrate that the contribution of the hillslope to the storm hydrograph is of critical importance. When we used larger threshold in order to equalize the hortonian drainage density to the one of the monitored network, the *Slope-Area* method performed better than the *Area* method. This is due to the ability of the *Slope-Area* method to account for uneven drainage densities which results in a better representation of the hillslope-to-channel distance. It is also important to mention that the hydrodynamic dispersion in the channel has not been taken into account in the calculation of the travel time distribution. However, a large positive skewness is already achieved when the hillslope and channel velocities are separated by two orders of magnitude. We also acknowledge that our approach of using spatially constant hillslope and channel velocities is simplistic and the velocities should vary spatially as proposed by *Grimaldi et al.* (2010). However, our goal is to discuss the effect of the channel network on the travel time

estimation and not the validity of the spatially varying velocities. Finally, we argue that taking into account the state of the channels (intermittent or perennial) could play an important role in modeling the storm hydrograph in the RWF formalism. Even though the timing of the maximum streamflow was well captured when only the perennial network was used in the travel time estimation, the difference was larger for the recession events. However, unless field campaigns are undertaken, it is a difficult task to identify the perennial part of the channel network based solely on remote sensing techniques. Further research is needed first to understand and model possible ephemeral character of the active drainage network which can be conceptually linked to a seasonal evolution induced, for instance, by snowmelt in snow covered catchment.

Even though the *Slope-Area* method was outperforming the *Area* method, the discrepancies in the travel time estimation between the *Slope-Area* method and the monitored network were important. As a result, we can safely recommend avoiding standardized extraction criteria for defining the proper channeled portion of high altitude landscapes and estimating travel time distribution. In these environments, slope-dependent or plain area thresholding methodologies for channel network extraction are far from optimal, while statistical approaches blending different topographic attributes (here topographic curvature and openness) seem optimal. To that end, however, highly detailed DEMs prove necessary. Landform curvature in particular, owing to its capability to detect convex surfaces when using high resolution topography at one meter DEM, overcomes all issues affecting thresholding analysis of A and S.

In our study, the extracted networks were systematically compared to the field monitored network. However, some errors can also be introduced during the field campaign of the channel heads and channels. The location of the channel heads is not always well defined in the field, especially for the case of the groundwater channel heads when the soil around the channel head is saturated. However, the error on the channel head positions is relatively low and partially considered by moving the monitored channel position to the nearest convergent cell. Some parts of the channel network can be activated during snowmelt season or for short periods of time after large storm events. It is therefore important to undertake field campaign of channel heads and channel network when the river is in its low flow regime as was done in this study.

2.6 Conclusions

The accurate representation of stream network is a key topic in many hydrological and geomorphological applications. Few studies have examined the impact of drainage density on hydrological modeling. In this work, we studied the influence of spatially heterogeneous drainage densities on common geomorphological parameters, hillslope-to-channel distance and travel time estimation in the rescaled width function analysis. The channel network and the channel heads were carefully mapped in the field using a high precision GPS device. We compared the monitored channel network with different channel networks obtained on one

hand with a statistical approach that considers statistical analysis of surface morphology and topographic parameters such as curvature and openness and on the other hand with classical approaches using threshold related to cumulative drainage area and local slope. The thresholds used for the area and slope-area threshold are based on the monitored channel heads. The influence of the channel network on the travel time estimation proves important. Even though the different networks are able to reproduce the timing of the maximum streamflow satisfactory, larger discrepancies are observed for the recession part of storm hydrographs when classical channel extraction methods were used. The discrepancies are larger with decreasing hillslope velocities. The travel time distribution estimated with the statistical approach outperforms the classical approaches and is comparable to the travel time distribution obtained with the monitored network. For mountainous environments, we therefore recommend to avoid standardized channel network extraction criteria and to use novel techniques relying on the analysis of surface morphology via high resolution DTMs. Finally, we extend previous findings to Alpine contexts, specifically with reference to the inadequacy of the classical definition of hortonian drainage densities where the spatial distribution of the channel heads stems from diverse channel initiation processes resulting in widely heterogeneous drainage densities for first order catchments.

Table 2.4: Moments of the travel time estimation for the three different cases of hillslope velocities. The units of the mean, the standard deviation (STD) and time to peak t_{max} are expressed in minutes whereas the skewness (SKW) and kurtosis (KTS) are unitless.

		case 1		u_c= 2 m/s u_h= 0.2 m/s			case 2		u_c= 2 m/s u_h= 0.1 m/s	
Extraction method	t_{max}	MEAN	STD	SKW	KTS	t_{max}	MEAN	STD	SKW	KTS
Monitored network	49.92	56.01	24.66	0.65	3.63	49.83	79.43	43.61	1.02	3.99
Statistical approach	45.33	56.30	24.77	0.66	3.52	45.17	80.03	44.17	1.05	3.99
Area network	46.17	42.52	16.21	-0.01	2.5	46.17	50.92	19.86	0.19	2.82
Slope Area network	43.17	39.72	15.84	0.04	2.42	46.5	45.02	17.97	0.22	2.81
Area network 2	51.83	48.43	18.24	-0.02	2.54	62.00	63.41	26.56	0.32	2.80
Slope Area network 2	46.17	51.38	20.91	0.22	2.71	54	69.64	32.54	0.52	2.88
Perennial network	60.17	67.85	31.18	0.54	2.99	60.33	104.42	59.82	0.86	3.31

		case 3		u_c= 2 m/s u_h= 0.04 m/s	
Extraction method	t_{max}	MEAN	STD	SKW	KTS
Monitored network	50.25	149.68	106.08	1.17	4.07
Statistical approach	50.25	151.14	107.86	1.20	4.16
Area network	51.08	76.15	36.61	0.77	3.76
Slope Area network	50.33	60.92	28.52	0.87	4.31
Area network 2	64.58	108.35	58.49	0.75	3.32
Slope Area network 2	59.00	124.4	73.20	0.76	3.11
Perennial network	60.17	214.12	150.34	0.99	3.49

Bibliography

Beven, K. (2011), *Rainfall-Runoff Modelling: The Primer, 2nd ed.*, 2nd ed. ed., Wiley-Blackwell, Chichester, U.K.

Bishop, K., I. Buffam, M. Erlandsson, J. Fölster, H. Laudon, J. Seibert, and J. Temnerud (2008), Aqua incognita: the unknown headwaters, *Hydrological Processes*, *22*(8), 1239–1242, doi: 10.1002/hyp.7049.

Borga, M., P. Boscolo, F. Zanon, and M. Sangati (2007), Hydrometeorological analysis of the 29 August 2003 flash flood in the Eastern Italian Alps, *Journal of Hydrometeorology*, *8*(5), 1049–1067, doi:10.1175/JHM593.1.

Botter, G., and A. Rinaldo (2003), Scale effect on geomorphologic and kinematic dispersion, *Water Resources Research*, *39*(10), doi:10.1029/2003WR002154.

Botter, G., S. Basso, I. Rodriguez-Iturbe, and A. Rinaldo (2013), Resilience of river flow regimes, *Proceedings of the National Academy of Sciences*, *110*(32), 12,925–12,930, doi:10.1073/pnas. 1311920110.

Buttle, J., S. Boon, D. Peters, C. Spence, H. (Ilja) van Meerveld, and P. Whitfield (2012), An overview of temporary stream hydrology in Canada, *Canadian Water Resources Journal / Revue canadienne des ressources hydriques*, *37*(4), 279–310, doi:10.4296/cwrj2011-903.

Cavalli, M., S. Trevisani, F. Comiti, and L. Marchi (2013), Geomorphometric assessment of spatial sediment connectivity in small Alpine catchments, *Geomorphology*, *188*(0), 31 – 41, doi:10.1016/j.geomorph.2012.05.007.

Ceola, S., E. Bertuzzo, G. Singer, T. J. Battin, A. Montanari, and A. Rinaldo (2014), Hydrologic controls on basin-scale distribution of benthic invertebrates, *Water Resources Research*, *50*(4), 2903–2920, doi:10.1002/2013WR015112.

Davies, J., K. Beven, L. Nyberg, and A. Rodhe (2011), A discrete particle representation of hillslope hydrology: hypothesis testing in reproducing a tracer experiment at Gårdsjön, Sweden, *Hydrological Processes*, *25*(23), 3602–3612, doi:10.1002/hyp.8085.

Davies, J., K. Beven, A. Rodhe, L. Nyberg, and K. Bishop (2013), Integrated modeling of flow and residence times at the catchment scale with multiple interacting pathways, *Water Resources Research*, *49*(8), 4738–4750, doi:10.1002/wrcr.20377.

Bibliography

Di Lazzaro, M. (2009), Regional analysis of storm hydrographs in the Rescaled Width Function framework, *Journal of Hydrology*, *373*(3 - 4), 352 – 365, doi:10.1016/j.jhydrol.2009.04.027.

Di Lazzaro, M., and E. Volpi (2011), Effects of hillslope dynamics and network geometry on the scaling properties of the hydrologic response, *Advances in Water Resources*, *34*(11), 1496 – 1507, doi:10.1016/j.advwatres.2011.07.012.

D'Odorico, P., and R. Rigon (2003), Hillslope and channel contributions to the hydrologic response, *Water Resources Research*, *39*(5), doi:10.1029/2002WR001708.

Evans, I. S. (1972), General geomorphometry, derivatives of altitude, and descriptive statistics, in *Spatial Analysis in Geomorphology*, edited by R. J. Chorley, pp. 17–90, Harper & Row.

Evans, I. S. (1979), *An Integrated System of Terrain Analysis and Slope Mapping. Final Report (Report 6) on Grant DA-ERO-591-73-G0040*, 192 pp., Department of Geography, University of Durham.

Gandolfi, C., and G. B. Bischetti (1997), Influence of the drainage network identification method on geomorphological properties and hydrological response, *Hydrological Processes*, *11*(4), 353–375, doi:10.1002/(SICI)1099-1085(19970330)11:4<353::AID-HYP436>3.0.CO;2-L.

Giannoni, F., J. A. Smith, Y. Zhang, and G. Roth (2003), Hydrologic modeling of extreme floods using radar rainfall estimates, *Advances in Water Resources*, *26*(2), 195 – 203, doi: 10.1016/S0309-1708(02)00091-X.

Giannoni, F., G. Roth, and R. Rudari (2005), A procedure for drainage network identification from geomorphology and its application to the prediction of the hydrologic response, *Advances in Water Resources*, *28*(6), 567 – 581, doi:10.1016/j.advwatres.2004.11.013.

Godsey, S. E., and J. Kirchner (2014), Dynamic, discontinuous stream networks: hydrologically driven variations in active drainage density, flowing channels, and stream order, *Hydrological Processes*, *28*(23), 5791–5803, doi:10.1002/hyp.10310.

Goovaerts, P. (1997), *Geostatistics for Natural Resources Evaluation*, Applied geostatistics series, Oxford University Press.

Gregory, K. J., and D. E. Walling (1968), The variation of drainage density within a Catchment, *International Association of Scientific Hydrology. Bulletin*, *13*(2), 61–68, doi:10.1080/02626666809493583.

Grimaldi, S., A. Petroselli, G. Alonso, and F. Nardi (2010), Flow time estimation with spatially variable hillslope velocity in ungauged basins, *Advances in Water Resources*, *33*(10), 1216 – 1223, doi:10.1016/j.advwatres.2010.06.003.

Grimaldi, S., A. Petroselli, and F. Nardi (2012), A parsimonious geomorphological unit hydrograph for rainfall–runoff modelling in small ungauged basins, *Hydrological Sciences Journal*, *57*(1), 73–83, doi:10.1080/02626667.2011.636045.

40

Gupta, V. K., and O. J. Mesa (1988), Runoff generation and hydrologic response via channel network geomorphology — Recent progress and open problems, *Journal of Hydrology*, *102*(1–4), 3 – 28, doi:10.1016/0022-1694(88)90089-3.

Henkle, J. E., E. Wohl, and N. Beckman (2011), Locations of channel heads in the semiarid Colorado Front Range, USA, *Geomorphology*, *129*(3–4), 309 – 319, doi:10.1016/j.geomorph. 2011.02.026.

Horton, R. (1932), Drainage basin characteristics, *Transactions of the American Geophysical Union*, *13*, 350–361.

Horton, R. (1945), Erosional development of streams and their drainage basins; hydrophysical approach to quantitative morphology, *Geological Society of America Bulletin*, *56*(3), 275–370.

Jaboyedoff, M., T. Oppikofer, A. Abellán, M.-H. Derron, A. Loye, R. Metzger, and A. Pedrazzini (2012), Use of LIDAR in landslide investigations: a review, *Natural Hazards*, *61*(1), 5–28, doi:10.1007/s11069-010-9634-2.

Jaeger, K., D. Montgomery, and S. Bolton (2007), Channel and perennial flow initiation in headwater streams: Management implications of variability in source-area size, *Environmental Management*, *40*(5), 775–786, doi:10.1007/s00267-005-0311-2.

Jefferson, A. J., and R. W. McGee (2012), Channel network extent in the context of historical land use, flow generation processes, and landscape evolution in the North Carolina Piedmont, *Earth Surface Processes and Landforms*, *38*(6), 601–613, doi:10.1002/esp.3308.

Kirkby, M. J. (1976), Tests of the random network model, and its application to basin hydrology, *Earth Surface Processes*, *1*(3), 197–212, doi:10.1002/esp.3290010302.

Marani, M., E. Belluco, A. D'Alpaos, A. Defina, S. Lanzoni, and A. Rinaldo (2003), On the drainage density of tidal networks, *Water Resources Research*, *39*(2), 1040, doi:10.1029/2001wr001051.

McDonnell, J. J. (1990), A rationale for old water discharge through macropores in a steep, humid catchment, *Water Resources Research*, *26*(11), 2821–2832, doi:10.1029/WR026i011p02821.

McDonnell, J. J., and K. Beven (2014), Debates—the future of hydrological sciences: A (common) path forward? A call to action aimed at understanding velocities, celerities and residence time distributions of the headwater hydrograph, *Water Resources Research*, *50*(6), 5342–5350, doi:10.1002/2013WR015141.

McGlynn, B. L., and J. J. McDonnell (2003), Quantifying the relative contributions of riparian and hillslope zones to catchment runoff, *Water Resources Research*, *39*(11), doi:10.1029/2003WR002091.

Bibliography

McGlynn, B. L., J. McDonnell, M. Stewart, and J. Seibert (2003), On the relationships between catchment scale and streamwater mean residence time, *Hydrological Processes*, *17*(1), 175–181, doi:10.1002/hyp.5085.

Mesa, O., and E. Mifflin (1986), On the relative role of hillslope and network geometry in hydrologic response, in *Scale Problems in Hydrology, Water Science and Technology Library*, vol. 6, edited by V. Gupta, I. Rodrìguez-Iturbe, and E. Wood, pp. 1–17, Springer Netherlands, doi:10.1007/978-94-009-4678-1_1.

Montgomery, D. R., and W. E. Dietrich (1989), Source areas, drainage density, and channel initiation, *Water Resources Research*, *25*(8), 1907–1918, doi:10.1029/WR025i008p01907.

Montgomery, D. R., and W. E. Dietrich (1992), Channel initiation and the problem of landscape scale, *Science*, *255*(5046), 826–830, doi:10.1126/science.255.5046.826.

Nardi, F., S. Grimaldi, M. Santini, A. Petroselli, and L. Ubertini (2008), Hydrogeomorphic properties of simulated drainage patterns using digital elevation models: the flat area issue, *Hydrological Sciences Journal*, *53*(6), 1176–1193, doi:10.1623/hysj.53.6.1176.

Noto, L., and G. La Loggia (2007), Derivation of a distributed unit hydrograph integrating GIS and remote sensing, *Journal of Hydrologic Engineering*, *12*(6), 639–650, doi:10.1061/(ASCE)1084-0699(2007)12:6(639).

O'Callaghan, J. F., and D. M. Mark (1984), The extraction of drainage networks from digital elevation data, *Computer Vision, Graphics, and Image Processing*, *28*(3), 323–344, doi:10.1016/s0734-189x(84)80011-0.

Orlandini, S., P. Tarolli, G. Moretti, and G. Dalla Fontana (2011), On the prediction of channel heads in a complex alpine terrain using gridded elevation data, *Water Resources Research*, *47*(2), doi:10.1029/2010WR009648.

Passalacqua, P., P. Tarolli, and E. Foufoula-Georgiou (2010a), Testing space-scale methodologies for automatic geomorphic feature extraction from lidar in a complex mountainous landscape, *Water Resources Research*, *46*(11), doi:10.1029/2009wr008812.

Passalacqua, P., T. Do Trung, E. Foufoula-Georgiou, G. Sapiro, and W. E. Dietrich (2010b), A geometric framework for channel network extraction from lidar: Nonlinear diffusion and geodesic paths, *Journal of Geophysical Research: Earth Surface*, *115*(F1), doi:10.1029/2009JF001254.

Petroselli, A. (2012), LIDAR data and hydrological applications at the basin scale, *GIScience & Remote Sensing*, *49*(1), 139–162, doi:10.2747/1548-1603.49.1.139.

Prima, O. D. A., A. Echigo, R. Yokoyama, and T. Yoshida (2006), Supervised landform classification of Northeast Honshu from DEM-derived thematic maps, *Geomorphology*, *78*(3–4), 373–386, doi:10.1016/j.geomorph.2006.02.005.

Quinn, P., K. Beven, P. Chevallier, and O. Planchon (1991), The prediction of hillslope flow paths for distributed hydrological modelling using digital terrain models, *Hydrological Processes*, *5*(1), 59–79, doi:10.1002/hyp.3360050106.

Rinaldo, A., W. E. Dietrich, R. Rigon, G. K. Vogel, and I. Rodrlguez-lturbe (1995), Geomorphological signatures of varying climate, *Nature*, *374*(6523), 632–635, doi:10.1038/374632a0.

Robinson, J. S., and M. Sivapalan (1997), Temporal scales and hydrological regimes: Implications for flood frequency scaling, *Water Resources Research*, *33*(12), 2981–2999, doi:10.1029/97wr01964.

Rodhe, A., L. Nyberg, and K. Bishop (1996), Transit times for water in a small till catchment from a step shift in the Oxygen 18 content of the water input, *Water Resources Research*, *32*(12), 3497–3511, doi:10.1029/95WR01806.

Schaefli, B., L. Nicótina, C. Imfeld, P. Da Ronco, E. Bertuzzo, and A. Rinaldo (2014), SEHR-ECHO v1.0: a Spatially-Explicit Hydrologic Response model for ecohydrologic applications, *Geoscientific Model Development Discussions*, *7*(2), 1865–1904, doi:10.5194/gmdd-7-1865-2014.

Simoni, S., F. Zanotti, G. Bertoldi, and R. Rigon (2008), Modelling the probability of occurrence of shallow landslides and channelized debris flows using GEOtop-FS, *Hydrological Processes*, *22*(4), 532–545, doi:10.1002/hyp.6886.

Singh, P., S. Mishra, and M. Jain (2014), A review of the synthetic unit hydrograph: from the empirical UH to advanced geomorphological methods, *Hydrological Sciences Journal*, *59*(2), 239–261, doi:10.1080/02626667.2013.870664.

Sofia, G., P. Tarolli, F. Cazorzi, and G. Dalla Fontana (2011), An objective approach for feature extraction: distribution analysis and statistical descriptors for scale choice and channel network identification, *Hydrology and Earth System Sciences*, *15*(5), 1387–1402, doi:10.5194/hess-15-1387-2011.

Szilágyi, J., and M. B. Parlange (1999), A geomorphology-based semi-distributed watershed model, *Advances in Water Resources*, *23*(2), 177 – 187, doi:10.1016/S0309-1708(99)00021-4.

Tarboton, D., R. Bras, and I. Rodriguez Iturbe (1991), On the extraction of channel networks from digital elevation data, *Hydrological Processes*, *5*(1), 81–100, doi:10.1002/hyp.3360050107.

Tarolli, P. (2014), High-resolution topography for understanding Earth surface processes: Opportunities and challenges, *Geomorphology*, *216*(0), 295 – 312, doi:10.1016/j.geomorph.2014.03.008.

Tarolli, P., and G. Dalla Fontana (2009), Hillslope-to-valley transition morphology: New opportunities from high resolution DTMs, *Geomorphology*, *113*(1–2), 47–56, doi:10.1016/j.geomorph.2009.02.006.

Bibliography

Tarolli, P., G. Sofia, and G. Dalla Fontana (2012), Geomorphic features extraction from high-resolution topography: landslide crowns and bank erosion, *Natural Hazards*, *61*(1), 65–83, doi:10.1007/s11069-010-9695-2.

Troutman, B. M., and M. R. Karlinger (1985), Unit hydrograph approximations assuming linear flow through topologically random channel networks, *Water Resources Research*, *21*(5), 743–754, doi:10.1029/WR021i005p00743.

Tucker, G., F. Catani, A. Rinaldo, and R. Bras (2001), Statistical analysis of drainage density from digital terrain data, *Geomorphology*, *36*(3-4), 187–202, doi:10.1016/S0169-555X(00)00056-8.

van der Tak, L. D., and R. L. Bras (1990), Incorporating hillslope effects into the geomorphologic instantaneous unit hydrograph, *Water Resources Research*, *26*(10), 2393–2400, doi:10.1029/WR026i010p02393.

Widder, S., K. Besemer, G. A. Singer, S. Ceola, E. Bertuzzo, C. Quince, W. T. Sloan, A. Rinaldo, and T. J. Battin (2014), Fluvial network organization imprints on microbial co-occurrence networks, *Proceedings of the National Academy of Sciences*, *111*(35), 12,799–12,804, doi:10.1073/pnas.1411723111.

Yokoyama, R., and R. J. Pike (2002), Visualizing topography by openness: a new application of image processing to digital elevation models, *Photogrammetric engineering and remote sensing*, *68*(3), 257–266.

Zoccatelli, D., M. Borga, F. Zanon, B. Antonescu, and G. Stancalie (2010), Which rainfall spatial information for flash flood response modelling? A numerical investigation based on data from the Carpathian range, Romania, *Journal of Hydrology*, *394*(1–2), 148 – 161, doi:10.1016/j.jhydrol.2010.07.019.

3 Geomorphic signatures on base flow recession analysis

This chapter was previously published with the following citation:

Abstract: *This paper addresses the signatures of catchment geomorphology on base flow recession curves. Its relevance relates to the implied predictability of base flow features, which are central to catchment-scale transport processes and to ecohydrological function. Moving from the classical recession curve analysis method, originally applied in the Finger Lakes Region of New York, a large set of recession curves has been analyzed from Swiss streamflow data. For these catchments, digital elevation models have been precisely analyzed and a method aimed at the geomorphic origins of recession curves has been applied to the Swiss dataset. The method links river network morphology, epitomized by time-varying distribution of contributing channel sites, with the classic parametrization of recession events. This is done by assimilating two scaling exponents, β and b_G with $|dQ/dt| \propto Q^\beta$ where Q is at-a-station gauged flow rate and $N(l) \propto G(l)^{b_G}$ where l is the downstream distance from the channel heads receding in time, $N(l)$ is the number of draining channel reaches located at distance l from their heads, and $G(l)$ is the total drainage network length at a distance greater or equal to l, the active drainage network. We find that the method provides good results in catchments where drainage density can be regarded as spatially constant. A correction to the method is proposed which accounts for arbitrary local drainage densities affecting the local drainage inflow per unit channel length. Such corrections properly vanish when the drainage density become spatially constant. Overall, definite geomorphic signatures are recognizable for recession curves, with notable theoretical and practical implications.*

3.1 Introduction

Groundwater is the main contributor of a river catchment's base flow whose predictability during recession events is of crucial importance for water resource management. Recession curves have been widely studied in the past and their characteristics used to establish basin scale parameters (see *Tallaksen* (1995) for a review). In particular, *Brutsaert and Nieber* (1977) analyzed daily discharge values of six basins in the Finger Lakes region of the northeastern US and proposed an analytical tool to characterize the recession flow based on the description of the discharge change rate dQ/dt as a function of the discharge Q. Unlike many non-linear recession flow models, this method avoids the knowledge of the precise beginning of the recession event which can be difficult to evaluate due to the continuous nature of streamflow measurements. The main feature of their method is the comparison of the observations with analytical solutions of the Boussinesq equation for an unconfined rectangular aquifer under particular boundary conditions. Two exact solutions of the Boussinesq equation (*Boussinesq*, 1904; *Polubarinova-Kochina*, 1962) and an approximated linearized solution (*Boussinesq*, 1903) can be expressed in the form

$$\frac{dQ}{dt} = -kQ^\beta \tag{3.1}$$

where β and k are constants depending on the flow regime considered. In order to avoid contributions from relatively fast subsurface flow, overland flow and evapotranspiration, *Brutsaert and Nieber* (1977) recommended the use of the lower envelope of the point cloud in the $\ln(-dQ/dt)$ versus $\ln Q$ plot, corresponding to the slowest recession rate. Based on their study, they identified two typical values β describing the rate of decline in streamflow recessions: ≈ 1.5 for low Q (long-term response) and ≈ 3 for high Q (short-term response). Moreover, some parameters of the watershed such as the saturated hydraulic conductivity stemming from the Boussinesq equation have been computed from the intercept of the $\ln(-dQ/dt)$ versus lnQ plot.

The method has been widely applied to estimate basin scale parameters in relatively natural areas (*Brutsaert and Lopez*, 1998; *Brutsaert and Sugita*, 2008; *Brutsaert and Hiyama*, 2012; *Eng and Brutsaert*, 1999; *Malvicini et al.*, 2005; *Mendoza et al.*, 2003; *Parlange et al.*, 2001; *Szilágyi et al.*, 1998; *Troch et al.*, 1993; *Vogel and Kroll*, 1992; *Zecharias and Brutsaert*, 1988) and in engineered catchments (*Rupp et al.*, 2004; *Wang and Cai*, 2010), to formulate base flow in a watershed model (*Szilágyi and Parlange*, 1999), in order to separate the base flow (*Szilagyi and Parlange*, 1998) or to assess long term groundwater storage changes (*Brutsaert*, 2008). *Rupp and Selker* (2006a,b) showed some limitations of the method e.g. in the case of sloping aquifers. Recession curve studies moving from *Brutsaert and Nieber* (1977) work have proved of central importance in a broad range of topics ranging from comprehensive water resource management to studies on fluvial biodiversity, catchment-scale transport, eco-hydrology and the so-called old-water paradox (*Bertuzzo et al.*, 2007; *Botter et al.*, 2007a,b, 2009, 2010; *Ceola et al.*, 2010; *Harman et al.*, 2009; *Kirchner*, 2009; *Kondolf et al.*, 1987; *Palmroth et al.*, 2010; *Rinaldo et al.*, 1995a,b, 2006; *Rodriguez-Iturbe et al.*, 2009; *Tague and Grant*, 2004; *Thompson*

and Katul, 2012; *Wittenberg*, 1999; *Zaliapin et al.*, 2010).

Recently, several studies (*Biswal and Marani*, 2010; *Biswal and Nagesh Kumar*, 2012; *McMillan et al.*, 2011; *Rupp et al.*, 2009; *Shaw and Riha*, 2012) analyzed the recession events on a seasonal or event-based timescale and discussed their shifts in the $\ln(-dQ/dt)$ versus lnQ plot, linking them to different antecedent soil moisture and evapotranspiration happening over the season. In particular, *Biswal and Marani* (2010), *Biswal and Nagesh Kumar* (2012) and *Shaw and Riha* (2012) proposed to obtain the parameters β and k of Eq. 3.1 by fitting a linear model to every recession event in order to obtain a distribution of the parameters instead of fitting a line to the lower envelope of the point cloud. With this method, the authors found that the slopes of the individual recession curves, i.e. the parameter β, were in general larger than the one of the lower envelope, resulting in an underestimation of the streamflow decline rate when described by a unique $dQ/dt - Q$ relationship. Moreover, *Biswal and Marani* (2010) proposed to link recession event parameterization to river morphology through a time-varying geometry of saturated channel sites. In particular, they developed a theory based on geomorphological arguments to link the exponent β of Eq. 3.1 to that characterizing an empirical relation resulting from the analysis of Digital Elevation Models (DEM). In this model, the variation of the discharge is linked to the direct drainage into a time-varying Active Drainage Network (ADN). When the recession hydrograph at an outlet is dominated by drainage of the unconfined aquifer as in *Brutsaert and Nieber* (1977), the ADN is the length of the channel network instantaneously intersecting it. The model relies on four main assumptions. First, the authors assume that the recession flow could be studied as a succession of steady flows since the timescale at which the discharge varies is much longer than the timescale of water propagating in the network. Second, by assuming a spatially constant discharge per unit length q_L, the total discharge $Q(t)$ can be expressed as:

$$Q(t) = q_L(t)G(l(t)) \tag{3.2}$$

where $G(l(t))$ is the total length of the drainage network actively contributing at time t and $l(t)$ is the distance between the actual source of the ADN and their location at the beginning of the recession event (Figure 3.1). Third, they assume that all sources of the ADN recede at the same speed $c = dl/dt$, constant in space and time such that the change in time of the network length is proportional to the number of sources N ($dG/dt = dG/dl.dl/dt \propto N.c$). Equation 3.2 can be differentiated in time:

$$\frac{dQ(t)}{dt} = -q_L(t)cN(t) + \frac{dq_L(t)}{dt}G(t) \tag{3.3}$$

where the third assumption has been employed. The first term at right-hand side of Eq. 3.3 embeds the geomorphologic signature and the second the Brutsaert recession proper. Fourth, they studied the case where the variation in time of the ADN, assumed to be much larger than the variation in time of the discharge per unit length, dominates the second term in Eq. 3.3 which can thus be neglected. This work has clearly established that baseflow recession curves bear the signatures of the geomorphological structure of the contributing river basin.
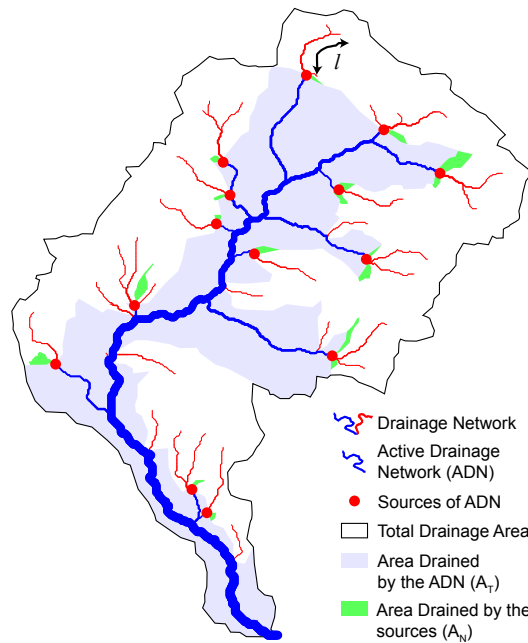
Figure 3.1: Idealized example of a recession described by the geomorphological conceptual models. The Active Drainage Network ADN is represented in blue solid lines and the dry part of the ADN is represented in red solid lines. The sources (here $N = 14$) are represented in red solid circles, the blue shaded area represent the fraction of the basin drained by the ADN (A_T).

However, the innovative method proposed by *Biswal and Marani* (2010) postulates constant drainage density, classically defined as the total length of stream channels divided by the area they drain (*Horton*, 1932, 1945) and properly described by a random space function endowed with spatial correlation (*Tucker et al.*, 2001). Other formulations have also been proposed (*Marani et al.*, 2003) as it was shown that networks with the same hortonian drainage density may embed rather different distributions of unchanneled pathways, and thus different extents of the actual density of the drainage network. Random functions are defined by the statistical properties of the length of the (steepest-descent) distance from any unchanneled site to the first occurrence of a stream channel (*Tucker et al.*, 2001). The consequences are far from obvious. In fact, the Hortonian definition applies reasonably well only in cases where locally the mean unchanneled lengths vary little from subcatchment to subcatchment, thus postulating that channel initiation processes are homogeneous – technically, whenever automatic network extractions assume it, like e.g. in the case of constant support area (for a review see e.g. (*Rodriguez-Iturbe and Rinaldo*, 2001)). This is seldom the case in nature (e.g *Montgomery and Dietrich* (1988, 1992)). Typically, in proglacial catchments, mean unchanneled distances exhibit a broad range varying from tens of meters in shallow-soiled topographically concave source areas to a few km in deep moraines (e.g. *Montgomery and Foufoula-Georgiou* (1993); *Tarolli and Dalla Fontana* (2009)). Thus one wonders whether the geomorphic framework proposed by *Biswal and Marani* (2010) for predicting the shape of Brutsaert recession curves

can be suitably generalized to account for spatially uneven drainage densities. In practice, one needs to relax certain assumptions therein and check empirically whether geomorphic signatures could still be interpreted in such context, possibly improving the explanatory power of the original method and reducing to it in the limit case of constant drainage density. This is precisely what this paper addresses.

3.2 Study areas and available data

We analyze 26 catchments located in Switzerland (Figure 3.2) presenting different sizes, relief, slope and soil properties. The watersheds are all characterized by relatively little anthropogenic influence on the streamflow behavior. The hourly averaged streamflow data of the 26 gauging stations are obtained from the Swiss Federal Office for the Environment. The rainfall data is obtained through SwissMetNet, a network of automatic weather stations operated by MeteoSwiss. All the stations are measuring the precipitation within a maximum radius of 10 km from the corresponding discharge gauging station. The DEM of the 26 basins were extracted from a 25 meter resolution DEM of Switzerland provided by the Swiss Federal Office of Topography with standard commercial GIS software. Table 3.1 summarizes the principal characteristics of the 26 catchments.
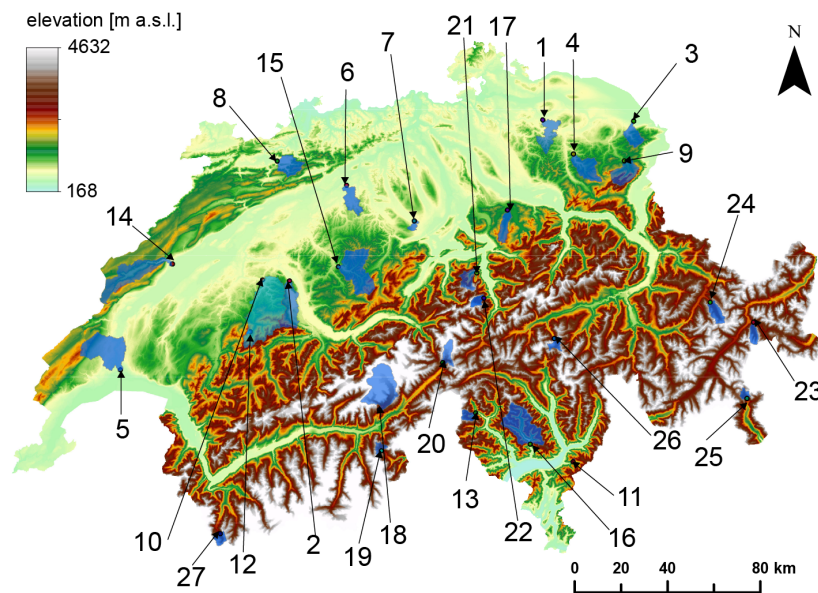
Figure 3.2: Map of the experimental catchments used in this study. Some geomorphologic characteristics and description of the available data are listed in Table 3.1

We also analyze the Val Ferret catchment (catchment 27 in Table 3.1), an experimental site we have monitored since 2008 (see *Simoni et al.* (2011)). Stream flow data are available every 5 minutes and obtained through water level measurements and a rating curve that was derived using the salt-dilution method on a yearly basis for the period 2008-2012. Recently, *Weijs et al.* (2013) decreased the error on the rating curve by combining the waterlevel with the natural

electrical conductivity of streamwater which appears particularly useful for Alpine watersheds. The rainfall data for the Val Ferret catchment is obtained along with other forcing parameters by a wireless network of up to 26 small meteorological stations deployed on representative sites of the catchment (*Simoni et al.*, 2011). For this catchment we used both a 5 meter resolution LiDAR-derived DEM and the 25 meter resolution DEM provided by the Swiss Federal Office of Topography. Moreover, the actual channel network of the Val Ferret catchment has been surveyed by Differential Global Positioning System during an extensive field campaign in 2011.

3.3 Methods

In order to compute the recession exponents, measured discharge has been averaged from hourly values to daily values in order to filter out the diurnal contributions of snow or icemelt to the streamflow daily periodicity. Precipitation has been integrated over the same period and used to define recession events as 6 consecutive days without precipitation. Moreover, following *Biswal and Marani* (2010), we only considered events with peak discharge larger than the average discharge in order to enhance the geomorphic signature on the baseflow recession and to insure that the whole catchment is active at the onset of recession – unlike the original method from *Brutsaert and Nieber* (1977) where the focus was on the groundwater hydraulics signature. The discharge variations and values have been computed as $-dQ/dt = (Q_t - Q_{t+\Delta t})/\Delta t$ and $Q = (Q_t + Q_{t+\Delta t})/2$ following *Brutsaert and Nieber* (1977), where Δt is the time step of one day used in the analysis. Recession events with non-monotonically decreasing discharge values were discarded from the analysis (i.e. events containing days with $dQ/dt = 0$ were removed from the analysis). In the log-log plot, the single $-dQ/dt$ versus Q curves tend to be shifted depending on the maximum peak discharge, antecedent soil moisture and evapotranspiration. According to *Biswal and Marani* (2010), *Biswal and Nagesh Kumar* (2012) and *Shaw and Riha* (2012), a value of the exponent β is obtained for every recession event by fitting a linear model in the log-log space using ordinary least squares. In the following, we will refer to the recession exponent β of a catchment as the median of the exponent β's frequency distribution. This event-based approach differs from the previous studies linking the analyzed recession discharges based on a one-to-one relationship between the amount of water stored in the catchment and the discharge occurring during recessions.

The variables $N(t)$ and $G(t)$, instrumental for the geomorphological analysis, can be obtained from the analysis of DEMs by extracting the channel network on the basis of standard topographic threshold methods (*O'Callaghan and Mark*, 1984; *Tarboton et al.*, 1991) or slope- or topographic curvature-dependent support areas mimicking different channel initiation processes (*Montgomery and Dietrich*, 1988, 1992; *Montgomery and Foufoula-Georgiou*, 1993; *Sofia et al.*, 2011; *Tarolli and Dalla Fontana*, 2009), the latter being capable of rendering spatially heterogeneous drainage densities. As done in *Biswal and Marani* (2010), we use a simple flow accumulation threshold as channel network extraction method to standardize procedures, except for the case where ground truthing was available (for catchment 27, see Section 3.2). After a certain time t, the number of sources $N(t)$ is determined by the number of reaches

located at distance $l = c(t - t_0)$ from their farthest upstream initial source (Figure 3.1). Under the assumption that the ADN varies quickly, such that the term in dq_L/dt can be neglected, one has $dQ/dt \propto -N(t)$ from Eq. 3.3 and $Q \propto Gt(t)$ from Eq. 3.2. Inserting these two relations in Eq. 3.1, one finally has:

$$N(l) \propto G(l)^{b_G} \tag{3.4}$$

where $b_G = \beta$ if the geomorphological exponent correctly captures the exponent obtained from the analysis of the recession curves.

In this work, we propose a revised approach of the conceptual model developed in *Biswal and Marani* (2010). We assume that the directly contributing discharge Q is drawn not from an unconfined aquifer like in the traditional way but in our case by the unchanneled area draining directly in the ADN:

$$Q(t) = \sum_{i \in ADN(t)} a_i q_i \sim q \sum_{i \in ADN(t)} a_i \propto \sum_{i \in ADN(t)} a_i = A_T(t) \tag{3.5}$$

where ADN is the Active Drainage Network at time t, A_T is the area draining directly in the ADN, a_i is the directly contributing area at site i and q_i is the discharge-per-pixel at site i (see Figure 3.1). The second approximation derives from assuming q constant as done in *Biswal and Marani* (2010). As such we assume that the variation of the contributing discharge is proportional to the rate of change in directly contributing area therein and hence on local drainage density in the sense of *Tucker et al.* (2001):

$$\frac{dQ}{dt} \propto \frac{d}{dl}\left(\sum_{i \in ADN(t)} a_i\right)\frac{dl}{dt} \propto c\frac{d}{dl}\sum_{i \in ADN(t)} a_i = c\frac{dA_T}{dl} \tag{3.6}$$

where c is the speed at which the sources recede, assumed constant in space and time as in a negative traveling wave. The approach is thus based on the computation of the direct drainage areas of the ADN. Moreover, the change in direct drainage area is given by the area A_N draining directly in the sources of the ADN at time t:

$$\frac{dA_T}{dl} \propto A_N(l) \tag{3.7}$$

Combining Eq. 3.1, 3.5, 3.6 and 3.7, we obtain similarly to Eq. 3.4:

$$A_N \propto A_T^{b_A} \tag{3.8}$$

where $b_A = \beta$ if the geomorphological exponent obtained with the new method matches the exponent obtained from the analysis of the recession curves. In this study, we propose to compute the geomorphological exponents b_G of Eq. 3.4 and b_A of Eq. 3.8 for the 27 watersheds considered and to compare them with the values of the recession exponent β obtained from the recession analysis. Then, we study the differences between the two methods in terms of mean catchment altitude, aiming at improving our understanding of the geomorphological

origin of the recession curves.

3.4   Results

Examples of three catchments (basins 15, 25 and 27, see Table 3.1 for geomorphological characteristics) where the two different methods have been applied are shown in Figure 3.3. The examples present different cases and results characteristic of the correction we propose in this work. The channel network has been suitably extracted from the DEM using a flow accumulation threshold of 100 pixels and is here color-coded in blue in the upper panels, row a). Different flow accumulation threshold values and another channel network extraction method (depending on a slope-area threshold) have been used without appreciable changes in the following results. For the study of the Val Ferret catchment (watershed 27 in Table 3.1), the monitored network (see Section 3.2) has been used as the basis for the determination of the ADN. The distribution of the distance from any unchanneled site to its nearest stream channel following the steepest path has been studied in relevant sub-catchments of the watersheds. It appears that the hillslope distance to the nearest channel and therefore the local drainage density (*Tucker et al.*, 2001) cannot be considered constant in most high mountain catchments and especially in the case of the Val Ferret catchment where the real monitored network has been used.

The recession slope analysis has been carried out for each of the 27 basins by fitting each recession event separately with least squares and by computing the frequency distribution of the β values. Some examples of individual fits are color coded in the second row b) of plots in Figure 3.3, along with the cloud of points obtained for all the events (gray dots). The solid black line represents the fit of all the events. As expected, the exponent β of Eq. 3.1 obtained with the global fit is less than the average of the coefficients fitted on single events. The results of the recession slope analysis are presented in Table 3.2. In the following, the values of a catchment's median exponent β are used as a comparative basis for the scaling exponents b_G and b_A of the different geomorphological models. Note that, in general, the standard deviations of the exponent β are relatively large due to the inferences of fast responses of the catchments to precipitation or glacier melts. The low extreme ($\beta = 1.06$, basin 20, see in Table 3.2) corresponds to a largely glaciated, high altitude catchment whereas the high extreme ($\beta = 6.24$, basin 6, Table 3.2) corresponds to a highly urbanized catchment. Both cases have been discarded in the following calculations.

The comparison of the two models is shown in the lower panels of Figure 3.3. In c), as per the method developed in *Biswal and Marani* (2010), we show the number of sources N plotted versus the total length G of the ADN. As postulated by the original method, the number of sources decreases or stays constant in time, resulting in a monotonically decreasing function $N(G)$. The plots result in a piecewise constant function at low values of the network length since low order channels have dried out already so that the ADN stems mainly from high-order streams. In order to better estimate the geomorphological parameters b_G and b_A, the data
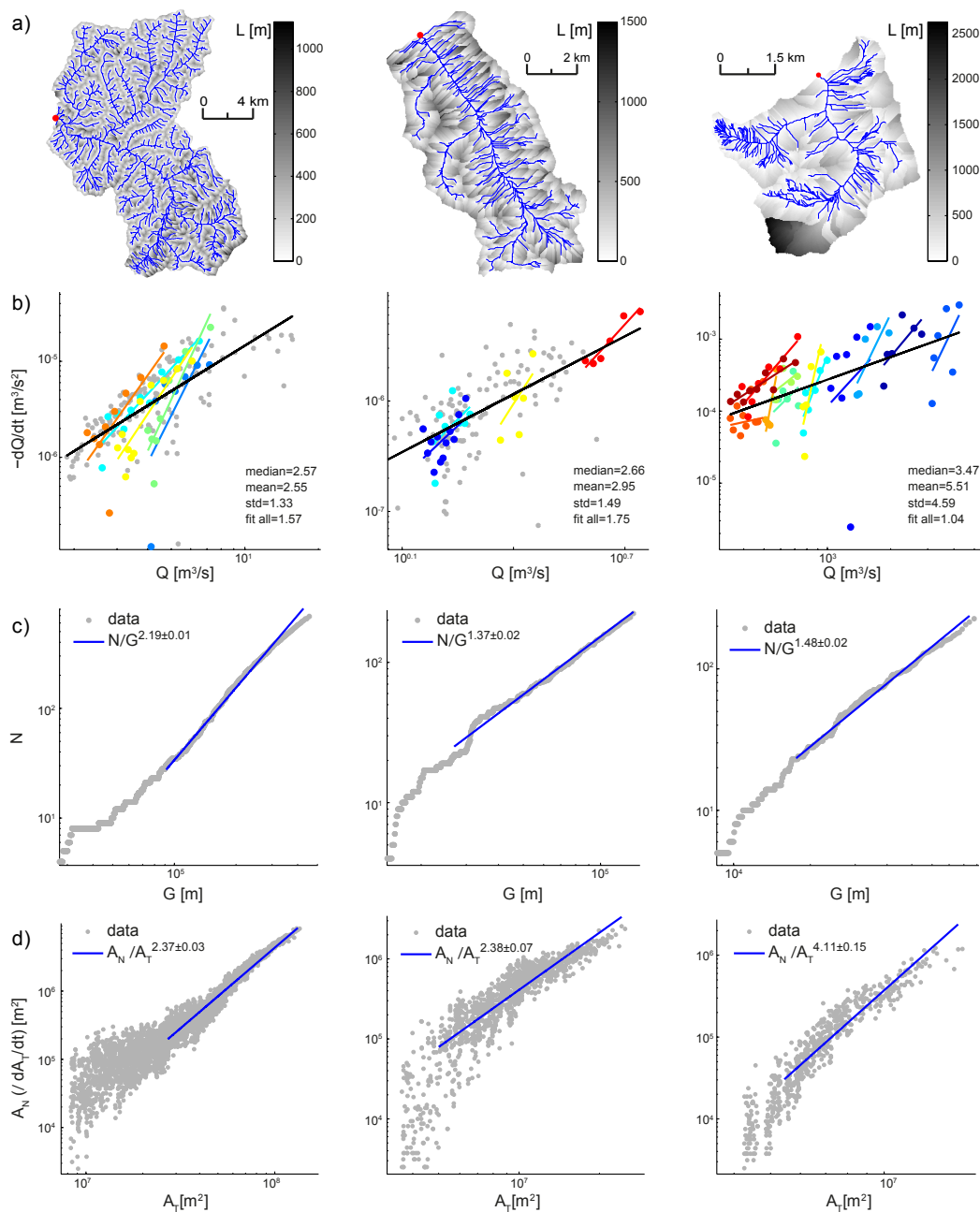
Figure 3.3: Example of the results obtained for watershed 15 (column 1), watershed 24 (column 2) and watershed 27 (column 3), see basins characteristics in Table 3.1. The different lines correspond to a) the channel network obtained with the area threshold method in blue and in black and white the distance L to the nearest channel following the steepest path (except for watershed 27, column 3 where the real, monitored network has been used), b) the cloud of points in gray obtained from the recession analysis with some events and their fit represented in different colours. Note that only few events are presented in colours for better visibility, c): Number of sources $N(l)$ versus ADN length $G(l)$ from which we obtain the geomorphologic exponent b_G and d) total area draining directly in all sources of the ADN A_N versus total area draining directly in the ADN A_T from which we obtain the geomorphologic exponent b_A.

have been fitted only up to when 80% of the initial ADN has receded in order to avoid the last part where $N(G)$ is piecewise constant. In d) of Figure 3.3, according to the proposed revision of the original method, we show the area A_N draining directly in the sources of the ADN versus the total area A_T draining in the ADN. In the three plots, the cloud of points is quite noisy at the end of the recession (that is, for the smallest total areas) which is a signature of the watershed geometrical attributes and of uneven local drainage densities. All the values of the exponents b_G and b_A are presented in Table 3.2. The two exponents b_G and b_A are similar in the case of catchment 15 (first column in Figure 3.3), a catchment with fairly constant hillslope to channel distance. This supports our ansatz that the different methods provide indistinguishable results in cases where drainage density can be regarded as relatively uniform in space. In the case of catchment 24 (second column in Figure 3.3) and especially in the case of catchment 27 (third column in Figure 3.3), major differences arise from the two methods. Both catchments exhibit very variable patterns in the hillslope distance to the nearest channel. Remarkably, however, it appears that a scaling relation between A_N and A_T can still be found and that allows a fair determination of the scaling exponent b_A. In the case of catchment 27, the exponents b_G obtained with the two DEM of different resolution were very similar but relatively different for the exponent b_A (see Table 3.2). The values computed with the 5 meter resolution DEM have been used in the following for the catchment 27.

(a)   (b)
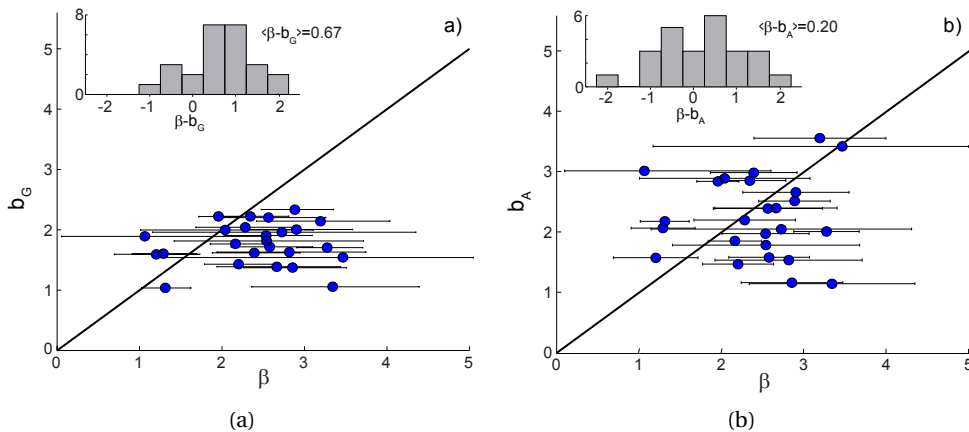
Figure 3.4: Recession exponent β versus geomorphological exponent for a) b_G with the N versus G method and b) b_A with the A_N versus A_T method. The insets in a) and b) correspond to a simple frequency distribution of the residuals $\beta - b_G$ and $\beta - b_A$ respectively.

The geomorphological exponents of the two conceptual models, b_G and b_A, have been compared to the recession exponents β of all the basins in Figure 3.4 a-b respectively. The horizontal uncertainty bars represent the standard deviation of the recession exponents β computed on a single event basis and the solid black line represents the one-to-one relation. The upper plot is visibly more scattered than the lower plot where the points are more aligned along the one to one line. More formally, a simple frequency distribution of the difference between the geomorphological exponents b_G and b_A and the median recession exponents β is presented

in the insets of Figures 3.4 a-b respectively. With a mean residual of 0.20, it appears clearly that, on average, the exponent b_A obtained with the new method matches better the exponent β of the recession analysis than the exponent b_G obtained with the first method (mean residual of 0.67).

The improvement of the new method is even more remarkable when the residuals are classified along mean basin altitudes, see color coding in Figure 3.5. For low altitude basins (mean altitude below 1000 m, first line in green in Figure 3.5), the mean residuals decrease between the first and the second method. For the watersheds at medium mean altitudes (mean altitude between 1000 m and 2000 m in red in Figure 3.5) and especially for watersheds at high mean altitudes (mean altitude above 2000 m in blue in Figure 3.5), the new method improves the results with a larger decrease in the mean residual. Assuming increasing spatial complexity of the channel network with mean basin altitude, our results suggest that the proposed revised method provides better results in catchments where local drainage density is naturally heterogeneous reflecting the variety of channel initiation processes (i.e. proglacial, high altitude catchments). In the case of low altitude catchments, where local drainage density tends to be uniform in space, the two methods provide similar results.
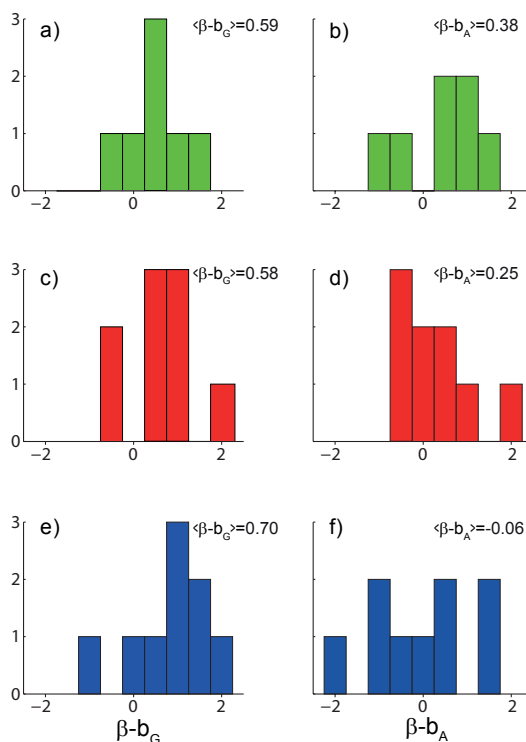
Figure 3.5: Histogram of the residuals between the recession exponent β and the geomorphological exponents b_G (left histograms a, c and e) and b_A (right histograms b, d and f) classified along mean basin altitude, from top to bottom in green (first row, a and b) for basins at mean altitude below 1000 m, in red (c and d) for basins at mean altitude between 1000 m and 2000 m and in blue (e and f) for basins at mean altitude above 2000 m.

	Number of events	Coeff. β for all events together	Median coeff. β for separated events	Mean coeff. β for separated events	Standard deviation of β	b_G (N vs G)	residuals median β-b_G	b_A (A_N vs A_T)	residuals median β-b_A
1	30	1.75	2.58	2.70	0.98	1.70±0.01	0.87	1.56± 0.03	1.02
2	36	2.21	3.28	3.27	0.80	1.69±0.01	1.59	1.99± 0.03	1.29
3	30	1.66	2.16	2.12	0.65	1.75±0.01	0.41	1.83± 0.07	0.34
4	23	1.24	1.96	1.83	0.51	2.21±0.01	-0.25	2.82± 0.05	-0.86
5	59	1.73	2.54	2.80	1.06	1.89±0.01	0.64	1.95± 0.02	0.59
6	25	2.55	6.24	6.96	4.52	2.45±0.02	3.78	2.52± 0.07	3.71
7	19	1.03	2.54	3.26	2.28	1.80±0.02	0.74	1.76± 0.11	0.78
8	19	1.73	2.35	2.26	0.87	2.21±0.02	0.13	2.83± 0.07	-0.49
9	14	1.88	2.89	2.61	0.87	2.32±0.02	0.56	2.49± 0.05	0.40
10	25	1.81	2.91	2.86	1.29	1.99±0.01	0.91	2.64± 0.02	0.27
11	56	1.82	3.34	3.91	2.01	0.79±0.09	2.56	1.12± 0.15	2.22
12	13	1.48	1.20	1.77	1.03	1.10±0.06	0.11	1.55± 0.13	-0.35
13	36	1.15	2.20	2.17	0.86	1.42±0.01	0.79	1.44± 0.06	0.76
14	44	1.80	2.28	2.55	1.23	2.03±0.01	0.25	2.18± 0.02	0.11
15	20	1.57	2.57	2.55	1.33	2.19±0.01	0.38	2.37± 0.03	0.20
16	23	1.87	2.39	2.70	1.05	1.60±0.01	0.79	2.96± 0.04	-0.57
17	10	1.51	1.29	1.70	0.78	1.59±0.01	-0.30	2.04± 0.06	-0.75
18	17	0.74	2.04	2.49	2.07	1.98±0.01	0.06	2.87± 0.03	-0.83
19	12	1.42	2.86	3.01	1.23	1.36±0.02	1.50	1.14± 0.07	1.72
20	13	0.89	1.06	2.65	2.94	1.88±0.01	-0.81	2.99± 0.12	-1.92
21	25	1.73	2.73	3.63	3.16	1.94±0.02	0.78	2.03± 0.06	0.70
22	14	0.59	1.31	1.32	0.59	1.02±0.01	0.29	2.15± 0.13	-0.84
23	14	1.53	3.20	3.48	1.61	2.12±0.08	1.07	3.53± 0.25	-0.34
24	18	1.75	2.66	2.95	1.49	1.37±0.02	1.29	2.38± 0.07	0.29
25	40	1.79	3.90	4.29	3.18	1.37±0.02	2.53	1.29± 0.08	2.62
26	11	1.72	2.82	2.81	1.79	1.62±0.01	1.20	1.51± 0.09	1.31
27	12	1.05	3.47	5.51	4.59	1.48±0.02 (a)	1.99	4.11±0.15 (a)	-0.64
						1.53±0.01 (b)	1.94	3.40±0.04 (b)	0.07

Table 3.2: Summary of the results obtained from the recession analysis (exponent β), from the model comparing N versus G (geomorphological exponent b_G) and from the model comparing A_N versus A_T (geomorphological exponent b_A) and their respective residuals compared to *beta*. For watershed 27, the results are obtained with (a) the 25 m resolution and (b) the 5 m resolution DEM.

3.5 Discussion

We find that the discrepancies arising between the exponent β obtained from the analysis of the recession curves and the geomorphological parameter b_G obtained from the original method proposed in *Biswal and Marani* (2010) are relatively small for low altitude basins but larger for higher altitude basins. Compared to the watersheds studied in *Biswal and Marani* (2010), the watersheds chosen in this study are probably less suited to the original conditions envisioned by *Brutsaert and Nieber* (1977): they are relatively smaller, structurally inconsistent with the conceptual model of simple drainage of an unconfined aquifer and generally exhibiting faster responses to rainfall impulses especially due to steep hillslopes. Often, as highlighted in the physical features of Table 3.1, the catchment response shows signatures of snow or ice melt, both leading to larger uncertainties in the evaluation of the recession exponent β. Moreover, such discrepancy is very large in the case of an urbanized watershed (basin 6 in Table 3.1 and Table 3.2), confirming that the method is mostly suited to

watersheds with little anthropogenic influence. However, the discrepancies between b_G and β cannot be explained only by the uncertainty in the exponent β, and some assumptions made by the method must be relaxed when hydrologic and geomorphic conditions required are not met.

Our proposed correction of the method indeed accounts for uneven local drainage density, because it assumes that the local contributing discharge per unit length of receding ADN is limited by the local hillslope to channel distance and its directly contributing area. This is typically occurring in high altitude, proglacial dominated catchments where channel initiation processes are most diverse and unchanneled distances may vary from tens to thousands of meters. The inclusion aims at improving our understanding of the geomorphological origin of the recession curves, as noted in the Methods section. The system is described by the evolution in time of A_T, the area draining directly into the ADN relative to the area A_N draining into the sources of the ADN, leading to an empirical relation $A_N \propto A_T^{b_A}$. Our results suggest that the new geomorphological parameter b_A is closer to the exponent β, resulting in a decrease of the residuals between the two exponents (Figure 3.4). In particular, the correction is substantial in the Val Ferret catchment (number 27) where the real, monitored network has been used for the calculations. For this high-altitude catchment, endowed with highly uneven local drainage density, the residuals between the exponents $\beta - b_G$ and $\beta - b_A$ decrease from 1.99 to -0.64 and from 1.94 to 0.07 between the two methods for the 25 meter resolution and the 5 meter resolution DEM respectively. In other particular cases where the local drainage density is more even, the two methods produce very similar results (see catchments 3, 5 or 7) and the two methods give comparable results as expected from the fact that the approaches tend to collapse into the same formulation.

We acknowledge several sources of uncertainty introduced in the model, chiefly through the resolution of the DEM and through the area threshold method adopted for the channel network extraction (which is known to fail in complex terrain where heterogeneities of channel initiation processes are major). In the Val Ferret catchment, the uncertainty in the channel network extraction is dramatically decreased by an accurate field channel network monitoring resulting in improved results for the method proposed here. However, the time series available for measured streamflows for this watershed is less compared to the 26 others leading to a greater uncertainty in the exponent β. Field campaigns in other small watersheds aimed at monitoring channel initiations would probably improve the performance and the reliability of this conceptual model. In the Val Ferret catchment, our results were not affected by the DEM resolution since the geomorphological parameter b_A was closer to β than b_G to β in both DEM resolution cases. Therefore, the uncertainty introduced by the DEM resolution might only alter the accuracy of the predicted exponent but not the essence of our method. We also acknowledge larger uncertainties in the estimation of the parameter b_A due to the larger scatter in the A_N versus A_T plots which is the mark of uneven local drainage densities. We note, however, that the error in the estimate of the parameter b_A is still small compared to the error in the exponent β. Finally, we note that our study pinpoints that the most critical assumption of the conceptual model lies in neglecting the term dq/dt in Eq. 3.3 with respect

to the change in the ADN geometry. Further studies are thus needed in order to combine the results of the method here formulated with a possibly geomorphically-controlled integration, modeling the speed of the negative travelling wave of active stream switch-offs.

3.6   Concluding remarks

Catchment recession curves bear the signatures of geomorphology. Two conceptual models based on empirical relations obtained solely from the analysis of DEMs have been compared. Both models describe the impact of geomorphology on the recession curves of the stream network, described in the first model by the evolution of the number of sources in the active channel network versus the total active channel network length, and in the latter by the area draining in the sources of the receding network versus the total area draining directly in the network. From the analysis of 27 catchments relatively unaffected by anthropogenic influence, our results suggest that the two models give similar results in the cases where local drainage density is approximately constant. In the cases of spatially uneven local drainage density, the first model does not hold and the new model presented here improves the results for high altitude basins. In general, we suggest that this conceptual model might be useful to estimate the low flow regime of natural ungauged basins by predicting its features solely from information remotely acquired and objectively manipulated through DEM data.

Acknowledgments

Table 3.1: Summary of geomorphological characteristics, discharge and precipitation data for the 27 watersheds.(1)

N. basin	Name	Geomorphology Basin surface [km²]	Mean basin altitude [m]	Maximal basin altitude [m]	Mean basin slope [m/km]	Glacier extension [%]	Discharge data Coordinates gauging station [m] X	Y	Station altitude [m]	Precipitation data Name	Coordinates gauging station [m] X	Y	Dist. from discharge station [km]	Measure start	Measure end
1	Murg-Wängi	78	650	1035	25.5	0	714105	261720	466	Eschlikon	715095	258260	3.60	01.01.1974	01.01.2010
2	Gürbe-Belp, Mülimatt	117	849	2176	52.2	0	604810	192680	522	Belp	605140	193805	1.17	01.01.1974	01.01.2010
3	Goldach Bleiche	49.8	833	1251	39.3	0	753190	261590	399	Arbon	749840	263150	3.70	01.01.1974	01.01.2010
4	Necker-Mogelsberg, Aachsäge	88.2	959	1532	35.6	0	727110	247290	606	Mogelsberg	728220	247010	1.14	01.01.1974	01.01.2010
5	Venoge-Ecublens, Les Bois	231	700	1431	-	0	532040	154160	383	Marcelin	527060	152160	5.37	01.01.1979	01.01.2010
6	Murg-Murgenthal, Walliswil	207	637	1119	18.6	0	629340	233555	419	Wynau	626400	233850	2.95	01.06.1980	01.01.2010
7	Sellenbodenbach-Neuenkirch	10.5	615	838	36.5	0	658530	218290	515	Sempach	657010	220940	3.05	01.09.1990	01.01.2010
8	Scheulte-Vicques	72.8	785	1302	30.9	0	599485	244150	463	Mervelier	604610	243670	5.15	01.01.1992	01.01.2010
9	Sitter-Appenzell	74.2	1252	2500	139.6	0.08	749040	244220	769	Appenzell	747735	244475	1.33	01.01.1974	01.01.2010
10	Sense-Thörishaus, Sensematt	352	1068	2190	25.4	0	593350	193020	553	Schwarzenburg	593150	184720	8.30	01.01.1977	01.01.2010
11	Melera-Melera (Valle Morobbia)	1.05	1419	1728	-	0	726988	114670	944	Bellinzona	721060	116800	6.30	01.01.1974	01.01.2010
12	Rotenbach-Plaffeien, Schweinsberg	1.65	1454	1628	151.3	0	587980	170590	1275	Sangernboden	593220	173905	6.20	01.08.1995	01.01.2010
13	Riale di Calneggia-Cavergno, Pontit	24	1996	2921	231	0	684970	135970	890	Bosco-Gurin	681160	130025	7.06	01.01.1974	01.01.2010
14	Areuse-Boudry	377	1060	1607	-	0	554350	199940	444	Combe-Garot	551220	201450	3.48	01.01.1983	01.01.2010
15	Ilfis-Langnau	188	1051	2092	30.9	0	627320	198600	685	Kurzeneialp	630575	207010	9.02	01.04.1989	01.01.2010
16	Verzasca-Lavertezzo, Campiöi	185	1661	2864	72.4	0	708420	122290	490	Cimetta	704370	117515	6.26	01.08.1989	01.01.2010
17	Alp-Einsiedeln	46.4	1155	1899	40.8	0	698640	223020	840	Altmatt	695420	220770	3.93	01.02.1991	01.01.2010
18	Massa-Blatten bei Naters	195	2945	4195	183.17	65.9	643700	137290	1446	Brig	640570	129080	8.79	01.01.1974	01.01.2010
19	Krummbach-Klusmatten	19.8	2276	3268	121.8	3	644500	119420	1795	Simplon-Dorf	647570	116110	4.51	01.01.1974	01.01.2010
20	Rhone-Gletsch	38.9	2719	3622	-	52.2	670810	157200	1761	Grimsel Hospiz	668583	158215	2.45	01.01.1974	01.01.2010
21	Grosstalbach-Isenthal	43.9	1820	2952	211.1	9.3	685500	196050	767	Isenthal	685460	196110	0.07	01.01.1974	01.01.2010
22	Alpbach-Erstfeld, Bodenberg	20.6	2200	3198	414	27.7	688560	185120	1022	Altdorf	690174	193558	8.59	01.01.1974	01.01.2010
23	Ova da Cluozza-Zernez	26.9	2368	3165	180	2.2	804930	174830	1509	Zernez	802720	175230	2.25	01.01.1974	01.01.2010
24	Dischmabach-Davos Kriegsmatte	43.3	2372	3146	129.4	2.1	786220	183370	1668	Dischma	786600	182990	0.54	01.01.1974	01.01.2010
25	Poschiavino-La Rösa	14.1	2283	3032	91.3	0.35	802120	142010	1860	Cavaglia	799850	138470	4.21	01.01.1974	01.01.2010
26	Rein da Sumvitg-Sumvitg, Encardens	21.8	2450	3168	165.5	6.7	718810	167690	1490	Vrin	727220	168670	8.47	01.01.1977	01.01.2010
27	Val Ferret, Ferret	20.4	2422.8	3206	385	2.1	574932	83779	1773	Val Ferret	various	various	0.08	01.05.2008	01.11.2012

(1) The coordinates are given in the Swiss Coordinate System.

Bibliography

Bertuzzo, E., A. Maritan, M. Gatto, I. Rodriguez-Iturbe, and A. Rinaldo (2007), River networks and ecological corridors: Reactive transport on fractals, migration fronts, hydrochory, *Water Resources Research*, *43*(4), doi:10.1029/2006wr005533.

Biswal, B., and M. Marani (2010), Geomorphological origin of recession curves, *Geophysical Research Letters*, *37*(24), doi:10.1029/2010gl045415.

Biswal, B., and D. Nagesh Kumar (2012), Study of dynamic behaviour of recession curves, *Hydrological Processes*, doi:10.1002/hyp.9604.

Botter, G., F. Peratoner, A. Porporato, I. Rodriguez-Iturbe, and A. Rinaldo (2007a), Signatures of large-scale soil moisture dynamics on streamflow statistics across U.S. climate regimes, *Water Resources Research*, *43*(11), doi:10.1029/2007wr006162.

Botter, G., A. Porporato, E. Daly, I. Rodriguez-Iturbe, and A. Rinaldo (2007b), Probabilistic characterization of base flows in river basins: Roles of soil, vegetation, and geomorphology, *Water Resources Research*, *43*(6), doi:10.1029/2006wr005397.

Botter, G., A. Porporato, I. Rodriguez-Iturbe, and A. Rinaldo (2009), Nonlinear storage-discharge relations and catchment streamflow regimes, *Water Resources Research*, *45*(10), doi:10.1029/2008wr007658.

Botter, G., E. Bertuzzo, and A. Rinaldo (2010), Transport in the hydrologic response: Travel time distributions, soil moisture dynamics, and the old water paradox, *Water Resources Research*, *46*(3), doi:10.1029/2009wr008371.

Boussinesq, J. (1903), Sur le débit, en temps de sécheresse, d'une source alimentée par une nappe d'eaux d'infiltration, *CR Acad. Sci*, *136*, 1511–1517.

Boussinesq, J. (1904), Recherches théoriques sur l'écoulement des nappes d'eau infiltrées dans le sol et sur le débit des sources, *Journal de mathématiques pures et appliquées*, pp. 5–78.

Brutsaert, W. (2008), Long-term groundwater storage trends estimated from streamflow records: Climatic perspective, *Water Resources Research*, *44*(2), doi:10.1029/2007WR006518.

Bibliography

Brutsaert, W., and T. Hiyama (2012), The determination of permafrost thawing trends from long-term streamflow measurements with an application in eastern Siberia, *Journal of Geophysical Research: Atmospheres*, *117*(D22), doi:10.1029/2012JD018344.

Brutsaert, W., and J. P. Lopez (1998), Basin-scale geohydrologic drought flow features of riparian aquifers in the Southern Great Plains, *Water Resources Research*, *34*(2), 233–240, doi:10.1029/97WR03068.

Brutsaert, W., and J. L. Nieber (1977), Regionalized drought flow hydrographs from a mature glaciated plateau, *Water Resources Research*, *13*(3), 637–643, doi:10.1029/WR013i003p00637.

Brutsaert, W., and M. Sugita (2008), Is Mongolia's groundwater increasing or decreasing? The case of the Kherlen River basin, *Hydrological Sciences Journal*, *53*(6), 1221–1229, doi: 10.1623/hysj.53.6.1221.

Ceola, S., G. Botter, E. Bertuzzo, A. Porporato, I. Rodriguez-Iturbe, and A. Rinaldo (2010), Comparative study of ecohydrological streamflow probability distributions, *Water Resources Research*, *46*(9), doi:10.1029/2010WR009102.

Eng, K., and W. Brutsaert (1999), Generality of drought flow characteristics within the Arkansas River basin, *Journal of Geophysical Research*, *104*(D16), 19,435–19,441, doi: 10.1029/1999jd900087.

Harman, C. J., M. Sivapalan, and P. Kumar (2009), Power law catchment-scale recessions arising from heterogeneous linear small-scale dynamics, *Water Resources Research*, *45*(9), doi:10.1029/2008WR007392.

Horton, R. (1932), Drainage basin characteristics, *Transactions of the American Geophysical Union*, *13*, 350–361.

Horton, R. (1945), Erosional development of streams and their drainage basins; hydrophysical approach to quantitative morphology, *Geological Society of America Bulletin*, *56*(3), 275–370.

Kirchner, J. W. (2009), Catchments as simple dynamical systems: Catchment characterization, rainfall-runoff modeling, and doing hydrology backward, *Water Resources Research*, *45*(2), doi:10.1029/2008wr006912.

Kondolf, G. M., L. M. Maloney, and J. G. Williams (1987), Effects of bank storage and well pumping on base flow, Carmel River, Monterey County, California, *Journal of Hydrology*, *91*, 351–369, doi:10.1016/0022-1694(87)90211-3.

Malvicini, C. F., T. S. Steenhuis, M. T. Walter, J. Y. Parlange, and M. F. Walter (2005), Evaluation of spring flow in the uplands of Matalom, Leyte, Philippines, *Advances in Water Resources*, *28*(10), 1083–1090, doi:10.1016/j.advwatres.2004.12.006.

Marani, M., E. Belluco, A. D'Alpaos, A. Defina, S. Lanzoni, and A. Rinaldo (2003), On the drainage density of tidal networks, *Water Resources Research*, *39*(2), 1040, doi:10.1029/2001wr001051.

McMillan, H. K., M. P. Clark, W. B. Bowden, M. Duncan, and R. A. Woods (2011), Hydrological field data from a modeller's perspective: Part 1. Diagnostic tests for model structure, *Hydrological Processes, 25*(4), 511–522, doi:10.1002/hyp.7841.

Mendoza, G. F., T. S. Steenhuis, M. T. Walter, and J. Y. Parlange (2003), Estimating basin-wide hydraulic parameters of a semi-arid mountainous watershed by recession-flow analysis, *Journal of Hydrology, 279*(1–4), 57–69, doi:10.1016/s0022-1694(03)00174-4.

Montgomery, D., and W. Dietrich (1988), Where do channels begin?, *Nature, 336*(6196), 232–234, doi:10.1038/336232a0.

Montgomery, D. R., and W. E. Dietrich (1992), Channel initiation and the problem of landscape scale, *Science, 255*(5046), 826–830, doi:10.1126/science.255.5046.826.

Montgomery, D. R., and E. Foufoula-Georgiou (1993), Channel network source representation using digital elevation models, *Water Resources Research, 29*(12), 3925–3934, doi:10.1029/93wr02463.

O'Callaghan, J. F., and D. M. Mark (1984), The extraction of drainage networks from digital elevation data, *Computer Vision, Graphics, and Image Processing, 28*(3), 323–344, doi:10.1016/s0734-189x(84)80011-0.

Palmroth, S., G. G. Katul, D. Hui, H. R. McCarthy, R. B. Jackson, and R. Oren (2010), Estimation of long-term basin scale evapotranspiration from streamflow time series, *Water Resources Research, 46*(10), doi:10.1029/2009wr008838.

Parlange, J. Y., F. Stagnitti, A. Heilig, J. Szilagyi, M. B. Parlange, T. S. Steenhuis, W. L. Hogarth, D. A. Barry, and L. Li (2001), Sudden drawdown and drainage of a horizontal aquifer, *Water Resources Research, 37*(8), 2097–2101, doi:10.1029/2000wr000189.

Polubarinova-Kochina, P. Y. (1962), Theory of ground water movement princeton university press, *Princeton, NJ.*

Rinaldo, A., W. E. Dietrich, R. Rigon, G. K. Vogel, and I. Rodrlguez-lturbe (1995a), Geomorphological signatures of varying climate, *Nature, 374*(6523), 632–635, doi:10.1038/374632a0.

Rinaldo, A., G. K. Vogel, R. Rigon, and I. Rodriguez-Iturbe (1995b), Can one gauge the shape of a basin?, *Water Resources Research, 31*(4), 1119–1127, doi:10.1029/94wr03290.

Rinaldo, A., G. Botter, E. Bertuzzo, A. Uccelli, T. Settin, and M. Marani (2006), Transport at basin scales: 1. Theoretical framework, *Hydrology and Earth System Sciences, 10*(1), 19–29, doi:10.5194/hess-10-19-2006.

Rodriguez-Iturbe, I., and A. Rinaldo (2001), *Fractal river basins: chance and self-organization,* 547 pp., Cambridge Univ Pr, Cambridge, UK.

Bibliography

Rodriguez-Iturbe, I., R. Muneepeerakul, E. Bertuzzo, S. A. Levin, and A. Rinaldo (2009), River networks as ecological corridors: A complex systems perspective for integrating hydrologic, geomorphologic, and ecologic dynamics, *Water Resources Research*, *45*(1), doi:10.1029/2008wr007124.

Rupp, D. E., and J. S. Selker (2006a), Information, artifacts, and noise in dQ/dt-Q recession analysis, *Advances in Water Resources*, *29*(2), 154–160, doi:10.1016/j.advwatres.2005.03.019.

Rupp, D. E., and J. S. Selker (2006b), On the use of the Boussinesq equation for interpreting recession hydrographs from sloping aquifers, *Water Resources Research*, *42*(12), doi:10.1029/2006wr005080.

Rupp, D. E., J. M. Owens, K. L. Warren, and J. S. Selker (2004), Analytical methods for estimating saturated hydraulic conductivity in a tile-drained field, *Journal of Hydrology*, *289*(1–4), 111–127, doi:10.1016/j.jhydrol.2003.11.004.

Rupp, D. E., J. Schmidt, R. A. Woods, and V. J. Bidwell (2009), Analytical assessment and parameter estimation of a low-dimensional groundwater model, *Journal of Hydrology*, *377*(1–2), 143 – 154, doi:10.1016/j.jhydrol.2009.08.018.

Shaw, S. B., and S. J. Riha (2012), Examining individual recession events instead of a data cloud: Using a modified interpretation of dQ/dt–Q streamflow recession in glaciated watersheds to better inform models of low flow, *Journal of Hydrology*, *434-435*(0), 46 – 54, doi:10.1016/j.jhydrol.2012.02.034.

Simoni, S., S. Padoan, D. F. Nadeau, M. Diebold, A. Porporato, G. Barrenetxea, F. Ingelrest, M. Vetterli, and M. B. Parlange (2011), Hydrologic response of an alpine watershed: Application of a meteorological wireless sensor network to understand streamflow generation, *Water Resources Research*, *47*(10), doi:10.1029/2011wr010730.

Sofia, G., P. Tarolli, F. Cazorzi, and G. Dalla Fontana (2011), An objective approach for feature extraction: distribution analysis and statistical descriptors for scale choice and channel network identification, *Hydrology and Earth System Sciences*, *15*(5), 1387–1402, doi:10.5194/hess-15-1387-2011.

Szilagyi, J., and M. B. Parlange (1998), Baseflow separation based on analytical solutions of the Boussinesq equation, *Journal of Hydrology*, *204*(1–4), 251 – 260, doi:10.1016/S0022-1694(97)00132-7.

Szilágyi, J., and M. B. Parlange (1999), A geomorphology-based semi-distributed watershed model, *Advances in Water Resources*, *23*(2), 177 – 187, doi:10.1016/S0309-1708(99)00021-4.

Szilágyi, J., M. B. Parlange, and J. D. Albertson (1998), Recession flow analysis for aquifer parameter determination, *Water Resources Research*, *34*(7), 1851–1857, doi:10.1029/98wr01009.

Tague, C., and G. E. Grant (2004), A geological framework for interpreting the low-flow regimes of Cascade streams, Willamette River Basin, Oregon, *Water Resources Research*, *40*(4), doi:10.1029/2003wr002629.

Tallaksen, L. M. (1995), A review of baseflow recession analysis, *Journal of Hydrology*, *165*(1–4), 349–370, doi:10.1016/0022-1694(94)02540-r.

Tarboton, D., R. Bras, and I. Rodriguez Iturbe (1991), On the extraction of channel networks from digital elevation data, *Hydrological Processes*, *5*(1), 81–100, doi:10.1002/hyp. 3360050107.

Tarolli, P., and G. Dalla Fontana (2009), Hillslope-to-valley transition morphology: New opportunities from high resolution DTMs, *Geomorphology*, *113*(1–2), 47–56, doi:10.1016/j. geomorph.2009.02.006.

Thompson, S. E., and G. G. Katul (2012), Multiple mechanisms generate Lorentzian and $1/f^\alpha$ power spectra in daily stream-flow time series, *Advances in Water Resources*, *37*(0), 94–103, doi:10.1016/j.advwatres.2011.10.010.

Troch, P. A., F. P. De Troch, and W. Brutsaert (1993), Effective water table depth to describe initial conditions prior to storm rainfall in humid regions, *Water Resources Research*, *29*(2), 427–434, doi:10.1029/92wr02087.

Tucker, G., F. Catani, A. Rinaldo, and R. Bras (2001), Statistical analysis of drainage density from digital terrain data, *Geomorphology*, *36*(3-4), 187–202, doi:10.1016/S0169-555X(00)00056-8.

Vogel, R. M., and C. N. Kroll (1992), Regional geohydrologic-geomorphic relationships for the estimation of low-flow statistics, *Water Resources Research*, *28*(9), 2451–2458, doi:10.1029/ 92wr01007.

Wang, D., and X. Cai (2010), Recession slope curve analysis under human interferences, *Advances in Water Resources*, *33*(9), 1053–1061, doi:10.1016/j.advwatres.2010.06.010.

Weijs, S. V., R. Mutzner, and M. B. Parlange (2013), Could electrical conductivity replace water level in rating curves for alpine streams?, *Water Resources Research*, *49*(1), 343–351, doi:10.1029/2012WR012181.

Wittenberg, H. (1999), Baseflow recession and recharge as nonlinear storage processes, *Hydrological Processes*, *13*(5), 715–726, doi:10.1002/(SICI)1099-1085(19990415)13:5<715:: AID-HYP775>3.0.CO;2-N.

Zaliapin, I., E. Foufoula-Georgiou, and M. Ghil (2010), Transport on river networks: A dynamic tree approach, *Journal of Geophysical Research*, *115*, doi:10.1029/2009jf001281.

Zecharias, Y. B., and W. Brutsaert (1988), Recession characteristics of groundwater outflow and base flow from mountainous watersheds, *Water Resources Research*, *24*(10), 1651–1658, doi:10.1029/WR024i010p01651.

4 Controls on the diurnal streamflow cycles in the Val Ferret watershed

This chapter has been submitted for publication with the following citation:

Abstract: *In high altitude alpine catchments, streamflow diurnal cycles are typically dominated by snowmelt or ice melt. During a field campaign in the summer 2012 in an alpine catchment in the Swiss Alps (Val Ferret catchment, 20.4 km^2, glaciarized area: 2%), we observed a transition in the early season from a snowmelt to an evapotranspiration-induced diurnal streamflow cycle in one of the two monitored sub-basins. The two different cycles were of comparable amplitudes and the transition happened within a time span of several days. In the second monitored sub-basin, we observed an ice melt-dominated diurnal cycle during the entire season due to the presence of a small glacier. Comparisons between ice melt and evapotranspiration cycles showed that the two processes were happening at the same times of day but with a different sign and a different shape. The amplitude of the ice melt cycle decreased exponentially during the season and was larger than the amplitude of the evapotranspiration cycle which was relatively constant during the season. Our study suggests that an evapotranspiration-dominated diurnal streamflow cycle could damp the ice melt-dominated diurnal streamflow cycle. The two types of diurnal streamflow cycles were separated using a method based on the identification of the active riparian area and measurement of evapotranspiration.*

4.1 Introduction

During recession events or during low flow conditions, daily or sub-daily streamflow variations can take place in many different types of watersheds. The study of those daily variations can improve our understanding of the processes happening at different scales and improve hydrological modeling (*Kirchner*, 2009). As raised by *Lundquist and Cayan* (2002), when caused by solar radiation and temperature variations, the study of streamflow diurnal cycles can also be used to assess the impact of climate change on the watershed behavior. Streamflow or groundwater level diurnal cycles have been observed in very diverse places (see *Gribovszki et al.* (2010) for a review). For instance, *Lundquist and Cayan* (2002) detected streamflow diurnal changes in a large variety of watersheds in the Western United States featuring both snowmelt and evapotranspiration/infiltration driving processes and classified the watersheds by the diurnal cycle properties. The characteristics of the streamflow diurnal cycles can therefore serve as a comparison tool between catchments. Diurnal streamflow cycles are characterized through their amplitude, timing of the minimum or maximum streamflow (*Bren*, 1997; *Bond et al.*, 2002; *Caine*, 1992; *Graham et al.*, 2013; *Lundquist and Cayan*, 2002; *Lundquist et al.*, 2005; *Wondzell et al.*, 2007), shape and asymmetry (*Caine*, 1992; *Lundquist and Cayan*, 2002).

In alpine regions, diurnal streamflow cycles are mainly caused by ice melt or snowmelt resulting in a streamflow increase. These perturbations are observed at gauging stations with delays depending on the size of the watershed (*Lundquist et al.*, 2005). Ice melt or snowmelt diurnal streamflow cycle characteristics have been used to study catchment scale snowpack properties (*Caine*, 1992; *Kobayashi and Motoyama*, 1984; *Lundquist and Dettinger*, 2005), estimate hydraulic parameters of the riparian zone (*Loheide II and Lundquist*, 2009), characterize the glacier drainage network (*Collins*, 1995, 1979) or to study suspended sediment transport at the snout of a glacier (*Singh et al.*, 2005). High temporal resolution hydrological models are now able to reproduce diurnal streamflow cycles in alpine regions even though simple degree-day models remain widely used (see *Hock* (2005) for a review). For instance, *Simoni et al.* (2011) successfully applied a modified version of the simple degree-day formulation taking into account the daily and hourly mean air temperatures to reproduce hourly ice melt and snowmelt in a high-altitude Swiss catchment. Several studies achieved more accurate results at hourly resolutions by adding a shortwave or net radiation term in the classical degree-day method (*Cazorzi and Fontana*, 1996; *Jost et al.*, 2012; *Kane et al.*, 1997; *Kustas et al.*, 1994; *Martinec*, 1989; *Tobin et al.*, 2013). More sophisticated distributed energy balance models (*Lehning et al.*, 2006; *Rigon et al.*, 2006) have also successfully reproduced diurnal streamflow cycles, but are less commonly used due to the need of spatially distributed hydrometeorological forcing data. Even though the robustness of hydrological models are usually evaluated on larger timescales, diurnal streamflow cycles are of critical importance for calibration and performance evaluation of hydrological models running at hourly or higher resolution timescales (*Reusser et al.*, 2009).

Diurnal streamflow cycles characterized by a decrease in streamflow have been associated with

processes such as evapotranspiration and groundwater recharge in losing streams. Diurnal streamflow cycles induced by groundwater recharge processes are related to the daily fluctuations of streamwater and streambed temperatures (*Constantz et al.*, 1994; *Constantz*, 1998; *Ronan et al.*, 1998). These diurnal streamflow variations are the largest when the streamflow is low and/or the hydraulic radius is small and when the stream is unshaded and highly exposed to solar radiative fluxes (*Lundquist and Cayan*, 2002).

Diurnal streamflow cycles induced by evapotranspiration have been studied for decades with diurnal groundwater level cycles in a broad range of watersheds and their origin are still investigated (*Barnard et al.*, 2010; *Bren*, 1997; *Graham et al.*, 2013). Several methods have been proposed to estimate daily evapotranspiration based on diurnal groundwater level fluctuations (*White*, 1932; *Dolan et al.*, 1984; *Hays*, 2003; *Gribovszki et al.*, 2008; *Loheide II*, 2008; *Soylu et al.*, 2012; *Szilágyi et al.*, 2008). These methods can be used for estimation of evapotranspiration at relatively low cost compared to evapotranspiration measured with fast-response sensors or lysimeters. Diurnal streamflow cycles have also been used to estimate evapotranspiration of riparian zones by simply computing the difference between the curve that connects daily maximums and actual streamflow rates (*Bond et al.*, 2002; *Boronina et al.*, 2005; *Cadol et al.*, 2012; *Meyboom*, 1965; *Tschinkel*, 1963).

At catchment scale, evapotranspiration rates are often estimated with eddy covariance or alternatively measured with lysimeters, though both are much less common (*Brutsaert*, 1986; *Katul and Parlange*, 1992; *Parlange and Katul*, 1992; *Parlange et al.*, 1995). When measured evapotranspiration rates are available along with evaporated water estimated with the analysis of diurnal streamflow cycles, the area contributing to the overall measured evapotranspiration can be estimated (*Bond et al.*, 2002; *Cadol et al.*, 2012; *Stagnitti et al.*, 1989; *Tsang et al.*, 2014; *Weisman*, 1977). However, few studies have tried to geographically identify those areas of active riparian evapotranspiration (see (*Orellana et al.*, 2012) for a review). *Tsang et al.* (2014) proposed to establish this area by applying a threshold on a modeled depth to the groundwater around the channel network whereas *Boronina et al.* (2005) estimated this area based on land-use maps. Remotely sensed infrared imagery (*Loheide II and Gorelick*, 2006; *Pfister et al.*, 2010) as well as field campaigns aimed at mapping the perennial portion of the stream network (*Godsey and Kirchner*, 2014; *Penna et al.*, 2011) allow for better determination of the extent of the active riparian area. These riparian area estimations are critical for linking observed evapotranspiration-induced diurnal streamflow cycles to catchment scale processes.

In general, most of the aforementioned studies have analyzed cases where only one type of diurnal streamflow cycle was observed. Hence, possible transitions from snowmelt or ice melt to evapotranspiration-dominated diurnal streamflow cycles have been poorly documented. Moreover, the two types of diurnal streamflow cycles might happen at similar times of the day, but separating them by visual inspection can be difficult, especially if one of the processes is dominant. This issue is addressed in this study by using a paired catchment approach in an intensively monitored catchment in the Swiss Alps. Previously, diurnal streamflow cycles were solely attributed to ice melt during the low flow season in this catchment (*Simoni et al.*, 2011).

However, in our study, one sub-basin experiences a transition from a snowmelt-dominated streamflow diurnal cycle to an evapotranspiration-dominated cycle. In the second sub-basin, diurnal streamflow cycles are dominated by ice melt due to the presence of a small glacier. In particular, we assess the impact of evapotranspiration on the ice melt-dominated streamflow cycle in the second sub-basin.

4.2 Study Area and Instrumentation

4.2.1 The Val Ferret Watershed

Since 2009, a relatively small watershed is monitored in the Swiss Alps to study streamflow generation in steep alpine environments. The experimental site shown in Figure 4.1 is located in the southernmost ridge bordering Italy, covering a total surface area of 20.4 km^2 with elevations ranging from 1773 m above sea level (asl) at the outlet of the catchment, to 3236 m asl at the highest point (mean elevation is 2423 m asl). The mean annual precipitation of the area is of 1360 mm. More specific details on the climatic regime of the site can be found in *Simoni et al.* (2011). Since 2012, two sub-basins of the Val Ferret catchment are also intensively monitored (see Figure 4.1). The land cover of the watershed is summarized in Table 4.1 and features a small glacier (*Glacier des Angroniettes*). The riparian area of the watershed is mainly composed of grassland, moss and debris but almost no vegetation with deep roots. The geology of the site is complex, the strata consist mainly of sedimentary shale, quartzite, limestone and sandstone. The analyses of several soil samples revealed a dominance of sandy silt loam and light clay types of soils. One of the appealing factors of this watershed for hydrological studies is the fact that apart from a small drinking water intake of maximum 17 l/s, there is very little anthropogenic influence on the streamflow regime.

Table 4.1: Summary of land cover, expressed in percent of the total area, and geomorphological characteristics of the watershed and the two monitored sub-basins. The terms *altitude* and *slope* refer to mean values.

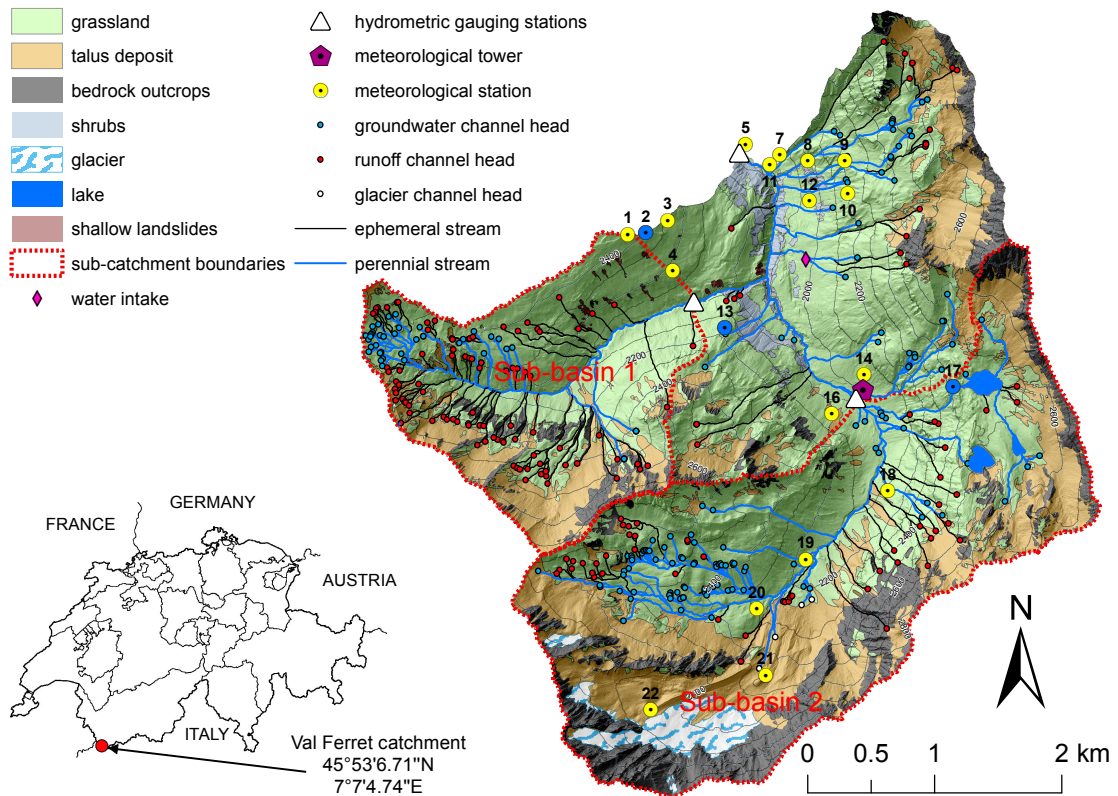|	Land Cover [%]						Geomorphology		
	grass	talus	bedrock	glacier	lake	shrubs	Area [km^2]	altitude [m]	slope [°]
watershed	58.3	24.7	12.8	2.0	0.2	1.8	20.4	2423.2	31.6
sub-basin 1	69.7	22.9	7.4	0	0	0	4.5	2357.7	31.1
sub-basin 2	43.1	32.1	19.5	4.4	0.9	0	9.3	2535.1	31.5

Figure 4.1: Map of the Val Ferret watershed showing the locations of the meteorological stations (in blue if operated during winter), the meteorological tower, the hydrometric gauging stations, the land cover, the locations of the mapped channel heads and the channel network. The intermittent and perennial parts of the channel network are represented respectively by the solid black and blue lines. Based on field observation, the channel heads have been classified as groundwater channel heads (wet, represented in blue), runoff channel heads (dry, represented in red) or glacier channel heads (wet and coming out of the moraine, represented in white).

4.2.2 Channel network survey

During fall 2011, an intensive field observation campaign was conducted to accurately map the stream network, the location of the channel heads and the perennial part of the stream network. The watershed was systematically walked along the main drainage lines up to the catchment divide with a high precision Global Navigation Satellite System device (based both on GPS and GLONASS with typical horizontal error of tens of centimeters) and the locations of 373 channel heads were mapped (see Figure 4.1). Based on field observations, the channel heads have been classified into two main categories: 1) 183 dry runoff channel heads initiated by soil erosion or land sliding processes due to surface or sub-surface runoff activated during rainfall or snowmelt events, 2) 190 wet groundwater channel heads due to groundwater surfacing process, driven by perennial flow (see Figure 4.2a for an illustration). Four other channel heads coming out of the moraine and fed by glacier-melt were also mapped and

named accordingly in Figure 4.1.
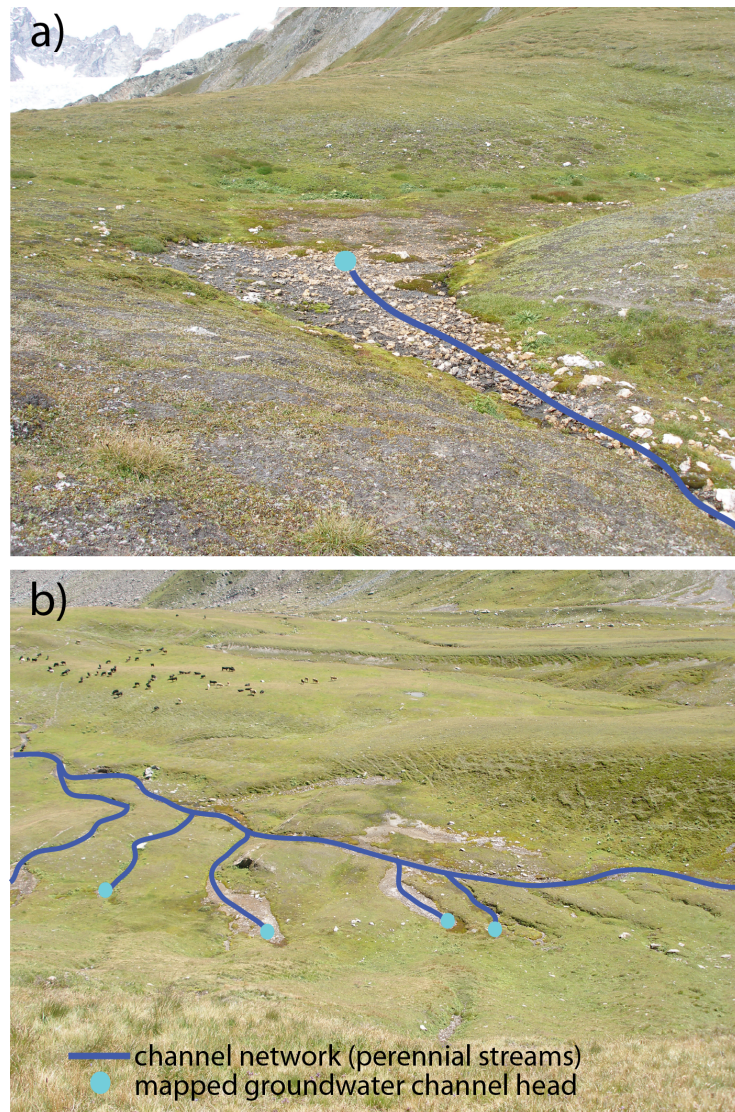
Figure 4.2: Examples of a) a mapped groundwater channel head and b) a mapped part of the watershed with a high density of groundwater surfacing channel heads and large riparian area. Both pictures were taken in the westernmost part of sub-basin 2.

A one meter resolution Lidar derived Digital Elevation Model (DEM) and the mapped channel heads served as the basis for channel network mapping. The channel network was reconstructed by following the flow direction, i.e. the steepest path, from all channel head locations down to the outlet (see Figure 4.2b for an illustration). This field observation based channel network has been used successfully in a geomorphological model predicting properties of baseflow recession events (*Mutzner et al.*, 2013). According to the channel head type and field survey, i.e. runoff or groundwater, the channels have been classified into intermittent and perennial streams, respectively shown in red and blue in Figure 4.1. Over the total network

length, we observed that 52.9% of the channels are perennial whereas the remaining 47.1% are intermittent. This field observation campaign serves as basis for estimating the riparian area of the sub-basins (see Section 4.3 and Section 4.4), that is linked to the evapotranspiration-induced diurnal streamflow cycle.

4.2.3 Meteorological data

The watershed has been heavily monitored since 2009 with a wireless network of small meteorological stations (Sensorscope stations (*Ingelrest et al.*, 2010)) distributed over the entire catchment (see Figure 4.1). In the Val Ferret catchment, these stations were previously used to study the impact of the spatial variability of air temperature and precipitation on a simple hydrological model (*Simoni et al.*, 2011), to improve snowmelt modeling based on the degree-method (*Tobin et al.*, 2013) and to analyze extreme rainfall events (*Thibaud et al.*, 2013). These stations were also used in an urban environment to study the spatial variability of sensible heat flux (*Nadeau et al.*, 2009). The stations typically provide near-surface air temperature and humidity, wind speed and direction, incoming shortwave radiation, surface temperature, rainfall, soil moisture, soil temperature and soil water potential at a temporal resolution of one minute. In this particular study, data of near-surface air temperature and rainfall are used, both measured at all stations. Rainfall is measured with an unheated tipping bucket rain gauge (Davis Rain Collector II) installed 0.4 m above the ground. The air temperature measurements were collected at 1.5 m above the surface using a Sensirion SHT75 sensor protected by a radiation shield.

The locations of the stations were determined to best represent catchment morphological features in terms of slope, aspect and elevation. For most of the stations, it is not possible to maintain them during winter due their exposure to avalanche activity. Most of the stations are therefore usually deployed in late spring and uninstalled in the fall. During the 2012 campaign, all the stations were deployed after the 5th of June and most of them uninstalled the 23rd of October, 18 days before uninstalling the stream water level sensors (see the following section). This was done for logistical and safety reasons to avoid the snowfalls and resulting difficult access to remote parts of the watershed and possible avalanche activity. To capture snowmelt processes, three stations were maintained during the winter, namely stations 2, 13 and 17 in Figure 4.1. In addition, two automatic cameras were installed at station 2, facing south-east and south-west directions respectively. Photographs were recorded at a resolution of 10 megapixels every 2 hours during daytimes of the entire period to estimate snowcover throughout the season.

During fall 2012, a short-term deployment was undertaken, aimed at isolating large coherent turbulent structures in the atmospheric boundary layer as has been previously done above a lake (*Calaf et al.*, 2013). For that purpose, a meteorological tower equipped with fast-response sensors was deployed to measure all the components of the surface energy budget and has been therefore used in this study to establish evapotranspiration rates. The station was

installed at an elevation of 2004 m asl near the outlet of sub-basin 2 and at 1.5 km from the outlet of sub-basin 1 (see Figure 4.1). The station was equipped with two sonic anemometers (CSAT3,Campbell Scientific Inc, USA) mounted parallel to the surface at elevations of 2 m and 4 m above ground. An open-path infrared fast-response CO_2-H_2O analyzer (Li-7500, Li-Cor, USA) was mounted with the lower sonic anemometer for eddy covariance flux measurements. The three sensors were sampling at a frequency of 20 Hz in conjunction with a CR-5000 data logger (Campbell Scientific Inc, USA) and calibrated before deployment. The station was also equipped with a four-component radiometer (Pyranometer CM21 and Pyrgeometer CG4, Kipp & Zonen B.V., The Netherlands) mounted parallel to the surface to measure the components of the radiation balance. The meteorological tower was deployed from September 5th 2012 until October 6th 2012, with a notable gap of 9 days in the data.

4.2.4 Streamflow data

Stream water levels were monitored at the outlet of the catchment and at two locations upstream (see Figure 4.1). Water levels were recorded using pressure sensors (HyMADD, MADD Technologies, Switzerland) with a temporal resolution of one sample every 5 minutes. The loggers were installed inside a metal tube fixed at relatively constant cross-sections of the respective catchment main rivers. The data were downloaded from the loggers and quality-checked on a bi-weekly basis to avoid measurement errors and thermal artifacts (*Cuevas et al.*, 2010; *McLaughlin and Cohen*, 2011) by comparing the logged water level with manual water level measurements. However, the water level sensor installed at the outlet of the watershed suffered from continuous fine sediment deposition during the 2012 campaign resulting in unreliable measurements, which were therefore discarded in the present study. The water level sensors of sub-basin 1 and sub-basin 2 were both operational from July 17th of 2012 to November 7th of 2012. The water level sensors were not deployed during winters because of snow and ice blockage that would lead to unreliable measurements. The water-level sensors were only operational from the 17th of July 2012 because of large snow accumulation in the valley floor due to avalanche activity. The streamflow was regularly measured using the salt dilution method. In total, 7 and 12 gaugings were used to model the rating curve of sub-basins 1 and 2 with a power function (*Weijs et al.*, 2013). The water temperature and electrical conductivity were also monitored at the gauging stations at a temporal resolution of 5 minutes.

Throughout the deployment, the discharge observed at the outlet of sub-basin 1 varied between 0.080 m^3/s and 0.69 m^3/s (see Figure 4.3a). A seasonal decreasing trend in streamflow can be observed along with peaks due to rainfall events. The discharge peak of 0.69 m^3/s was measured during a rainfall event on September 24th (cumulative precipitation of 29.46 mm) accompanied by high soil moisture. At the outlet of sub-basin 2, the discharge varied between 1.2 m^3/s and 0.24 m^3/s (see Figure 4.3b). Similarly to previous years, when the streamflow composition was analyzed in detail (*Simoni et al.*, 2011), the runoff was dominated by snowmelt during July whereas groundwater release and melted water from the glacier are more dominant in the rest of the season. During the entire deployment, diurnal cycles in streamflow could be observed in both sub-basins 1 and 2 and are analyzed in detail in Section 4.4.
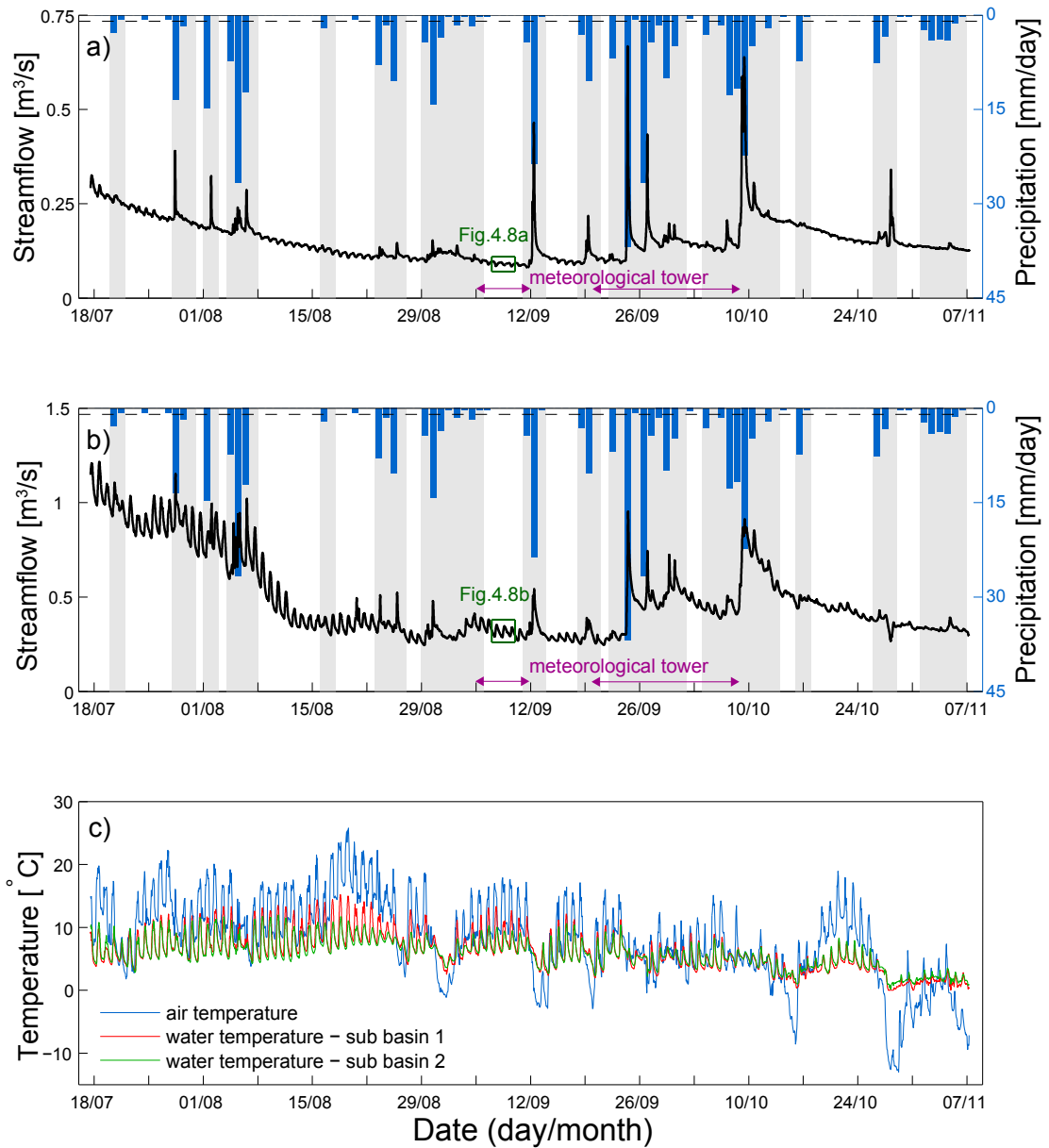
Figure 4.3: Time series of a) streamflow of sub-basin 1 and precipitation, b) streamflow of sub-basin 2 and precipitation and c) air temperature and water temperature at the outlets of sub-basin 1 and sub-basin 2. The days discarded from the analysis (days with precipitation exceeding the dashed line 1 mm threshold and subsequent days, see Methods section) are represented as grey areas. The purple arrows in a) and b) correspond to periods when the meteorological tower was operational. The small green box highlights the period used as illustration in Figure 4.8 for estimating evapotranspirated and melted volumes of water in Section 4.4. In c), the black dashed line corresponds to the zero degree line.

4.3   Methods

This study mainly focuses on the diurnal cycle signal of the streamflow. To isolate days with relatively undisturbed diurnal cycles, days with influence of precipitation on streamflow have been discarded. To that end, the precipitation collected over all stations was integrated from a resolution of one minute to daily values. Only three stations were maintained after October 23rd and station 13 was chosen for its relative central location in the watershed. Days with median precipitation above 1 mm were discarded from the analysis (see Figure 4.3). The first subsequent day was also discarded from the analysis to avoid the steep part of the recession curve. The threshold value of 1 mm and median precipitation over all stations were used to reduce sensitivity to measurement errors of the tipping bucket rain gauges.

The daily streamflow variation is obtained by subtracting a 24-hour moving average window from the measured streamflow and is referred to as detrended streamflow in the following. Several characteristics are analyzed and used to compare the two types of diurnal streamflow cycles: 1) the sign of the perturbation (increase or decrease during the day), 2) the hours of occurrence of the minimum and maximum streamflow during the day, 3) the amplitude of the diurnal streamflow cycles, defined as half the difference between maximum and minimum detrended streamflow and 4) their shape, studied through the duration of rise and decline times of the diurnal streamflow cycles, defined as the time elapsed from minimum streamflow to next maximum streamflow occurrence for the rise time and vice versa for the decline time. We also quantify the total volume of water gained or lost due to the diurnal streamflow cycles. This is done by integrating the area between the detrended streamflow and the curve connecting two subsequent maximums (if the diurnal cycle induces a streamflow decrease) or between two subsequent minimums (if the diurnal cycle induces a streamflow increase) (*Boronina et al.*, 2005; *Gribovszki et al.*, 2010).

The data from the fast-response sensors installed at the meteorological tower were processed to obtain daily evapotranspiration rates. They were first estimated over 30 minutes periods by applying the eddy covariance method. After spike removals, the classical double rotation and tilt corrections were applied to account for errors in the deployment of the sonic anemometers. Finally, density-induced fluctuations are accounted for by applying the well known WPL-correction (*Webb et al.*, 1980). Evapotranspiration rates were then integrated to daily values for the nine rainless days according to the data available at the meteorological tower (see Figure 4.3).

4.4 Results

The diurnal streamflow cycles obtained for sub-basin 1 and sub-basin 2 by subtracting the detrended streamflow and by considering rainless days are presented in Figure 4.4 and Figure 4.5, respectively. In sub-basin 1, the diurnal streamflow patterns varied seasonally as depicted in Figure 4.4. Early in the season, i.e late July, the fluctuations are characterized by an increase of streamflow during the afternoon (see red parts in Figure 4.4b) and a minimum streamflow in the morning. During this period, some snow patches were still visible in the pictures taken by the automatic cameras. This increase of streamflow during the day is therefore linked to snowmelt processes. Later in the season (mid-August) when there is no snow left in the sub-basin, we observe a streamflow decrease during the day, with a typical minimum in the middle of the afternoon and a maximum in the early morning (see blue parts on the right side of Figure 4.4b). This decrease of streamflow during the day is linked to evapotranspiration forcings. Late in the season (the 30th of October), after a small snowfall event recorded by the automatic cameras, we observed a return to a snowmelt-dominated streamflow variation cycle (see Figure 4.4b).

Figure 4.4: Observed diurnal streamflow cycles at the gauging station of sub-basin 1. The streamflow variation has been obtained by subtracting a detrended streamflow hydrograph. In a), the dates are color coded whereas the streamflow variation is color coded in b). The dashed line in b) corresponds to noontime.

The variation of the diurnal streamflow cycles observed at sub-basin 2 is depicted in Figure 4.5. In sub-basin 2, the fluctuations are characterized by an increase of streamflow during the day (see the increase color-coded in red/orange in Figure 4.5b) and a streamflow minimum in the morning. The diurnal streamflow cycle in sub-basin 2 is mainly due to snowmelt and ice melt from the small glacier (see Figure 4.1). In the following, the diurnal cycles observed in the two sub-basins are analyzed in detail.
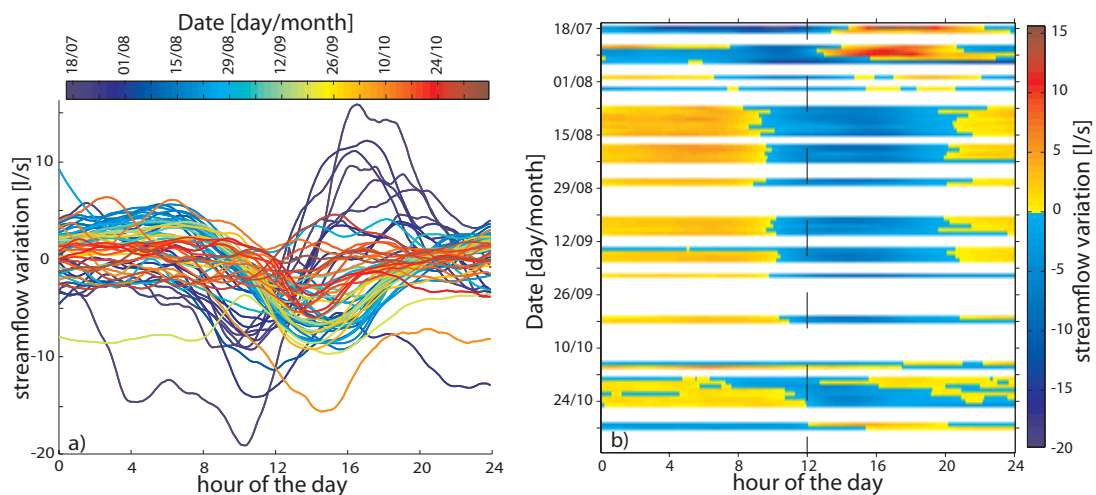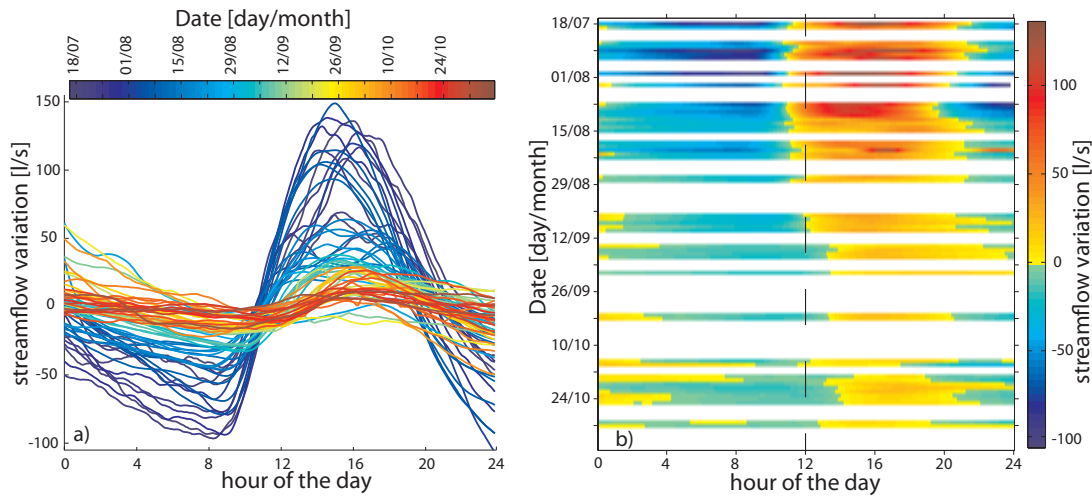
Figure 4.5: Observed diurnal streamflow cycles at the gauging station of sub-basin 2. The streamflow variation has been obtained by subtracting a detrended streamflow hydrograph. In a), the dates are color-coded whereas the streamflow variation is color-coded in b). The dashed line in b) corresponds to noontime.

The hour at which minimum and maximum detrended streamflow occurs is presented in Figure 4.6. In the case of sub-basin 1 (Figure 4.6a), at the beginning of the season, the maximum streamflow occurs in the middle of the afternoon during the snowmelt-dominated period (median at 16h25 until the 29/07) whereas the minimum streamflow is observed in the morning (median at 10h30 until the 29/07). Afterwards, three large precipitation events were observed between July 29th and August 7th (see Figure 4.3a). Two days with diurnal streamflow cycles were observed during this period. These two diurnal streamflow cycles were characterized by a minimum steamflow occurrence late in the morning, similar to the period dominated by snowmelt, but the maximum streamflow occurred in the early morning (see Figure 4.6a). After August 7th, the maximum and minimum streamflow are respectively observed in the early morning (median at 5h50) and in the afternoon (median at 14h05). During this period, the diurnal streamflow cycles are dominated by evapotranspiration processes. Therefore, the period between July 29th and August 7th is considered as a transition from the snowmelt-dominated period to the evapotranspiration-dominated period (see Figure 4.6a). During the latter period, the hour of minimum streamflow occurrence slowly shifts from the middle of the afternoon towards noon as the season progresses (-3.1 ± 1.7 min/day with uncertainty given as 95% confidence intervals here and in the following), whereas no seasonal trend was observed for the hour of maximum streamflow occurrence.

In the case of sub-basin 2 (Figure 4.6b), the maximum and minimum streamflow occurrences are always in the afternoon and morning, respectively. The time difference between the peaks is relatively constant during the season (mean difference of 6h55, standard deviation of 1h40). However, the maximum and minimum streamflows occur later as the season progresses (daily shift of $+0.91 \pm 0.67$ min/day for the maximum and $+1.04 \pm 0.60$ min/day for the minimum). It
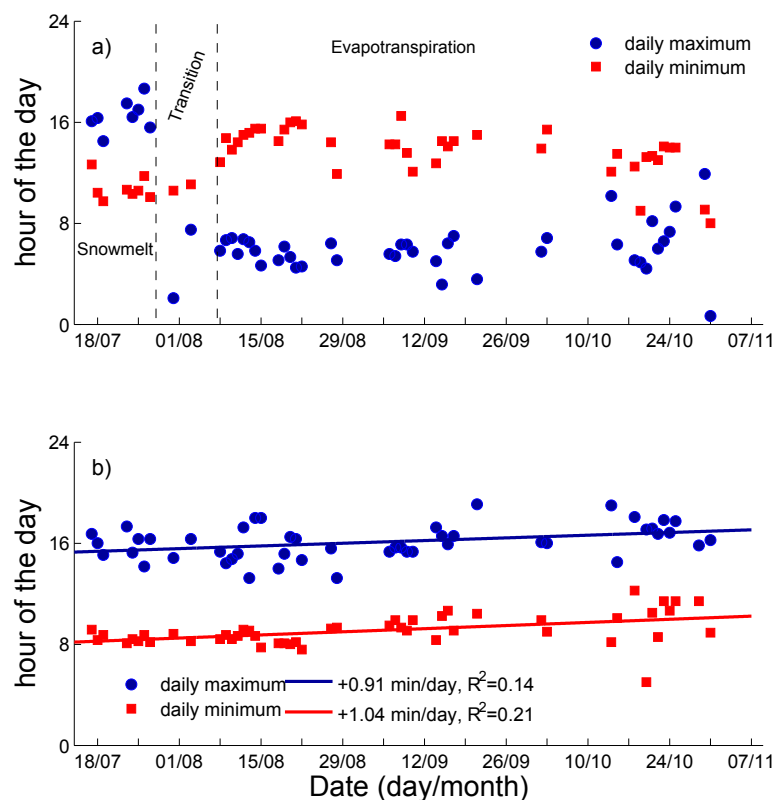
Figure 4.6: Hours of minimum and maximum streamflow occurrence during diurnal cycles in a) sub-basin 1, b) sub-basin 2 as a function of the time of year. The solid lines in b) represent a linear regression line. In a), the terms *Snowmelt, Transition* and *Evapotranspiration* refer to the main drivers of the streamflow diurnal cycles of sub-basin 1.

is also noteworthy to observe from Figure 4.6 that the minimum streamflow of sub-basin 1 tends to occur at the same time as the maximum streamflow of sub-basin 2.

The amplitude of the diurnal streamflow cycles is represented in Figure 4.7. In the case of sub-basin 1, the amplitude decreases from 16 l/s to 5 l/s in the snowmelt-dominated period from the beginning of the season until July 29th (see Figure 4.7a). After the 7th of August, during the period dominated by evapotranspiration, the amplitude decreases slowly from values around 7 l/s towards 2-3 l/s at the end of the field campaign (with a variation of -0.037±0.014 l/s/day). In the case of sub-basin 2, the amplitude decreases exponentially with a decay constant of 46±10 days (exponential fit with $R^2 = 0.72$ (see Figure 4.7b). The amplitude of the diurnal signal observed in sub-basin 2 was best predicted by the daily mean discharge ($R^2 = 0.53$) and by the daily total incoming shortwave radiation measured at the small meteorological stations ($R^2 = 0.53$) with a higher predictive power when both are combined ($R^2 = 0.79$). In contrast, the mean daily air temperature had a lower predictive power ($R^2 = 0.24$), and even weaker
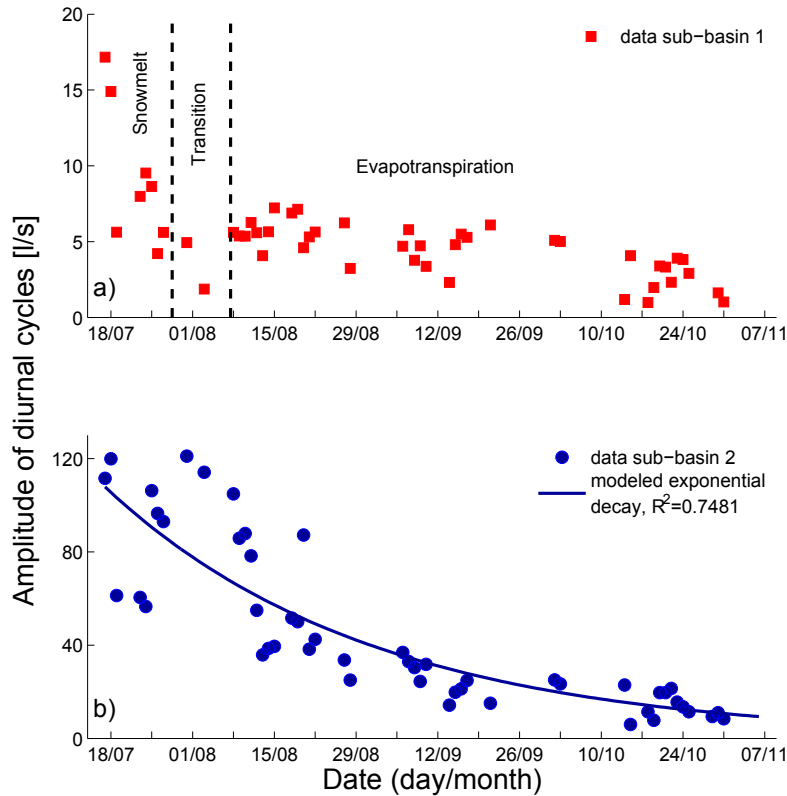
Figure 4.7: Amplitude of the diurnal cycle, defined as half the difference between daily maximum and minimum streamflow, as a function of the time of year for a) sub-basin 1 and b) sub-basin 2. The solid blue line in b) represents an exponential regression model. Note the difference in amplitude mangitude between the two sub-basins.

when raised to a power of four to approximate the long-wave radiation correlation ($R^2 = 0.09$).

The rise and decline times of the diurnal streamflow cycles are reported in Table 4.2. In the case of sub-basin 1, we observe that the mean rise and decline times of the snowmelt-dominated and evapotranspiration-dominated signals are different. This illustrates that the two different cycles have a different shape, as could be observed in Figure 4.4a. We note that for the cases of streamflow increase during the day (i.e. the snowmelt-dominated period in sub-basin 1 and the ice melt signal in sub-basin 2), the diurnal streamflow cycles are characterized by a short mean rise time and a longer mean decline time. On the contrary, when the streamflow decreases during the day (i.e. the evapotranspiration-dominated period in sub-basin 1), the diurnal streamflow cycles are characterized by a short mean decline time and a longer mean rise time. The two types of observed diurnal streamflow cycles are therefore characterized by faster changes in the direction of the perturbation.

Table 4.2: Mean rise and decline times of the diurnal streamflow cycles observed in the two sub-basins, classified by the dominant process. The uncertainty refers to the standard deviation of the rise and decline times.

	dominant process	t_{rise} [hours]	$t_{decline}$ [hours]
sub-basin 1	snowmelt	5.73 ± 1.93	17.52 ± 1.75
sub-basin 1	evapotranspiration	15.98 ± 1.84	7.70 ± 2.70
sub-basin 2	icemelt	6.99 ± 1.67	17.07 ± 1.30

In order to evaluate and decipher the origin of the evapotranspiration diurnal cycle observed in sub-basin 1, the volume of evaporated water during the rainless days was estimated as mentioned in the Methods section and illustrated in Figure 4.8a. Therein, baseflow is assumed to vary linearly between two consecutive maximums of daily streamflow. These estimated volumes of water are then linked to the evapotranspiration measured through eddy covariance at the meteorological tower installed in the watershed (see Figure 4.1) by computing an active area of evapotranspiration as mentioned in the Methods section. According to the data available from the meteorological tower, this active evapotranspiration area has been computed for nine days among which five were consecutive (see Figure 4.3a), leading to a mean and median area of respectively 23.16 ha and 17.43 ha, corresponding respectively to 4.9% and 3.7% of the total sub-basin area (minimum, maximum and standard deviation of 9.31 ha, 55.6 ha and 7.41 ha corresponding to 2.1% 12.1% and 1.6% of the total sub-basin area). Similar to *Tsang et al.* (2014), we make the hypothesis that this active evapotranspiration area corresponds to the riparian area of sub-basin 1 and comment this assumption in the Discussion section.
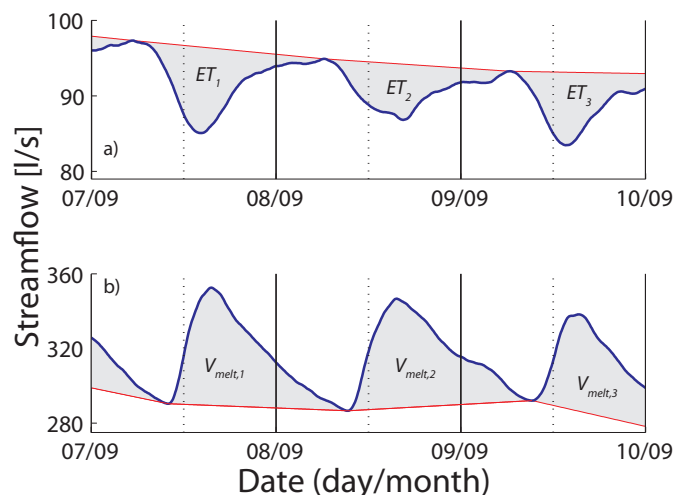
Figure 4.8: Examples of calculations for three consecutive days of a) the evaporated and b) melted volumes of water. The blue and red solid lines represent the measured streamflow and the baseflow respectively. The grey area between the two lines is the volume of evaporated (ET_j) in a) and melted water ($V_{melt,j}$) in b). Vertical solid and dotted lines represent midnight and noon respectively. Note the different axis scales between a) and b).

As mentioned in the Methods, we make use of the mapped channel network to estimate the riparian area of sub-basin 1. When considering the entire channel network length, the riverbank width should be of 5.7 meters for the riparian area to be equal to the active evapotranspiration area. However, in some parts of the catchment this is not reasonable, especially in the steep intermittent streams which do not contribute to the evapotranspiration cycle since they are dry most of the time (see Figure 4.1). Moreover, in some areas, the riverbank width is larger, especially for the low order channel heads (see Figure 4.2b for an illustration). We therefore only took into account the perennial part of the channel network which corresponds to 41% of the total network in sub-basin 1. As mentioned in the Methods, a slope threshold larger than the longitudinal mean channel slope and less than the ridge slope was set to separate the riparian and hillslope areas. By comparing results to the orthophotos and pictures taken during the field survey, we identified a slope threshold value of 25 degrees to be suitable to distinguish riparian and hillslope zones in the vicinity of the perennial channel network. With this threshold, we obtained a riparian area of 19.71 ha, corresponding to 4.2% of the sub-basin area.

A similar procedure has been applied to sub-basin 2 to study the diurnal ice melt-induced streamflow cycles. Analogous to sub-basin 1, daily volumes of ice melt water were computed as illustrated in Figure 4.8b. Therein, baseflow is assumed to vary linearly between two consecutive minimums of daily streamflow. The two sub-basins represent similar geomorphology as seen in the map of Figure 4.1, with areas covered by rocks in the southern parts of the sub-basins and grassland areas in the northern parts of the sub-basins. Interestingly, there is also an area in sub-basin 2 with a relatively large density of groundwater channel heads and low slopes. It is therefore possible that similar diurnal cycles occur in sub-basin 2 due to evapotranspiration. However, those diurnal cycles might not be detectable due to the larger amplitude of the ice melt diurnal cycle compared to the evapotranspiration signal of opposite sign (see Figure 4.7), both happening at similar times (see Figure 4.6). To quantify a possible underestimation of the total amount of ice melted in the glacier, we separated the observed ice melt-induced signal in a pure ice melt component and an evapotranspiration component. To estimate the latter one, we applied the same method for establishing the riparian area at the origin of the evapotranspiration diurnal cycle observed in sub-basin 1. In sub-basin 2, using the same slope threshold of 25 degrees as in sub-basin 1, we obtained an active evapotranspiration area of 26.9 ha, corresponding to 2.9% of the sub-basin area. For the nine rainless days of reliable evapotranspiration estimated from the meteorological tower dataset, an evaporated volume of water V_{ET} was computed as the product of the measured evapotranspiration rates times the active evapotranspiration area. Therefore, the total volume of ice melt water was computed as the sum of the volume of melted ice obtained from the streamflow measurements ($V_{melt,j}$ in Figure 4.8b) and of the evaporated volume of water V_{ET}. On average, the estimated total volume of water melted from the glacier during daytime was increased by 26 %.

4.5 Discussion

The diurnal streamflow cycle in the Val Ferret catchment was previously attributed to ice melt during the low flow season (*Simoni et al.*, 2011). However, we observed a diurnal cycle in sub-basin 1 with a decrease of streamflow during daytime mainly due to evapotranspiration. At the beginning of the season, diurnal streamflow cycles in sub-basin 1 are dominated by snowmelt (see Figure 4.4). The amplitude of this snowmelt cycle was of the same order of magnitude as the amplitude of the evapotranspiration cycle. Unfortunately, most of the snow was already melted in sub-basin 1 when the water level probes were installed so that the largest amplitudes of the snowmelt-induced diurnal cycles were not monitored. We found that the smowmelt and evapotranspiration diurnal streamflow cycles of sub-basin 1 occur at different times of the day (see Figure 4.6a). Moreover, they are characterized by different rise and decline times (see Table 4.2) illustrating a different shape, in accordance with observations in Californian watersheds (*Lundquist and Cayan*, 2002). Therefore, the evapotranspiration-dominated diurnal streamflow cycles in sub-basin 1 cannot only be due to thermal artifacts as questioned by *Cuevas et al.* (2010) and *McLaughlin and Cohen* (2011). Moreover, the transition from the snowmelt-dominated diurnal cycles to the evapotranspiration-dominated diurnal cycles happened during a short period of time characterized by similar diurnal air temperature variations. Therefore, the pressure fluctuations induced by air temperature variations resulting in erroneous waterlevel measurements should be similar for both types of diurnal cycles. A pure thermal artifact of the waterlevel decrease during the day can therefore be reasonably rejected. Furthermore, the water level probes were carefully and regularly checked to exclude seasonal drift or sediment accumulation.

Other effects such as groundwater recharge in losing reaches could also induce diurnal streamflow decrease. During the periods when streamflow decrease was observed during daytime, the measured water electrical conductivity was also decreasing in phase with the water level over a diurnal cycle. In case of groundwater recharge being the only process for streamflow decrease, the electrical conductivity should stay relatively constant during the day. Indeed, infiltration of water along all streams to the groundwater through the hyporheic zone should affect the water mass balance, but not the electrical conductivity, which reflects the water salinity. Moreover, the water temperature remained relatively cold during the campaign, fluctuating between $1.2\,°C$ and $15\,°C$ during the season with typical daily fluctuations of $7 - 8\,°C$ (see Figure 4.3c). Groundwater recharge depends on the hydraulic conductivity which is inversely proportional to the temperature-dependent water viscosity. Diurnal cycles of water temperature could therefore induce a diurnal variation of the hydraulic conductivity, resulting in diurnal patterns in groundwater recharge. However, water with low temperature has a larger water viscosity and therefore a lower hydraulic conductivity, resulting in low infiltration rates. Groundwater recharge has therefore been neglected in our study and the daily streamflow variation in sub-basin 1 has been attributed to evapotranspiration. The determination of physical mechanisms leading to such diurnal cycles are still debated and are beyond the scope of this article. The readers are referred to *Graham et al.* (2013) for a review of hypothetical

physical mechanisms leading to evapotranspiration-induced diurnal cycles.

In sub-basin 2, the diurnal streamflow cycles were mainly due to ice melt from the small glacier. During days with observed diurnal streamflow cycles, the minimum and maximum streamflow always occurred respectively during the morning and the afternoon (see Figure 4.6b), but the occurrence of minimum and maximum streamflow shifted during the season by approximately one minute per day. This shift can be attributed to smaller water velocities as shown by the decrease of the streamflow amplitude resulting in longer travel times, longer travel distances due to the seasonal glacier ablation and eventually to the shift of sunrise occurrence. The amplitude of the ice melt-induced diurnal cycle in sub-basin 2 decreased exponentially during the field campaign and was characterized by a large scatter (see Figure 4.7b). The origin of this amplitude decrease can be attributed to the seasonal glacier ablation. The seasonal decrease of the ice melt-induced diurnal cycle casts some doubts on the previous understandings of the Val Ferret catchment where the glacier contribution to total runoff was considered to be constant during the season (*Simoni et al.*, 2011). Moreover, the amplitude of the diurnal streamflow cycle was better predicted by the total incoming solar shortwave radiation than by the mean daily temperature. This supports the effort of including radiation measurements in the simple degree-day method for snowmelt or ice melt modeling.

Active areas of evapotranspiration have been computed in sub-basin 1 by dividing daily volumes of evapotranspirated water by evapotranspiration measured at the meteorological station. On average, we found that this area corresponds to 4.17% of the total area of sub-basin 1. While *Bond et al.* (2002) and *Boronina et al.* (2005) reported smaller values (0.1 to 0.7 %), our results are comparable to the values found recently by *Tsang et al.* (2014) (10% of the watershed area), but this area is very site specific, depending on the land cover and the catchment geomorphology.

Several errors can influence the estimation of the active areas of evapotranspiration. First, some errors can be introduced when computing the volumes of evapotranspirated water from the streamflow measurements. Recession flows usually exhibit an exponential streamflow decay, but the error made by discretizing the recession flow with a straight line between two subsequent days is relatively little. Moreover, this approach does not introduce any recession timescale parameter as is usually needed with the use of an exponential decay. However, this assumption results in a small overestimation of the evapotranspirated water. Finally, groundwater recharge have been ruled out as principal process for inducing the decreasing streamflow diurnal cycle, but can still contribute to streamflow losses and therefore result in a small overestimation of the evapotranspirated water. Second, some errors can be introduced by using the evapotranspiration rates measured at the meteorological station. Measurement errors of the fast-response sensors are minimized by the calibration that was done before the deployment and regular data quality checks undertaken during the deployment. The spatial variability of evapotranspiration is not considered in this study and can be of critical importance. The topographical shading and local aspect as well as land use are some factors that can vary local evapotranspiration values. However, the location of the eddy covariance tower

was relatively central in the catchment. The site was comparable to both zones of sub-basins 1 and 2 where a large amount of groundwater channel heads were mapped, characterized by relatively flat areas and very humid soils. The measured latent heat fluxes were generally in excess of sensible heat fluxes so that the vegetation was not moisture limited. For estimating evapotranspiration, direct measurements were preferred to formulations based on the energy budget like the Penman-Monteith equation, since the latter one introduces parameters such as the surface and aerodynamic resistances. Moreover, as the net radiation is only measured at the meteorological tower, the number of days with evapotranspiration estimates would be the same as when obtained with the eddy covariance method. As the soil in the vicinity of the meteorological tower was always almost saturated, it is believed that the difference between eddy covariance evapotranspiration estimates and Penman-Monteith evapotranspiration estimates would be very similar.

In our study, the evapotranspiration-induced diurnal streamflow cycles observed in sub-basin 1 has been attributed to the evapotranspiration in the riparian area. However, we note that there is no physical evidence for such assumption. During rainless periods, transpiration is high in the vegetation close to the river due to soil saturation and evaporation from streams is high in the low order streams originating from the groundwater channel heads where the flow rate is the lowest. In particular, we observed a high density of first order perennial streams in the westernmost part of the sub-basins as illustrated in Figure 4.2a. The soil around and upstream those first order channels was always saturated and hydrologically connected to the channel network, i.e. contributing to total streamflow. Moreover, the riparian vegetation observed in sub-basin 1 was characterized by relatively shallow roots (see section 4.2.1). A separation between the evaporation and transpiration is beyond the scope of this study but we acknowledge that the diurnal streamflow cycle might be dominated by direct evaporation from streams only, which needs further research.

To geographically identify the active evapotranspiration area, we make use of only the perennial part of the channel network which reduces the error on the riparian area estimation. Most studies rely on an objective, automatic extraction of the channel network based on a critical support area (i.e., *O'Callaghan and Mark*, 1984), which assumes constant drainage density. This classical method makes no distinction between intermittent and perennial streams, resulting in an overestimation of the riparian area, especially during low flow conditions when most of the intermittent streams are dry. Note that it is also of critical importance to use a high resolution DEM to better recognize the channel network (*Tarolli*, 2014) and therefore reduce the error in the riparian area estimation. Moreover, we do not account for a possible temporal evolution of the riparian zone which could be induced by a temporal evolution of the channel network, especially during longer dry periods where some parts of the streams could dry out.

The comparison of the different diurnal streamflow cycles shows that the amplitude of the evapotranspiration cycle of sub-basin 1 can be regarded as constant in contrast to the amplitude of the ice melt cycle of sub-basin 2 (see Figure 4.7). However, the two types of diurnal cycles occur at similar times of the day but with an opposite sign (see Figure 4.6). Therefore,

by visual inspection of the diurnal cycle measured at sub-basin 2 alone, it is almost impossible to detect the occurrence of a diurnal cycle of evapotranspirative nature. Even though the amplitude of the evapotranspiration cycle was much lower than the amplitude of the ice melt signal, the effect on the estimation of the daily icemelted volume of water was not negligible, with an increased volume of 26%. This was achieved by separating the observed ice melt-dominated diurnal streamflow cycle by a pure ice melt component and an evapotranspiration component. We acknowledge that this method might only be applicable in relatively small basins. In our case, the travel times are sufficiently short so that we observed occurrences of evapotranspiration and ice melt diurnal streamflow cycles at similar times of the day. In larger basins, timing and transport issues might hinder a clear separation between different types of diurnal cycles as the travel distances are longer. Indeed, for large streams and even more late in the season, snowmelt or ice melt-induced signals are subject to longer travel times and wave dispersion, resulting in a delayed appearance and perhaps less pronounced shapes of melt-water diurnal signals. In our case, the ice melt signal was induced locally by one glacier but several snowmelt or ice melt signals might be added in larger basins which could hinder the identification of diurnal streamflow cycles. Evapotranspiration signals can be induced locally, but as well by riparian areas at longer distances from the gauging station. All these factors must be considered carefully when adding and subtracting diurnal signals for establishing water mass balances, and our result suggest that evapotranspiration diurnal cycles should be included when assessing conceptual models for snowmelt or ice melt.

4.6   Conclusions

Diurnal streamflow cycles in high alpine catchments are typically dominated by snowmelt or ice melt in the presence of glaciers. We observed a transition from a snowmelt-dominated diurnal streamflow cycle to an evapotranspiration-dominated diurnal streamflow cycle in a sub-basin of a well monitored high altitude catchment in the Swiss Alps. The two processes induced diurnal streamflow cycles of opposite signs at similar times during the day. In another sub-basin of the catchment, we observed a diurnal streamflow cycle throughout the season dominated by the ice melt from a small glacier. The amplitude of the ice melt-induced diurnal streamflow cycle was larger than the amplitude of the evapotranspiration-induced cycle. Even though the impact of the evapotranspiration cycles was not visible in the observed ice melt cycles, our study suggests that damping of the ice melt cycle by the evapotranspiration cycle is not negligible. Diurnal ice melt streamflow cycles are expected to be amplified with warming climate. It is therefore of crucial importance to obtain accurate estimates of evapotranspiration in mountainous areas for future glacier mass balance estimations and for hydrological models to correctly simulate discharge at sub-daily temporal resolutions.

Bibliography

Barnard, H. R., C. B. Graham, W. J. Van Verseveld, J. R. Brooks, B. J. Bond, and J. J. McDonnell (2010), Mechanistic assessment of hillslope transpiration controls of diel subsurface flow: a steady-state irrigation approach, *Ecohydrology*, *3*(2), 133–142, doi:10.1002/eco.114.

Bond, B. J., J. A. Jones, G. Moore, N. Phillips, D. Post, and J. J. McDonnell (2002), The zone of vegetation influence on baseflow revealed by diel patterns of streamflow and vegetation water use in a headwater basin, *Hydrological Processes*, *16*(8), 1671–1677, doi:10.1002/hyp. 5022.

Boronina, A., S. Golubev, and W. Balderer (2005), Estimation of actual evapotranspiration from an alluvial aquifer of the Kouris catchment (Cyprus) using continuous streamflow records, *Hydrological Processes*, *19*(20), 4055–4068, doi:10.1002/hyp.5871.

Bren, L. J. (1997), Effects of slope vegetation removal on the diurnal variations of a small mountain stream, *Water Resources Research*, *33*(2), 321–331, doi:10.1029/96WR02648.

Brutsaert, W. (1986), Catchment-Scale Evaporation and the Atmospheric Boundary Layer, *Water Resources Research*, *22*(9S), 39S–45S, doi:10.1029/WR022i09Sp0039S.

Cadol, D., S. Kampf, and E. Wohl (2012), Effects of evapotranspiration on baseflow in a tropical headwater catchment, *Journal of Hydrology*, *462-463*(0), 4 – 14, doi:10.1016/j.jhydrol.2012. 04.060.

Caine, N. (1992), Modulation of the diurnal streamflow response by the seasonal snowcover of an alpine basin, *Journal of Hydrology*, *137*(1-4), 245 – 260, doi:10.1016/0022-1694(92) 90059-5.

Calaf, M., M. Hultmark, H. J. Oldroyd, V. Simeonov, and M. B. Parlange (2013), Coherent structures and the k^{-1} spectral behaviour, *Physics of Fluids*, *25*(12), 125107, doi:10.1063/1. 4834436.

Cazorzi, F., and G. D. Fontana (1996), Snowmelt modelling by combining air temperature and a distributed radiation index, *Journal of Hydrology*, *181*(1–4), 169 – 187, doi:10.1016/ 0022-1694(95)02913-3.

Bibliography

Collins, D. N. (1979), Quantitative determination of the subglacial hydrology of two alpine glaciers, *Journal of Glaciology*, *23*, 347–361.

Collins, D. N. (1995), Daily patterns of discharge, solute content and solute flux in meltwaters draining from two alpine glaciers, *Biogeochemistry of Seasonally Snow-Covered Catchments (Proceedings of a Boulder Symposium)*, *228*, 371–378.

Constantz, J. (1998), Interaction between stream temperature, streamflow, and groundwater exchanges in alpine streams, *Water Resources Research*, *34*(7), 1609–1615, doi:10.1029/98WR00998.

Constantz, J., C. L. Thomas, and G. Zellweger (1994), Influence of diurnal variations in stream temperature on streamflow loss and groundwater recharge, *Water Resources Research*, *30*(12), 3253–3264, doi:10.1029/94WR01968.

Cuevas, J., M. Calvo, C. Little, M. Pino, and P. Dassori (2010), Are diurnal fluctuations in streamflow real?, *Journal of Hydrology and Hydromechanics*, *58*(3), 149–162, doi:10.2478/v10098-010-0014-0.

Dolan, T. J., A. J. Hermann, S. E. Bayley, and J. Z. Jr. (1984), Evapotranspiration of a Florida, U.S.A., freshwater wetland, *Journal of Hydrology*, *74*(3-4), 355 – 371, doi:10.1016/0022-1694(84)90024-6.

Godsey, S. E., and J. Kirchner (2014), Dynamic, discontinuous stream networks: hydrologically driven variations in active drainage density, flowing channels, and stream order, *Hydrological Processes*, *28*(23), 5791–5803, doi:10.1002/hyp.10310.

Graham, C. B., H. R. Barnard, K. L. Kavanagh, and J. P. McNamara (2013), Catchment scale controls the temporal connection of transpiration and diel fluctuations in streamflow, *Hydrological Processes*, *27*(18), 2541–2556, doi:10.1002/hyp.9334.

Gribovszki, Z., P. Kalicz, J. Szilágyi, and M. Kucsara (2008), Riparian zone evapotranspiration estimation from diurnal groundwater level fluctuations, *Journal of Hydrology*, *349*(1–2), 6 – 17, doi:10.1016/j.jhydrol.2007.10.049.

Gribovszki, Z., J. Szilágyi, and P. Kalicz (2010), Diurnal fluctuations in shallow groundwater levels and streamflow rates and their interpretation - A review, *Journal of Hydrology*, *385*(1–4), 371 – 383, doi:10.1016/j.jhydrol.2010.02.001.

Hays, K. B. (2003), Water use by saltcedar (Tamarix sp.) and associated vegetation on the Canadian, Colorado and Pecos rivers in Texas, Ph.D. thesis, Texas A & M University.

Hock, R. (2005), Glacier melt: a review of processes and their modelling, *Progress in Physical Geography*, *29*(3), 362–391, doi:10.1191/0309133305pp453ra.

Ingelrest, F., G. Barrenetxea, G. Schaefer, M. Vetterli, O. Couach, and M. B. Parlange (2010), SensorScope: Application-Specific Sensor Network for Environmental Monitoring, *ACM Trans. Sen. Netw.*, *6*(2), 1–32, doi:10.1145/1689239.1689247.

Jost, G., R. D. Moore, R. Smith, and D. R. Gluns (2012), Distributed temperature-index snowmelt modelling for forested catchments, *Journal of Hydrology*, *420–421*(0), 87 – 101, doi:10.1016/j.jhydrol.2011.11.045.

Kane, D., R. Gieck, and L. Hinzman (1997), Snowmelt Modeling at Small Alaskan Arctic Watershed, *Journal of Hydrologic Engineering*, *2*(4), 204–210, doi:10.1061/(ASCE)1084-0699(1997)2:4(204).

Katul, G. G., and M. B. Parlange (1992), Estimation of bare soil evaporation using skin temperature measurements, *Journal of hydrology*, *132*(1), 91–106, doi:10.1016/0022-1694(92)90174-T.

Kirchner, J. W. (2009), Catchments as simple dynamical systems: Catchment characterization, rainfall-runoff modeling, and doing hydrology backward, *Water Resources Research*, *45*(2), doi:10.1029/2008wr006912.

Kobayashi, D., and H. Motoyama (1984), Effect of snow cover on time lag of runoff from a watershed, *Annals of Glaciology*, *6*, 123–125.

Kustas, W. P., A. Rango, and R. Uijlenhoet (1994), A simple energy budget algorithm for the snowmelt runoff model, *Water Resources Research*, *30*(5), 1515–1527, doi:10.1029/94WR00152.

Lehning, M., I. Völksch, D. Gustafsson, T. A. Nguyen, M. Stähli, and M. Zappa (2006), ALPINE3D: a detailed model of mountain surface processes and its application to snow hydrology, *Hydrological Processes*, *20*(10), 2111–2128, doi:10.1002/hyp.6204.

Loheide II, S. P. (2008), A method for estimating subdaily evapotranspiration of shallow groundwater using diurnal water table fluctuations, *Ecohydrology*, *1*(1), 59–66, doi:10.1002/eco.7.

Loheide II, S. P., and S. M. Gorelick (2006), Quantifying Stream–Aquifer Interactions through the Analysis of Remotely Sensed Thermographic Profiles and In Situ Temperature Histories, *Environmental Science & Technology*, *40*(10), 3336–3341, doi:10.1021/es0522074.

Loheide II, S. P., and J. D. Lundquist (2009), Snowmelt-induced diel fluxes through the hyporheic zone, *Water Resources Research*, *45*(7), doi:10.1029/2008WR007329.

Lundquist, J. D., and D. R. Cayan (2002), Seasonal and Spatial Patterns in Diurnal Cycles in Streamflow in the Western United States, *Journal of Hydrometeorology*, *3*(5), 591–603, doi:10.1175/1525-7541(2002)003<0591:SASPID>2.0.CO;2.

Lundquist, J. D., and M. D. Dettinger (2005), How snowpack heterogeneity affects diurnal streamflow timing, *Water Resources Research*, *41*(5), doi:10.1029/2004WR003649.

Lundquist, J. D., M. D. Dettinger, and D. R. Cayan (2005), Snow-fed streamflow timing at different basin scales: Case study of the Tuolumne River above Hetch Hetchy, Yosemite, California, *Water Resources Research*, *41*(7), doi:10.1029/2004WR003933.

Bibliography

Martinec, J. (1989), Hour-to-hour snowmelt rates and lysimeter outflow during an entire ablation period, *Snow Cover and Glacier Variations (Proceedings of the Baltimore Symposium)*, *183*, 19–28.

McLaughlin, D. L., and M. J. Cohen (2011), Thermal artifacts in measurements of fine-scale water level variation, *Water Resources Research*, *47*(9), doi:10.1029/2010WR010288.

Meyboom, P. (1965), Three observations on streamflow depletion by phreatophytes, *Journal of Hydrology*, *2*(3), 248 – 261, doi:10.1016/0022-1694(65)90040-5.

Mutzner, R., et al. (2013), Geomorphic signatures on Brutsaert base flow recession analysis, *Water Resources Research*, *49*, 5462–5472, doi:10.1002/wrcr.20417.

Nadeau, D., W. Brutsaert, M. Parlange, E. Bou-Zeid, G. Barrenetxea, O. Couach, M. O. Boldi, J. Selker, and M. Vetterli (2009), Estimation of urban sensible heat flux using a dense wireless network of observations, *Environmental Fluid Mechanics*, *9*(6), 635–653, doi:10.1007/s10652-009-9150-7.

O'Callaghan, J. F., and D. M. Mark (1984), The extraction of drainage networks from digital elevation data, *Computer Vision, Graphics, and Image Processing*, *28*(3), 323–344, doi:10.1016/s0734-189x(84)80011-0.

Orellana, F., P. Verma, S. P. Loheide, and E. Daly (2012), Monitoring and modeling water-vegetation interactions in groundwater-dependent ecosystems, *Reviews of Geophysics*, *50*(3), doi:10.1029/2011RG000383.

Parlange, M. B., and G. G. Katul (1992), Estimation of the diurnal variation of potential evaporation from a wet bare soil surface, *Journal of Hydrology*, *132*(1–4), 71 – 89, doi:10.1016/0022-1694(92)90173-S.

Parlange, M. B., W. E. Eichinger, and J. D. Albertson (1995), Regional scale evaporation and the atmospheric boundary layer, *Reviews of Geophysics*, *33*(1), 99–124, doi:10.1029/94RG03112.

Penna, D., H. J. Tromp-van Meerveld, A. Gobbi, M. Borga, and G. Dalla Fontana (2011), The influence of soil moisture on threshold runoff generation processes in an alpine headwater catchment, *Hydrology and Earth System Sciences*, *15*(3), 689–702, doi:10.5194/hess-15-689-2011.

Pfister, L., J. J. McDonnell, C. Hissler, and L. Hoffmann (2010), Ground-based thermal imagery as a simple, practical tool for mapping saturated area connectivity and dynamics, *Hydrological Processes*, *24*(21), 3123–3132, doi:10.1002/hyp.7840.

Reusser, D. E., T. Blume, B. Schaefli, and E. Zehe (2009), Analysing the temporal dynamics of model performance for hydrological models, *Hydrology and Earth System Sciences*, *13*(7), 999–1018, doi:10.5194/hess-13-999-2009.

Rigon, R., G. Bertoldi, and T. M. Over (2006), GEOtop: A Distributed Hydrological Model with Coupled Water and Energy Budgets., *Journal of Hydrometeorology*, *7*(3).

Ronan, A. D., D. E. Prudic, C. E. Thodal, and J. Constantz (1998), Field study and simulation of diurnal temperature effects on infiltration and variably saturated flow beneath an ephemeral stream, *Water Resources Research*, *34*(9), 2137–2153, doi:10.1029/98WR01572.

Simoni, S., S. Padoan, D. F. Nadeau, M. Diebold, A. Porporato, G. Barrenetxea, F. Ingelrest, M. Vetterli, and M. B. Parlange (2011), Hydrologic response of an alpine watershed: Application of a meteorological wireless sensor network to understand streamflow generation, *Water Resources Research*, *47*(10), doi:10.1029/2011wr010730.

Singh, P., U. K. Haritashya, K. S. Ramasastri, and N. Kumar (2005), Diurnal variations in discharge and suspended sediment concentration, including runoff-delaying characteristics, of the Gangotri Glacier in the Garhwal Himalayas, *Hydrological Processes*, *19*(7), 1445–1457, doi:10.1002/hyp.5583.

Soylu, M. E., J. D. Lenters, E. Istanbulluoglu, and S. P. Loheide (2012), On evapotranspiration and shallow groundwater fluctuations: A Fourier-based improvement to the White method, *Water Resources Research*, *48*(6), doi:10.1029/2011WR010964.

Stagnitti, F., J.-Y. Parlange, and C. W. Rose (1989), Hydrology of a small wet catchment, *Hydrological Processes*, *3*(2), 137–150, doi:10.1002/hyp.3360030204.

Szilágyi, J., Z. Gribovszki, P. Kalicz, and M. Kucsara (2008), On diurnal riparian zone groundwater-level and streamflow fluctuations, *Journal of Hydrology*, *349*(1–2), 1 – 5, doi:10.1016/j.jhydrol.2007.09.014.

Tarolli, P. (2014), High-resolution topography for understanding Earth surface processes: Opportunities and challenges, *Geomorphology*, *216*(0), 295 – 312, doi:10.1016/j.geomorph.2014.03.008.

Thibaud, E., R. Mutzner, and A. C. Davison (2013), Threshold modeling of extreme spatial rainfall, *Water Resources Research*, *49*(8), 4633–4644, doi:10.1002/wrcr.20329.

Tobin, C., B. Schaefli, L. Nicotina, S. Simoni, G. Barrenetxea, R. Smith, M. Parlange, and A. Rinaldo (2013), Improving the degree-day method for sub-daily melt simulations with physically-based diurnal variations, *Advances in Water Resources*, *55*(0), 149 – 164, doi:10.1016/j.advwatres.2012.08.008.

Tsang, Y.-P., G. Hornberger, L. A. Kaplan, J. D. Newbold, and A. K. Aufdenkampe (2014), A variable source area for groundwater evapotranspiration: impacts on modeling stream flow, *Hydrological Processes*, *28*(4), 2439–2450, doi:10.1002/hyp.9811.

Tschinkel, H. M. (1963), Short-termFfluctuation in Streamflow As Related to Evaporation and Transpiration, *Journal of Geophysical Research*, *68*(24), 6459–6469, doi:10.1029/JZ068i024p06459.

Webb, E. K., G. I. Pearman, and R. Leuning (1980), Correction of flux measurements for density effects due to heat and water vapour transfer, *Quarterly Journal of the Royal Meteorological Society*, *106*(447), 85–100, doi:10.1002/qj.49710644707.

Bibliography

Weijs, S. V., R. Mutzner, and M. B. Parlange (2013), Could electrical conductivity replace water level in rating curves for alpine streams?, *Water Resources Research*, *49*(1), 343–351, doi:10.1029/2012WR012181.

Weisman, R. N. (1977), The effect on evapotranspiration on streamflow recession, *Hydrological Sciences Bulletin*, *22*(3), 371–377, doi:10.1080/02626667709491731.

White, W. N. (1932), Method of estimating ground-water supplies based on discharge by plants and evaporation from soil - Results of investigation in Escalante Valley, Utah, *Water Supply paper, 659-A*.

Wondzell, S. M., M. N. Gooseff, and B. L. McGlynn (2007), Flow velocity and the hydrologic behavior of streams during baseflow, *Geophysical Research Letters*, *34*(24), doi:10.1029/2007GL031256.

5 Application of a meteorological wireless sensor network to understand the influence of soil water status on streamflow generation

This chapter presents preliminary results and analysis of data collected by the wireless network of meteorological stations deployed in the Val Ferret catchment during summers 2011 to 2013. The results are aimed to be submitted for publication with the following citation:

Mutzner, R., Weijs S.V. and Parlange M.B. (2015): Influence of soil water potential and moisture on streamflow generation in an alpine catchment. *in progress.*

Summary

A field observation campaign was conducted during three consecutive summers from 2011 to 2013 in a 20.4 km^2 alpine catchment in the Swiss Alps. A wireless network of 20 meteorological stations was deployed, along with river streamflow monitoring. The objective of the study was to understand dominant mechanisms of streamflow generation during precipitation events by analyzing antecedent soil water content and antecedent soil water potential monitored at the weather stations. Our result show a relatively sharp threshold in the relation between antecedent soil water potential and runoff coefficients yet unreported in previous studies. On the other hand, threshold relationship between antecedent soil water content and runoff coefficients were less evident. Our study suggests that hysteresis effect in the water-retention curve at the hillslope scale could largely affect streamflow generation at the catchment scale.

5.1   Introduction

Hydrologic systems are complex *per se* due to the heterogeneous nature of the geological, pedological and morphological structure of the watershed. In hydrologic systems, non-linear and threshold behaviors are the rule rather than the exception and manifest at different temporal and spatial scales (*Zehe and Sivapalan*, 2009). Recently, hydrologists have devoted a lot of attention to study threshold-based processes leading to a paradigm shift in the field of streamflow generation and storage-discharge relationship (*Ali et al.*, 2013; *McDonnell*, 2003; *Spence*, 2010). Understanding the processes leading to threshold behavior of hydrological systems is of fundamental importance for modeling and conceptualization purposes (*Tetzlaff et al.*, 2008).

In particular, streamflow generation is not completely understood yet at the hillslope and headwater catchment scale. For steep and humid catchments, chemical and isotopic tracers have identified subsurface flow as being an important component of stormflow generation beside overland flow (*Brutsaert*, 2005, Chap. 11). A lot of effort is currently spent by the hydrological community to understand the origin of threshold behaviors in stormflow generation but few mechanisms have been proposed to explain such threshold behaviors. The proposed mechanisms, namely connectivity of lateral preferential flowpaths (*Lin*, 2010; *Sidle et al.*, 2001) and the fill and spill hypothesis (*Spence and Woo*, 2003; *Tromp-van Meerveld and McDonnell*, 2006a), all underline the importance of the soil-bedrock interface in the generation of stormflow. Ongoing research is trying to reproduce such threshold behaviors in hydrological models at hillslope or small catchment scales (*Fu et al.*, 2013a; *Graham and McDonnell*, 2010; *Hopp and McDonnell*, 2009; *Lehmann et al.*, 2007)

Many studies reported the existence of stormflow generation threshold behaviors that are analyzed and described by linking stormflow characteristics to a combination of soil water content at the hillslope scale and total precipitation amount. Most of the time, stormflow is characterized by runoff coefficients, defined as the ratio between stormflow (obtained by subtracting baseflow from total flow) and total precipitation amount (see *Blume et al.* (2007) for a review). Some studies analyzed the relation between runoff coefficients and Antecedent Soil Moisture (ASM), defined as the soil moisture before the onset of precipitation. For instance, *Western and Grayson* (1998) reported a marked increase of surface runoff above an ASM threshold of 41-46% in the Tarrawarra catchment, South-eastern Australia. The data collected in this very intensively monitored 10.5 ha catchment lead to some pioneer study on the spatial organization, variation and connectivity of soil moisture (*Western et al.*, 1998, 1999, 2001). Similarly, *James and Roulet* (2007, 2009) observed a very clear threshold at approximately 23% ASM above which runoff ratios passed from low values (less than 0.05) to values ranging between 0.1 and 0.6. In a small alpine watershed in Northern Italy, *Penna et al.* (2009) found that the runoff coefficients were significantly increasing above ASM of 45% (averaged over the 0-30 cm depth). Below this threshold, runoff coefficients were lower (<0.1) and were attributed to the direct precipitation interception by the streams and saturation excess overland flow in the riparian area.

On the contrary, *Zhang et al.* (2011) reported an absence of threshold relationship between ASM and runoff coefficients in small semiarid watersheds in Arizona which was explained by low temporal variability of soil moisture in these environments. Recently, *von Freyberg et al.* (2014) reported the absence of a threshold behavior between runoff coefficients and antecedent conditions in a small prealpine headwater watershed in Switzerland. However, antecedent conditions were defined as initial discharge and total precipitation amount seven days prior to the event instead of ASM to characterize the wetness state of the catchment before the event.

Some studies analyzed threshold behaviors at the hillslope or catchment scale by inspecting the relation between runoff coefficients and total precipitation amount (*Buttle et al.*, 2004; *Fu et al.*, 2013b; *Graham et al.*, 2010; *Guebert and Gardner*, 2001; *Noguchi et al.*, 2001; *Tromp-van Meerveld and McDonnell*, 2006b). *Tani* (1997) reported the precipitation threshold to be depending on ASM. Alternatively, the streamflow response above the precipitation threshold is shown to be different before dry or wet ASM conditions in terms of response timings (*Tromp-van Meerveld and McDonnell*, 2006b). Additional studies reported clear thresholds between runoff coefficients and the sum of total precipitation and stored water, referred to as ASM index (*Detty and McGuire*, 2010a,b; *Fu et al.*, 2013b; *Haga et al.*, 2005; *Penna et al.*, 2014). ASM index is obtained by integrating the different soil moisture values over the soil thickness to obtain a depth of stored water. The main advantage of using a threshold based on ASM index and total precipitation is that it allows for better representation of mass balance at the hillslope or catchment scale. However, the computation of the ASM index needs a precise knowledge of the soil depth to correctly estimate the total amount of water available in the soil. Moreover, the estimation of total volume of water available in the soil relies on a discrete number of soil moisture content measurements which can lead to non negligible systematic errors (*Lunati et al.*, 2012).

In most of the aforementioned studies, the hillslopes or catchments have been instrumented with soil moisture sensors, piezometers, rain and stream gauges. However, among them, very few have instrumented their study sites with tensiometers even though their use has proven to be fundamental in experimental hydrology (*McDonnell*, 1990). *Fu et al.* (2013b) used soil suction in a very seminal way to analyze the effect of bedrock depressions on the threshold behavior on the catchment scale. *Latron and Gallart* (2008) reported a clear threshold on the seasonal scale between soil water potential and daily runoff or groundwater level in a small Mediterranean catchment. In a sprinkler-irrigation experiment in a steep unchanneled hillslope, *Torres et al.* (1998) recognized the influence of the soil water retention curve on the hydrologic response and observed a propagation of a pressure head wave advancing much faster than the wetting front. In other fields, monitoring soil water suction have helped to understand threshold on occurrence of landslides (*Berti and Simoni*, 2010; *Matsushi and Matsukura*, 2007) and is actively used for irrigation management (*McCutchan and Shackel*, 1992).

However, soil moisture and soil water potential are intrinsically related by the Soil Water

Retention Curve (SRWC), different for every type of soil (*Brutsaert*, 2005, Chap. 11). The SWRC is usually obtained by fitting soil moisture and soil water potential to a widely used parametric model (*Van Genuchten*, 1980) from which the unsaturated hydraulic conductivity can also be obtained (*Mualem*, 1976). Yet hysteresis effects are not negligible and different wetting or drying SWRC are used (*Parlange*, 1976). Perhaps hysteresis effects have hampered hydrologists to present results showing threshold behavior between soil water potential and runoff coefficient or maybe the cost, maintenance effort and skills required to operate tensiometers have hindered their use in experimental watersheds. On the other hand, if hysteresis effects are negligible on a seasonal scale, the threshold value of antecedent soil water potential could be easily obtained from the antecedent soil moisture threshold through the SWRC.

In the present study, we use the dataset collected in the Val Ferret experimental catchment during a field campaign that was undertaken during three consecutive summers. Both soil moisture and soil water potential are measured at two depths and several locations of this high altitude, steep catchment, along with semi distributed streamflow measurements. The main objective is to study the relation between streamflow response to precipitation events and soil antecedent conditions in terms of soil moisture and soil water potential. The main questions raised are the followings: (i) Do we observe threshold behaviors in the Val Ferret catchment? (ii) Is there a threshold relationship between stormflow and antecedent soil water potential? (iii) Are local hysteresis effects in the SWRC important for the streamflow generation at the catchment scale? The Chapter is organized as follows: after a short description of the available dataset for the analysis, we present the methods and results of the study, followed by a discussion where we comment the assumptions and weak points of the study before concluding and give recommendations for future deployments.

5.2   The Field Campaigns in the upper Val Ferret Watershed

For a general description of the watershed, the reader is referred to the Study Area description in the Introduction of the thesis.

Wireless network of weather stations

During the summers 2011 to 2013, a wireless network of small meteorological stations was deployed, among others, to measure the spatial variability of main hydrological variables. The stations are relying on Sensorscope technology (*Ingelrest et al.*, 2010) and were deployed in representative locations of the watershed in terms of morphological features such as slope, aspect and elevation (see Figure 5.1 and Figure 5.2). Due to their high exposure to avalanche activity and snow accumulation, most of the stations were not operated during the winter except for stations 1033 and 1238. The stations 1232 was operated during the winter from 2012 to 2013. The other stations have been deployed in late Spring until Fall (see Table 5.1 for a summary of the deployments). A high precision GPS and pictures taken in the field were used to deploy the stations at consistent locations. All the stations were equipped to measure wind

speed and direction, precipitation, near surface and skin temperature, incoming shortwave radiation and air humidity. An additional meteorological station connected to the network was also deployed at the outlet of the catchment to measure the water level of the stream with an ultrasound sensor (MB7060 XL-MaxSonar-WR1, MaxBotix Inc.).
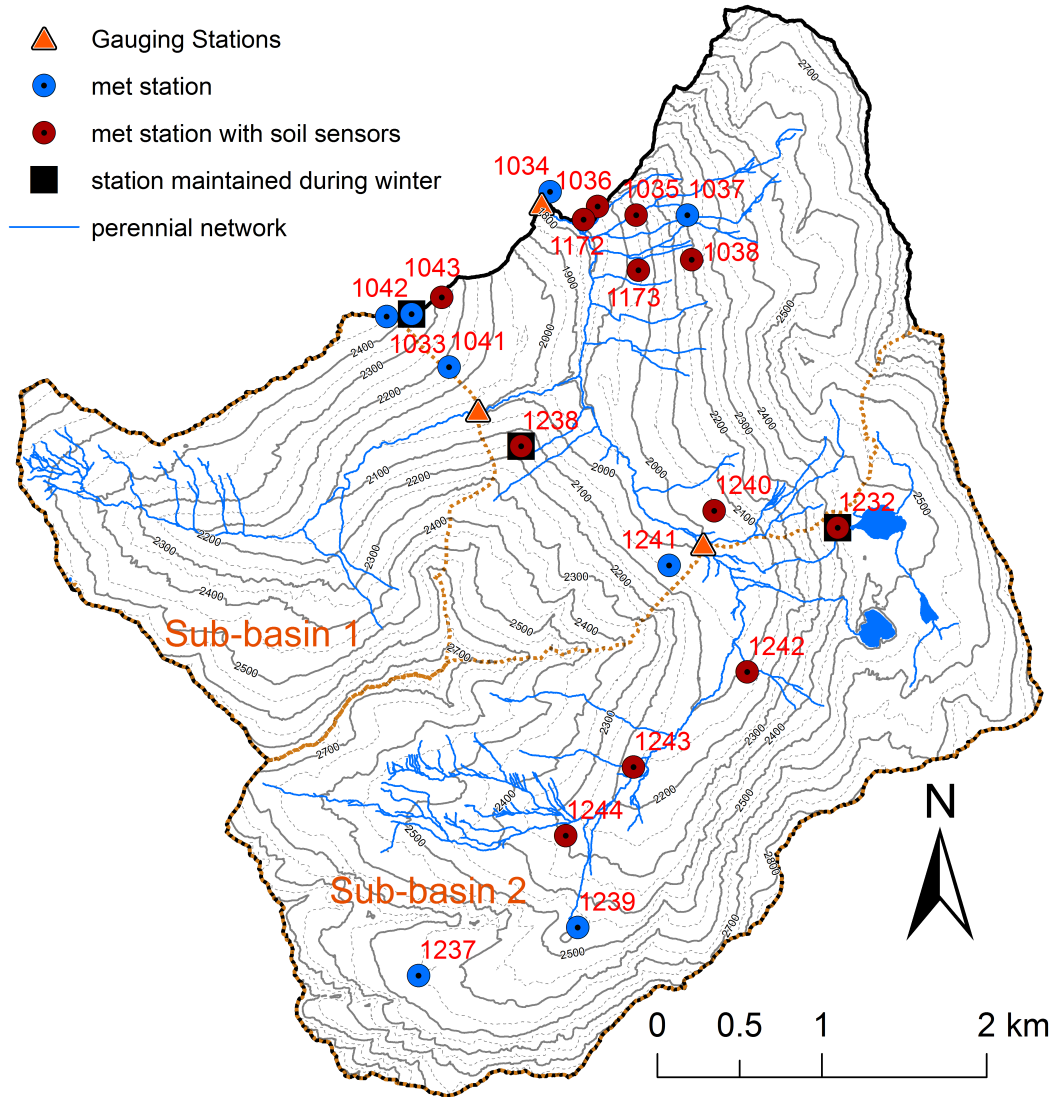

Figure 5.1: Map of the experimental watershed. Filled and dashed contour line show 100 meters, respectively 50 meters contourlines. Red and blue points represent meteorological stations with and without soil sensors.

Among the 20 meteorological stations, 12 were also equipped to measure soil temperature and soil Volumetric Water Content (*VWC* [%], measured with 5-TM sensors from Decagon Devices Inc.) and Soil Water Potential (*SWP* [kPa], measured with MPS-1 sensors from Decagon Devices Inc.), see red stations in Figure 5.1. All the parameters were recorded at a time resolution of one minute. The soil sensors were systematically installed at depth of 20 cm and 40 cm below surface, see Figure 5.3 for an illustration of sensor installation. As suggested by the
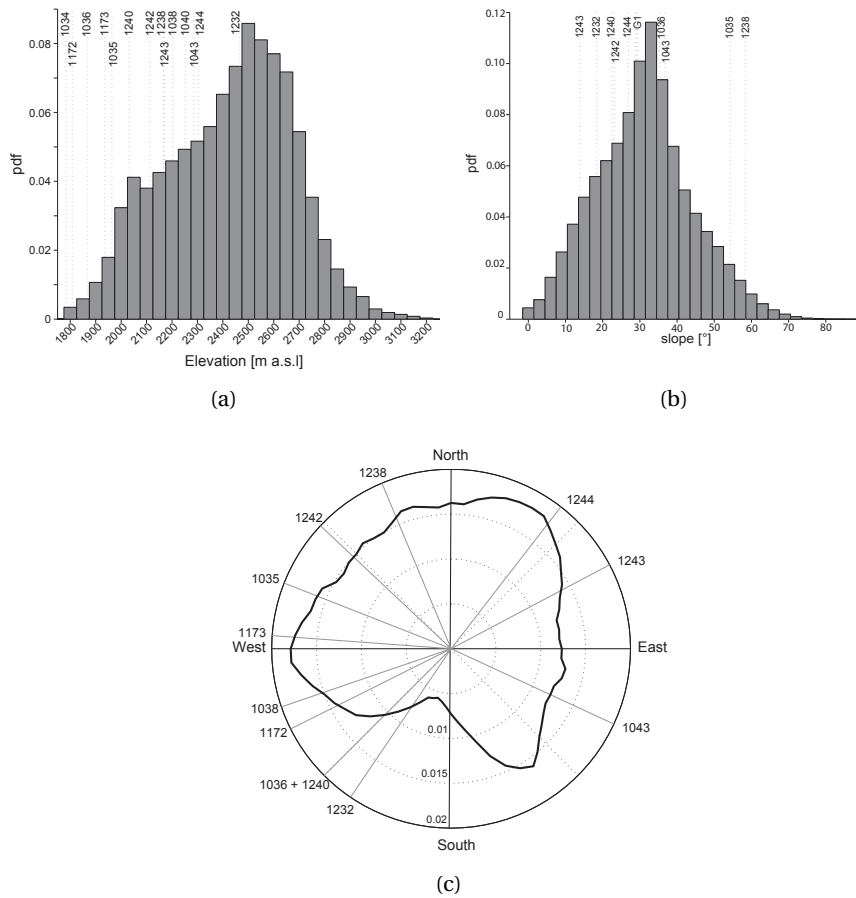
(a)

(b)

(c)

Figure 5.2: (a) Normalized histogram of elevations in the watershed with station elevations. (b) Normalized histogram of slopes in the watershed along with station slopes. G1 stands for stations 1173, 1038 and 1172. (c) Normalized radial histogram of aspects in the watershed. Note that pdf stands for probability density function.

manufacturer, the sensors were installed very carefully in the soil. The hole that was excavated to install the sensors was back-filled and repacked to obtain native bulk-density. However, the data corresponding to the five first days of measurements were systematically discarded from the analysis to let the sensors equilibrate with the surrounding. The soil sensors were always deployed far enough from the tipping bucket rain gauge to avoid interference with the measurements in the soil. Even though the stations were installed at similar locations from year to year, the soil sensors were not exactly deployed at the same locations but within a radius of 2 meters from the station. It was not possible to collect large undisturbed soil samples at all the locations and at the two different depths to calibrate the soil sensors so that the standard calibration equation provided by the manufacturer was used. Some small soil samples were collected in previous studies for soil water retention analysis in laboratory and are presented in Appendix 5.C of this chapter. The MPS-1 sensor can measure SWP between -9 kPa to -500 kPa with a resolution of 1 kPa from -9 kPa to -100 kPa and of 4 kPa from

(a) location 1
          (b) location 2

Figure 5.3: Installation of soil sensors at 20 cm and 40 cm at two different locations with different type of soil

-100 to -500 kPa with an accuracy of ±40%. The lower range and accuracy of the MPS-1 is a limiting monitoring factor in our analysis (see Figure 5.21) and will be discussed thoroughly in the Discussion section. The 5-TM sensors can measure VWC between 0 and 100% with a resolution of 0.08% and an accuracy of ±3%. Precipitation, soil moisture and soil water potential were aggregated to 15 minutes intervals for the analysis.

Table 5.1: Summary of the field campaigns undertaken from 2011 to 2013 in the Val Ferret Catchment.

	2011			2012			2013		
	start	end	# stations	start	end	# stations	start	end	# stations
Q outlet	15.04	17.11	2	10.03	22.10	1	19.04	09.10	2
Q sub-basin 1	*NO DATA*		0	17.07	07.11	1	*NO DATA*		0
Q sub-basin 2	08.07	07.11	2	05.06	31.12	1	11.07	31.12	1
meteo. stations	12.05	15.10	26	06.06	22.10	24	02.07	07.10	20

Streamflow data

For this study, we make use of the streamflow data collected during the three field campaigns. During the year 2012, the pressure sensor located at the outlet suffered from continuous deposition of fine sediment during the entire deployment. The pressure probe was therefore buried most of the time even though a lot of maintenance efforts were undertaken to clean the gauging site during the campaign. For the 2012 campaign, we therefore used the water level measured with the ultrasound sensor installed on the meteorological station at the outlet. As mentioned in the Introduction and Chapter 4 of this dissertation, it was not possible to install a weir in the stream and rating curves had to be established for each location for each field campaign. Table 5.2 summarizes the coefficients of the rating curves obtained during the different campaigns. The streamflow data was also aggregated to 15 minutes intervals for the analysis.

Table 5.2: Rating curves for the different years

		α [-]	h_0 [cm]	β [-]	R^2	# of gaugings
2011	outlet	3.648×10^{-1}	12.799	2.4066	0.962	37
	sub-basin 2	1.0792	0.543	1.708	0.52	10
2012	outlet	4.285×10^{-5}	1.094	4.0377	0.934	14
	sub-basin 2	1.78×10^{-5}	-0.587	4.576	0.984	12
	sub-basin 1	2.93×10^{-5}	3.565	4.349	0.996	7
2013	outlet	7.85×10^{-5}	9.091	2.822	0.938	14
	sub-basin 2	2.46×10^{-4}	0.821	3.8663	0.982	9

5.3 Methods

5.3.1 Rainfall-runoff event selection and runoff coefficients

We adopted a similar approach as proposed by *Penna et al.* (2011). Rainfall-runoff events were selected automatically when the precipitation was exceeding a total amount of 6 mm and were considered as distinct when at least 6 hours without precipitation were observed. Runoff coefficients were computed to link rainfall-runoff response of the catchment to antecedent soil state conditions. To that end, the total streamflow has to be separated in eventflow and baseflow components. Several methods have been proposed in the past for hydrograph separation: graphical methods (*Hewlett and Hibbert*, 1967; *McNamara et al.*, 1997; *Sujono et al.*, 2004; *Szilagyi*, 1999), digital filtering methods (*Arnold and Allen*, 1999; *Blume et al.*, 2007; *Chapman*, 1999; *Wittenberg*, 1999) and analytical solutions of the Boussinesq equation (*Szilagyi and Parlange*, 1998). However, for all those methods, identifying the end of the event (i.e. return to baseflow) and interpolating the baseflow variation during the event remains challenging. In our case, the end of the storm was identified graphically as done in *Penna et al.* (2011) and baseflow was assumed to vary with constant slope between onset and end of the event. The baseflow component was then subtracted from the total streamflow and the event runoff coefficients were computed as the ratio between event stormflow and the total precipitation. Table 5.4 summarizes the main characteristics of the precipitation events observed in the Val Ferret catchment.

When computing the runoff coefficient of an event for an entire basin, one intrinsically assumes a uniform precipitation over the watershed which might not be realistic for large scales and especially in mountainous areas where spatial variations of precipitation are the rule rather than the exception. To get a representative catchment-wide precipitation, we selected for each year five meteorological stations with the lowest percentage of missing precipitation data and manually checked that those stations were not neighboring stations. For each 15-min timestamp, we took the median amount of precipitation measured at those five stations to create a dataset which is used for the runoff coefficient calculations. We also computed the runoff coefficients of the two monitored sub-watersheds. For the sub-basin 1,

we used the median precipitation of the stations 1033, 1043 and 1238; the median of the stations 1240, 1232, 1242, 1243 and 1244 for the sub-basin 2.

5.3.2 Volumetric water content corrections based on soil water retention curves

We observed a large year to year variation of the mean VWC at most of the locations and at the different depths whereas the SWP was more consistent from year to year, see Figure 5.9 to Figure 5.20 in the Appendix of the Chapter. As mentioned earlier, the soil sensors had to be reinstalled every year due to logistical and safety reasons. To compare the VWC values between the different years, we corrected the measured VWC from year to year based on the assumption that the Soil Water Retention Curve (SWRC) was similar for a given location and a given depth below surface. In other words, we assumed that the soil is homogeneous in a radius of two meters from the meteorological stations. The radius of two meters corresponds to the maximum distance from the meteorological stations where the soil sensor were installed. To that end, we used one of the most popular SWRC parametrization used in soil science (*Van Genuchten*, 1980):

$$\theta(\psi) = \theta_r + \frac{\theta_s - \theta_r}{[1 + (\alpha|\psi|)^n]^{1-1/n}} \tag{5.1}$$

where ψ is the SWP [cm of water], $\alpha\,(>0)$ [cm^{-1}] and $n\,(>1)$ are two parameters related to the inverse of the air entry suction and to the pore-size distribution, θ_s is the saturated VWC, θ_r is the residual VWC [m^3 m^{-3}]. For each location, each year and each depth, we fitted an *in situ* SWRC curve through the data averaged on an hourly basis. The residual VWC was used to compare the SWRC obtained *in situ* from the different years and eventually to correct the soil moisture measurements. Note that it is outside the scope of this study to compare *in situ* SWRC and under controlled conditions SWRC as reported in 5.C. The residual VWC was used instead of the saturation VWC since the SWP sensor used in this study are not operational near saturation. The example of station 1232 at 20 cm depth is illustrated in Figure 5.4. For instance, the data obtained for the 2011 deployment has a residual VWC of 5.91% whereas for 2012 and 2013, the residual VWC is of 17.31%. Note that the station 1232 was maintained on site during the winter 2012 to 2013 so that the SWRC obtained with the 2012 and 2013 compares reasonably well without any correction. In this example, we therefore shifted all the 2011 soil moisture values by +11.4% so that the three SWRC overlap (see Figure 5.4b). For all the stations, the measurements of the 2012 campaign were taken as reference as it was the deployment with the largest time span and relatively little data missing. Note that we only corrected the VWC measurements but not the SWP measurements.

5.3.3 Computation of antecedent conditions and response time

For each event and station with installed soil sensors, we computed the antecedent VWC and SWP as the mean in the hour preceding the onset of precipitation. For the computation of the
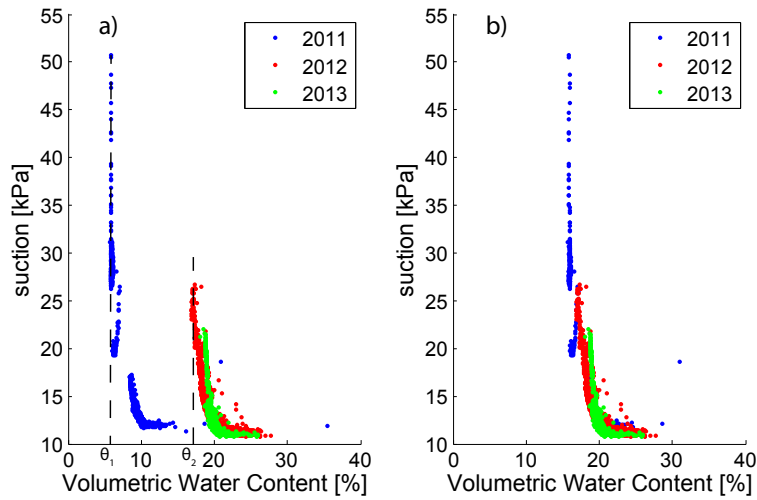
Figure 5.4: Example of a) raw SWRC at station 1232 and 20 cm depth and b) corrected SWRC obtained with corrected VWC.

antecedent conditions, we used the precipitation measured at each station. If the precipitation data was missing at a station for a given event, we used the precipitation measurements of the closest station having a percentage of missing values less than 5 % for that given event.

To study the dynamical properties of the streamflow response to precipitation, we computed the response time of discharge, soil moisture and soil water potential. The response time T_{res} is defined as the delay between onset of the precipitation and the occurrence of the maximum of the parameter analyzed. For the discharge response time, we used the same precipitation dataset as used for the runoff coefficient calculation (i.e. median of 5 distributed locations). For the soil moisture and soil water potential response time, we used the precipitation measured at each station for the computation of the antecedent conditions.

5.4 Results

5.4.1 Streamflow response to precipitation

The runoff coefficients were highly variable over the three field campaigns. The values ranged between 0.004 and 0.496 with mean, median and standard deviation values of respectively 0.0634, 0.0427 and 0.0760. We could not observe a clear relation between runoff coefficient and total precipitation amount or maximum precipitation intensity. The response of the catchment was highly non linear, as illustrated with the highest runoff coefficient (0.496) obtained for the event of the 20th of June 2012 with a relatively small total precipitation of 6.35 mm. At this time of the year, the watershed is typically partially covered by snow. It is out of our scope to understand the origin of such a high runoff coefficient value but a complex interaction between precipitation and snow patches such as a flushing effect could be

important. Moreover, the streamflow was the largest at this time of the year so that small errors in the computation of the end of the event can have larger effect on the runoff coefficient.

The runoff coefficients of the sub-basin 2 ranged between 0.005 and 0.419 with mean, median and standard deviation of 0.0835, 0.0532 and 0.0857. In general, they were larger than the runoff coefficients computed for the entire catchment, with a mean and median difference between the coefficients of 0.016 and 0.010. Concerning sub-basin 1, only 16 events could be analyzed, and the runoff coefficients ranged between 0.003 and 0.154 with mean, median and standard deviation of 0.046, 0.029 and 0.041. Similarly to sub-basin 2, the runoff coefficients were on average larger than the ones computed for the entire catchment (mean and median difference of 0.013 and 0.002).

Two elements could explain the fact that the runoff coefficients are larger in both sub-basins. In sub-basin 1, the drainage density is larger than the one of the entire catchment (7.82 km/km^2 compared to 5.27 km/km^2) so that a larger amount of precipitation is directly intercepted by the riparian area and converted to streamflow. In sub-basin 2, the drainage density is lower (4.13 km/km^2) than for the entire basin but the land cover is different and could affect stormflow generation. Whereas grassland covers more than half of the total area in sub-basin 1 and over the entire catchment (respectively 70% and 60% of sub-basin 1 and outlet, 41% of sub-basin 2), the talus deposit and bedrock outcrops cover more than half of sub-basin 2 (52% of the sub-basin 2, 29% and 38% of sub-basin 1 and of the entire watershed). Obviously, soil covered areas have larger storage capacities compared to bare rock/moraine areas which could partially explain the higher coefficients observed in sub-basin 2.

5.4.2 Thresholds on streamflow generation

The relation between runoff coefficients and antecedent VWC or SWP are shown in Figure 5.5 to Figure 5.8. For most of the locations, a threshold relationship between antecedent SWP and runoff coefficients could be observed at both depths. On the other hand, threshold relationships between VWC and runoff coefficients were less evident to determine. We identified VWC thresholds at stations 1035, 1036, 1173 and 1238 even though at these locations, the SWP threshold is easier to identify. The VWC thresholds will be commented on in the Discussion section but are not taken into account in the following results since they are more uncertain than the SWP thresholds. Table 5.3 summarizes the thresholds of SWP observed at the different locations. When taking into account all the locations and depths, a threshold relationship between antecedent SWP and runoff coefficients could be observed at 83% of the cases. It is remarkable to notice from Figure 5.5 to Figure 5.8 that the total precipitation amount was not playing a significant role in the relation between runoff coefficient and antecedent soil parameters as there is no clear pattern in the colors associated to the total precipitation. This was also the case when event duration, maximum or mean precipitation intensity were used.

We could not observe a SWP threshold at station 1172 at 40 cm and at stations 1240, 1242 and 1243 at 20 cm depth. Concerning station 1172 and 1243, not enough antecedent conditions

could be established due to the gaps in the data. Concerning stations 1240 and 1242, the relation between runoff coefficient and antecedent SWP is more scattered, i.e. the absence of threshold relationship can not be explained by a lack of observable antecedent conditions. Compared to the other stations, the 20 cm depth SWP signal obtained during the campaign 2012 at stations 1240 and 1242 was slowly increasing during the season until the beginning of July without any type of response to precipitation. It is therefore believed that the SWP sensors at stations 1240 and 1242 were not correctly installed during the 2012 campaign. This could be due to small soil disturbance or air gaps.
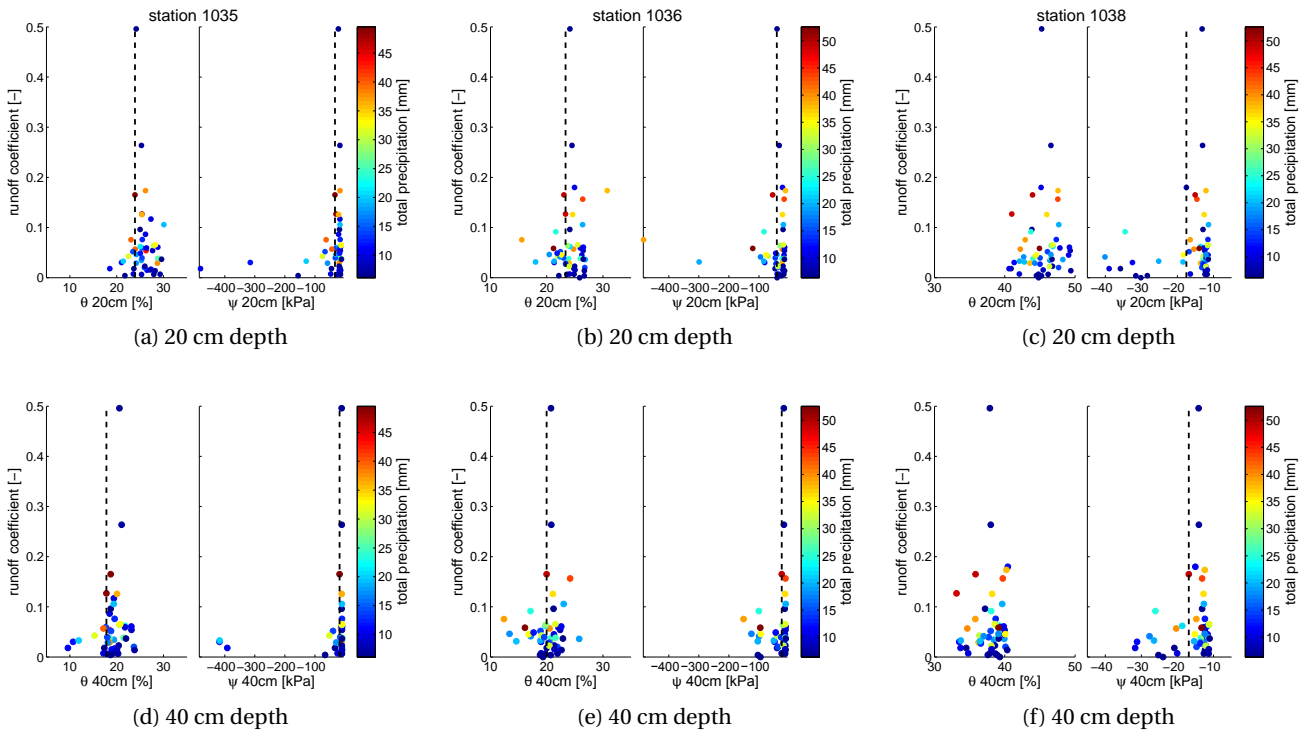

Figure 5.5: Relation between runoff coefficients and VWC (θ, left of each subfigure) or SWP (ψ, right of each subfigure). The upper and lower lines show the data from the sensors installed at respectively 20 cm and 40 cm depth. The columns one to three correspond to the data from stations 1035, 1036 and 1038. The dashed line correspond to the threshold of SWP and VWC on runoff generation. Every point is color-coded with the total precipitation amount of the event.

The value of the SWP thresholds reported in Table 5.3 have been established manually since no objective and automatic criterion could be defined to extract them. However, a quantity describing the sharpness of the threshold relationship was introduced, defined by the product of the standard deviation of the antecedent SWP values above the threshold and the standard deviation of the runoff coefficients of the events with antecedent SWP values under the threshold. The criterion is reported as *sharpness* in Table 5.3 and tends to zero in the case of a perfect threshold relationship. With this criterion, we can objectively report that the sharpest

threshold relationships between runoff coefficients and antecedent SWP were observed at stations 1238 and 1232.

Table 5.3: Threshold values for the different locations and different depth. The term *not observed* means that no threshold relationship between antecedent SWP and runoff coefficient could be identified and the term *a.u* stands for arbitrary unit.

location	SWP$_{20\,cm}$ [kPa]	sharpness [a.u]	SWP$_{40\,cm}$ [kPa]	sharpness [a.u]
1035	-33.381	0.229	-17.814	0.019
1036	-40.605	0.312	-24.009	1.501
1038	-17.523	0.041	-16.852	0.063
1043	-19.207	0.030	-14.171	0.100
1172	-32.405	0.056	*not observed*	
1173	-16.358	0.052	-13.247	0.014
1232	-15.568	0.033	-12.788	0.039
1238	-11.002	0.005	-10.937	0.007
1240	*not observed*		-20.373	1.786
1242	*not observed*		-18.641	0.103
1243	*not observed*		-15.438	0.034
1244	-20.532	0.126	-40.475	1.150

Similar thresholds were observed when we used the runoff coefficients of the sub-basin 2 and the stations belonging to the sub-basin 2 (i.e. stations 1232, 1240, 1242 and 1244). For sake of clarity, the relations between runoff coefficients and antecedent VWC or SWP are not shown in Figure 5.5 to Figure 5.8. For sub-basin 1, only few events were available for computation of the runoff coefficients. However, a similar threshold was observed for stations 1238 and 1043 at both depths.
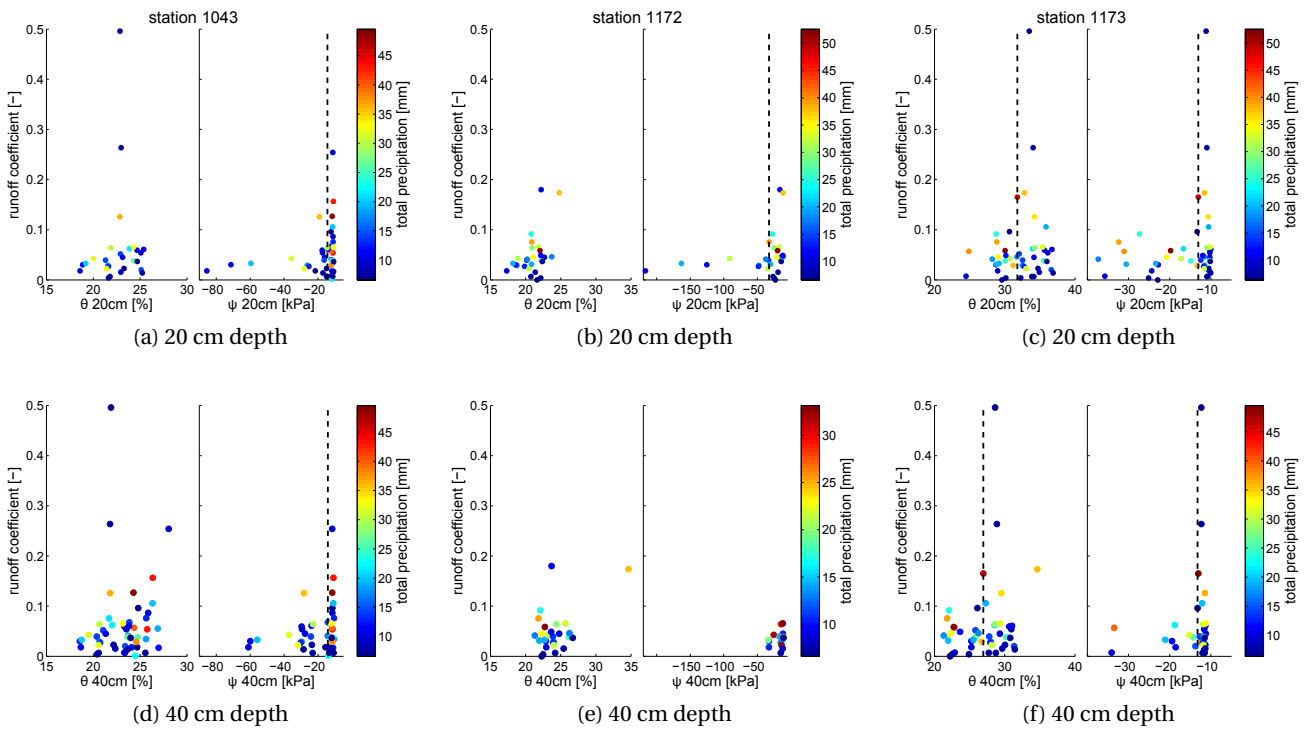
Figure 5.6: Same as Figure 5.5 for stations 1043, 1172 and 1173.
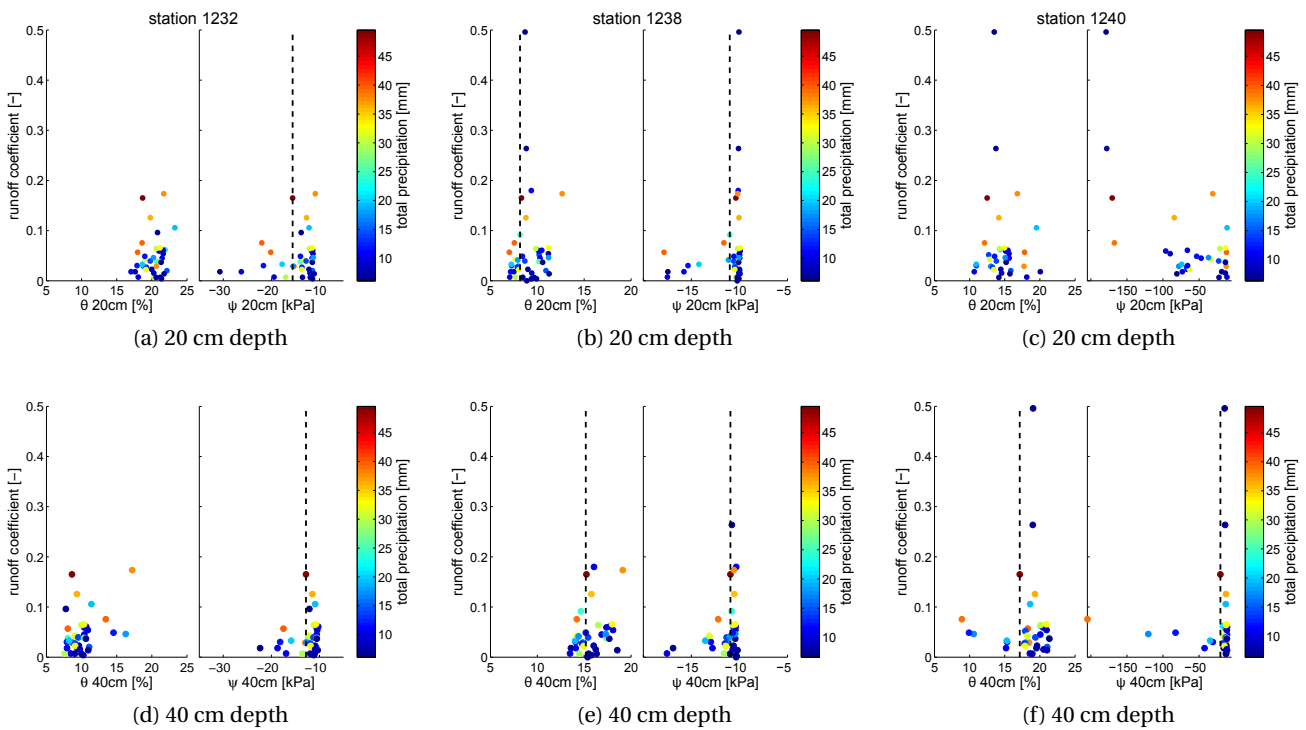

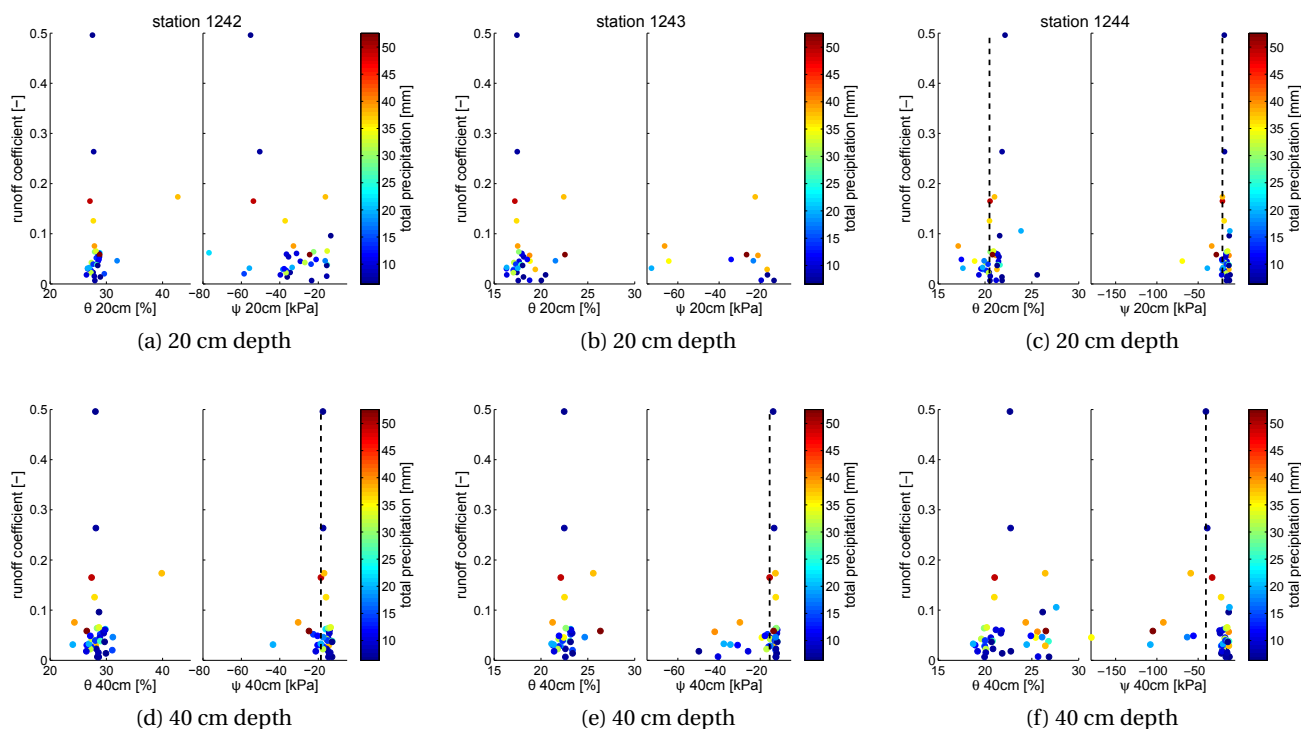Figure 5.7: Same as Figure 5.5 for stations 1232, 1238 and 1240.

Figure 5.8: Same as Figure 5.5 for stations 1242, 1243 and 1244.

Response time of discharge, soil moisture and soil water potential

Some simple calculations based on the response time of the soil parameters and discharge were done to see if the streamflow generation dynamics could be different above or under the SWP thresholds. The response time of the discharge at the outlet was highly variable (see Table 5.4) but is highly correlated to the event duration (Pearson linear correlation coefficient: 0.7145, $p = 5.42 \times 10^{-12}$). Needless to say, the response time of soil moisture and soil water potential was found to be always shorter than the discharge. Moreover, the response time of the soil moisture was on average shorter than the response time of the soil water potential for all the locations at both depths. Compared to the soil moisture sensors, the soil water potential sensor needs a longer time to equilibrate with the surrounding matrix, specified by the manufacturer between 10 minutes and one hour. Hysteresis effects in the SWRC could also explain the differences in the response times of the two parameters. However, understanding such differences in the dynamics of the soil moisture and soil water potential would require numerical simulations using Richards equation and our dataset as boundary conditions which is outside of the scope of this study.

According to the various thresholds observed, the events were classified for each location and each depth as wet (above SWP threshold) or dry (under SWP threshold) antecedent conditions. The difference between the discharge response time and the VWC or SWP response times has

been computed for both populations. We found that when taking into account all locations and depth with observed thresholds, the difference between discharge response time and VWC response time is 29% larger when dry antecedent conditions were preceding the event, 18% larger in the case of the difference between discharge response time and SWP response time.

5.5 Discussion

We find a clear threshold relationship between antecedent SWP and runoff coefficients at various sites of the catchment and various depth below surface. To our knowledge, this threshold behavior has been reported for soil water content and/or the sum of soil water content and precipitation amount but has not been reported for SWP. We acknowledge that several aspects could possibly alter the observed threshold relationships and are discussed in the following.

First, there are certainly some errors in the computation of the runoff coefficients. We used a graphical method for selecting the end of the event and assumed that the baseflow was varying with a constant slope during the storm events (*Blume et al.*, 2007). The main objective of the analysis is not to study the dynamics leading to the runoff coefficients but rather to use them as a quantitative tool to analyze the effect of antecedent soil conditions on stormflow generation. As long as the uncertainty in the runoff coefficient is relatively small, we don't think that the threshold relationships obtained in our analysis are affected by the error on the computation of the runoff coefficients. Actually, we obtained similar threshold behaviors when the baseflow was not separated from the total flow, i.e. when runoff coefficients were computed as the total streamflow divided by the total precipitation amount. We therefore believe that this threshold relationship is robust and not depending on a method of baseflow separation technique.

Second, the accuracy and range of detection of the soil sensors are also important factors in our study. As specified by the manufacturer, the MPS-1 sensors used to measure SWP is not adapted to very wet soils since it does not measure values above -9 kPa. However, we can see from the Figures reported in the Appendix of this Chapter (Figure 5.9 to Figure 5.20) that in general, the SWP measured at the different locations were fluctuating and not always at the upper limit of the measurable range. With the sensor that we use, we have no details on the SWP when the soil is close to saturation, which might occur during important precipitation events. On the other hand, the 5-TM sensors used for measuring the VWC have no range limitation and are able to measure VWC close to saturation. However, the threshold behavior observed at some locations was not as well defined as in studies reported earlier (*James and Roulet*, 2007, 2009; *Penna et al.*, 2011; *Western and Grayson*, 1998). Maybe if we would have the full range of SWP measurement possible, then the relation between antecedent SWP and runoff coefficients would be more scattered and look like the relation observed for the VWC.

We acknowledge that the VWC measurements become relative with the corrections based

on the SWRC. However, if we would not carry out those corrections, the relation between antecedent VWC and runoff coefficients would be even more scattered. For all the locations and depths, we investigated the existence of thresholds on a yearly basis without correcting the VWC data. Yet no such threshold behavior were observed on the yearly basis. The fact that VWC thresholds are less easily observable than SWP thresholds can therefore not be explained by the SWRC-based corrections.

The year to year variability of the VWC measurements was not negligible even though the meteorological stations were installed every year at similar locations. With the correction based on the SWRC, we can correct the range (i.e mean) of the VWC. However, for some locations, we see that the dynamics are very different from year to year. The VWC measured at station 1172 is a good illustration of this problem. From Figure 5.13), we can observe large variation of the VWC at 40 cm depth during precipitation events in the year 2013. This is not the case in the year 2012 with little variation even though the value of the mean VWC are comparable from year to year. Compared to the MPS-1 sensors, the 5-TM sensors are more sensitive to bad installation, for instance due to the presence of stones or pebbles in the vicinity of the sensor.

Based on the criterion introduced to quantify the sharpness of the threshold behavior, we observed that the most pronounced threshold relationships were identified at stations 1238 and 1232. Those two stations were maintained during the winters. Most likely, it is not a coincidence that the threshold relationship is the best for the stations where the soil sensors were not moved between deployments and installed just once, even though the effect of the measurable range of the MPS-1 can also affect this sharpness. However, for future studies in the Val Ferret watershed, it is highly suggested to keep the soil sensors on site during the winter. This represents a challenge not negligible given the large avalanche activity that is observed in the Valley during winters.

We did not intend to establish threshold relationship between total amount of precipitation and stored amount of water as done in earlier studies (*Fu et al.*, 2013b; *Haga et al.*, 2005; *Detty and McGuire*, 2010a,b). The knowledge of the soil/bedrock interface is of critical importance to correctly estimate the total amount of water available in the soil before the event. Obviously, this information is extremely difficult to estimate at the catchment scale, especially in mountainous catchment where the geology is complex.

The analysis of the response time of the discharge, VWC and SWP showed the importance of subsurface flow in the stormflow generation. The difference between the occurrence of the soil moisture peak and the streamflow peak was lower for wet antecedent conditions. Based on our results, it is hard to speculate whether the fill and spill hypothesis (*Spence and Woo*, 2003; *Tromp-van Meerveld and McDonnell*, 2006a) or connectivity of lateral preferential flowpaths (*Lin*, 2010; *Sidle et al.*, 2001) can better explain the threshold behaviors observed in our experimental watershed. Our understanding of the phenomena is that above a certain threshold of SWP, the transport of water through the unsaturated zone is enhanced by

increasing hydraulic conductivity. In other words, the SWP thresholds that we observed could actually reflect thresholds of the hydraulic conductivity (*Torres*, 2002). Our results also strongly suggest to investigate hysteresis effects at the hillslope scale, illustrated in our study site by the presence of SWP thresholds and almost no VWC thresholds. *Torres et al.* (1998) recognized the influence of hysteresis effects near saturation in an irrigation-controlled unchanneled hillslope, but less attention has been paid to this phenomena on larger and naturally driven hillslope or headwater catchments.

Some non negligible differences were observed in the values of the SWP thresholds regarding both location and depth. Further investigations will need to clarify the role of the topography, distance to stream, land cover and porosity effects on these thresholds. Moreover, we found interesting to identify such clear thresholds with relatively little accurate sensors for which we used the manufacturer's default calibration. At the time of writing, Decagon Inc. has launched the version #6 of the MPS sensor with a marked increase in accuracy compared to the sensors deployed in the study. However, the upper limit of the measurable range remains similar but this drawback is partially compensated by the lower costs and little maintenance needed compared to classical tensiometers.

5.6   Conclusion

Many recent studies have reported threshold relationships between antecedent soil moisture and runoff coefficients during precipitation events at the hillslope or small headwater catchment scale. The existence of such threshold behaviors were investigated in the Val Ferret watershed with a deployment of 20 meteorological stations during three consecutive summers from 2011 to 2013. Among the 20 meteorological stations, 12 were equipped with sensors deployed at 20 cm and 40 cm to monitor soil moisture and soil water potential. The analysis of 69 precipitation events showed that there is a clear threshold behavior between soil water potential and runoff coefficients, observed at 83% of the locations. The value of the soil water potential thresholds was varying both in space and depth. Above this threshold, the runoff coefficients were larger and the response time of the watershed was shorter. Threshold relationship between soil moisture and runoff coefficients were less systematically observed.

However, two issues related to measurement challenges are mitigating our results. First, the sensors had to be reinstalled every year due to their high exposure to avalanche activities. This created some year to year variability of the soil moisture and soil water potential measurements even though the meteorological stations were deployed at consistent locations. The soil water potential sensors were less sensible to this issue and showed less variability compared to the soil moisture sensors. A correction based on *in situ* Soil Water Retention Curves was proposed to account for this logistical issue. Second, the sensors used to measure the soil water potential had a limited measurable range which does not cover states near saturation. However, even though this issue was not negligible in our study, the threshold relationship between soil water potential and runoff coefficients remains valid but could possibly be more scattered if the full

range of soil water potential was measurable.

Our results underline that hysteresis effects at the hillslope scale might play an important role in stormflow generation. In our opinion, tensiometers are not being sufficiently deployed in experimental hydrological studies, where streamflow, precipitation and soil moisture are regularly monitored. Given that the cost of tensiometers have decreased along with increasing accuracy, we recommend to use them more systematically in hillslope or catchment hydrology. Hysteresis effects of soil water retention need to be further investigated through numerical simulations or at intensively monitored slopes as they are possibly linked to recently proposed mechanisms of threshold-based stormflow generation.

5.A   Plots of data

Figures 5.9 to 5.20 show the data recorded at the meteorological stations equipped with soil sensors. In each figure, the three columns correspond to the deployments 2011, 2012 and 2013. The first line shows the discharge time series along with the precipitation dataset used in the study. The second and third line show the Volumetric Water Content (VWC) and soil water temperature respectively, obtained with the 5-TM sensors. The VWC data shown has not been corrected with the method relying on the Soil Water Retention Curves. The fourth line shows the Soil Water Potential (SWP) obtained with the MPS-1 sensors. In lines two to four, the solid blue lines and red lines show the data measured at 20 cm depth, respectively 40 cm depth. While the axis of lines one to three are similar for all figures, note that the axis for the SWP have been adapted for each measurement location.

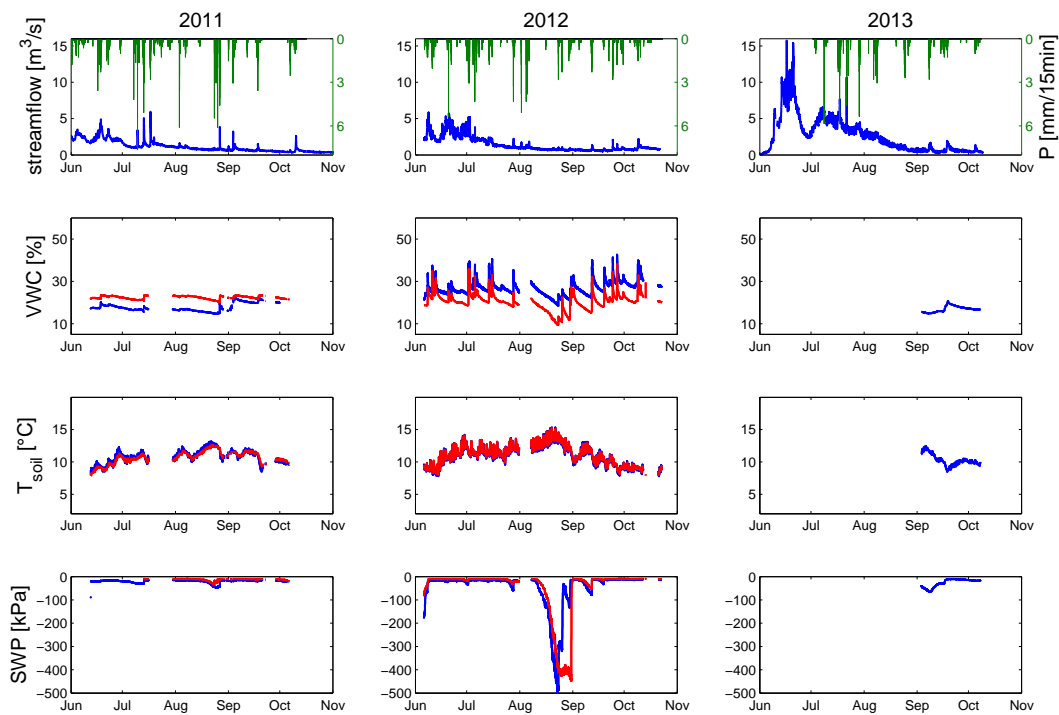Figure 5.9: station 1035. Blue and red lines correspond to data measured at 20 cm and 40 cm below surface.
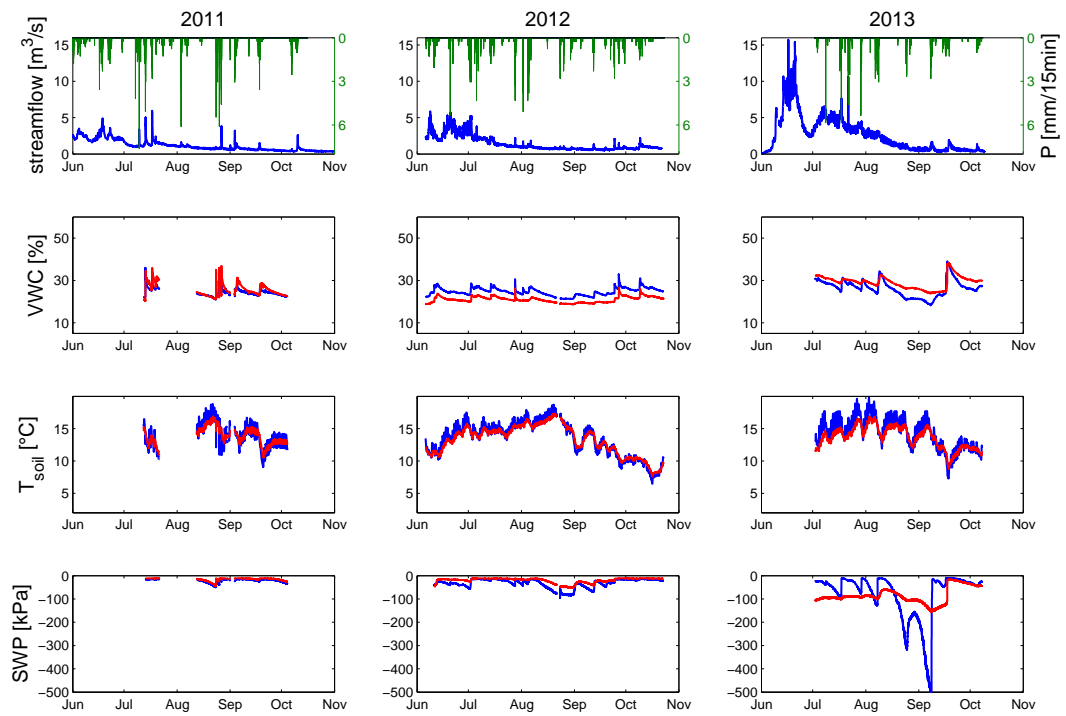
Figure 5.10: station 1036

Figure 5.11: station 1038

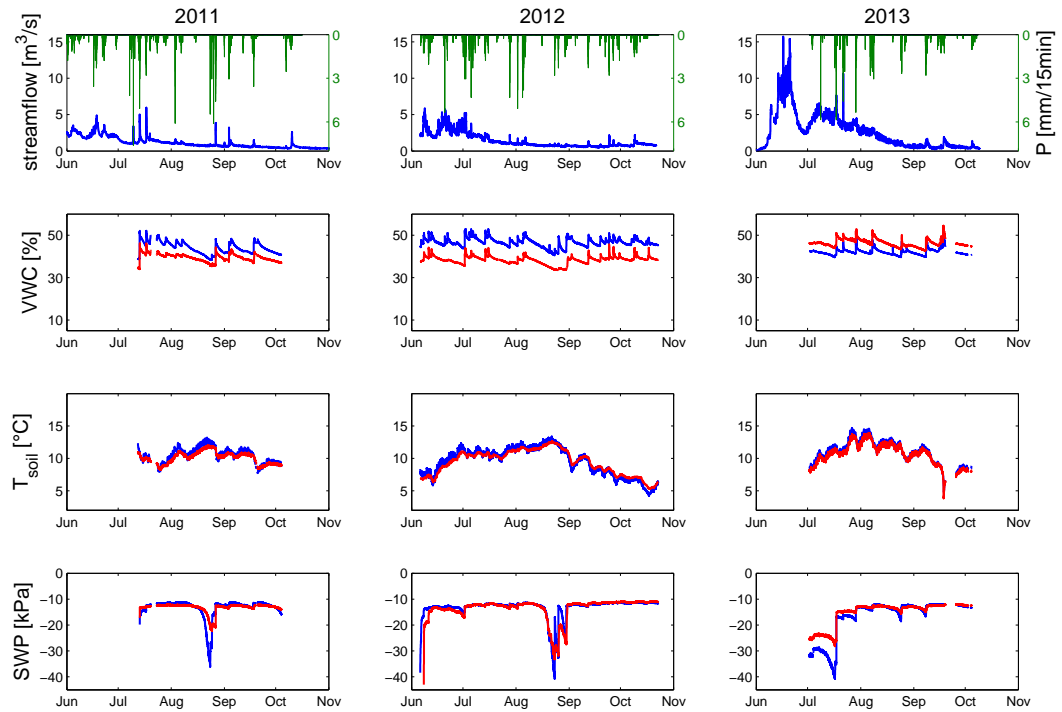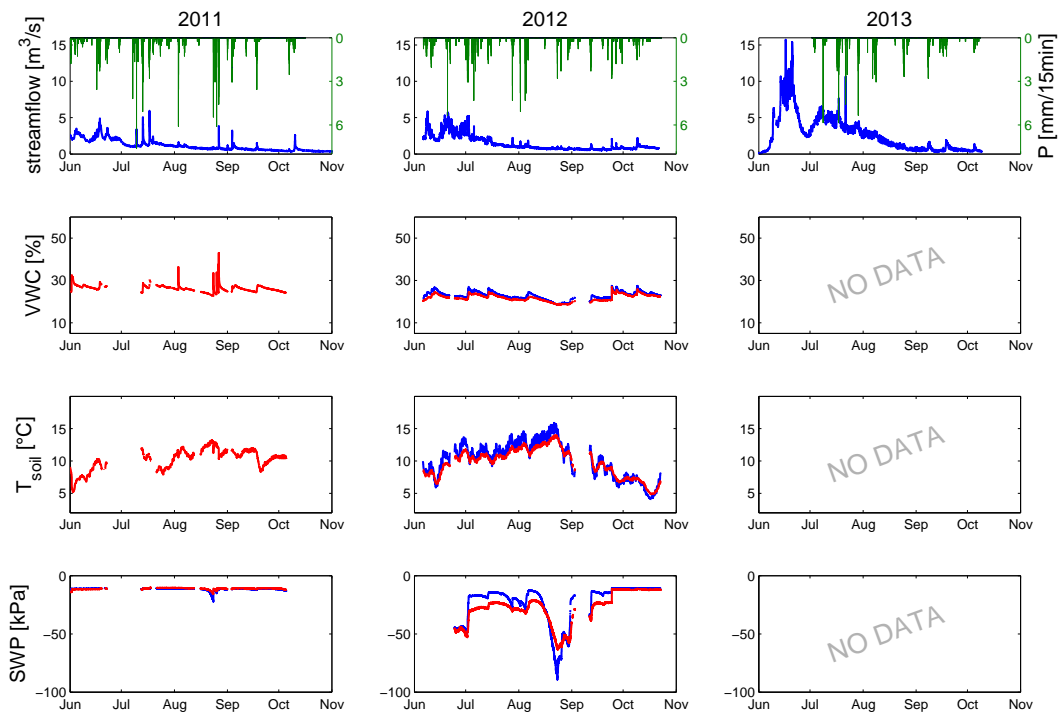Figure 5.12: station 1043
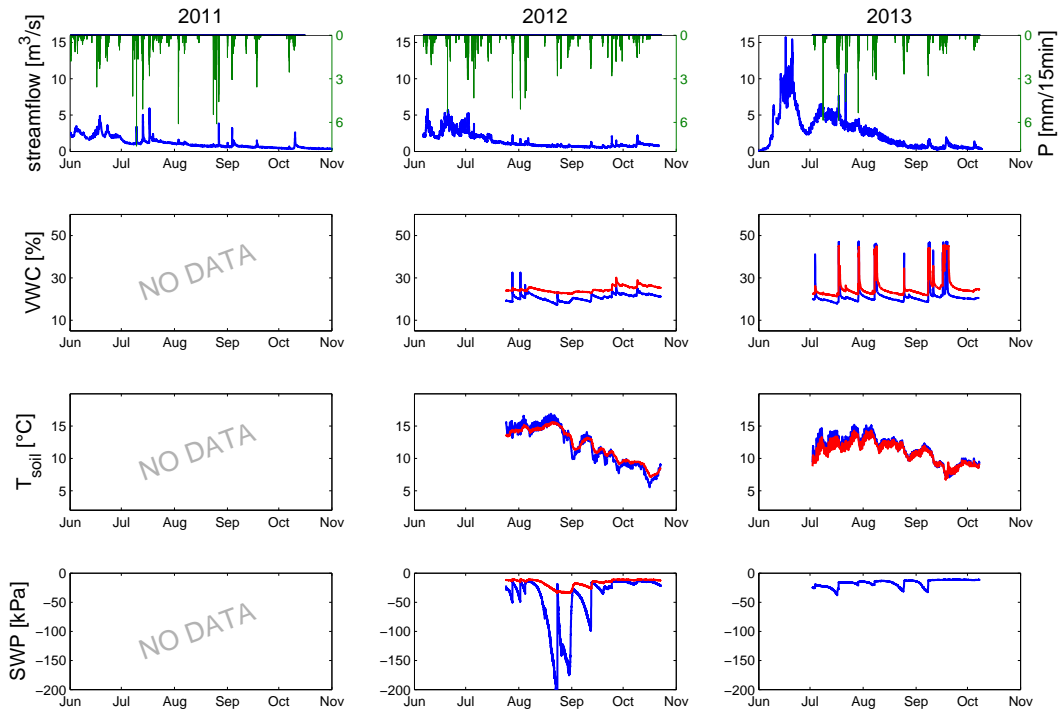
Figure 5.13: station 1172
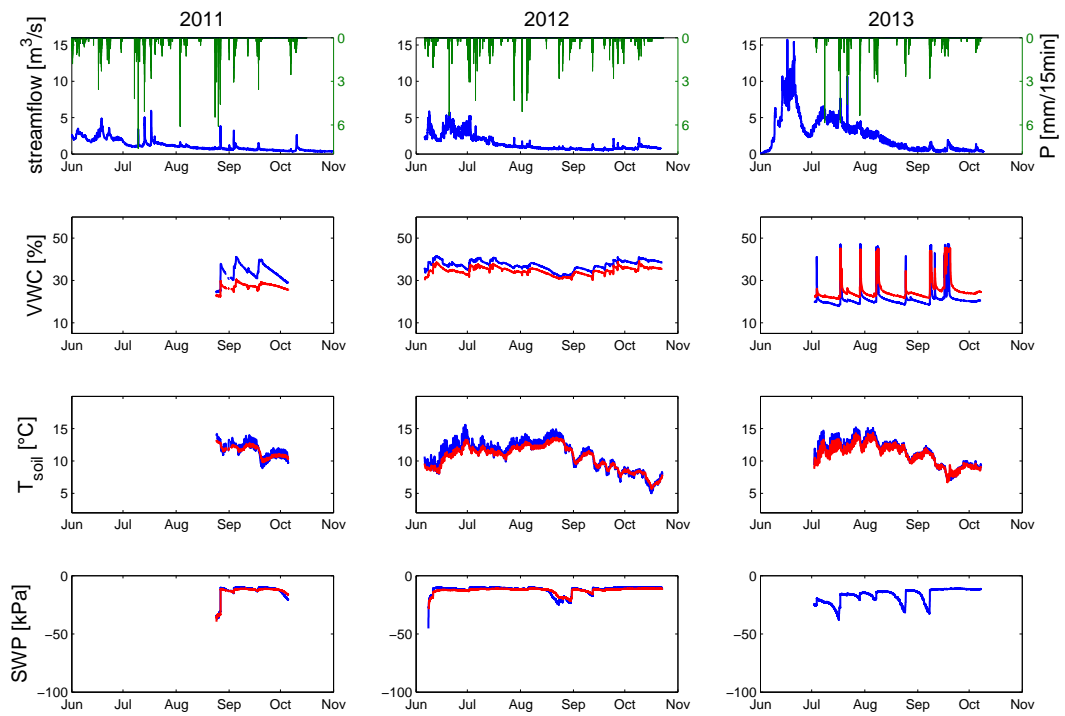
Figure 5.14: station 1173
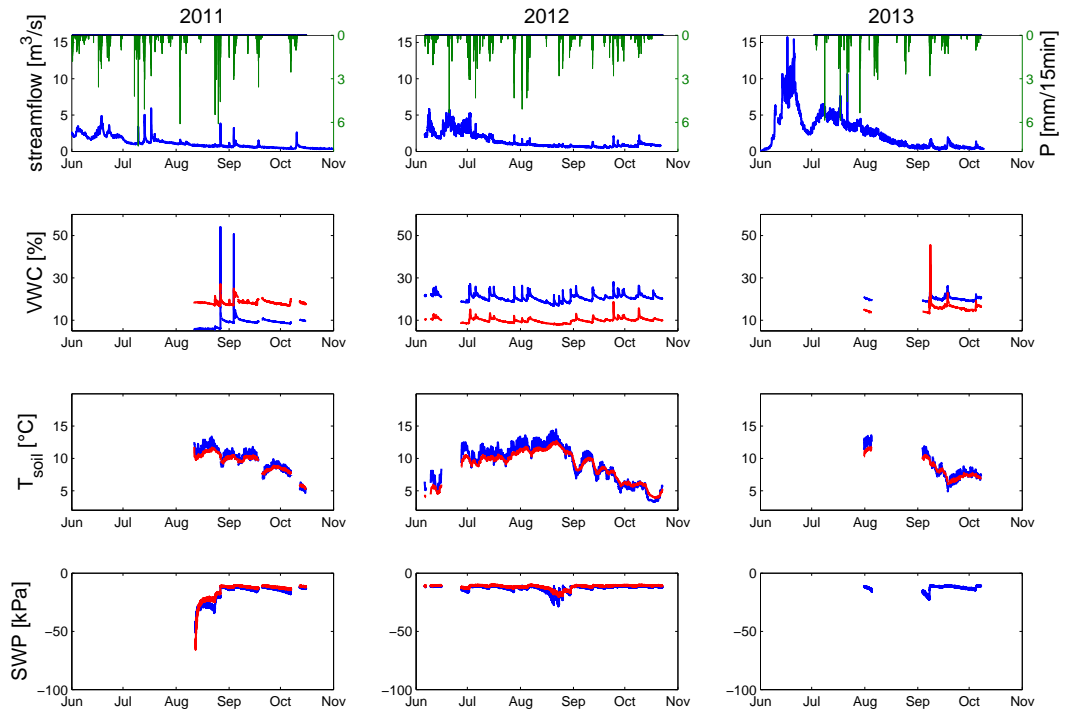
Figure 5.15: station 1232
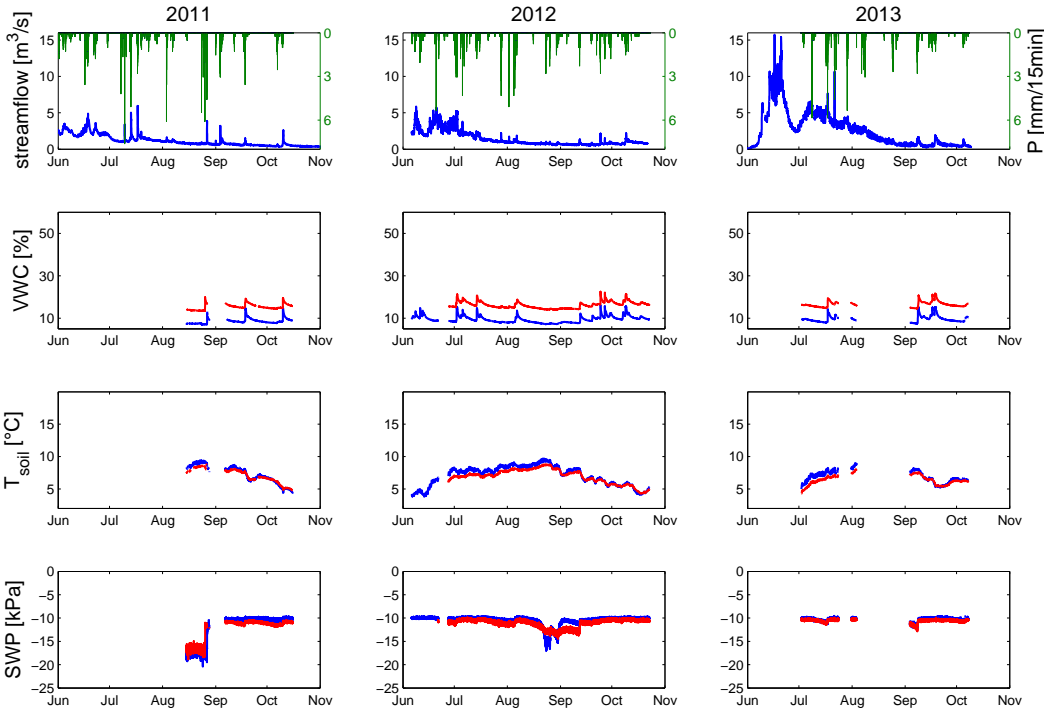
Figure 5.16: station 1238
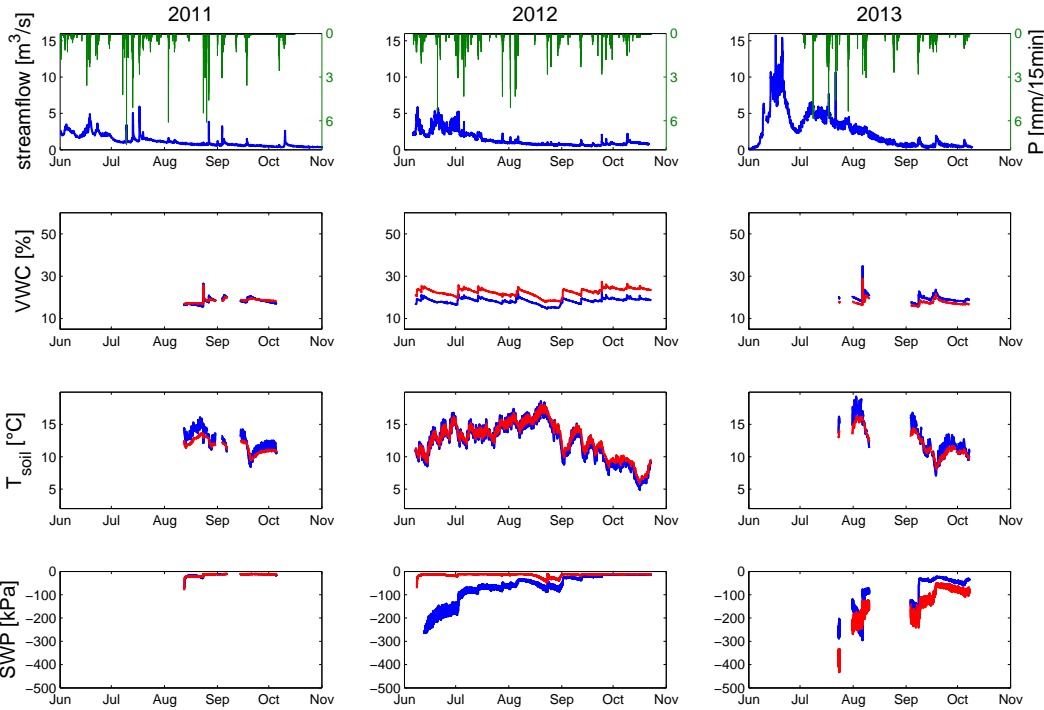
Figure 5.17: station 1240
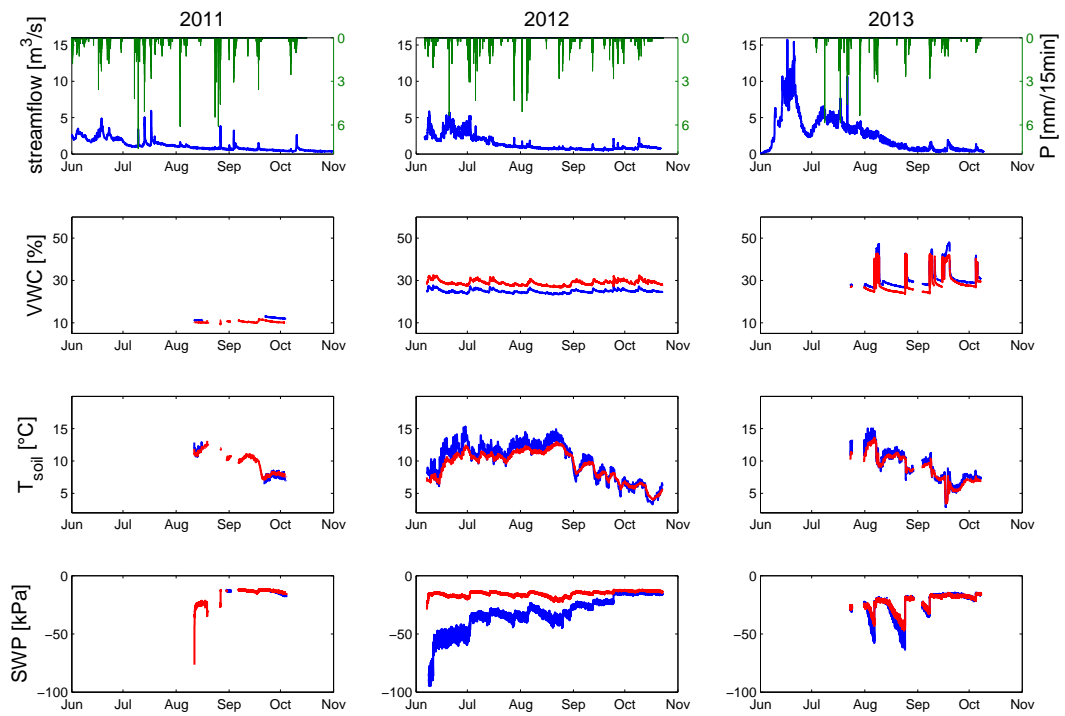
Figure 5.18: station 1242
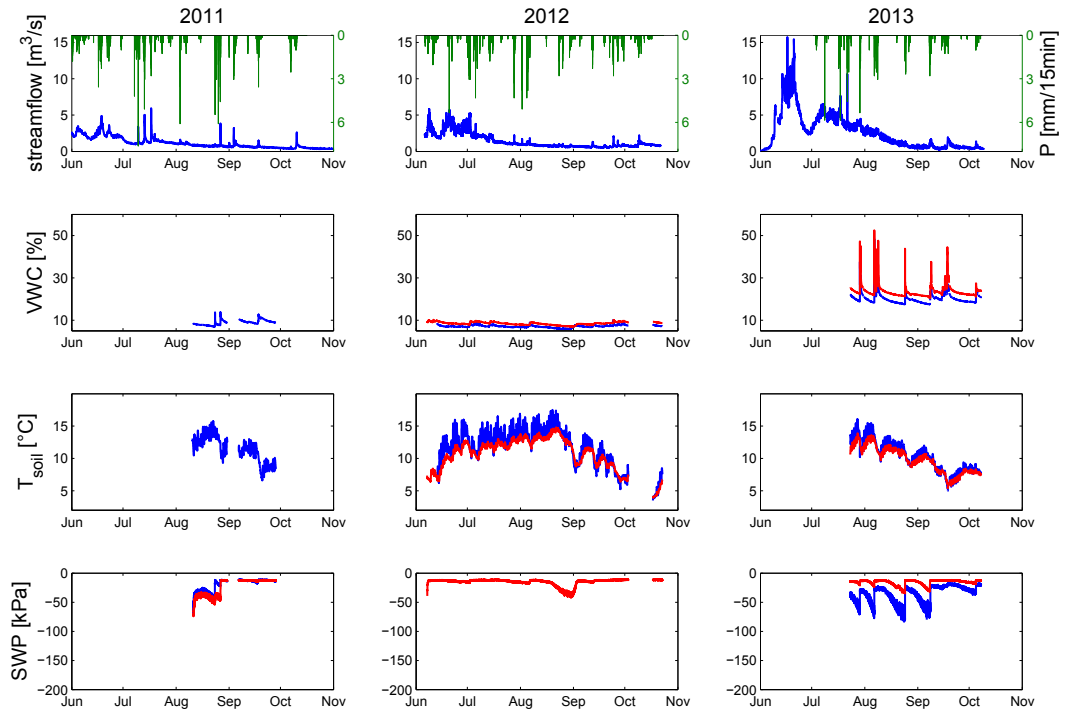
Figure 5.19: station 1243
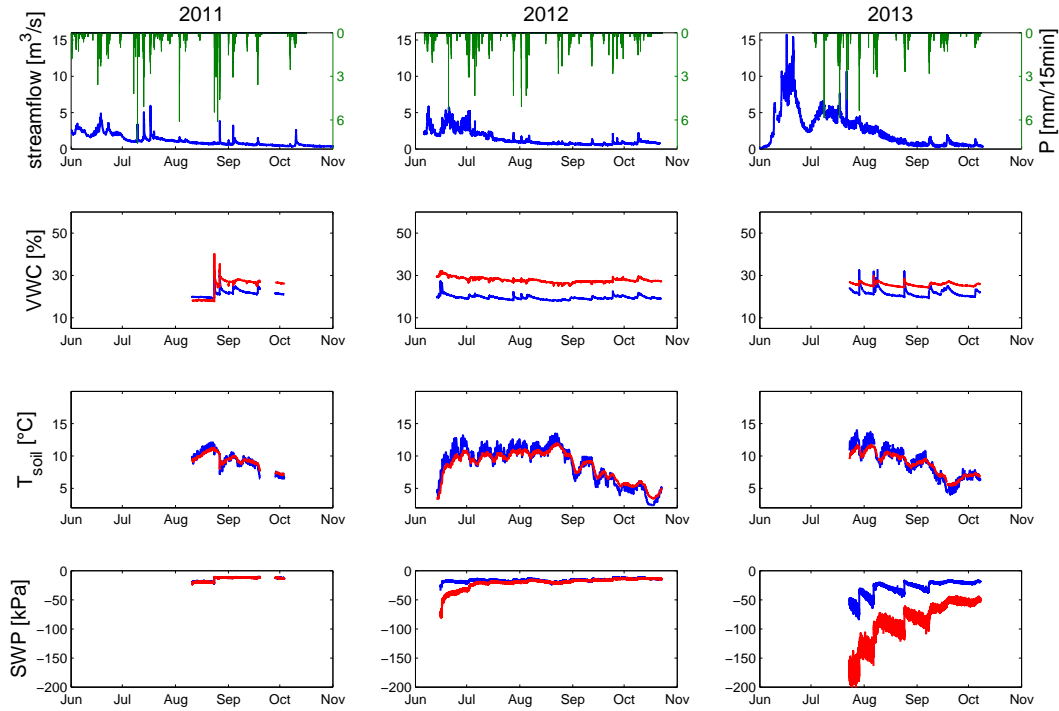
Figure 5.20: station 1244

5.B Selected Events

Table 5.4: Summary of the storm events and streamflow response at the three monitored locations. ΔQ is the difference between baseflow and streamflow peak, T_{res} the difference in time between precipitation onset and maximum streamflow occurrence, *rf coeff* is the runoff coefficient defined as total stormflow divided by the total precipitation.

| Date	rainfall P_{total} [mm]	duration [h]	outlet ΔQ [l/s]	rf coeff. [-]	T_{res} [h]	sub-basin 1 ΔQ [l/s]	rf coeff. [-]	T_{res} [h]	sub-basin 2 ΔQ [l/s]	rf coeff. [-]	T_{res} [h]
13.05.2011	20.45	3.5	1256.7	0.076	3.75	-	-	-	-	-	-
14.05.2011	8.00	8.25	167.7	0.007	2.75	-	-	-	-	-	-
26.05.2011	17.02	25	512.4	0.041	5	-	-	-	-	-	-
30.05.2011	14.10	2.25	1255.2	0.068	3	-	-	-	-	-	-
31.05.2011	11.94	13.5	233.4	0.018	12.5	-	-	-	-	-	-
01.06.2011	22.35	5.75	20.6	0.001	1.25	-	-	-	-	-	-
03.06.2011	9.40	10.75	808.1	0.254	22	-	-	-	-	-	-
07.06.2011	18.54	48	187.7	0.055	32.75	-	-	-	-	-	-
16.06.2011	9.65	8.25	763.3	0.087	3	-	-	-	-	-	-
17.06.2011	42.93	22.25	1741.9	0.054	20.5	-	-	-	-	-	-
21.06.2011	12.19	17.25	343.5	0.017	9	-	-	-	-	-	-
22.06.2011	10.03	6.75	699.4	0.117	4.5	-	-	-	-	-	-
29.06.2011	10.92	13.25	83.2	0.015	1	-	-	-	-	-	-
07.07.2011	8.51	9.25	101.4	0.006	1	-	-	-	-	-	-
09.07.2011	13.72	1.75	2392.1	0.059	2.25	-	-	-	981.2	0.020	2
12.07.2011	48.39	35.5	3806.7	0.127	20.75	-	-	-	1223.5	0.095	20.5
16.07.2011	43.31	18.5	4718.3	0.156	13.5	-	-	-	1283.1	0.092	12.5
19.07.2011	18.92	32.25	937.3	0.036	3.25	-	-	-	338.2	0.054	2.75
03.08.2011	17.78	21.25	591.2	0.034	10.25	-	-	-	230.7	0.024	10
06.08.2011	12.70	15.75	335.4	0.076	6	-	-	-	121.2	0.050	5.75
23.08.2011	6.60	1.75	206.1	0.018	1.25	-	-	-	92.2	0.019	1
25.08.2011	10.16	0.75	138.4	0.007	2.25	-	-	-	113.4	0.006	1.75
26.08.2011	39.62	9	3155.5	0.057	7.5	-	-	-	1361.4	0.097	7
31.08.2011	6.73	3	587.2	0.096	2.25	-	-	-	320.8	0.106	2
03.09.2011	25.40	2.75	2500.3	0.038	3	-	-	-	1205.0	0.053	3
04.09.2011	19.56	27.5	734.6	0.106	3.75	-	-	-	491.6	0.167	3.25
11.09.2011	6.86	12	75.1	0.007	2	-	-	-	113.5	0.014	1.25
17.09.2011	37.85	29.75	875.1	0.029	20	-	-	-	810.7	0.095	19.5
06.10.2011	29.21	22.5	249.4	0.007	10.5	-	-	-	106.0	0.011	10
06.06.2012	6.10	8.75	326.8	0.004	8	-	-	-	123.7	0.086	3.75
07.06.2012	14.22	11.5	1372.1	0.389	20.25	-	-	-	2096.0	0.393	3.25
10.06.2012	21.59	8.75	993.6	0.062	7	-	-	-	510.9	0.037	8
12.06.2012	14.73	18.75	366.7	0.020	2.5	-	-	-	158.1	0.037	5.75
20.06.2012	6.35	8.25	1880.8	0.496	4.75	-	-	-	807.0	0.198	1
21.06.2012	7.11	6	1001.3	0.264	6	-	-	-	155.1	0.031	0.25
01.07.2012	49.53	28.5	2677.7	0.165	13.75	-	-	-	1488.4	0.139	21.5
04.07.2012	10.16	3.75	812.7	0.059	3	-	-	-	277.8	0.035	2.75
05.07.2012	8.64	15.75	1811.1	0.054	8.25	-	-	-	647.9	0.063	8
06.07.2012	6.86	5	258.2	0.014	2	-	-	-	293.3	0.053	1.75
13.07.2012	36.07	14	1078.4	0.126	4.25	-	-	-	333.7	0.016	13.25
15.07.2012	10.67	5.5	519.6	0.061	3.5	-	-	-	32.7	0.006	3
20.07.2012	7.37	12.75	99.7	0.023	11.25	4.1	0.003	2.75	34.1	0.009	1.25
28.07.2012	17.53	25.5	1196.7	0.029	7	187.8	0.026	6.75	395.6	0.046	6.5
01.08.2012	13.21	2.5	750.3	0.027	3.25	138.6	0.019	3	312.1	0.023	3
04.08.2012	32.26	23	468.2	0.022	1.5	71.5	0.017	15.25	423.5	0.049	1.25
06.08.2012	10.41	4.75	902.2	0.045	3.25	111.2	0.032	3	404.1	0.097	3.25
23.08.2012	10.41	14.5	300.9	0.018	4.25	29.7	0.014	3.75	211.3	0.015	4
25.08.2012	11.68	5.25	332.9	0.030	2	41.2	0.012	3	229.8	0.029	2
29.08.2012	19.81	34	340.3	0.033	9.75	49.9	0.016	9.5	228.2	0.044	9.25
11.09.2012	31.75	20.5	715	0.043	11.25	390.3	0.065	14.75	308.3	0.039	11
18.09.2012	14.22	16.5	272	0.039	12.75	127.2	0.052	12	132.5	0.055	6.5
22.09.2012	7.37	8.5	82	0.007	3.75	17.6	0.013	9.25	46.5	0.005	3
24.09.2012	29.97	8.75	1548.9	0.064	4.75	586.5	0.093	5.25	717.5	0.103	5.5
26.09.2012	26.42	9.5	824.7	0.038	7.75	313.8	0.058	7.75	365.6	0.044	7.5
28.09.2012	6.60	18.25	322.5	0.037	18.5	61.6	0.100	18.5	318.0	0.264	18
06.10.2012	8.38	14	187.7	0.015	5.25	77.1	0.069	5.5	111.9	0.087	5.75
08.10.2012	33.15	25.5	1492.3	0.066	17.5	508.7	0.154	16.75	514.2	0.086	17
03.07.2013	6.86	7.75	15.4	0.004	0.25	-	-	-	-	-	-
08.07.2013	6.60	1	11.3	0.004	3.5	-	-	-	-	-	-
16.07.2013	17.78	6	1078.9	0.041	3.75	-	-	-	987.7	0.127	6
17.07.2013	24.64	4.25	2485.2	0.092	2.75	-	-	-	3356.4	0.268	2.75
21.07.2013	11.18	3	6443.6	0.180	3.25	-	-	-	4368.6	0.368	2.75
29.07.2013	34.80	16.75	989.5	0.046	12.5	-	-	-	1499.4	0.115	13
06.08.2013	52.58	50	1056.4	0.121	21.25	-	-	-	1313.8	0.146	47.5
24.08.2013	19.94	14	476.3	0.031	4.75	-	-	-	252.5	0.036	4.25
07.09.2013	39.37	34.25	1171.9	0.076	25.25	-	-	-	593.6	0.116	19.25
16.09.2013	17.78	12	512.9	0.046	11	-	-	-	116.6	0.021	10.25
17.09.2013	37.85	38.5	1507.7	0.159	28.25	-	-	-	477.9	0.126	39
04.10.2013	12.07	5.75	911.7	0.049	6.25	-	-	-	492.0	0.095	6

5.C Soil samples analysis

Small soil samples were collected during the summer of 2009 (stations 1033 to 1042) and summer 2011 (stations 1232 to 1244) in the vicinity of the meteorological stations and analyzed under controlled conditions. The results of the laboratory analysis are shown in Figure 5.21. At each location, three samples were collected to reduce the error on the analysis so that each value presented in Figure 5.21 is an average of three measurements. At each location, we parametrized the SWRC with a widely used model (*Van Genuchten*, 1980), see Eq. 5.1, and the results are shown in Table 5.5. For sake of clarity, the parametrization is not shown in Figure 5.21. The dashed line in Figure 5.21 represents the lower limit that the sensors (MPS-1) used in this Chapter can measure.
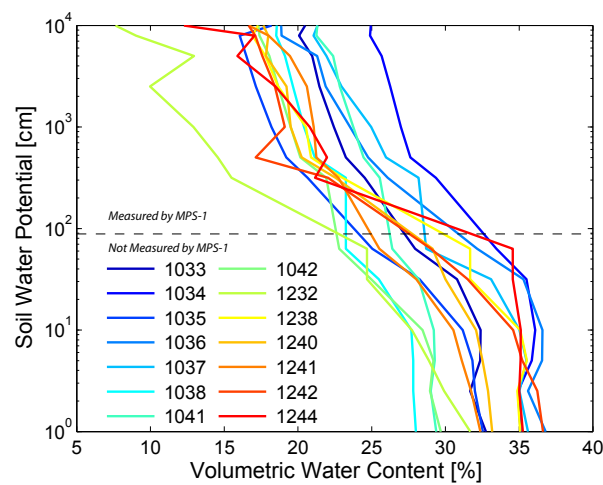
Figure 5.21: SWRC obtained under controlled conditions in the laboratory.

Table 5.5: Parameters of the SWRC model.

	α	n	θ_r	θ_s	R^2
1033	0.027	1.450	19.34	32.51	0.994
1034	0.011	1.669	24.69	35.59	0.991
1035	0.038	1.559	16.19	32.33	0.993
1036	0.019	1.376	16.68	36.66	0.992
1037	0.076	1.141	11.44	35.94	0.982
1038	0.095	1.179	14.45	28.35	0.980
1041	0.053	1.113	13.58	29.47	0.989
1042	0.120	1.259	15.13	30.00	0.988
1232	0.046	1.285	4.36	30.42	0.977
1238	0.017	1.576	16.22	35.15	0.993
1240	0.019	1.619	17.13	32.74	0.995
1241	0.139	1.162	11.22	32.65	0.988
1242	0.026	1.714	16.68	35.92	0.987
1244	0.010	1.663	14.37	35.45	0.970

Bibliography

Ali, G., C. J. Oswald, C. Spence, E. L. H. Cammeraat, K. J. McGuire, T. Meixner, and S. M. Reaney (2013), Towards a unified threshold-based hydrological theory: necessary components and recurring challenges, *Hydrological Processes*, *27*(2), 313–318, doi:10.1002/hyp.9560.

Arnold, J. G., and P. M. Allen (1999), Automated methods for estimating baseflow and ground-water recharge grom streamflow records, *Journal of the American Water Resources Association*, *35*(2), 411–424, doi:10.1111/j.1752-1688.1999.tb03599.x.

Berti, M., and A. Simoni (2010), Field evidence of pore pressure diffusion in clayey soils prone to landsliding, *Journal of Geophysical Research: Earth Surface*, *115*, doi:10.1029/2009JF001463.

Blume, T., E. Zehe, and A. Bronstert (2007), Rainfall—runoff response, event-based runoff coefficients and hydrograph separation, *Hydrological Sciences Journal*, *52*(5), 843–862, doi:10.1623/hysj.52.5.843.

Brutsaert, W. (2005), *Hydrology: An Introduction*, Cambridge University Press.

Buttle, J., P. Dillon, and G. Eerkes (2004), Hydrologic coupling of slopes, riparian zones and streams: an example from the Canadian Shield, *Journal of Hydrology*, *287*(1–4), 161 – 177, doi:10.1016/j.jhydrol.2003.09.022.

Chapman, T. (1999), A comparison of algorithms for stream flow recession and baseflow separation, *Hydrological Processes*, *13*(5), 701–714, doi:10.1002/(SICI)1099-1085(19990415)13:5<701::AID-HYP774>3.0.CO;2-2.

Detty, J. M., and K. J. McGuire (2010a), Threshold changes in storm runoff generation at a till-mantled headwater catchment, *Water Resources Research*, *46*(7), doi:10.1029/2009WR008102.

Detty, J. M., and K. J. McGuire (2010b), Topographic controls on shallow groundwater dynamics: implications of hydrologic connectivity between hillslopes and riparian zones in a till mantled catchment, *Hydrological Processes*, *24*(16), 2222–2236, doi:10.1002/hyp.7656.

Fu, C., J. Chen, H. Jiang, and L. Dong (2013a), Threshold behavior in a fissured granitic catchment in southern China: 2. Modeling and uncertainty analysis, *Water Resources Research*, *49*(5), 2536–2551, doi:10.1002/wrcr.20193.

Bibliography

Fu, C., J. Chen, H. Jiang, and L. Dong (2013b), Threshold behavior in a fissured granitic catchment in southern China: 1. Analysis of field monitoring results, *Water Resources Research*, *49*(5), 2519–2535, doi:10.1002/wrcr.20191.

Graham, C. B., and J. J. McDonnell (2010), Hillslope threshold response to rainfall: (2) Development and use of a macroscale model, *Journal of Hydrology*, *393*(1–2), 77 – 93, doi:10.1016/j.jhydrol.2010.03.008.

Graham, C. B., R. A. Woods, and J. J. McDonnell (2010), Hillslope threshold response to rainfall: (1) A field based forensic approach, *Journal of Hydrology*, *393*(1–2), 65 – 76, doi:10.1016/j.jhydrol.2009.12.015.

Guebert, M. D., and T. W. Gardner (2001), Macropore flow on a reclaimed surface mine: infiltration and hillslope hydrology, *Geomorphology*, *39*(3–4), 151 – 169, doi:10.1016/S0169-555X(00)00107-0.

Haga, H., Y. Matsumoto, J. Matsutani, M. Fujita, K. Nishida, and Y. Sakamoto (2005), Flow paths, rainfall properties, and antecedent soil moisture controlling lags to peak discharge in a granitic unchanneled catchment, *Water Resources Research*, *41*(12), doi:10.1029/2005WR004236.

Hewlett, J., and A. Hibbert (1967), Factors affecting the response of small watersheds to precipitation in humid areas, *Forest hydrology*, pp. 275–290.

Hopp, L., and J. McDonnell (2009), Connectivity at the hillslope scale: Identifying interactions between storm size, bedrock permeability, slope angle and soil depth, *Journal of Hydrology*, *376*(3–4), 378 – 391, doi:10.1016/j.jhydrol.2009.07.047.

Ingelrest, F., G. Barrenetxea, G. Schaefer, M. Vetterli, O. Couach, and M. B. Parlange (2010), SensorScope: Application-Specific Sensor Network for Environmental Monitoring, *ACM Trans. Sen. Netw.*, *6*(2), 1–32, doi:10.1145/1689239.1689247.

James, A., and N. Roulet (2009), Antecedent moisture conditions and catchment morphology as controls on spatial patterns of runoff generation in small forest catchments, *Journal of Hydrology*, *377*(3–4), 351 – 366, doi:10.1016/j.jhydrol.2009.08.039.

James, A. L., and N. T. Roulet (2007), Investigating hydrologic connectivity and its association with threshold change in runoff response in a temperate forested watershed, *Hydrological Processes*, *21*(25), 3391–3408, doi:10.1002/hyp.6554.

Latron, J., and F. Gallart (2008), Runoff generation processes in a small Mediterranean research catchment (Vallcebre, Eastern Pyrenees), *Journal of Hydrology*, *358*(3–4), 206 – 220, doi:10.1016/j.jhydrol.2008.06.014.

Lehmann, P., C. Hinz, G. McGrath, H. J. Tromp-van Meerveld, and J. J. McDonnell (2007), Rainfall threshold for hillslope outflow: an emergent property of flow pathway connectivity, *Hydrology and Earth System Sciences*, *11*(2), 1047–1063, doi:10.5194/hess-11-1047-2007.

Lin, H. (2010), Linking principles of soil formation and flow regimes, *Journal of Hydrology*, *393*(1–2), 3 – 19, doi:10.1016/j.jhydrol.2010.02.013.

Lunati, I., F. Ciocca, and M. B. Parlange (2012), On the use of spatially discrete data to compute energy and mass balance, *Water Resources Research*, *48*(5), doi:10.1029/2012WR012061.

Matsushi, Y., and Y. Matsukura (2007), Rainfall thresholds for shallow landsliding derived from pressure-head monitoring: cases with permeable and impermeable bedrocks in Boso Peninsula, Japan, *Earth Surface Processes and Landforms*, *32*(9), 1308–1322, doi:10.1002/esp.1491.

McCutchan, H., and K. Shackel (1992), Stem-water potential as a sensitive indicator of water stress in prune trees (*Prunus domestica* L. cv. French), *Journal of the American Society for Horticultural Science*, *117*(4), 607–611, doi:117(4):607-611.

McDonnell, J. J. (1990), A rationale for old water discharge through macropores in a steep, humid catchment, *Water Resources Research*, *26*(11), 2821–2832, doi:10.1029/WR026i011p02821.

McDonnell, J. J. (2003), Where does water go when it rains? Moving beyond the variable source area concept of rainfall-runoff response, *Hydrological Processes*, *17*(9), 1869–1875, doi:10.1002/hyp.5132.

McNamara, J. P., D. L. Kane, and L. D. Hinzman (1997), Hydrograph separations in an arctic watershed using mixing model and graphical techniques, *Water Resources Research*, *33*(7), 1707–1719, doi:10.1029/97WR01033.

Mualem, Y. (1976), A new model for predicting the hydraulic conductivity of unsaturated porous media, *Water Resources Research*, *12*(3), 513–522, doi:10.1029/WR012i003p00513.

Noguchi, S., Y. Tsuboyama, R. C. Sidle, and I. Hosoda (2001), Subsurface runoff characteristics from a forest hillslope soil profile including macropores, Hitachi Ohta, Japan, *Hydrological Processes*, *15*(11), 2131–2149, doi:10.1002/hyp.278.

Parlange, J.-Y. (1976), Capillary hysteresis and the relationship between drying and wetting curves, *Water Resources Research*, *12*(2), 224–228, doi:10.1029/WR012i002p00224.

Penna, D., M. Borga, D. Norbiato, and G. D. Fontana (2009), Hillslope scale soil moisture variability in a steep alpine terrain, *Journal of Hydrology*, *364*(3–4), 311 – 327, doi:10.1016/j.jhydrol.2008.11.009.

Penna, D., H. J. Tromp-van Meerveld, A. Gobbi, M. Borga, and G. Dalla Fontana (2011), The influence of soil moisture on threshold runoff generation processes in an alpine headwater catchment, *Hydrology and Earth System Sciences*, *15*(3), 689–702, doi:10.5194/hess-15-689-2011.

Bibliography

Penna, D., H. J. van Meerveld, O. Oliviero, G. Zuecco, R. S. Assendelft, G. Dalla Fontana, and M. Borga (2014), Seasonal changes in runoff generation in a small forested mountain catchment, *Hydrological Processes*, p. *in press*, doi:10.1002/hyp.10347.

Sidle, R. C., S. Noguchi, Y. Tsuboyama, and K. Laursen (2001), A conceptual model of preferential flow systems in forested hillslopes: evidence of self-organization, *Hydrological Processes*, *15*(10), 1675–1692, doi:10.1002/hyp.233.

Spence, C. (2010), A paradigm shift in hydrology: Storage thresholds across scales influence catchment runoff generation, *Geography Compass*, *4*(7), 819–833, doi:10.1111/j.1749-8198.2010.00341.x.

Spence, C., and M.-k. Woo (2003), Hydrology of subarctic Canadian shield: soil-filled valleys, *Journal of Hydrology*, *279*(1–4), 151 – 166, doi:10.1016/S0022-1694(03)00175-6.

Sujono, J., S. Shikasho, and K. Hiramatsu (2004), A comparison of techniques for hydrograph recession analysis, *Hydrological Processes*, *18*(3), 403–413, doi:10.1002/hyp.1247.

Szilagyi, J. (1999), On the use of semi-logarithmic plots for baseflow separation, *Ground Water*, *37*(5), 660–662, doi:10.1111/j.1745-6584.1999.tb01157.x.

Szilagyi, J., and M. B. Parlange (1998), Baseflow separation based on analytical solutions of the Boussinesq equation, *Journal of Hydrology*, *204*(1–4), 251 – 260, doi:10.1016/S0022-1694(97)00132-7.

Tani, M. (1997), Runoff generation processes estimated from hydrological observations on a steep forested hillslope with a thin soil layer, *Journal of Hydrology*, *200*(1–4), 84 – 109, doi:10.1016/S0022-1694(97)00018-8.

Tetzlaff, D., J. J. McDonnell, S. Uhlenbrook, K. J. McGuire, P. W. Bogaart, F. Naef, A. J. Baird, S. M. Dunn, and C. Soulsby (2008), Conceptualizing catchment processes: simply too complex?, *Hydrological Processes*, *22*(11), 1727–1730, doi:10.1002/hyp.7069.

Torres, R. (2002), A threshold condition for soil-water transport, *Hydrological Processes*, *16*(13), 2703–2706, doi:10.1002/hyp.5060.

Torres, R., W. E. Dietrich, D. R. Montgomery, S. P. Anderson, and K. Loague (1998), Unsaturated zone processes and the hydrologic response of a steep, unchanneled catchment, *Water Resources Research*, *34*(8), 1865–1879, doi:10.1029/98WR01140.

Tromp-van Meerveld, H. J., and J. J. McDonnell (2006a), Threshold relations in subsurface stormflow: 2. The fill and spill hypothesis, *Water Resources Research*, *42*(2), doi:10.1029/2004WR003800.

Tromp-van Meerveld, H. J., and J. J. McDonnell (2006b), Threshold relations in subsurface stormflow: 1. A 147-storm analysis of the Panola hillslope, *Water Resources Research*, *42*(2), doi:10.1029/2004WR003778.

Van Genuchten, M. T. (1980), A closed-form equation for predicting the hydraulic conductivity of unsaturated soils, *Soil Science Society of America Journal*, *44*, 892–898, doi:10.2136/sssaj1980.03615995004400050002x.

von Freyberg, J., D. Radny, H. E. Gall, and M. Schirmer (2014), Implications of hydrologic connectivity between hillslopes and riparian zones on streamflow composition, *Journal of Contaminant Hydrology*, *169*(0), 62 – 74, doi:http://dx.doi.org/10.1016/j.jconhyd.2014.07.005.

Western, A. W., and R. B. Grayson (1998), The Tarrawarra Data Set: Soil moisture patterns, soil characteristics, and hydrological flux measurements, *Water Resources Research*, *34*(10), 2765–2768, doi:10.1029/98WR01833.

Western, A. W., G. Blöschl, and R. B. Grayson (1998), Geostatistical characterisation of soil moisture patterns in the Tarrawarra catchment, *Journal of Hydrology*, *205*(1–2), 20 – 37, doi:10.1016/S0022-1694(97)00142-X.

Western, A. W., R. B. Grayson, G. Blöschl, G. R. Willgoose, and T. A. McMahon (1999), Observed spatial organization of soil moisture and its relation to terrain indices, *Water Resources Research*, *35*(3), 797–810, doi:10.1029/1998WR900065.

Western, A. W., G. Blöschl, and R. B. Grayson (2001), Toward capturing hydrologically significant connectivity in spatial patterns, *Water Resources Research*, *37*(1), 83–97, doi:10.1029/2000WR900241.

Wittenberg, H. (1999), Baseflow recession and recharge as nonlinear storage processes, *Hydrological Processes*, *13*(5), 715–726, doi:10.1002/(SICI)1099-1085(19990415)13:5<715::AID-HYP775>3.0.CO;2-N.

Zehe, E., and M. Sivapalan (2009), Threshold behaviour in hydrological systems as (human) geo-ecosystems: manifestations, controls, implications, *Hydrology and Earth System Sciences*, *13*(7), 1273–1297, doi:10.5194/hess-13-1273-2009.

Zhang, Y., H. Wei, and M. A. Nearing (2011), Effects of antecedent soil moisture on runoff modeling in small semiarid watersheds of southeastern Arizona, *Hydrology and Earth System Sciences*, *15*(10), 3171–3179, doi:10.5194/hess-15-3171-2011.

6 Conclusions and Future Work

This dissertation focused on investigating streamflow generation processes in a high altitude alpine catchment. Particular attention was paid to the influence of the basin geomorphology on stormflow generation, recession curves and diurnal streamflow cycles. To that end, a one meter resolution DEM was acquired and an ambitious field observation campaign was undertaken in the upper Val Ferret area. A wireless network of automatic meteorological stations was deployed and the streamflow was measured at three different sites during three consecutive summers.

In Chapter 2, we showed that the channel network carefully monitored on site was spatially very heterogeneous and that none of the classical channel network extraction methods were able to reproduce complex features of the channel network. We analyzed in detail the travel time distribution of water in the catchment during storm flow in the framework of the Rescaled Width Function and showed that the drainage network had a non negligible influence on the modeled storm hydrograph. Even though the classical methods were able to reproduce the amplitude and timing of the streamflow peak satisfactorily, the discrepancies with the hydrograph obtained with the monitored network were larger for the receding part of the events.

Recession events were also analyzed in Chapter 3, we showed that recession curves bear the signature of a basin geomorphology. Based on a recent study, we proposed a new conceptual recession model that accounts for spatially varying drainage density. Therein, the discharge variation is linked to the area draining directly in a time varying channel network. The discharge and DEM of the Val Ferret and 26 other catchments were analyzed in detail with this conceptual model. Our results show that the modifications proposed by the new model are of utter importance for high altitude catchments where heterogeneous drainage densities are the rule rather than the exception. Moreover, the new model is of great interest for prediction of low flow regimes in poorly gauged mountainous basins given that it is based solely on the analysis of the DEM.

In Chapter 4, we examined glacier-fed ice melt and evaporation-induced diurnal streamflow

cycles observed during recession events in two monitored sub basins of the Val Ferret watershed. The melt and evaporation induced diurnal streamflow variations occurred at similar times of the day, but with perturbations in opposite directions. Comparisons between the water deficit of the diurnal cycles and evaporation measured at an eddy covariance station revealed that the area contributing to the evaporation cycle could be attributed to the riparian area of the perennial network. In the other sub basin where ice melt was dominant throughout the campaign, we assessed how much ice must have melted to give the observed signal if evaporation in the riparian area would damp the ice melt dominated streamflow cycle. Our results suggests that damping of the ice melt cycle by the evaporation cycle is not negligible and that the perennial part of the network plays a significant role in daily fluctuations of the streamflow during recession events.

Finally, in Chapter 5, we studied the influence of antecedent soil moisture and soil water potential on streamflow generation by analyzing the data from the wireless sensor network. We observed a clear threshold behavior between antecedent soil water potential and runoff coefficients for 83% of all the monitored sites. The stations were deployed at representative sites of the catchment in terms of elevation, slope and aspect, such that confident speculations can be made that the observed threshold behavior can be attributed to the entire watershed. However, the observed threshold values varied both in space and depth. Above this threshold, the runoff coefficients were larger and the response time of the watershed shorter. Unlike many recent studies, we did not observe a threshold behavior between antecedent soil moisture and runoff coefficients. However, our results are hampered 1) by the measurable range of the sensor used to measure soil water potential, which does not operate close to saturation and 2) by some very small year to year variability of the soil sensors deployment locations in the vicinity of each meteorological stations. The soil moisture measurements were more sensitive to these small deployment inconsistencies. Nonetheless, our results tend to show that hysteresis effects in the soil water retention curve might play a dominant role in the subsurface streamflow generation mechanisms, which is a debated and intensively investigated topic in the hydrological community.

The results from Chapters 2-4 underline the importance of accurately representing the channel network of the watershed. In particular, the differentiation between the perennial and intermittent parts of the network was instrumental to the conclusions drawn from the analysis of the evaporation-induced diurnal streamflow cycle. However, the extraction of the drainage network is often overlooked by hydrologists in their journey of modeling a catchment with spatially distributed models. This step is usually performed once, but the sensitivity and uncertainty of the model to the stream network is seldom studied.

Many questions and new research opportunities have arisen from this dissertation. We have shown that the soil water potential was a key descriptor in the processes happening at both the hillslope and catchment scale. However, we did not fully conclude what physical processes lead to such threshold behavior. Unfortunately, due to the lack of information concerning the soil thickness and topography of the soil-bedrock interface, we could not complete *forensic* in-

vestigations on subsurface streamflow generation processes. Possible links between proposed mechanisms (i.e., fill spill hypothesis or connectivity of lateral preferential flowpaths) need to be explored in future studies. However, we strongly suggest future deployments in hillslope or catchment hydrology to deploy tensiometers more systematically, given that our results point out some strong hysteresis behavior at the hillslope scale.

In the quest of upscaling observed threshold behaviors at the hillslope scale to the catchment scale, hydrological connectivity will be or is already a major source of research in catchment hydrology. The model proposed in Chapter 3 needs to be investigated and tested in more detail as it has large potential for studying hydrological connectivity at the catchment scale. Further research will be needed to study the spatio-temporal dynamics of the channel network. A suggested strategy is to relax certain assumptions made in the geomorphological recession model, especially the hypothesis concerning the spatially uniform recession speed of the channel network. The increasing use of drones, possibly equipped with Infra-red cameras for riparian zone monitoring, or the deployment of optical fibers to measure the temperature as a proxy of the stream state (i.e. wet or dry) could open new possibilities in catchment hydrology. This is in line with important ongoing efforts toward mapping and understanding the dynamics of the perennial part of the stream network. This could, for instance, give us more insights into the spatial patterns of storage at the catchment scale.

A Other Author's Contribution

Electrical conductivity in rating curves of alpine streams

This study is based on streamflow measurements undertaken in the Val Ferret watershed and aims at establishing rating curves based on water level and/or water electrical conductivity. The results have been published with the following citation:

Weijs S.V, Mutzner R. and Parlange M.B, **2013**: Could electrical conductivity replace water level in rating curves for alpine streams? *Water Resources Research, 49,* 1-9. doi: 10.1029/2012WR012181

Could electrical conductivity replace water level in rating curves for alpine streams?

Steven V. Weijs,[1] Raphaël Mutzner,[1] and Marc B. Parlange[1]

[1] Streamflow time series are important for inference and understanding of the hydrological processes in alpine watersheds. Because streamflow is expensive to continuously measure directly, it is usually derived from measured water levels, using a rating curve modeling the stage-discharge relationship. In alpine streams, this practice is complicated by the fact that the streambed constantly changes due to erosion and sedimentation by the turbulent mountain streams. This makes the stage-discharge relationship dynamic, requiring frequent discharge gaugings to have reliable streamflow estimates. During an ongoing field study in the Val Ferret watershed in the Swiss Alps, 93 streamflow values were measured in the period 2009–2011 using salt dilution gauging with the gulp injection method. The natural background electrical conductivity in the stream, which was measured as by-product of these gaugings, was shown to be a strong predictor for the streamflow, even marginally outperforming water level. Analysis of the residuals of both predictive relations revealed errors in the gauged streamflows. These could be corrected by filtering disinformation from erroneous calibration coefficients. In total, extracting information from the auxiliary data enabled to reduce the uncertainty in the rating curve, as measured by the root-mean-square error in log-transformed streamflow relative to that of the original stage-discharge relationship, by 43.7%.

1. Introduction

[2] Streamflow, as a spatially integrated watershed response, is one of the most important inputs for hydrological modeling [*Brutsaert and Nieber*, 1977; *Szilagyi et al.*, 1998]. Because of the difficulties of continuously measuring streamflow (Q) directly in an inexpensive and simple way, streamflow records are often based on permanent measurements of water levels (h), sometimes even obtained remotely [*Liebe et al.*, 2009], in combination with a stage-discharge relation, $Q(h)$. The stage-discharge relation is based on regular gaugings in different conditions. In the case of fixed structures, like flumes, $Q(h)$ is well defined and can also be derived theoretically, while in more natural situations, the relationship needs to be calibrated and can be influenced by, for example, vegetation or sediment dynamics.

[3] The role of dynamic morphology is especially important in alpine watersheds, where the streams are never lying quietly in their beds, but constantly changing them under the influence of the steep gradients and turbulent erosion of the sediments. Together with the often hard to reach locations and challenging conditions, this makes it difficult to monitor streamflow in alpine watersheds. The resulting uncertainty in streamflow records has a negative impact on hydrological modeling, especially because it is often not explicitly accounted for.

[4] One remedy to reduce the impact of uncertainties on hydrological modeling is to quantify the uncertainties in the discharge signal, so that the model knows what it can learn from the data and what it cannot learn. Over the last decade, significant progress has been made to address uncertainties in the data (both input and output) and models [*Ciach and Krajewski*, 1999; *Anagnostou et al.*, 1999; *Szilagyi and Parlange*, 1999; *Vrugt et al.*, 2005; *Kavetski et al.*, 2006; *Thyer et al.*, 2009; *Di Baldassarre and Montanari*, 2009; *Schoups and Vrugt*, 2010; *Kuczera et al.*, 2010; *Kampf and Burges*, 2010; *Westerberg et al.*, 2011]. Other approaches focused on including observational uncertainties in information theoretical evaluation criteria for probabilistic forecasts [*Weijs and Van de Giesen*, 2011] and provided arguments why explicitly representing uncertainties in the model and data formulation and calibrating with information-theoretical measures has advantages from a philosophy of science viewpoint [*Weijs et al.*, 2010]. Because using the same information twice can be logically inconsistent, it might be important to formulate models for the data uncertainty independently of the formulation of hydrological models. In the case of discharge measurements, this means replacing a simple curve representing the stage discharge relationship by a probabilistic

---

[1]School of Architecture Civil and Environmental Engineering, École Polytechnique Fédérale de Lausanne, Lausanne, Switzerland.

Corresponding author: S. V. Weijs, School of Architecture, Civil and Environmental Engineering, École Polytechnique Fédérale de Lausanne, EPFL Station 2, Bat. GR, CH-1015 Lausanne, Switzerland. (steven.weijs@epfl.ch)

model that may employ several sources of information for estimating streamflow and its uncertainty.

[5] In this paper, we investigate the potential for stream water natural electrical conductivity (EC), measured before each of the 93 discharge gaugings, as an auxiliary information source for improving streamflow estimates in morphologically dynamic alpine streams. For our study area, we found the natural EC to have a predictive power for the measured streamflow comparable to that of water level. When a single relation was sought for the entire 3 year measurement period, the stage-discharge relationship was even slightly outperformed by the EC-streamflow relationship.

[6] Although strong relations between EC and streamflow have been observed before [*Collins*, 1979; *Collins and Young*, 1981; *Gurnell and Fenn*, 1985; *Evans and Davies*, 1998; *Duffy and Cusumano*, 1998; *Dzikowski and Jobard*, 2011], its potential for improving streamflow records has, to our knowledge, not been discussed. Although these relations are often complex, with lags and hysteresis, we focus on simple models that can be derived without continuous data. An extensive review of possible mechanisms at work behind the relations is therefore outside the scope of this paper but can be found in the aforementioned references. Since methods for explicitly incorporating output (streamflow) uncertainty in hydrological models are advancing and probabilistic treatment of uncertainties in a Bayesian framework has the potential of optimally combining various sources of information, we believe that future more extensive continuous measurements of EC have the potential to improve streamflow records and advance understanding of alpine hydrology.

2. Site, Data, and Methods

2.1. Val Ferret Watershed

[7] Val Ferret, situated in the Swiss canton of Valais, is an alpine valley draining into the Dranse de Ferret, the Dranse, and eventually the Rhone. The area of study measures around 20 km^2 and ranges in elevation between 1775 m above sea level (asl) to 3206 m asl, with a mean of 2423 m asl. The slopes are moderate to steep (mean 31.6°, maximum 88.9°) and partly soil mantled. Vegetation is mainly grasses while some patches of firs are found at lower elevations. The river is partly fed by the melt of the small glacier des Angroniettes in the upper part of the catchment. See *Simoni et al.* [2011] for a more detailed description of the study site. The streamflow shows a regular diurnal signal, which gradually decreases in amplitude going from spring to autumn. Also, the average flow itself shows this decreasing trend over the season, suggesting a snow melt-dominated flow regime in spring, gradually changing to a signal of groundwater outflow recession curves, a small diurnal signal from glacier melt, and response to rainfall events. The main stream has a bankfull width of around 4 m and an average bed slope of 5% around the measurement location. The bed material consists mostly of rocks and pebbles of 5–30 cm, with some finer sediments deposited in the stiller pools, especially after flood events. The morphology around the measurement point is braided, while more upstream, the stream is confined to a narrow gorge, with some small waterfalls occurring.

2.2. Water Level Measurements

[8] Water levels of the stream were monitored at the outlet of the studied catchment, at the bridge at l'Ars Dessus. They were recorded using a pressure sensor with logger, placed close to the bank, 1 m upstream from the bridge, where the water is fairly stagnant. During winter, reliable measurements are unavailable due to snow and ice blockage. The embankments under the bridge are stabilized, constraining the stream width, while the river bed consists of rocks and finer sediments that can be moved by the water. The time series have a temporal resolution of one sample per minute. For use in the rating curve, averages over a window of 60 min, centered around the salt peak, are used. The standard deviations within these windows are shown in Figure 1.

2.3. Streamflow Measurements Using Salt Dilution Gauging

[9] To measure streamflow, salt dilution gaugings, using the slug injection method [*Day*, 1976; *Kite*, 1993; *Moore*, 2005], are taken regularly under different flow conditions. In total, we took into account 93 gaugings from the year 2009 to 2011. By injecting a known mass of salt M, usually 5 or 10 kg, and measuring the concentration of injected salt 210 m downstream as a function of time, $c(t)$, we obtained the streamflow, Q, using

$$Q = \frac{M}{\int_0^\infty c(t)\mathrm{d}t}. \tag{1}$$

The measurement is cut off by the time the injected salt concentration is within the measurement accuracy, i.e., when the total ionic concentration is indistinguishable from the natural ionic concentration. Because this is relatively short (in our case, usually around 15 min) compared to the timescale of variation in the natural background concentration, we can assume the latter to be constant during the measurement. Another assumption behind the method is that, the concentration we measure downstream at time t is representative for the ratio between the mass of salt that passes the cross section and the volume of water passing the cross section. In other words, the salt should be well mixed within the cross section or the places in the cross-section with different concentration do not contribute to the flow significantly.

2.3.1. Calibration Procedure

[10] The time-varying signal of the injected salt concentration, $c(t)$, cannot be measured directly. Instead, the EC $\sigma(t)$ of the water is measured by means of an alternating current. In the range of measurement, the (temperature compensated) EC has a linear relation with the salt concentration, which is calibrated on site before the gauging by repeatedly pipetting 1 ml of calibration solution (10 g/L) into 500 mL of water from the stream. This results in linear relations of the form:

$$c(t) = \kappa[\sigma(t) - \sigma_b(t)], \tag{2}$$

where $\sigma_b(t)$ is the natural conductivity or base conductivity of the stream, which depends on the natural ionic concentrations in the stream water, and κ is the linear calibration
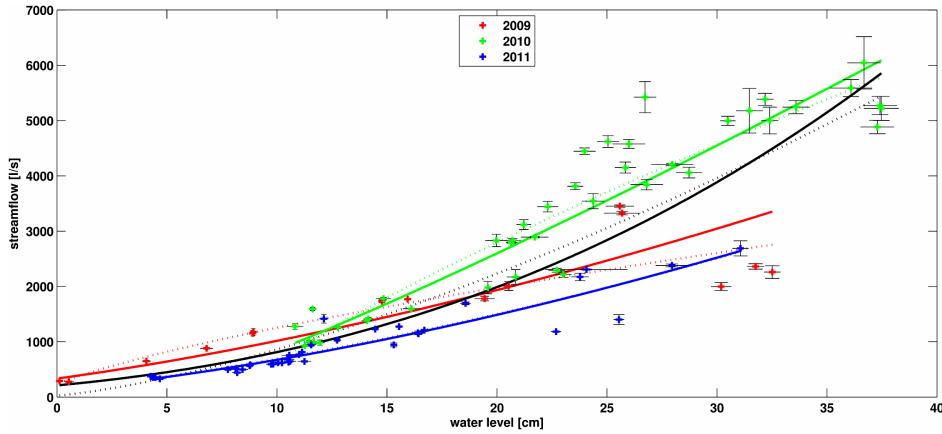
Figure 1. Stage-discharge rating curves for the different years and for all years combined (black). The dotted lines indicate those fitted with a homoscedastic Gaussian error model (least squares in linear space), while the solid lines are fitted to log$Q$, which is consistent with a more realistic heteroscedastic lognormal error model. The horizontal error bars give the $\pm$ one standard deviation of the water level in a 60 min window centered around the time of the Q-gauging, while the vertical error bars give the Q values determined from the two independent probes.

coefficient with unit $(mg/L)/(\mu S/cm)$. The calibrations have coefficients of determination R^2 close to one, with a minimum of 0.98 over all calibrations.

[11] For the salt dilution gaugings, we used the MRS-4, by Sommer mess–systemtechnik, a device with a built-in capability of integrating the signal and calculating the streamflow. The device has two EC probes, which were placed at different points in one cross-section to check the cross-sectional mixing. For each probe, the calibration and streamflow calculation is done independently, resulting in two streamflow values. The device stores the raw EC data at a 1 s sampling rate and some auxiliary data, including the individual calibration points, probe temperatures, and the natural EC of the stream σ_b at the time before the gauging. These data are used for the analysis in this paper.

2.4. Stage-Discharge Model

[12] Traditionally, the $Q(h)$ relation is modeled as a power function, which is often fitted with least squares [*Singh*, 2010]:

$$Q(h) = \alpha(h - h_0)^\beta, \qquad (3)$$

$$\alpha, \beta, h_0 = \arg\min_{\alpha,\beta,h_0}\left[\sum_{i=1}^{n}(Q(h_{obs}(t_i), \alpha, \beta, h_0) - Q_{obs}(t_i))^2\right], \quad (4)$$

where α, β, and h_0 are the parameters of the $Q(h)$-relation, $h_{obs}(t_i)$ and $Q_{obs}(t_i)$ are the observed water level and calculated discharge during the gauging number i at time t_i. This assumption of least squares is equivalent to assuming independent and identically distributed (iid) Gaussian errors. In the case of streamflow measurements, heteroscedastic errors are usually a better description, as uncertainties in the gaugings tend to grow with discharge [*Sorooshian and Dracup*, 1980]. A heteroscedastic error model was achieved by finding a least-squared fit on the log-transformed discharge, implicitly assuming a Gaussian uncertainty in the

log-transformed discharge, i.e., a lognormal error in discharge. Furthermore, this serves to avoid assigning probability to negative streamflow values, as is the case with the Gaussian error assumption underlying equation (4). Figure 1 shows the rating curves for fitting Q (lin) and log Q (log) with least squares, with the corresponding equations and R^2 values listed in Table 1. The residuals of both lin and log fits were checked for normality using QQ-plots (not shown) and the Shapiro-Wilk test. The p value for that test gives the maximum confidence level (accepted probability of falsely rejecting) at which one would not reject the null hypothesis that the residuals are normally distributed with unknown mean and variance. This indicated that the log-transformed Gaussian error model is satisfactory ($p = 0.08$), while the linear is less so ($p < 0.001$).

2.5. EC Measurements and Model

[13] The measurements of EC in the stream were obtained as a by-product of the salt dilution gaugings used to determine discharge. The EC measured in the stream before injecting the salt varied from gauging to gauging and reflects changes in the natural ionic composition in the stream. This resulted in 93 measured EC values at the outlet of the study catchment, spread over the years 2009–2011.

[14] To use EC as predictor, its relation to streamflow must be modeled. The behavior of EC as function of

Table 1. Parameters and Coefficients of Determination for $Q(h)^a$

	Lin				Log			
	2009	2010	2011	All	2009	2010	2011	All
α	227.4	386.4	9.75	25.28	9.79	102.6	7.93	0.14
β	0.71	0.80	1.56	1.47	1.56	1.16	1.61	2.69
h_0	1.08	−8.19	5.50	1.00	9.62	−3.85	5.77	15.38
R^2	0.77	0.90	0.87	0.80	0.90	0.92	0.91	0.87

^{a}Curves of the form $Q = \alpha(h - h_0)^\beta$ as depicted in Figure 1.
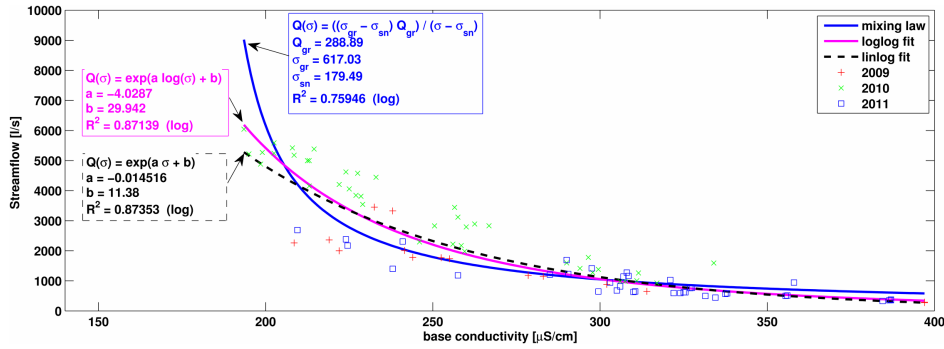
Figure 2. Three different relationships fitted to describe the EC-streamflow relationship. The mixing law employs a two reservoir mixing model, the "linlog" fit is a linear regression model between σ and $\log Q$ (see Figure 6). The "loglog" fit is a linear regression model between $\log \sigma$ and $\log Q$.

streamflow has been investigated previously, mainly in the field of glaciology, where EC measurements have been used to distinguish between subglacial and englacial contributions to flow at proglacial streams. *Gurnell and Fenn* [1985] studied the relation between EC and streamflow in a Swiss alpine valley relatively close to our field site and considered different spatial and temporal sampling strategies, focusing mostly on a location relatively closer to the glacier snout. They reported an R^2 value of 0.91 for a linear relation predicting EC from the logarithm of the streamflow for hourly values measured in June and July 1978. *Collins* [1979] noted a similar inverse relation between the diurnal cycles of streamflow and those of EC for two alpine proglacial streams and tried to separate different flow components based on a mixing model. Recently, such mixing models were further investigated in relation to measurements taken in a French high-alpine valley [*Dzikowski and Jobard*, 2011].

[15] Since our interest is primarily in obtaining estimates of streamflow and not enough data are available to formulate mechanistic models, we focused on simple empirical relationships. For comparison, we also considered a simple conceptual two member mixing model and fitted the parameters empirically. The limited temporal resolution and spatial extent of the EC data precluded more detailed analysis of the true mixing processes, full ionic composition, or sources of solutes, which could possibly lead to more

accurate models [see, e.g., *Walter et al.*, 2007; *Salmon et al.*, 2001; *Botter et al.*, 2008, 2009; *Duffy*, 2010].

3. Results

[16] For the fit on the entire data set, Figure 2 shows different alternative functional relations. The mixing law relation is a conceptual model in which a constant, high EC groundwater outflow is mixed with a varying flow of low EC water from, e.g., snow melt or rainfall fast runoff. The empirical logarithmic relationship and the power law have a significantly better fit than the two-reservoir mixing model. As more distributed measurements of streamflow and EC of the different contributing water sources will become available after continued field campaigns, it will be interesting to find a better conceptual model capturing the (dynamic) relationship, possibly enhancing generalization.

[17] The quantile-quantile plots in Figure 3, which compare the distribution of errors around the curve to a normal distribution, show that the heteroscedastic error model for Q, which assumes Gaussian errors in $\log Q$, is more realistic than least squares on Q when checked a posteriori. This indicates that a least squares fit on log-transformed streamflow is the preferred method of inference on a relationship and that a heteroscedastic error model of this type can be used to describe the "measurement" uncertainty in a
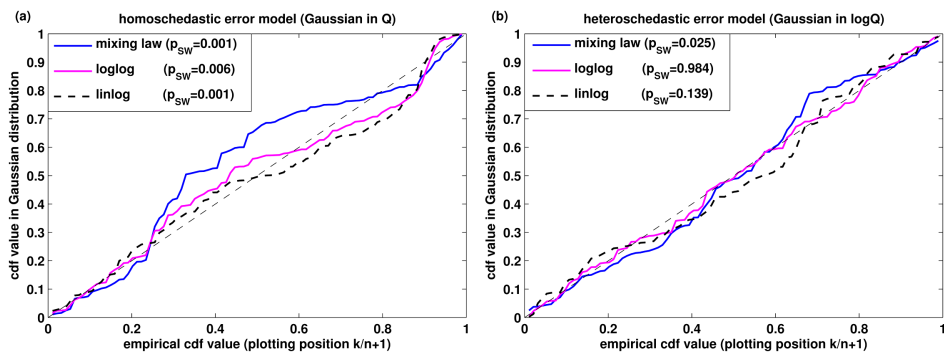
Figure 3. The quantile plots for the relations shown in Figure 2. The fit on (b) $\log Q$ matches better with the Gaussian error assumption than the fit on (a) Q directly, as can be seen by the p values of the Shapiro-Wilk normality test shown in the legend.

4
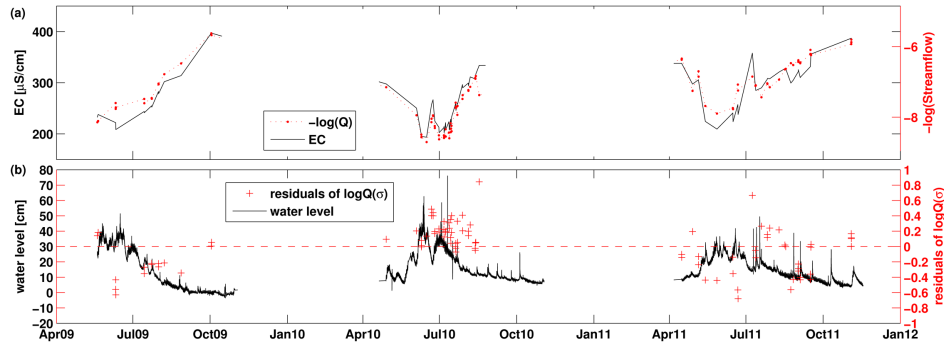
Figure 4. (a) Streamflow and EC over 3 years, with *y* axes matched according to the linear regression. (b) Residuals of regression for $Q(\sigma)$, alongside water level.

streamflow time series derived from continuous EC measurements. It also confirms that the R^2 values calculated on the log-transformed streamflow are adequate measures of predictive power or mutual information.

[18] Figure 4 shows that the slow fluctuations and the higher frequency fluctuations between streamflow and EC follow each other (note that the negative log of streamflow is plotted to obtain equal signs). Figure 4b shows the residuals of the logarithmic $Q(\sigma)$ relation next to the measured water level and is intended to reveal whether residuals are associated with certain hydrological events. Apart from the consistent underprediction during 2010, there is no obvious pattern in the data, although future analysis in conjunction with meteorological data might reveal further relationships. The residuals were also plotted against time of year, time of day, and water temperature (not shown), but this did not reveal any patterns or correlations to explain them.

[19] When looking at the residuals of the linear relation between $\log Q$ and σ on the one hand and of the relation between $\log Q$ and $\log h$ on the other, it appears that both series of residuals are correlated. Furthermore, a clustering is visible of the results of different years; see Figures 4 and 5. This is particularly interesting, since the information provided by water level and EC would be expected to be more or less independent. Possible explanations are discussed in the next section, which also proposes a correction to the measurements of Q that partly solves the problem of correlated residuals (right-hand side of Figure 5). An
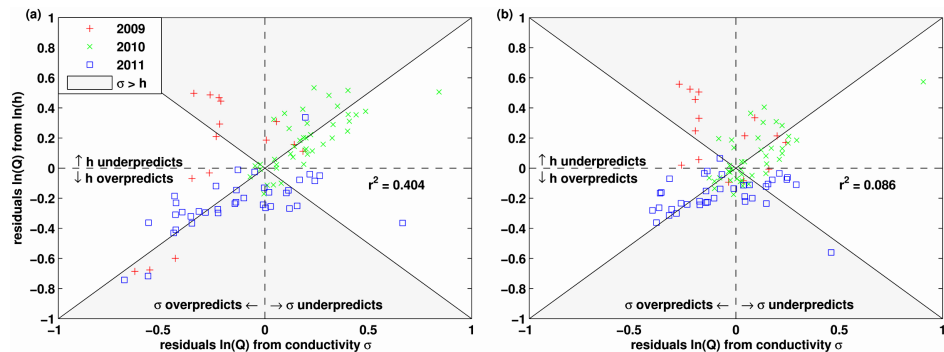
overview of the coefficients of determination for the relations is given in Table 2. Note that the $Q(\sigma)$ relation outperforms $Q(h)$ for the complete dataset, probably indicating that performance of $Q(h)$ is affected by interannual morphological shifts in the river bed.

4. Discussion

[20] The general inverse relationship between Q and σ seems consistent with the conceptual idea of the functioning of the catchment, where a relatively constant, solute-enriched base flow is mixed with a fluctuating low ion content flow from snow melt or rainfall response. From Figure 4, it can be seen that the EC follows the seasonal pattern of streamflow, which is mainly caused by snow melt. While a hyperbolic relationship may be physically more plausible, we found the logarithmic $Q(\sigma)$ relationship to have the most predictive power. This result is in accordance with a relation found by *Gurnell and Fenn* [1985] in a similar watershed. To obtain more insight into the dynamics and finding possible explanations for the logarithmic relationship in Val Ferret, continuous EC measurements are currently ongoing.

4.1. Analysis of Residuals

[21] The relatively high correlation between the residuals, depicted in Figure 5 on the left, is quite surprising and somewhat suspicious. Since relations between deviations in

Figure 5. (a) Relation between the residuals in predicting $\log Q$ from $\log h$ on the one hand and $\log Q$ from σ on the other, the gray area indicates σ performs best. (b) Same, after the correction of Q to $Q^{\star}$, as proposed in section 4.

Table 2. R^2 Coefficients of Determination of Several Linear Relationships[a]

Linear Relation (Response; Predictors)	2009	2010	2011	All	All, $Q^\star$	$Q^\star$, val
$\log(Q)$; h,C	0.7684	0.8597	0.8676	0.8411	0.9093	0.9048
$\log(Q)$; $\log(h-h_0),C$	0.8947	0.9173	0.9074	0.8665	0.9251	0.9215
$\log(Q)$; σ,C	0.9261	0.9101	0.8054	0.8735	0.9320	0.9291
h; σ,C	0.8142	0.9210	0.8578	0.8751	0.8751	0.8690
$\log(h)$; σ,C	0.9306	0.9474	0.8713	0.8942	0.8942	0.8895
$\log(\sigma)$; $\sigma,\log(h-h_0),C$	0.9305	0.9263	0.908	0.8945	0.9546	0.9517
$\log(Q)$; $\sigma,\log(h-h_0),t_{\mathrm{hourofday}},T_w,C$	0.9381	0.9326	0.9283	0.8974	0.9590	0.9538

[a]R^2 calculated on the log-transformed streamflow values. Predictor C stands for a constant, i.e., a linear relation with intercept. Parameter h_0 is estimated for each column separately. $Q^\star$ are the corrected streamflow measurements, which are introduced in section 4. The last column shows the resulting R^2 values for leave-one-out cross validation. This allows a fairer comparison between models of different complexity.

h and σ from their respective estimates based on Q are a priori not very likely, the correlation may be the result of errors in the measurements of Q obtained from the salt dilution gaugings. This suspicion is supported by the fact that the R^2 of a direct relation between $\log h$ and σ is sometimes stronger than that of both variables' relation to Q (Table 2), while, logically, the causality in the relation would indicate Q as a cause and σ and h as effects.

[22] Because the calibration data from the gaugings were available, we were able to further investigate possible sources of errors in the gaugings of Q. One of the stored variables was the set of calibration coefficients κ [(mg/L)/ (μS/cm)] describing the slopes of the linear relations between σ and the concentration of the added NaCl salt in the water for each calibration preceding a gauging. Each calculation of Q_i from the salt wave (equation (1)) uses the values of κ_i from the calibration preceding gauging i. The EC measurement is temperature compensated, and therefore the calibration coefficient would be expected to be constant. Differences in the coefficient could occur either (1) as a result of probe fouling, poor connections, or other electronical causes or (2) as a result of differences (errors) in the calibration procedure, such as incorrect concentration in the calibration fluid, volume in the pipette, or initial water volume in the calibration reservoir.

[23] The first type of errors would not influence the gaugings of Q, since they are present in both the calibration and the actual gauging conductivities, but they would influence the measurements of base conductivity. This would, however, not explain the correlation between the residuals depicted in Figure 5. The second type of errors, those in the calibration procedure, would influence the measurements of Q, through errors in calibration coefficient κ and therefore explain the correlated residuals. In that case, one would also expect the calibration coefficients to be correlated to the residuals of both the $Q(h)$ and the $Q(\sigma)$ relationship.

4.2. Correction for Discharge Measurements

[24] The results summarized in Table 3 confirm the second hypothesis and indicate that errors in the calibration procedure (whose exact sources are for the moment unknown) are a likely cause of errors in Q. Gauged values for Q are inversely proportional to the coefficients κ used in their calculation, which mostly varied in the range 0.37–0.55, with five outliers around 0.87. When we assume all variation in κ to be the result of calibration errors, the gauged values of Q can be corrected by undoing the calibration:

$$Q_i^\star = \frac{\kappa_i}{\overline{\kappa}} Q_i, \qquad (5)$$

where $Q_i^\star$ is the corrected value for Q_i at gauging i and $\overline{\kappa}$ is the mean over all calibration coefficients. When $Q^\star$ is used as a variable in the rating curves, the strength of both the $Q^\star(h)$ and $Q^\star(\sigma)$ relationships improve those of $Q(h)$ and $Q(\sigma)$, see Figures 6 and 7 and Table 4. The uncertainty as measured by the standard deviation of the residuals in $\log Q$ was reduced by 28.6% for $Q(\sigma)$. The R^2 for all relations using $Q^\star$ are shown in the last column of Table 2.

[25] It must be noted that we are dealing with reducing and quantifying observational uncertainty, without access to golden standard observations. This precludes objective, assumption-free evaluation of the predictions (in fact, this is true for all science but is generally less evident). The better fits on the relationships can therefore only be interpreted as improvements when the interpretations and assumptions on causes of the scatter (Table 3) hold. In absence of more likely explanations for the improvements in the predictions, we believe they are probably closer to the truth; see also the discussion in *Weijs and Van de Giesen* [2011].

[26] Under these assumptions, the total reduction in uncertainty due to the use of auxiliary information on the

Table 3. Coefficients of Determination for Identification of Measurement Error Causes

Variables	R^2	Interpretation
res $Q(h)$, res $Q(\sigma)$[a]	0.404	Measurement errors in Q or common cause for deviations in σ and h
κ, res $Q(h)$	0.476	Scatter in $Q(h)$ relationship partly explained by errors in Q induced by κ
κ, res $Q(\sigma)$	0.468	Scatter in $Q(\sigma)$ relationship partly explained by errors in Q induced by κ
κ, σ	0.001	Variations in measured EC not explained by instrumentation errors
res $Q^\star(h)$, res $Q^\star(\sigma)$	0.086	Correction of Q for variations in κ, reduces correlation between residuals
$Q^\star(h)$	0.925	Much sharper relation in the rating curve for h when Q is corrected
$Q^\star(\sigma)$	0.932	Much sharper relation in the rating curve for σ when Q is corrected
$Q^\star(h,\sigma)$	0.955	Combining h and σ further improves, adjusted $R^2 = 0.954$

[a]"res" indicates residuals in $\log Q$ from the given relationship All are calculated on the entire data set.
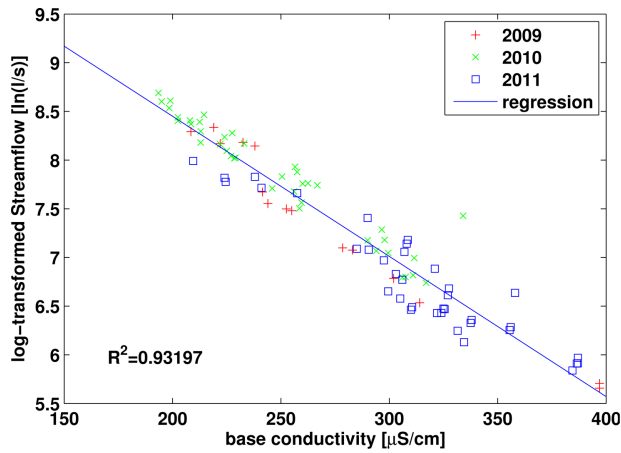
Figure 6. Relation between EC and the natural logarithm of the corrected streamflow.

calibration coefficients κ and base-conductivities σ_b can be calculated. This is done by comparing the initial scatter around the $Q(h)$ relation to the scatter around the rating curve $Q^\star(h, \sigma)$. The latter curve uses both water level and EC and corrects the streamflow gaugings by undoing the calibration procedure, using information from the previously applied calibration coefficients κ. Since the uncertainty is still best described by a lognormal heteroscedastic model, the relative errors are more of interest than the absolute, in terms of information gain. We, therefore, characterize the uncertainty by the root-mean-squared error in the log-transformed streamflows computed from the relations; see the scatter plots in Figure 8 and interpretation in Figure 9. The total percentual reduction in streamflow uncertainty around the rating curve can thus be characterized by

$$1 - \frac{\text{RMSE} \log Q^\star(h, \sigma)}{\text{RMSE} \log Q(h)} * 100\% = 43.7\%.$$

In terms of the untransformed Q, this means the RMS multiplicative error went down from a factor 1.36 to a factor 1.19.

5. Summary and Further Work

[27] The main finding of this work is that EC presents a major opportunity to improve continuous streamflow series

for alpine streams. For the stream considered in this paper, the EC has a predictive power apparently comparable to that of water level. Detailed analysis of the residuals of both relations in conjunction with the calibration data revealed the calibration coefficients as a likely correctable source of error in the gaugings. Assuming it is correct, this correction, combined with both water level and EC as streamflow predictors, leads to an additional reduction of uncertainty in the stage-discharge relationship, bringing the total reduction in uncertainty to 43.7%.

[28] The results presented here can have significant practical value, since salt dilution gauging is a common method for determining discharge in alpine streams. The predictive power of natural EC can be readily checked for other streams where data from salt dilution gaugings is available. Whether this power is present depends on the dynamics of the catchment. If a strong relation is found, it is advisable to monitor EC continuously and try to use it in a predictive model for streamflow. It should be noted, however, that time lags and hysteresis in the EC signal can cause artifacts in the discharge series. It is probably best to use EC alongside water level as a predictor, rather than replacing it. Furthermore, using a more physically based dynamic and mechanistic model is preferred over simple regression to optimally combine information from both sources to track variations in streamflow on all timescales. Such models could make predictions that are more transferable to other catchments and perform better under changing conditions such as land use.

[29] When predictive power is found in the EC snapshots from the Q gaugings, various analyses of the residuals, like the ones presented here, may further help to identify errors and point to their sources, in our case, the calibration coefficients as a source of error for measured Q. This is of course equipment and procedure specific rather than catchment specific. Especially, in morphologically dynamic streams, EC might be useful as an independent input to supplement standardized error checking procedures already in place at the agencies responsible for streamflow measurement [see, e.g., *Kennedy*, 1984; *Sauer*, 2002; *World Meteorological Organization* (*WMO*), 2010]. Although results may vary from case to case, we hope that this paper inspires ideas to take a closer look at the data underlying rating curves and discharge data, as this might significantly reduce uncertainties in the final streamflow series. This extraction of information from various data fits well into a more probabilistic view on streamflow measurements as
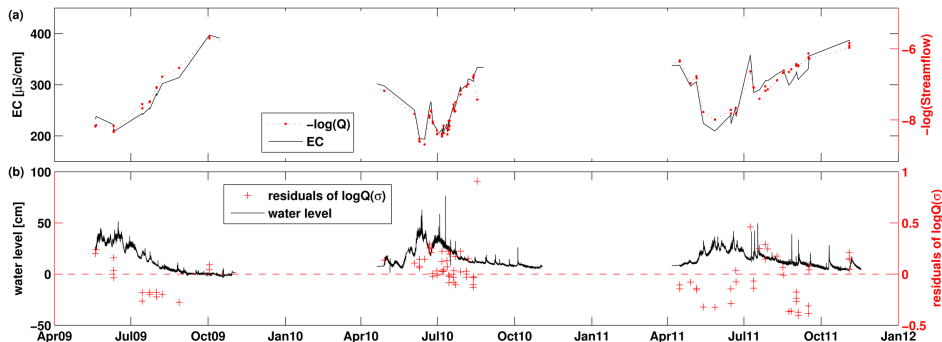
Figure 7. Updated version of Figure 4, now based on the corrected streamflow values $Q^\star$.

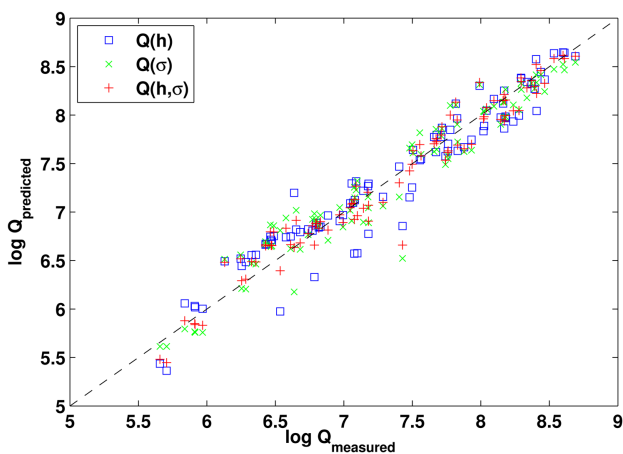**Table 4.** Parameters and Coefficients of Determination for $Q^\star(h)^a$

	Lin				Log			
	2009	2010	2011	All	2009	2010	2011	All
α	11.49	59.42	14.26	4.67	47.61	10.40	0.86	0.09
β	1.58	1.27	1.53	1.87	1.23	1.70	2.20	2.77
h_0	8.75	−2.29	2.69	5.81	4.14	3.36	10.70	16.68
R^2	0.97	0.93	0.97	0.93	0.99	0.92	0.96	0.92

[a]Curves of the form $Q^\star = \alpha(h - h_0)^\beta$. Updated version of Table 1 after correction of Q.
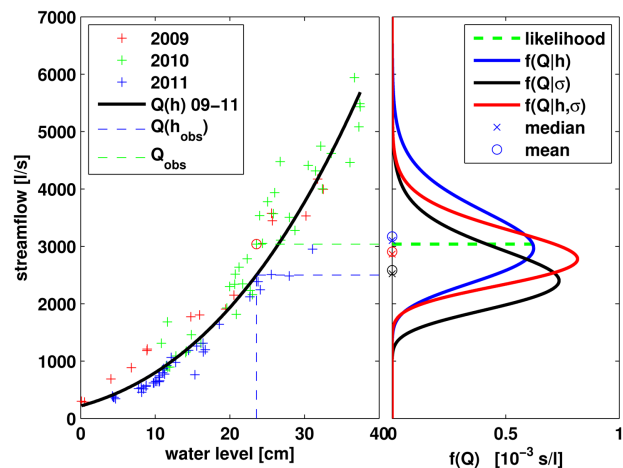
being model forecasts with predictive uncertainties, which should not be hidden but rather explicitly presented to aid hydrological modeling.

[30] While for the current analysis, only sparse EC measurements were available that were collected during the streamflow gaugings, continuous EC measurements at higher temporal resolution have now been deployed. This will give insight in the daily patterns. Since previous research has shown that EC signals can lag behind the streamflow signals by a few hours [*Gurnell and Fenn*, 1985], a model taking this into account may further improve the streamflow estimation and will possibly give more insight in hyporheic exchanges caused by diurnal cycles [*Loheide and Lundquist*, 2009]. This also allows more detailed analysis of temporal patterns of rainfall response or snow melt events, especially when tributaries are monitored for both EC and stage [*Lundquist et al.*, 2009]. Monitoring EC in different water sources, such as tributaries, groundwater wells, and glacier melt, may improve estimates and give more insight in the hydrological processes. In future research, we plan to advance this insight by using EC measurements in combination with analysis of isotopes, chemical analysis, and distributed modeling based, for instance, on travel time distributions [see e.g. *Szilagyi and Parlange*, 1999; *Rinaldo et al.*, 2006; *Kampf and Burges*, 2007; *Nicótina et al.*, 2008; *Botter et al.*, 2008].

[31] Ongoing research focuses on how to incorporate various sources of information in a dynamic model of

Figure 9. $Q(h)$ curve for 2009–2011 (left) with observations, (right) with predictive conditional distributions based on h, σ, and both h and σ, using the corrected streamflow values $Q^\star$, assuming constant variance in $\log Q$. Due to the backtransform, the curves fitted on the log-transformed values minimize mean relative error and give the median instead of the expected value for the distributions of Q. The green dashed line on the right gives the likelihood of the observed value, for the $Q(h)$ model.

streamflow uncertainty. Once a continuous EC signal is available, this enables the use of the long-term stable $Q(\sigma)$ relationship, while h can be used to track fast variations. The dynamic model can then combine both information sources to provide a probabilistic streamflow time series. These can subsequently be used to aid model inference while balancing maximum extraction of information and minimum extraction of misinformation. This is achieved by having sharp and reliable uncertainty estimates based on all available relevant information.

Figure 8. Scatter plot of gauged $\log Q^\star$ versus predicted by the final models based on water level, EC, and both predictors.

References

Anagnostou, E., W. Krajewski, and J. Smith (1999), Uncertainty quantification of mean-areal radar-rainfall estimates, *J. Atmos. Oceanic Technol.*, *16*(2), 206–215, doi:10.1175/1520-0426(1999)016<0206:UQOMAR>2.0.CO;2.

Botter, G., F. Peratoner, M. Putti, A. Zuliani, R. Zonta, A. Rinaldo, and M. Marani (2008), Observation and modeling of catchment-scale solute transport in the hydrologic response: A tracer study, *Water Resour. Res.*, *44*, W05409, doi:10.1029/2007WR006611.

Botter, G., E. Milan, E. Bertuzzo, S. Zanardo, M. Marani, and A. Rinaldo (2009), Inferences from catchment-scale tracer circulation experiments, *J. Hydrol.*, *369*(3–4), 368–380, doi:10.1016/j.jhydrol.2009.02.012.

Brutsaert, W., and J. Nieber (1977), Regionalized drought flow hydrographs from a mature glaciated plateau, *Water Resour. Res.*, *13*(3), 637–643, doi:10.1029/WR013i003p00637.

Ciach, G., and W. Krajewski (1999), Radar-rain gauge comparisons under observational uncertainties, *J. Appl. Meteorol.*, *38*(10), 1519–1525, doi:10.1175/1520-0450(1999)038<1519:RRGCUO>2.0.CO;2.

Collins, D. (1979), Quantitative determination of the subglacial hydrology of two alpine glaciers, *J. Glaciol.*, *23*(89), 347–362.

Collins, D., and G. Young (1981), Meltwater hydrology and hydrochemistry in snow and ice-covered mountain catchments, *Nord. Hydrol.*, *12*(4–5), 319–34, doi:10.2166/nh.1981.026.

Day, T. J. (1976), On the precision of salt dilution gauging, *J. Hydrol.*, *31*(3–4), 293–306, doi:10.1016/0022-1694(76)90130-X.

Di Baldassarre, G., and A. Montanari (2009), Uncertainty in river discharge observations: A quantitative analysis, *Hydrol. Earth Syst. Sci.*, *13*(6), 913–921, doi:10.5194/hess-13-913-2009.

Duffy, C., and J. Cusumano (1998), A low-dimensional model for concentration-discharge dynamics in groundwater stream systems, *Water Resour. Res.*, *34*(9), 2235–2247, doi:10.1029/98WR01705.

Duffy, C. J. (2010), Dynamical modelling of concentration-age-discharge in watersheds, *Hydrol. Processes*, *24*(12), 1711–1718, doi:10.1002/hyp.7691.

Dzikowski, M., and S. Jobard (2011), Mixing law versus discharge and electrical conductivity relationships: Application to an alpine proglacial stream, *Hydrol. Processes*, *26*(18), 2724–2732, doi:10.1002/hyp.8366.

Evans, C., and T. Davies (1998), Causes of concentration/discharge hysteresis and its potential as a tool for analysis of episode hydrochemistry, *Water Resour. Res.*, *34*(1), 129–137, doi:10.1029/97WR01881.

Gurnell, A., and C. Fenn (1985), Spatial and temporal variations in electrical conductivity in a pro-glacial stream system, *J. Glaciol.*, *31*(108), 108–114.

Kampf, S., and S. Burges (2007), A framework for classifying and comparing distributed hillslope and catchment hydrologic models, *Water Resour. Res.*, *43*, W05423, doi:10.1029/2006WR005370.

Kampf, S., and S. Burges (2010), Quantifying the water balance in a planar hillslope plot: Effects of measurement errors on flow prediction, *J. Hydrol.*, *380*(1–2), 191–202, doi:10.1016/j.jhydrol.2009.10.036.

Kavetski, D., G. Kuczera, and S. W. Franks (2006), Bayesian analysis of input uncertainty in hydrological modeling: 1. Theory, *Water Resour. Res.*, *42*, W03407, doi:10.1029/2005WR004368.

Kennedy, E. (1984), Discharge ratings at gaging stations, *U.S. Geol. Surv. Tech. of Water Resour. Invest.*, *10*(3), 59 p.

Kite, G. (1993), Computerized streamflow measurement using slug injection, *Hydrol. Processes*, *7*(2), 227–233, doi:10.1002/hyp.3360070212.

Kuczera, G., B. Renard, M. Thyer, and D. Kavetski (2010), There are no hydrological monsters, just models and observations with large uncertainties!, *Hydrol. Sci. J.*, *55*(6), 980–991, doi:10.1080/02626667.2010.504677.

Liebe, J., N. Van de Giesen, M. Andreini, M. Walter, and T. Steenhuis (2009), Determining watershed response in data poor environments with remotely sensed small reservoirs as runoff gauges, *Water Resour. Res.*, *45*, W07410, doi:10.1029/2008WR007369.

Loheide, S., II, and J. Lundquist (2009), Snowmelt-induced diel fluxes through the hyporheic zone, *Water Resour. Res.*, *45*, W07404, doi:10.1029/2008WR007329.

Lundquist, J., B. Huggett, H. Roop, and N. Low (2009), Use of spatially distributed stream stage recorders to augment rain gages by identifying locations of thunderstorm precipitation and distinguishing rain from snow, *Water Resour. Res.*, *45*, W00D25, doi:10.1029/2008WR006995.

Moore, R. (2005), Slug injection using salt in solution, *Streamline Watershed Manage. Bull.*, *8*(2), 1–6.

Nicótina, L., E. Alessi Celegon, A. Rinaldo, and M. Marani (2008), On the impact of rainfall patterns on the hydrologic response, *Water Resour. Res.*, *44*, W12401, doi:10.1029/2007WR006654.

Rinaldo, A., G. Botter, E. Bertuzzo, A. Uccelli, T. Settin, and M. Marani (2006), Transport at basin scales: 2. Applications, *Hydrol. Earth Syst. Sci.*, *10*(1), 31–48, doi:10.5194/hess-10-31-2006.

Salmon, C., M. Walter, L. Hedin, and M. Brown (2001), Hydrological controls on chemical export from an undisturbed old-growth Chilean forest, *J. Hydrol.*, *253*(1), 69–80, doi:10.1016/S0022-1694(01)00447-4.

Sauer, V. (2002), Standards for the analysis and processing of surface-water data and information using electronic methods, *U.S. Geol. Surv. Water Resour. Invest. Rep.*, *014044*, 91 pp.

Schoups, G., and J. A. Vrugt (2010), A formal likelihood function for parameter and predictive inference of hydrologic models with correlated, heteroscedastic, and non-Gaussian errors, *Water Resour. Res.*, *46*, W10531, doi:10.1029/2009WR008933.

Simoni, S., S. Padoan, D. Nadeau, M. Diebold, A. Porporato, G. Barrenetxea, F. Ingelrest, M. Vetterli, and M. Parlange (2011), Hydrologic response of an alpine watershed: Application of a meteorological wireless sensor network to understand streamflow generation, *Water Resour. Res.*, *47*, W10524, doi:10.1029/2011WR010730.

Singh, V. (2010), Derivation of rating curves using entropy theory, *Trans. ASABE*, *53*(6), 1811–1821.

Sorooshian, S., and J. Dracup (1980), Stochastic parameter estimation procedures for hydrologie rainfall-runoff models: Correlated and heteroscedastic error cases, *Water Resour. Res.*, *16*(2), 430–442, doi:10.1029/WR016i002p00430.

Szilagyi, J., and M. Parlange (1999), A geomorphology-based semi-distributed watershed model, *Adv. Water Resour.*, *23*(2), 177–187, doi:10.1016/S0309-1708(99)00021-4.

Szilagyi, J., M. Parlange, and J. Albertson (1998), Recession flow analysis for aquifer parameter determination, *Water Resour. Res.*, *34*(7), 1851–1857, doi:10.1029/98WR01009.

Thyer, M., B. Renard, D. Kavetski, G. Kuczera, S. Franks, and S. Srikanthan (2009), Critical evaluation of parameter consistency and predictive uncertainty in hydrological modeling: A case study using Bayesian total error analysis, *Water Resour. Res.*, *45*, W00B14, doi:10.1029/2008WR006825.

Vrugt, J. A., C. G. H. Diks, H. V. Gupta, W. Bouten, and J. M. Verstraten (2005), Improved treatment of uncertainty in hydrologic modeling: Combining the strengths of global optimization and data assimilation, *Water Resour. Res.*, *41*, W01017, doi:10.1029/2004WR003059.

Walter, M., B. Gao, and J. Y. Parlange (2007), Modeling soil solute release into runoff with infiltration, *J. Hydrol.*, *347*(3–4), 430–437, doi:10.1016/j.jhydrol.2007.09.033.

Weijs, S. V., and N. Van de Giesen (2011), Accounting for observational uncertainty in forecast verification: An information-theoretical view on forecasts, observations and truth, *Mon. Weather Rev.*, *139*(7), 2156–2162, doi:10.1175/2011MWR3573.1.

Weijs, S. V., G. Schoups, and N. van de Giesen (2010), Why hydrological predictions should be evaluated using information theory, *Hydrol. Earth Syst. Sci.*, *14*(12), 2545–2558, doi:10.5194/hess-14-2545-2010.

Westerberg, I., J. Guerrero, J. Seibert, K. Beven, and S. Halldin (2011), Stage-discharge uncertainty derived with a non-stationary rating curve in the Choluteca River, Honduras, *Hydrol. Processes*, *25*(4), 603–613, doi:10.1002/hyp.7848.

World Meteorological Organization (WMO) (2010), Manual on stream gauging, *Tech. Rep. 1044*, Geneva, Switzerland.

Extreme rainfall modeling in the Val Ferret watershed

The precipitation dataset collected in the Val Ferret watershed with the wireless network of meteorological station has been used to spatially model extreme rainfalls. The results of the study have been published with the following citation:

Thibaud E., Mutzner R. and Davison A.C., **2013**: Threshold modeling of extreme spatial rainfall, *Water Resources Research*, *49*, 4633-4644. doi: 10.1002/wrcr.20329.

The map of the Val Ferret catchment has been selected by the editor in chief to appear on the front of the August 2013 issue of *Water Resources Research*.

Mutzner Raphaël

Avenue de Milan 30, 1007 Lausanne, Switzerland
(+41) 76 439 41 20 / raphael.mutzner@gmail.com
Born the 19/06/1986
Swiss nationality (Maienfeld, GR)

PhD in Hydrology, Physicist

Education

2011-2015   **PhD. Candidate in Environmental Engineering**, École Polytechnique Fédérale de Lausanne, EPFL, laboratory of Environmental FLUid Mechanics (EFLUM)

2008-2010   **MSc., Physics**, École Polytechnique Fédérale de Lausanne, EPFL, Switzerland

2004-2008   **BSc., Physics**, École Polytechnique Fédérale de Lausanne, EPFL, Switzerland, with an exchange year (Erasmus) at **Universitat Barcelona**, Spain

---

Academic Projects

PhD thesis (2011 - 2015): Monitoring and modelling of hydrological processes in the upper Val Ferret

- **Project and team leader** of a monitoring campaign in the Val Ferret (VS): deployment and maintenance of 25 meteorological stations, discharge monitoring, water quality measurements.

- Study of hydrological processes in the Val Ferret catchment (streamflow diurnal cycles, spatial variability of evapotranspiration). Results published in *Water Resources Research*

- Development of a new geomorphological numerical model for recession discharge estimations in ungauged basins. Results published in *Water Resources Research*

Master Project at **CERN (Fall 2009)**: Study of collective effects in the Beam Delivery Service of the future Compact Linear Colider, establishing threshold for the beam pipe radius. Results presented at the **First International Particle Accelerator** (IPAC10) conference in Kyoto, Japan

---

Publications

1st author: **R. Mutzner et al.**, Geomorphic signatures on Brutsaert base flow recession analysis, *Water Resources Research*, 2013.
R. Mutzner et al., Controls on the diurnal streamflow cycles in a small alpine headwater catchment, *Water Resources Research*, 2014, *submitted*
R. Mutzner et al., Spatially heterogeneous drainage densities in a high-altitude alpine catchment and impact on travel time estimations, *Hydrological Processes*, 2014, *submitted*

2nd author: E. Thibaud et al., Threshold modeling of extreme spatial rainfall, *Water Resources Research*, 2013
S. Weijs et al., Could electrical conductivity replace water level in rating curves for alpine streams?, *Water Resources Research*, 2013

Languages

- French: native speaker
- German: native speaker
- English: professional working proficiency (C1)
- Spanish: fluent (B2)

Technical Skills / Expertise

Instrumentation: deployment and maintenance of **meteorological stations**, **discharge measurements** (Sommer Mess-systemtechnik MST-2, MADD SalinoMADD and Easyflow), **high frequency environmental sensors** (Sonic Anemometers, Li-Cor), numerous **data loggers** (Davis, Decagon, Hobo, MADD, Campbell Scientific), isotope analyser (Los Gatos Research), doppler wind lidar (halo photonics). Gestion de base de données.

Modelisation/ IT Skills: **Matlab** (advanced); Geographic Information Systems (**GIS**): **ArcGIS** (advanced), Quantum GIS; Programming languages: C++/C; Labview (beginner), Ansys (beginner), Igor Pro (beginner)

Soft Skills

- Significant contribution to the **writing of scientific publications** in peer-review journals, **reports** and **grant proposals**.
- Summarized data for presentation to local communities (commune d'Orsières, VS), scientific conferences (attendance of the American Geophysical Union meeting and the European Geosciences Union meeting several times)
- **Teaching assistant** for hydrology and mathematics courses. **Trained and supervised** students for academic projects and internships.

Awards

August 2013   Front page of the August 2013 *Water Resources Resources* Journal Issue

June 2012   2nd best poster at the Research Days of the School of Architecture, Civil and Environmental Engineering

June 2011   2nd best poster at the Research Days of the School of Architecture, Civil and Environmental Engineering

Professional Experience

Summer 2009   Internship at **CERN** with TERA Group, **medical physics**: optimization of the geometry and voltage parameters of a beam monitor used for hadrontherapy by means of numerical simulations with the software Ansys.

Spring 2007   Cell reconstruction by computer at the Blue Brain Project, EPFL

2002-2005   Working as an assistant 3 weeks per year at Glasbläserei Arthur Vuille AG CHUR, Switzerland, assembly of pH and redox electrodes. Acquired: work precision and reliability.